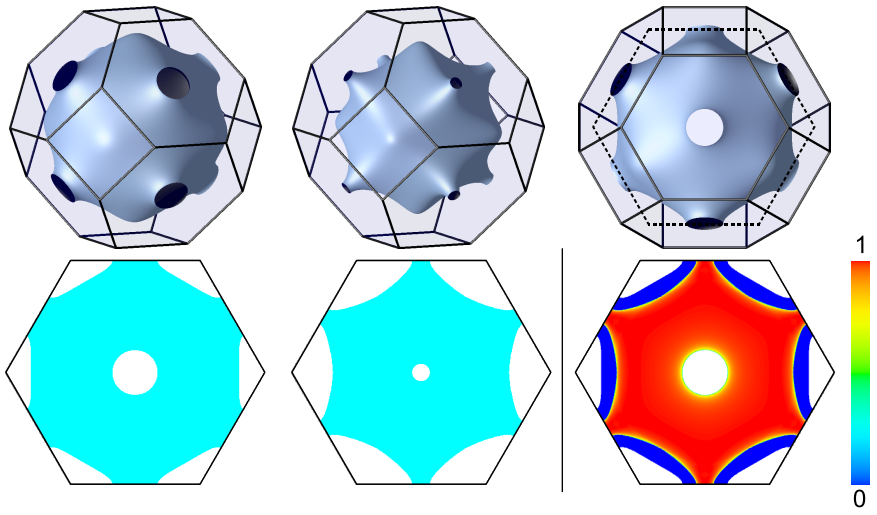


**SPIN TRANSPORT FROM FIRST-PRINCIPLES:
METALLIC MULTILAYERS AND A MODEL
SPIN-VALVE TRANSISTOR**



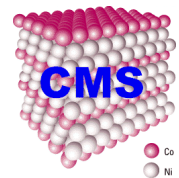
Mohand Talanana

Samenstelling promotiecommissie:

Prof. dr. H. Rogalla	Universiteit Twente, voorzitter
Prof. dr. P. J. Kelly	Universiteit Twente, promotor
Prof. dr. ir. D. H. A. Blank	Universiteit Twente
Prof. dr. W. J. Briels	Universiteit Twente
Prof. dr. R. A. de Groot	Radboud Universiteit Nijmegen
Dr. R. Jansen	Universiteit Twente
Prof. dr. P. Ordejón	Universitat Autònoma de Barcelona
Dr. M. Zwierzycki	Max-Planck-Institut, Stuttgart

MESA+

Institute for Nanotechnology



This work was supported financially by “MESA+ Research Institute” for nanotechnology, University of Twente, P.O Box 217, 7500 AE Enschede, The Netherlands.

The work described in this thesis was carried out at the “Computational Material Science” (CMS) group, Faculty of Science and Technology (TNW), University of Twente.

Spin transport from first-principles: metallic multilayers and a model spin-valve transistor.

M. Talanana,

ISBN: 90-365-2388-5

Thesis Universiteit Twente, Enschede.

Copyright © M. Talanana, 2006

Printed by FEBODRUK BV, Enschede

Cover: 3D Fermi surfaces, and their 2D projections, of Cu and Co maj. Bottom right is the transmission probability, $T(\mathbf{k}_{\parallel})$, for Cu|Co (111) maj. spin states (Fig. 2.5).

**SPIN TRANSPORT FROM FIRST-PRINCIPLES:
METALLIC MULTILAYERS AND A MODEL
SPIN-VALVE TRANSISTOR**

PROEFSCHRIFT

ter verkrijging van
de graad van doctor aan de Universiteit Twente,
op gezag van de rector magnificus,
prof. dr. W. H. M. Zijm,
volgens besluit van het College voor promoties
in het openbaar te verdedigen
op woensdag 12 juli 2006 om 15.00 uur

door

Mohand Talanana

geboren op 17 Maart 1973
te Iadjemat, Algerije

Dit proefschrift is goedgekeurd door:

Prof.dr. P. J. Kelly

promotor

*This work is dedicated to my beloved wife Dalila
to our son Masin
and to my parents and parents in law*

In memory of my aunt Fetta

Contents

1	Introduction	1
1.1	Magnetoelectronics	1
1.2	Electronic structure – DFT	6
1.3	Landauer–Büttiker approach	9
1.4	Spin-valve transistor	10
1.5	Thesis outline	12
	Bibliography	13
2	First-principles scattering matrices for spin-transport	17
2.1	Introduction	17
2.2	Theory	21
2.2.1	Muffin Tin Orbitals and the KKR equation	22
2.2.2	Eigenmodes of the leads	24
2.2.3	Scattering problem	26
2.2.4	Disorder	29
2.3	Calculations	31
2.3.1	Leads	32
2.3.2	Ordered Interfaces	35
2.3.3	Interface Disorder	42
2.3.4	Analysis of Interface Disorder Scattering	47
2.3.5	Interface resistance	49
2.4	Discussion	52
2.5	Summary	53
	Bibliography	54
3	Interface conductance and resistance of metallic multilayers	59
3.1	Introduction	59
3.2	Method	61
3.3	Cr Fe	62
3.3.1	Bulk materials	62

3.3.2	Interfaces without defects	66
3.3.3	Disordered interfaces	79
3.4	Interfaces with fcc materials: Cu Co, Cu Ni and Co Ni	81
3.4.1	Technical aspects	81
3.4.2	Magnetotransport results	84
3.5	Energy dependence	92
3.6	Discussion and Summary	97
	Bibliography	98
4	Orientation-dependent transparency of metallic interfaces	101
4.1	Introduction	101
4.2	Method	102
4.3	Orientation dependence of the transmission	103
4.4	Summary	107
	Bibliography	108
5	Parameter-free study of the electronic, magnetic and transport properties of a model spin-valve transistor structure	109
5.1	Introduction	109
5.2	Ground State Calculations	113
5.2.1	Method	114
5.2.2	Electronic Structure	115
5.3	Transmission Calculations	120
5.3.1	Defect-free Interfaces	122
5.3.2	Disordered interfaces	127
5.4	Discussion and Conclusion	130
	Bibliography	131
A	Appendix to Chapter 2	135
A.1	Velocities	135
A.2	Symmetry relations	136
	Bibliography	138
B	Appendix to Chapter 5	139
B.1	GaAs bulk band structure	139
	Bibliography	141
	Summary	143
	Résumé	147
	Samenvatting	151

Acknowledgments	155
List of publications	159
Curriculum vitae	161
Propositions	162
Summary for ITBE archives	165

Chapter 1

ntroduction

The topic of this thesis is to study spin-polarized transport through various hybrid interfaces, including metallic systems and the spin-valve transistor structure. In this chapter a general introduction is given to the field of magnetoelectronics. Some background of the calculation details, namely the density functional theory and the Landauer–Büttiker approach, are briefly introduced. A short description of the spin-valve transistor is provided.

1.1 Magnetoelectronics

The electron, akin to its electrical charge and mass, possesses another intrinsic property, resulting from its rotation around itself, which is the *spin*¹, an intrinsic angular momentum (\mathbf{S}) in quantum mechanics, and directly coupled to it a magnetic moment. The electron spin was virtually neglected in electronics until the interesting observation of the oscillatory interlayer exchange coupling observed in Fe|Cr and Co|Cu multilayers by Grünberg *et al.* [2] and Parkin *et al.* [3–5], and the near simultaneous discovery in 1988 by two research groups, in Paris and Jülich, of the *giant magnetoresistance* (GMR) effect first observed in Fe|Cr multilayers [6, 7]. The manipulation of this extra degree of freedom of the electron and the information it carries opened new and exciting challenges for conventional electronics. Since then a new discipline has emerged: magnetoelectronics [8, 9] which witnessed a dramatic grow and has developed into a vigorous field of research. It offers opportunities for a new generation of devices combining standard microelectronics with spin-dependent effects that arise from the interaction between spin of the carrier and the magnetic properties of the material. Adding the spin degree of freedom to conventional semiconductor charge-based electronics or using the spin degree of freedom alone will add substantially more capability and performance to electronic products.

GMR is a quantum mechanical effect observed in layered structures that are composed of alternating layers of ferromagnetic (FM) and nonmagnetic (NM) materials,

1. The spin of the electron was proposed theoretically in early 1925 by Kronig (unpublished) and Uhlenbeck and Goudsmit [1] after Stern-Gerlach experiment of 1921.

FM|NM|FM. Examples of GMR structures include various material combinations, namely Fe|Cr, Co|Cu, NiFe|Cu ... One ought to know that the electric current is carried by electrons of two different types according to whether their spin projection onto a given quantization axis is $\pm\hbar\frac{1}{2}$, two magnetic spin states, spin up and spin down. Nonmagnetic materials are characterized by the same number of electrons in both spin states. As for the magnetic materials there is an imbalance in the density of states at the Fermi energy (E_F) for spin up and spin down electrons. The dynamics and transport in these materials are different for the two types of electrons. According to Mott's "two current transport model"² [10–12] the transport in metals can be described in terms of two independent conducting channels, corresponding to the majority and minority spin carriers.

The GMR effect manifests itself as a significant decrease in resistance from the zero-magnetic-field state, when the magnetization of the adjacent ferromagnetic layers are antiparallel due to a weak anti-ferromagnetic coupling between layers, to a lower level of resistance when the magnetization of the adjacent layers align due to an applied external magnetic field. The directions of the magnetic moments are manipulated by external magnetic field that are applied to the materials. When the magnetic moments of the ferromagnetic layers are parallel, the spin-dependent scattering of the carriers is minimized, and the material has its lowest resistance. When the ferromagnetic layers are antialigned, the spin-dependent scattering of the carriers is maximized, and the material has its highest resistance. This change in resistance of the layered system under an applied magnetic field can be explained qualitatively as shown in Fig. 1.1. Each magnetic layer acts as a spin-selective valve. The magnetization orientation determines whether it transmits predominantly spin up or spin down electrons. Figs. 1.1c,d show the two current model that explains that this scattering results in a low-resistance for parallel alignment and a high resistance for antiparallel alignment. Note that the low resistance channel can correspond to the majority spin electrons, like in Cu|Co, or to the minority spin electrons, like in Cr|Fe, which can be explained from their respective band structures (see Chapter 3). The model above assumes that there is no spin flip, the spin up and down electrons travel independently in two separate spin channels. In practice electrons will change their spins due to spin-orbit coupling or magnon scattering.

The GMR phenomenon can be observed in two principal geometries: current in the plane of the layers (CIP) [6, 7] and current perpendicular to the planes (CPP) [13, 14] (Fig. 1.1). Most experiments in CPP-GMR are interpreted in terms of the two current series resistor model (2CSR) [15–17]. There are two types of structures where GMR can be observed, multilayers and spin-valves. In the first type, two or more ferromagnetic layers are separated by a very thin (~ 1 nm) non-ferromagnetic spacer (*e.g.* Fe|Cr|Fe). An antiferromagnetic coupling (mediated by a Ruderman-Kittel-Kasuya-Yosida (RKKY) type of interaction), at a certain thicknesses, is energetically preferable for the magnetizations of adjacent layers to align in anti-parallel.

2. The spin relaxation length, λ_{sf} , in metals is usually much larger than the elastic mean free path, ℓ_e . λ_{sf} expresses how far an electron can travel before it loses its spin information in diffusive transport. ℓ_e defines the average distance which an electron travels before it is elastically scattered at a defect.

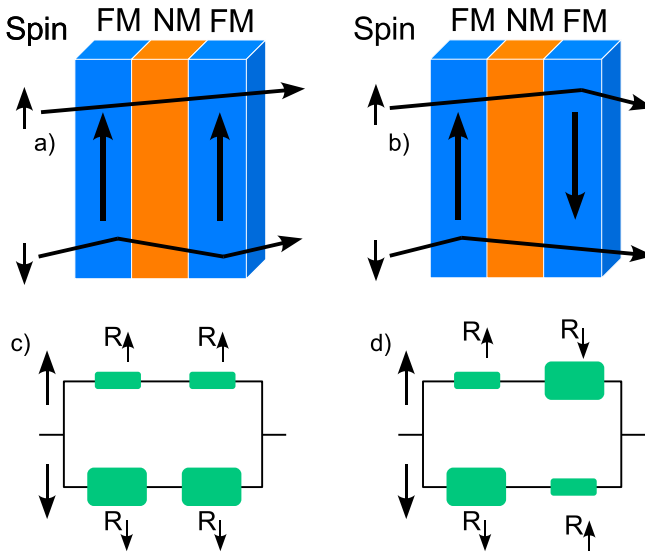


Figure 1.1: Schematic layout of the two states of a spin-valve structure and electron scattering in a magnetic|nonmagnetic multilayer. In antiparallel alignment (b) both type of electrons are subject to strong scattering while in the parallel orientation (a) only one type of electrons encounters a high resistant magnetic layer. The two current model shows that the parallel alignment (c) between the ferromagnetic layers results in a lower resistance than the antiparallel alignment (d).

The interlayer spacing in these devices typically corresponds to the second antiferromagnetic peak in the AFM-FM oscillation in the RKKY coupling. By applying an external magnetic field all the magnetizations are forced to align along the direction of the external field. In the second type, two ferromagnetic layers, separated by a thin (~ 3 nm) non-ferromagnetic layer (*e.g.* NiFe|Au|Co), have different coercivities or different switching properties therefore it is possible to switch them independently. In this way the relative orientation, parallel and anti-parallel alignment, between the two magnetic layers can be achieved. Transport from one electrode to the other is by conduction through these metals. Spin-valve GMR is the configuration that is most industrially useful, and is the configuration used in hard-drives. The magnetoresistance effect can also be observed in granular systems. It occurs in solid precipitates of a magnetic material in a non-magnetic matrix, *e.g.* matrices of copper containing cobalt granules.

Tunneling magnetoresistance (TMR) is another interesting phenomenon effect, sometimes referred to as junction magnetoresistance (JMR). In a spin-valve, the nonmagnetic spacer separating the two ferromagnetic electrodes is replaced by a thin (typically ~ 1 nm) insulator layer (FM|I|FM) to allow quantum mechanical current to flow. Such a structure is referred to as a magnetic tunnel junction (MTJ). For

device applications it is desirable to make the tunneling barrier as thin as possible to match the resistance of the MTJs to other electronic components. In the MTJ structure spin-polarized electrons tunnel from one ferromagnetic electrode through an insulating thin barrier into the second ferromagnetic electrode. The tunnel barrier is thin enough to allow a spatial overlapping between the wave functions from both electrodes. In general, the tunnel effect is a well-known textbook example where the quantum mechanical nature of electrons (or other particles in a world where the length scale is comparable to the de Broglie wavelength) is demonstrated. In short, the wavefunction of the particle can penetrate regions where the potential is higher than the particle total energy, for example scattering of a particle by a potential barrier. The phenomenon of TMR is a consequence of spin-dependent tunneling due to an imbalance in the electrical current carried by the spin down and spin up electrons.

In the past few years there was a tremendous scientific interest in studying the GMR and TMR effects as well as in the technological applications of the GMR elements and MTJ structures. They have attracted much attention of many researchers and engineers due to their potential application in magnetoelectronics devices such as magnetic field sensors, read-head for magnetic hard disk drives and magnetic random access memory (MRAMs). The latter store data using the spin information or magnetism than electrical charges, hence the nonvolatility of MRAMs. They retain their states even when the power is turned off. The memory is made from a two dimensional array of MTJs or GMR elements each serving as one bit. Reading is done by measuring the resistance (voltage response to a bias current pulse) and writing is performed with use of magnetic fields inductively induced by current pulses in an adjacent wire. Due to the size of magnetoresistance in GMR elements and MTJs, the former (with lower resistance) are suitable for hard drive technology and the latter (with larger resistance) for memory devices. Besides the nonvolatility, the advantages of these exotic devices combine increased data processing speed, decreased electric power consumption, increased integration densities and nondestructive readout.

The diversity of the physical phenomena that control the operation of these magnetoresistive devices makes GMR elements and MTJs also very attractive research subject from the fundamental physics point of view. They stimulated very intense research activity where many experiments and theoretical studies have been conducted, primarily, to understand the physical phenomena of GMR/TMR and to investigate the conditions to enhance the magnetoresistance ratio. Key players include electronic properties, nanoscale magnetism and spin transport which play an important role in the field of magnetic thin films. For more details of the physics relevant to GMR in CPP geometry and TMR effects we refer to the reviews [13, 18–23].

Electronically, the natural progression and crucial ingredient for *semiconductor based spintronics* is the ability to inject a (highly) spin-polarized current into a semiconductor [24]. A generic spin electronic device consists of a ferromagnetic injector at one end, a semiconducting transport medium (either an ordinary or magnetic semiconductor), and a spin detector on the other end. This should result in a conductance which depends on the relative orientation of the two contacts magnetizations [25]. It operates as follows: spin-polarized electrons are injected from a magnetic source (injector), manipulated and controlled with a gate above the semiconducting trans-

port medium before they are collected at the magnetic drain (detector). Connecting the many new possibilities of spin-dependent transport properties in ferromagnets with the semiconductor world require that the ferromagnetic injector and detector are materials having high spin polarization and compatibility with the transporting medium. This topic has been reviewed in [26].

To obtain a measurable spin-polarized current in the transport medium, the ratio of the conductivity of the injector-contact σ_{FM} to the conductivity of the transport medium (semiconductor) σ_{SC} has to be smaller or at least close to one, *i.e.* $\sigma_{FM}/\sigma_{SC} \sim 1$ [27]. This calculation neglects spin scattering at the interface among other assumptions, but it does point towards the difficulty of direct spin injection from a ferromagnet into a semiconductor. Up to now spin injection from a ferromagnetic metals, as Fe, into a semiconductor, as GaAs, have shown a current spin-polarization of only about 2% at room temperature [28]. Partial solutions to this problem have been suggested. This includes injection of spin-polarized electrons via an insulator tunnel barrier between the ferromagnet and the semiconductor [29]. Subsequent theoretical investigations examined the effect of spin-dependent interface resistance at the FM|SC contact, as shown in the example of Fe|InAs [30–32]. High spin injection efficiency of 30% extending to room temperature were reported experimentally [33]. Alternatively, a second and also practical solution would be to start with a less conventional ferromagnets: diluted magnetic semiconductors (DMS). One should mention that ferromagnetism of DMS is one of the most important topics in spintronics, experimentally as well as theoretically. DMS materials, however, are proved to be limited to low temperature since their ferromagnetic transition temperature, Curie T_C , is only of the order of 100 K [34, 35], and are *p*-type doped. Holes are known to lose their spin information by orders of magnitude faster than electrons due to spin-orbit coupling at the valence band. Another approach is to use half-metallic ferromagnets [36]. These materials are predicted to be 100% spin-polarized ferromagnetic injectors. One of the many challenges in spintronics and materials science is the search for optimizing these materials and the development of new ones. It would be desirable, as an ultimate goal, to be able to inject spins into silicon at room temperature. While GaAs is of great importance, the control of spin in silicon would raise hopes for seamless integration of spintronics with the current information technology.

Future progress in spin-polarized transport will be largely driven by the materials advances as well as theoretical understanding which takes into account accurately the ferromagnetic character of the materials. In the context of spin transport effects mentioned earlier (GMR, TMR, oscillatory exchange coupling and spin injection-detection in semiconductors [37]), typical magnetoelectronic structures are a combination of ferromagnetic metals (like Fe, Co, Ni and their alloys, namely soft magnetic permalloys) with thin layers of normal metals (Al, Cr, Cu, Au, . . .), insulators (*e.g.* MgO) and semiconductors (like GaAs) to form hybrid structures. Basic research in magnetoelectronics is moving rapidly to smaller structures and novel materials. As devices are reduced in size, interfaces start to dominate electrical transport making it essential to be able to describe reliably how they transmit and reflect electrons. Quantum mechanical calculations have shown that interface scattering is very significant [38, 39] and often dominates the device properties. It is clear that

a systematic materials-specific study of the effects of magnetic interfaces and materials inhomogeneities on spin-polarized transport, taking into account the non-trivial spin-dependence of the transmission and reflection of electrons at these magnetic interfaces, is the key to understanding the physical phenomena mentioned above. A comprehensive transport calculation [40] (Chapters 2 & 3) in the actual devices (Chapter 5) with detailed knowledge of the realistic electronic structure of the studied materials would provide valuable insights into both the spin-polarized transport in these materials and confrontation with experiments. For well-studied material combinations such as Co|Cu and Fe|Cr, modest spin-dependence of the interface transmission [41–43] of the order of 10-20% is sufficient to account for experimental observations [13].

1.2 Electronic structure – DFT

The computational method used in this work is based on the local spin-density approximation (LSDA) of the density functional theory (DFT) [44]. DFT is the most widely used method for sophisticated electronic structure calculations. The approach proposed by Kohn and Sham [45] allows the description of electronic systems, or many particle systems in general, whether they are atoms, molecules, or solids in terms of the electron density $n(\mathbf{r})$ (the number of electrons per unit volume at point \mathbf{r} in the material): it replaces the original many-body problem by an auxiliary independent-particle problem. This framework provides a means to construct an effective single-particle potential that determines electronic motion through the corresponding Schrödinger equation whose solutions determine the particle density. At the same time, the first-principles surface Green's function (SGF) technique [46], formulated within the framework of tight-binding linear muffin-tin orbitals (TB-LMTO) in atomic sphere approximation (ASA) [47], offers a very convenient way to solve this equation under the various boundary conditions that are associated with different geometric arrangements of atoms, *e.g.*, surfaces and interfaces, impurities, and disordered materials. To treat efficiently these inhomogeneities in a realistic band structure calculation we make use of the coherent potential approximation (CPA) [46]. In practice, it is often a good approximation to use the theory of LSDA, in which one applies relations involving the density of the homogeneous electron gas to the density at \mathbf{r} of the inhomogeneous system, the electron density $n(\mathbf{r})$ varies relatively little over a characteristic (local Fermi) wavelength ($\lambda_F = \frac{2\pi}{k_F} \equiv [3\pi^2 n(\mathbf{r})]^{-\frac{1}{3}} \approx 5\text{Å}$ for all transition metals) of the electrons in the system. This DFT-LSDA approach has become the primary tool for accurate calculations of the electronic properties in condensed matter, molecules and other finite systems.

The original formulation of the density functional theory was based on the paper written by P. Hohenberg and W. Kohn in 1964 [48]. Their approach is to formulate DFT as an exact theory of many body systems. These authors showed (first theorem) that a special role can be assigned to the electron density $n(\mathbf{r})$, it is considered as *the basic variable* (instead of the single particle wavefunction as in Hartree-Fock approximation) and all the ground state properties of the system (*e.g.* the total

energy), evolving in an external potential $V_{ext}(\mathbf{r})$, can be considered to be *unique functionals* of the ground state density. DFT becomes complete with the second theorem which provides a variational principle for the energy: for any particular $V_{ext}(\mathbf{r})$, the electron density $n(\mathbf{r})$ that minimizes the energy is the exact ground state density.

To obtain the ground state density $n(\mathbf{r})$, Kohn and Sham approach is to replace the difficult interacting many body system with a some different chosen non-interacting system where the external potential $V_{ext}(\mathbf{r})$ is replaced with an effective potential $V_{eff}(\mathbf{r})$. This leads to independent-particle equations for the non-interacting system that can be considered exactly soluble (numerically) with all the difficult many body terms incorporated into an *exchange-correlation functional of the electron density*. By solving the equations one finds the ground state density and energy of the original interacting system with the accuracy limited only on the type of functional used for the exchange-correlation potential. The single-particle Schrödinger equation for this non-interacting system is

$$H_{\sigma} \Psi_{i\sigma}(\mathbf{r}) = [-\nabla^2 + V_{eff}^{\sigma}(\mathbf{r})] \Psi_{i\sigma}(\mathbf{r}) = \varepsilon_{i\sigma} \Psi_{i\sigma}(\mathbf{r}), \quad (1.1)$$

σ (\uparrow or \downarrow) is the spin index. Let us note that we have made use of Rydberg's atomic units with $\hbar = 1$, $2m_e = 1$, and $e^2 = 2$, where m_e and e denote the electron mass and charge, respectively; and

$$\begin{aligned} V_{eff}^{\sigma}(\mathbf{r}) &= V_{ext}(\mathbf{r}) + V_H(\mathbf{r}) + V_{xc}^{\sigma}(\mathbf{r}) \\ &= V_{ext}(\mathbf{r}) + \int \frac{2n(\mathbf{r}')}{|\mathbf{r} - \mathbf{r}'|} d\mathbf{r}' + \frac{\delta E_{xc}[n_{\uparrow}, n_{\downarrow}]}{\delta n_{\sigma}(\mathbf{r})} \end{aligned} \quad (1.2)$$

$V_{ext}(\mathbf{r})$, $V_H(\mathbf{r})$ and $V_{xc}^{\sigma}(\mathbf{r})$ are the external potential (due to the interaction with ions and any other external fields), Hartree potential and the exchange-correlation potential of the electrons, respectively. The Kohn-Sham single-particle solutions $\Psi_{i\sigma}(\mathbf{r})$ of the equations (1.1) (there are N of them for N electrons in the system) can be used to express the ground state electron density $n_{\sigma}(\mathbf{r})$

$$n_{\sigma}(\mathbf{r}) = \sum_{i=1}^N |\Psi_{i\sigma}(\mathbf{r})|^2 \quad (1.3)$$

where the summation is carried out over all the N individual occupied orbitals.

The electron and magnetization densities are, respectively, given by

$$n(\mathbf{r}) = n_{\uparrow}(\mathbf{r}) + n_{\downarrow}(\mathbf{r}) \quad (1.4)$$

and

$$m(\mathbf{r}) = n_{\uparrow}(\mathbf{r}) - n_{\downarrow}(\mathbf{r}) \quad (1.5)$$

Eqs. (1.1), (1.2) and (1.3) are called the Kohn-Sham equations; in practice, they are solved *self-consistently*: one begins with a guess for $n_{\sigma}(\mathbf{r})$ and uses it to construct $V_{eff}^{\sigma}(\mathbf{r})$ from Eq. (1.2). This $V_{eff}^{\sigma}(\mathbf{r})$ is used in Eq. (1.1) to determine a set of orbitals,

$\Psi_{i\sigma}(\mathbf{r})$, which yield a new electron density through Eq. (1.3). The process is repeated until the difference between the input and the output electron densities (and potentials) falls below a predetermined value. The ground state total energy functional is given by

$$E = \sum_{i=1}^N \varepsilon_i - \iint \frac{n(\mathbf{r})n(\mathbf{r}')}{|\mathbf{r}-\mathbf{r}'|} d\mathbf{r} d\mathbf{r}' - \int V_{xc}(\mathbf{r})n(\mathbf{r})d\mathbf{r} + E_{xc}[n] \quad (1.6)$$

Note that the total energy is not the sum of orbital energies. The eigenvalues ε_i of the Kohn-Sham Hamiltonian H do not correspond to the quasi-particle excitation energies, only their sum which corresponds to a part of the total energy of the ground state Eq. (1.6). Idem for the single-particle Kohn-Sham solutions $\Psi_{i\sigma}(\mathbf{r})$, they do not correspond to one electron wavefunctions, conceptually, they are mathematical quantities which were introduced to solve the Kohn-Sham equations Eq. (1.1) and constructing the electron densities Eq. (1.3).

The Kohn-Sham equations, in principle, they allow an exact treatment of the ground state of the many body problem in terms of the theory of the independent-particle form. However, it should be mentioned that in reality an exact treatment is not possible because $E_{xc}[n]$ is not known exactly. This points out that approximations have to be made for further progress. Kohn-Sham suggested the use of the uniform-electron-gas formula for handling the unknown parts of the energy functional. Thus, one applies uniform-electron-gas results to infinitesimal volumes in the interacting system that contains $n(\mathbf{r})d\mathbf{r}$ electrons, and sums up these local contributions over all space. The resulting scheme is the most widely used approximation for $E_{xc}[n]$ and is called the local spin-density approximation (LSDA) to density functional theory. The exchange-correlation energy is given by

$$E_{xc}^{LSDA}[n_{\uparrow}, n_{\downarrow}] = \int n(\mathbf{r})\epsilon_{xc}[n_{\uparrow}(\mathbf{r}), n_{\downarrow}(\mathbf{r})]d\mathbf{r}, \quad (1.7)$$

where $\epsilon_{xc}[n_{\uparrow}(\mathbf{r}), n_{\downarrow}(\mathbf{r})]$ is the exchange-correlation energy per particle of uniform electron gas with uniform spin densities $n_{\uparrow}(\mathbf{r})$ and $n_{\downarrow}(\mathbf{r})$. Various expressions for the exchange-correlation energy and potential are available to be used in LSDA. The most frequently employed parametrizations are due to von Barth and Hedin [49], Ceperley and Alder [50] as parametrized by Perdew and Zunger [51] and Vosko, Wilk and Nusair [52].

The DFT-LSDA have been remarkably successful in describing the ground state properties of a large range of physical systems. It proved to be surprisingly powerful in band structure calculations of transition metals and alloys. Examples of these *first-principles* (no adjustable parameters are used) electronic structure and Fermi surface calculations for selected materials (Fe, Cr, Co, Ni, Cu, Al, Ag, ... and GaAs) are shown throughout this thesis. Other approximations used in these calculations, namely the wavefunctions and the shape of the potentials, are presented in Chapter 2

1.3 Landauer–Büttiker approach

Ab initio calculations of electronic transport became an important tool for the interpretation of quantum transport experiments on the atomic scale. In this section we describe briefly the Landauer–Büttiker approach and its basic assumptions. The Landauer–Büttiker scattering theory of transport is an established method for describing transport in *mesoscopic* systems, where the system size plays an important role in determining the conductances.

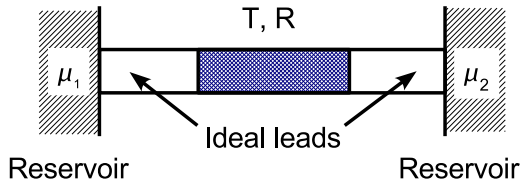


Figure 1.2: One dimensional wire connected at both ends to reservoirs via ideal leads illustrating the two-terminal transport configuration of the Landauer–Büttiker formalism.

Let us start by deriving the Landauer formula. Landauer [53, 54] related the linear response conductance of one-dimensional wire to the transmission and reflection probability at the Fermi energy. Let us consider the basic measuring setup as shown in Fig. 1.2. A sample wire, that we wish to study the transport properties, is connected at both ends to two ideal wires which are infinitely long and eventually connected to two big reservoirs (or contacts) which are at thermodynamic equilibrium, with small electrochemical potential difference $\Delta\mu = \mu_1 - \mu_2$. μ_1 and μ_2 represent the chemical potential of the two left and right reservoirs, respectively, and T and R are the transmission and reflection probability, respectively, of the wire. The conservation of the number of particles requires $T + R = 1$. The leads are assumed to be ballistic conductors. Further, we assume that all incident electrons are absorbed by the reservoir irrespective of their energy and phase, the reservoirs are reflectionless and they provide constantly electrons with energy below the chemical potential. Assuming zero temperature, current flows between the energy range μ_1 and μ_2 . Let v be the electron velocity at the Fermi energy and $dn/dE = 1/\pi\hbar v$ the density of states for electrons moving from left to right. Thus the total flowing current across the system is given by

$$I = (-e)v \frac{dn}{dE} T(\mu_1 - \mu_2) \quad (1.8)$$

The voltage difference $\mu_1 - \mu_2 = -eV_{21}$ and e is the electron charge and V_{21} between reservoir 2 (at right side of Fig. 1.2) and reservoir 1 (at left hand side of Fig. 1.2).

Therefore the two terminal conductance measured between 1 and 2 is given by

$$G = \frac{I}{V_{21}} = \frac{e^2}{\pi\hbar} T \quad (1.9)$$

which is finally the single-channel *Landauer formula*³ [53, 54]. This relation between the conductance and the transmission probability is frequently used as the basis of understanding the transport in mesoscopic systems. The potential drop associated with the resistance (inverse of the conductance) given by Eq. (1.9) occurs at the connections to the reservoirs. Note that it does not matter whether the transmission probability T in Eq. (1.9) is determined by a single highly localized barrier or by a more extended and complex potential profile.

Büttiker and coworkers have generalized the Landauer formula to systems in which multiple independent conducting channels are present [56]. They use the transmission matrix t of the scattering obstacle, which specifies the transmitted wave functions relative to the incident wave, utilizing the transverse eigenstates of the channel as a basis. The Landauer-Büttiker scattering formalism is an approach describing quantum-mechanically electronic transport in atomic sized structures [55]. In a two-terminal measurement, the The Landauer-Büttiker conductance of a spin-polarized system calculated at the Fermi energy is given by

$$G^\sigma = \frac{e^2}{2\pi\hbar} \text{Tr}(tt^\dagger) = \frac{e^2}{h} \sum_{i,j} |t_{ij}^\sigma|^2 \quad (1.10)$$

where $t_{i,j}^\sigma$ being the transmission probability amplitude between incoming states j from the left-lead and outgoing states i in the right-lead, σ labels the spin and e^2/h is the conductance quantum. Usually the leads are assumed to have periodical symmetry, hence the eigenmodes satisfy Bloch theorem. The details of our implementation of transport theory based on the Landauer-Büttiker scattering formalism is presented in Chapter 2.

1.4 Spin-valve transistor

In this section we will discuss the main features of a hybrid device containing ferromagnetic and semiconductor materials. This device is the *spin-valve transistor* (SVT). The SVT was introduced for the first time at the university of Twente in 1995 by Monsma and coworkers [57]. The SVT is a three terminal device which combines a metallic spin-valve (explained earlier) as a base together with semiconducting emitter and collector. The transport in the device, which is based on non-equilibrium hot-electrons rather than Fermi electrons, depends on the relative orientation of the magnetizations in the spin-valve. Thus the collector current depends on the magnetic

3. The original Landauer's formula is slightly more complicated, because the above conductance is not that of the wire but that of the system containing the leads. Basically the problem is where you actually measure the voltage. In a four-terminal measurement, *i.e.* if one applies a current through the reservoirs and then measures the voltage difference in the ideal leads, the conductance is given by slightly different relation than Eq. (1.9), the transmission T is replaced by $T/(1-T)$ [55].

state of the base. The SVT shows a huge magnetic response up to 400% at room temperature and in small magnetic fields of few Oe [58, 59]. The schematic layout of the SVT is sketched in Fig. 1.3. A review on the subject is presented in Jansen's paper [60].

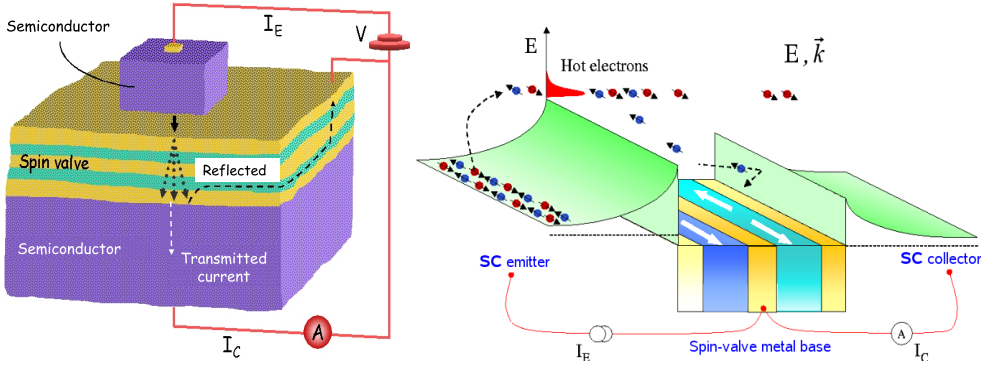


Figure 1.3: Left: Schematic structure of the SVT: semiconductor emitter (top), semiconductor collector (bottom) and in the base (middle) a spin-valve containing two ferromagnetic layers separated by a thin non-metallic material. Right: Energy band diagram of the SVT and the principle of operation.

The operation of the device is as follows (right hand side of Fig. 1.3). From the emitter side hot-electrons are injected above the Schottky barrier which is formed at the contact(s) ferromagnet|semiconductor interface(s). As these hot-electrons travel through the base they undergo various elastic as well inelastic scattering processes, which changes their energy as well as their momentum. Depending on the relative orientation of the magnetizations in the ferromagnetic layers, spin-up and spin-down electrons are scattered differently. Electrons are only able to enter the collector if they have retained sufficient energy to overcome the second Schottky barrier at the collector side and traveling with the right momentum. Hence the collector current depends sensitively on the scattering in the base. The change of the collector current as a function of the external magnetic field is called the *magnetocurrent* (MC), it is defined as $MC = (I_C^P - I_C^{AP})/I_C^{AP}$. The ratio of the collected to injected current, $\alpha = I_C/I_E$, is defined as the *transfer ratio* of the device. State of the art measurements were reported for an SVT structure consisting of $Si/Au(20\text{\AA})/NiFe(30\text{\AA})/Au(70\text{\AA})/Co(30\text{\AA})/Cu(40\text{\AA})/Si$ in which the magnetocurrent is reported to be 230% and the transfer ratio of the order of 10^{-4} [60]. Increasing the thickness of the magnetic layers can easily enhance magnetocurrent but at the expenses of the transfer ratio. There are various factors which may affect the electrical and magnetic response of the device, structural defects, scattering at the interfaces, grain boundaries ... etc. With the exception of the latter, the previous factors are taken into account in a study based on first-principles calculations of the electronic transport where a model structure for the SVT was considered. The details of this study is the subject of Chapter 5.

For completeness we would like to mention another hybrid device. Quite similar to the SVT (derived from it) is the *magnetic tunnel transistor* (MTT) which was proposed by Monsma *et al.* [57]. In this device a tunnel barrier is used as an emitter. The injected electrons can easily be tuned with an applied emitter voltage.

1.5 Thesis outline

The aim of the work presented in this thesis is to develop an efficient and flexible method which uses no adjustable parameters to study electronic transport in complex and inhomogeneous structures, *e.g.* various hybrid systems formed by magnetic, nonmagnetic and/or semiconductor materials. In Chapter 2 we present the details of such an efficient wave-function matching method suitable for the calculation of the transmission and reflection matrices from first-principles in layered materials. Our transport approach is based on the tight-binding muffin-tin orbitals (TB-MTO) implementation of the Landauer-Büttiker scattering formalism within DFT-LSDA. To illustrate our method we have carried out numerous calculations to study a variety of Co|Cu(111) interface-related problems. Because a minimal basis-set of localized orbitals is used, namely *spd(f)*, we are able to treat large lateral supercells. This allows us to study transport properties in the diffusive regime and modeling materials with large lattice mismatch. In this chapter we will show how we can analyze the detail of various types of scattering, namely the effect of disorder at interfaces.

In Chapter 3 we carry a systematic material-specific study of the electronic and the spin-dependent transport properties in nearly lattice matched materials, namely Cr|Fe, Cu|Co, Cu|Ni and Co|Ni along [001], [011] and [111] directions. The calculated 3d transition metals band structures and their Fermi surfaces will be used for the interpretation of the results of the transport calculations, *e.g.* to explain the anisotropy in transport properties for specular interfaces observed in the Cr|Fe system. The effect of defect scattering will be considered too. It reduces the transmission probability and thus increases the interface resistance for some systems (like in Cu|Co, Cu|Ni and Co|Ni systems). On the other hand the opposite happens for Cr|Fe system, that is, defect scattering enhances substantially the interface transmission. For the Cr|Fe (001) interface, with higher spin asymmetry, the interface resistance for the majority spin-channel decreases by a factor 3. This surprising large effect of defect scattering on this particular orientation of Cr|Fe system will be considered in more details by separating the ballistic versus the diffusive components of the interface transmission.

Chapter 4 is devoted to studying the orientation-dependent transparency of metallic interfaces. A large anisotropy is predicted for interfaces between the prototype free-electron materials Ag and Al, a factor of 2 difference between the (111) and (001) orientations was found. To interpret this behavior use is made of the calculated Fermi surfaces and their projections along these two directions. Similar results for Al/Au interfaces were obtained.

Motivated by the transport measurements (electrical and magnetic response) in the spin-valve transistor we have decided to carry out a study of a model structure to understand its spin-dependent transport properties. In Chapter 5 we will apply the

method developed in Chapter 2 to investigate the electronic, magnetic and transport properties in GaAs|Fe|Cr|Fe|GaAs model structure. The energy- and spin-dependence of the transmission will be explored. The effect of defect scattering at interfaces will be discussed.

Bibliography

- [1] G. Uhlenbeck and S. Goudsmit, *Nature* **117**, 164 (1926).
- [2] P. Grünberg, R. Schreiber, Y. Pang, M. B. Brodsky, and H. Sowers, *Phys. Rev. Lett.* **57**, 2442 (1986).
- [3] S. S. P. Parkin, N. More, and K. P. Roche, *Phys. Rev. Lett.* **64**, 2304 (1990).
- [4] S. S. P. Parkin, R. Bhadra, and K. P. Roche, *Phys. Rev. Lett.* **66**, 2152 (1991).
- [5] S. S. P. Parkin, *Phys. Rev. Lett.* **67**, 3598 (1991).
- [6] M. N. Baibich *et al.*, *Phys. Rev. Lett.* **61**, 2472 (1988).
- [7] G. Binasch, P. Grünberg, F. Saurenbach, and W. Zinn, *Phys. Rev. B* **39**, 4828 (1989).
- [8] G. A. Prinz, *Science* **282**, 1660 (1998).
- [9] S. A. Wolf *et al.*, *Science* **294**, 1488 (2001).
- [10] N. F. Mott, *Proc. Roy. Soc. London* **153**, 699 (1936).
- [11] N. F. Mott, *Proc. Roy. Soc. London* **156**, 368 (1936).
- [12] N. F. Mott, *Adv. Phys.* **13**, 325 (1964).
- [13] J. Bass and W. P. Pratt Jr., *J. Magn. & Magn. Mater.* **200**, 274 (1999).
- [14] W. P. Pratt, Jr. *et al.*, *Phys. Rev. Lett.* **66**, 3060 (1991).
- [15] S. F. Zhang and P. M. Levy, *J. Appl. Phys.* **69**, 4786 (1991).
- [16] T. Valet and A. Fert, *Phys. Rev. B* **48**, 7099 (1993).
- [17] S. F. Lee *et al.*, *J. Magn. & Magn. Mater.* **118**, L1 (1993).
- [18] M. A. M. Gijs and G. E. W. Bauer, *Adv. Phys.* **46**, 285 (1997).
- [19] J. P. Ansermet, *J. Phys.: Condens. Matter.* **10**, 6027 (1998).
- [20] E. Y. Tsymbal and D. G. Pettifor, *Solid State Physics* **56**, 113 (2001).
- [21] see the collection of articles, *Advances in condensed matter science*, in *Spin Dependent Transport in Magnetic NanoStructures*, edited by S. Maekawa and T. Shinjo Vol. 3, Taylor & Francis, London and New York, 2002.
- [22] E. Y. Tsymbal, O. N. Mryasov, and P. R. LeClair, *J. Phys.: Condens. Matter.* **15**, R109 (2003).
- [23] E. Y. Tsymbal *et al.*, p. cond (2005), unpublished.
- [24] Y. Ohno *et al.*, *Nature* **402**, 790 (1999).
- [25] S. Datta and B. Das, *Appl. Phys. Lett.* **56**, 665 (1990).
- [26] I. Žutić, J. Fabian, and S. D. Sarma, *Rev. Mod. Phys.* **76**, 323 (2004).
- [27] G. Schmidt, D. Ferrand, L. W. Molenkamp, A. T. Filip, and B. J. van Wees, *Phys. Rev. B* **62**, 4790 (2000).
- [28] H. J. Zhu *et al.*, *Phys. Rev. Lett.* **87**, 016601 (2001).

- [29] E. I. Rashba, Phys. Rev. B **62**, R16267 (2000).
- [30] M. Zwierzycki, K. Xia, P. J. Kelly, G. E. W. Bauer, and I. Turek, Phys. Rev. B **67**, 092401 (2003).
- [31] A. Fert and H. Jaffres, Phys. Rev. B **64**, 184420 (2001).
- [32] D. L. Smith and R. N. Silver, Phys. Rev. B **64**, 045323 (2001).
- [33] A. T. Hanbicki, B. T. Jonker, G. Itskos, G. Kioseoglou, and A. Petrou, Appl. Phys. Lett. **80**, 1240 (2002).
- [34] H. Ohno *et al.*, Appl. Phys. Lett. **69**, 363 (1996).
- [35] F. Matsukura, H. Ohno, A. Shen, and Y. Sugawara, Phys. Rev. B **57**, R2037 (1998).
- [36] R. A. de Groot, F. M. Mueller, P. G. van Engen, and K. H. J. Buschow, Phys. Rev. Lett. **83**, 2024 (1983).
- [37] see the collection of articles, in *Ultrathin Magnetic Structures I-IV*, edited by J. A. C. Bland and B. Heinrich, Springer-Verlag, Berlin, 1994-2005.
- [38] K. M. Schep, P. J. Kelly, and G. E. W. Bauer, Phys. Rev. Lett. **74**, 586 (1995).
- [39] P. Zahn, I. Mertig, M. Richter, and H. Eschrig, Phys. Rev. Lett. **75**, 2996 (1995).
- [40] K. Xia, M. Zwierzycki, M. Talanana, P. J. Kelly, and G. E. W. Bauer, Phys. Rev. B **73**, 064420 (2006).
- [41] K. M. Schep, J. B. A. N. van Hoof, P. J. Kelly, G. E. W. Bauer, and J. E. Inglesfield, Phys. Rev. B **56**, 10805 (1997).
- [42] M. D. Stiles and D. R. Penn, Phys. Rev. B **61**, 3200 (2000).
- [43] K. Xia *et al.*, Phys. Rev. B **63**, 064407 (2001).
- [44] R. G. Parr and W. Yang, *Density-Functional Theory of Atoms and Molecules* (Oxford University Press, New York, US, 1989), .
- [45] W. Kohn and L. J. Sham, Phys. Rev. **140**, A1133 (1965).
- [46] I. Turek, V. Drchal, J. Kudrnovský, M. Šob, and P. Weinberger, *Electronic Structure of Disordered Alloys, Surfaces and Interfaces* (Kluwer, Boston-London-Dordrecht, 1997).
- [47] O. K. Andersen, O. Jepsen, and D. Glötzel, in, in *Highlights of Condensed Matter Theory*, edited by F. Bassani, F. Fumi, and M. P. Tosi, pp. 59–176, North-Holland, Amsterdam, 1985.
- [48] P. Hohenberg and W. Kohn, Phys. Rev. **136**, B864 (1964).
- [49] U. von Barth and L. Hedin, J. Phys. C: Sol. State Phys. **5**, 1629 (1972).
- [50] D. M. Ceperley and B. J. Alder, Phys. Rev. Lett. **45**, 566 (1980).
- [51] J. P. Perdew and A. Zunger, Phys. Rev. B **23**, 5048 (1981).
- [52] S. H. Vosko, L. Wilk, and M. Nusair, Canadian Journal of Physics **58**, 1200 (1980).
- [53] R. Landauer, IBM J. Res. Dev. **1**, 223 (1957).
- [54] R. Landauer, Phil. Mag. **21**, 863 (1970).
- [55] S. Datta, *Electronic Transport in Mesoscopic Systems* (Cambridge University Press, Cambridge, 1995).
- [56] M. Büttiker, Y. Imry, R. Landauer, and S. Pinhas, Phys. Rev. B **31**, 6207 (1985).

-
- [57] D. J. Monsma, J. C. Lodder, T. J. A. Popma, and B. Dieny, Phys. Rev. Lett. **74**, 5260 (1995).
- [58] P. S. A. Kumar *et al.*, J. Magn. & Magn. Mater. **214**, L1 (2000).
- [59] R. Jansen *et al.*, Phys. Rev. Lett. **85**, 3277 (2000).
- [60] R. Jansen, J. Phys. D: Appl. Phys. **36**, R289 (2003).

Chapter 2

irst-principles scattering matrices for spin-transport

Details are presented of an efficient formalism for calculating transmission and reflection matrices from first principles in layered materials. Within the framework of spin density functional theory and using tight-binding muffin-tin orbitals, scattering matrices are determined by matching the wave-functions at the boundaries between leads which support well-defined scattering states and the scattering region. The calculation scales linearly with the number of principal layers N in the scattering region and as the cube of the number of atoms H in the lateral supercell. For metallic systems for which the required Brillouin zone sampling decreases as H increases, the final scaling goes as $H^2 N$. In practice, the efficient basis set allows scattering regions for which $H^2 N \sim 10^6$ to be handled. The method is illustrated for Cu|Co multilayers and single interfaces using large lateral supercells (up to 20×20) to model interface disorder. Because the scattering states are explicitly found, “channel decomposition” of the interface scattering for clean and disordered interfaces can be performed.

2.1 Introduction

One of the most important driving forces in condensed matter physics in the last thirty years has been the controlled growth of layered structures so thin that interface effects dominate bulk properties and quantum size effects can be observed. In doped semiconductors, the large Fermi wavelength of mobile charge carriers made it possible to observe finite size effects for layer thicknesses on a micron scale. Much thinner layers must be used in order to make such observations in metals because Fermi wavelengths are typically of the order of an interatomic spacing. Nevertheless, following rapidly on the heels of a number of important discoveries in semiconductor heterostructures, interface-dominated effects such as interface magnetic anisotropy, oscillatory exchange coupling and giant magnetoresistance (GMR) were found in artificially layered transition metal materials. Reflecting the shorter Fermi wavelength, the characteristic length scale is of order of nanometers.

Our main purpose in this paper is to give details of a scheme we have developed which is suitable for studying mesoscopic transport in inhomogeneous, mainly layered, transition metal magnetic materials. In the context of a large number of schemes designed to study transport either from first-principles [1–18] or based upon electronic structures calculated from first-principles [19–24] we will require our computational scheme to be (i) physically transparent, (ii) first-principles, requiring no free parameters, (iii) capable of handling complex electronic structures characteristic of transition metal elements and (iv) very efficient in order to be able to handle lateral supercells to study layered systems with different lattice parameters and to model disorder very flexibly. A tight-binding (TB) muffin-tin-orbital (MTO) implementation of the Landauer-Büttiker formulation of transport theory within the local-spin-density approximation (LSDA) of density-functional-theory (DFT) will satisfy these requirements.

Because wave transport through interfaces is naturally described in terms of transmission and reflection, the Landauer-Büttiker (LB) transmission matrix formulation of electron transport gained rapid acceptance as a powerful tool in the field of mesoscopic physics [25, 26], once the controversies surrounding the circumstances under which different expressions should be used had been resolved [25]. The two-terminal conductance of a piece of material is measured by attaching leads on either side, passing a current through these leads and measuring the potential drop across the scattering region. In the LB formulation of transport theory, the conductance G is expressed in terms of a transmission matrix $t \equiv t(E_F)$

$$G = \frac{e^2}{h} \text{Tr}\{tt^\dagger\} \quad (2.1)$$

where the element $t_{\mu\nu}$ is the probability amplitude that a state $|\nu\rangle$ in the left-hand lead incident on the scattering region from the left (see Fig. 2.1) is scattered into a state $|\mu\rangle$ in the right-hand lead. The trace simply sums over all incident and transmitted “channels” ν and μ and $\frac{e^2}{h}$ is the fundamental unit of conductance. In much current work on first-principles transport the conductance is calculated directly from Green’s functions expressed in some convenient localized orbital representation [27]. Explicit calculation of the scattering states is avoided by making use of the invariance properties of a trace. Because we want to make contact with a large body of theoretical literature [28] on mesoscopic physics and address a wider range of problems in the field of spin-dependent transport, we will calculate the microscopic transmission and reflection matrices t and r . By using a real energy, we will avoid the problems encountered in distinguishing propagating and evanescent states when a small but finite imaginary part of the energy is used. The Landauer-Büttiker formalism satisfies our first requirement of physical transparency.

In developing a scheme for studying transport in transition metal multilayers, a fundamental difference between semiconductors and transition metals must be recognized. Transition metal atoms have two types of electrons with different orbital character.

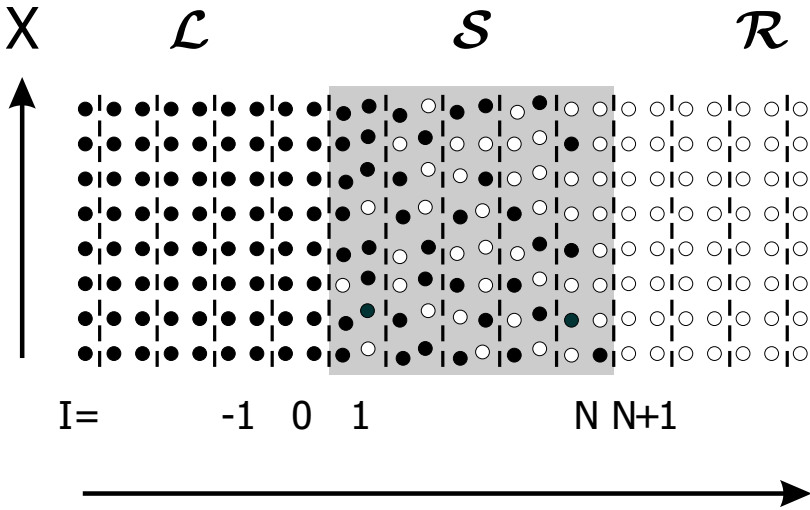


Figure 2.1: Sketch of the configuration used in the Landauer-Büttiker transport formulation to calculate the two terminal conductance. A (shaded) scattering region (S) is sandwiched by left- (L) and right-hand (R) leads which have translational symmetry and are partitioned into principal layers perpendicular to the transport direction. The scattering region contains N principal layers but the structure and chemical composition are in principle arbitrary.

The s electrons are spatially quite extended and, in solids, form broad bands with low effective masses; they conduct easily. The d electrons are much more localized in space, form narrow bands with large effective masses and are responsible for the magnetism of transition metal elements. The “magnetic” electrons, however, being itinerant do contribute to electrical transport. The appropriate framework for describing metallic magnetism, even for the late $3d$ transition metal elements, is band theory [29]. An extremely successful framework exists for treating itinerant electron systems from first-principles and this is the Local Density Approximation (LDA) of Density Functional Theory (DFT). For band magnetism, the appropriate extension to spin-polarized systems, the local spin-density approximation (LSDA) satisfies our second requirement of requiring no free parameters.¹

Oscillatory exchange coupling in layered magnetic structures was discussed by Bruno in terms of generalized reflection and transmission matrices [30] which were

1. Because the magnetism of transition metals depends very sensitively on atomic structure [29], it is important to know this structure quite accurately. The current drive to make devices whose lateral dimensions approach the nanoscale means that it is becoming increasingly important to know the atomic structures of these small systems microscopically while at the same time it is more difficult to do this characterization experimentally. It has become a practical alternative to determine minimum-energy structures theoretically by minimizing as a function of the atomic positions the total energy obtained by solving the Schrödinger equation self-consistently within the local density approximation (LDA) of Density Functional Theory (DFT), thereby avoiding the use of any free parameters.

calculated by Stiles [31–33] for realistic electronic structures using a scheme [34, 35] based on linearized augmented plane waves (LAPWs). At an interface between a non-magnetic and a magnetic metal, the different electronic structures of the majority and minority spin electrons in the magnetic material give rise to strongly spin-dependent reflection [1, 36]. Schep used transmission and reflection matrices calculated from first-principles with an embedding surface Green’s function method [37] to calculate spin-dependent interface resistances for specular Cu|Co interfaces embedded in diffusive bulk material [4]. The resulting good agreement with experiment indicated that interface disorder is less important than the spin-dependent reflection and transmission from a perfect interface. Calculations of domain wall resistances as a function of the domain wall thickness illustrated the usefulness of calculating the full scattering matrix [6, 38]. However, the LAPW basis set used by Stiles and Schep was computationally too expensive to allow repeated lateral supercells to be used to model interfaces between materials with very different, incommensurate lattice parameters or to model disorder. This is true of all plane-wave based basis sets which typically require of order 100 plane waves per atom in order to describe transition metal atom electronic structures reasonably well.

Muffin-tin orbitals (MTO) form a flexible, minimal basis set leading to highly efficient computational schemes for solving the Kohn-Sham equations of DFT [39–42]. For the close packed structures adopted by the magnetic materials Fe, Co, Ni and their alloys, a basis set of 9 functions (s , p , and d orbitals) per atom in combination with the atomic sphere approximation (ASA) for the potential leads to errors in describing the electronic structure which are comparable to the absolute errors incurred by using the local density approximation. This should be compared to typically 100 basis functions per atom required by the more accurate LAPW method. MTOs thus satisfy our third and fourth requirements of being able to treat complex electronic structures efficiently.

The tight-binding linearized muffin tin orbital (TB-LMTO) surface Green’s function (SGF) method has been developed to study the electronic structure of interfaces and other layered systems. When combined with the coherent-potential approximation (CPA), it allows the electronic structure, charge and spin densities of layered materials with substitutional disorder to be calculated self-consistently very efficiently [43]. In this paper we describe how we have combined a method for calculating transmission and reflection matrices based on wave-function matching (WFM), in a form given by Ando [44] for an empirical tight-binding Hamiltonian, with a first-principles TB-MTO basis [41]. Applications of the method to a number of problems of current interest in spin-transport have already been given in a number of short publications: to the calculation of spin-dependent interface resistances where interface disorder was modelled by means of large lateral supercells [9]; to the first principles calculation of the so-called mixing conductance parameter entering theories of current-induced magnetization reversal [45] and Gilbert-damping enhancement via spin-pumping [46]; to a generalized scattering formulation of the suppression of Andreev scattering at a ferromagnetic/superconducting interface [47]; to the problem of how spin-dependent interface resistances influence spin injection from a metallic ferromagnet into a III–V semiconductor [48–50]. These examples amply demonstrate that the fourth require-

ment is well satisfied.

In Sec. 2.2, we give technical details of the formalism and illustrate it in Sec. 2.3 where we calculate the transmission matrices for clean and disordered Cu|Co interfaces, document a number of convergence and accuracy issues and give a detailed “channel-decomposition” analysis of the scattering in the presence of disorder. A comparison with other methods is made in Sec. 2.4.

2.2 Theory

Central to the wave-function matching method for calculating the transmission and reflection matrices is the equation of motion (EoM) for electrons with energy ε , relating the vectors of coefficients \mathbf{C}_I for layers $I - 1$, I , and $I + 1$:

$$\mathcal{H}_{I,I-1}\mathbf{C}_{I-1} + (\mathcal{H} - \varepsilon)_{I,I}\mathbf{C}_I + \mathcal{H}_{I,I+1}\mathbf{C}_{I+1} = 0. \quad (2.2)$$

Here, $\mathbf{C}_I \equiv C_{Ii}$ describes the wavefunction amplitude in terms of some localized orbital basis $|i\rangle$ of dimension M where i labels the atomic orbital and atom site. [For the muffin-tin orbitals to be outlined in Sec. 2.2.1, i will be a combined index $\mathbf{R}\ell m$, where ℓ and m are the azimuthal and magnetic quantum numbers, respectively, of the MTO defined for an atomic-spheres-approximation (ASA) potential on the site \mathbf{R} .] The EoM does not restrict us to only considering nearest neighbour interactions since atoms can always be grouped into layers defined as to be so thick that the interactions between layers I and $I \pm 2$ are negligible (see Fig. 2.1). Such layers are called *principal layers*. Their thickness depends on the range of the interactions which in turn partly depends on the spatial extent of the orbital basis. It will be minimized by using the highly localized tight-binding MTO representation.

Consider the situation sketched in Fig. 2.1 where the scattering region \mathcal{S} is contacted with left (\mathcal{L}) and right (\mathcal{R}) leads which have perfect lattice periodicity and support well-defined scattering states. We assume that the ground state charge and spin densities and the corresponding Kohn-Sham independent electron potential have already been calculated self-consistently. The calculation of the scattering matrix can now be split into two distinct parts. In the first stage, to be discussed in Sec. 2.2.2, the eigenmodes of the leads $\mathbf{u}_\mu (= \mathbf{C}_0$ for the μ -th mode), of which there are $2M$, are calculated using an EoM appropriate to MTOs and making use of the lattice periodicity. By calculating their \mathbf{k} vectors (which are in general complex) and velocities $v_{\mathbf{k}}$, the eigenstates can be classified as being either left-going $\mathbf{u}_\mu(-)$ or right-going $\mathbf{u}_\mu(+)$. They form a basis in which to expand any left- and right-going waves and have the convenient property that their transformation under a lattice translation in the leads is easily calculated using Bloch’s theorem (with \mathbf{k} complex). We use the small Roman letters i, j to label the non-orthogonal basis and the small Greek letters μ, ν to label the lead eigenmodes.

In the second stage discussed in Sec. 2.2.3, a scattering region \mathcal{S} is introduced in the layers $1 \leq I \leq N$ which mixes left- and right-going lead eigenmodes. The scattering region can be a single interface, a complex multilayer, a tunnel junction etc., and the scattering can be introduced by disorder or simply by discontinuities in

the electronic structure at interfaces. The $\nu \rightarrow \mu$ element of the reflection matrix, $r_{\mu\nu}$, is defined in terms of the ratio of the amplitudes of left-going and right-going solutions in the left lead (in layer 0 for example) projected onto the ν^{th} right-going and μ^{th} left-going propagating states (\mathbf{k} vector real) and renormalized with the velocities so as to have unit flux. Determining these amplitudes requires finding the inverse of the Hamiltonian matrix of the scattering region modified by adding an embedding potential in order to incorporate the boundary conditions imposed by the leads. This matrix is finite and may be very sparse. Since only a few elements of its inverse are required, methods more efficient than direct matrix inversion can be used. The resulting numerical effort scales linearly with the extent of the scattering region in the transport direction.

2.2.1 Muffin Tin Orbitals and the KKR equation

Muffin-tin orbitals [39–42] (MTO) are defined for potentials in which space is divided into non-overlapping, atom-centred “muffin-tin” spheres inside which the potential is spherically symmetric and the remaining “interstitial” region where the potential is taken to be constant. The atomic spheres approximation (ASA) is obtained (i) by taking the kinetic energy in the interstitial region to be zero and (ii) by expanding the muffin-tin spheres so that they fill all space whereby the volume of the interstitial region vanishes; for monoatomic solids such spheres are called atomic Wigner-Seitz (WS) spheres. Inside a WS (or MT) sphere at \mathbf{R} , the solution of the radial Schrödinger equation regular at \mathbf{R} , $\phi_{R\ell}(\varepsilon, r_R)$ can be determined numerically for energy ε and angular momentum ℓ resulting in the partial wave

$$\phi_{R\ell m}(\varepsilon, \mathbf{r}_R) \equiv \phi_{RL}(\varepsilon, \mathbf{r}_R) \equiv \phi_{R\ell}(\varepsilon, r_R) Y_{\ell m}(\hat{\mathbf{r}}_R) \quad (2.3)$$

where $\hat{\mathbf{r}}$ is a unit vector, $\mathbf{r}_R \equiv \mathbf{r} - \mathbf{R}$, and $r_R \equiv |\mathbf{r} - \mathbf{R}|$. A continuous and differentiable orbital is constructed by attaching to the partial wave at the sphere boundary $r_R \equiv s_R$ a “tail” consisting of an appropriate linear combination of the solutions of the Laplace equation,

$$J_{RL}^0(\mathbf{r}_R) \equiv (r_R/\omega)^\ell [2(2\ell + 1)]^{-1} Y_L(\hat{\mathbf{r}}_R) \quad (2.4)$$

and

$$K_{RL}^0(\mathbf{r}_R) \equiv (r_R/\omega)^{-\ell-1} Y_L(\hat{\mathbf{r}}_R), \quad (2.5)$$

which are respectively, regular at \mathbf{R} and at infinity. ω is the average WS radius if the structure contains different atoms. In terms of the logarithmic derivative of $\phi_\ell(\varepsilon, r)$ at $r \equiv s$

$$D_\ell(\varepsilon, s) \equiv \frac{s\phi'_\ell(\varepsilon, s)}{\phi_\ell(\varepsilon, s)} \quad (2.6)$$

($\phi'_\ell(\varepsilon, s)$ is the radial derivative), the radial solutions are matched if for $r \geq s$,

$$\begin{aligned} \phi_\ell(\varepsilon, r) &= \frac{\ell - D_\ell}{2\ell + 1} \left(\frac{s}{\omega}\right)^{\ell+1} \phi_\ell(\varepsilon, s) \\ &\times \left[K_\ell^0(r) - 2(2\ell + 1) \left(\frac{\omega}{s}\right)^{2\ell+1} \left(\frac{D_\ell + \ell + 1}{D_\ell - \ell}\right) J_\ell^0(r) \right] \end{aligned} \quad (2.7)$$

where we drop the explicit \mathbf{R} -dependence when this does not give rise to ambiguity. Eq. (2.7) can be rewritten [51] in terms of the potential function,

$$P_\ell^0(\varepsilon) = 2(2\ell + 1) \left(\frac{\omega}{s}\right)^{2\ell+1} \frac{D_\ell(\varepsilon) + \ell + 1}{D_\ell(\varepsilon) - \ell}, \quad (2.8)$$

and normalization, $N_\ell^0(\varepsilon) = \frac{2\ell+1}{\ell-D_\ell} \left(\frac{\omega}{s}\right)^{\ell+1} \frac{1}{\phi_\ell(\varepsilon, s)}$, as

$$N_\ell^0(\varepsilon)\phi_\ell(\varepsilon, r) = K_\ell^0(r) - P_\ell^0(\varepsilon)J_\ell^0(r). \quad (2.9)$$

By subtracting from the partial wave, both inside and outside the MT sphere, the $J_{RL}^0(\mathbf{r}_R)$ component which is irregular at infinity, a function is formed which is continuous, differentiable and regular in all space, an energy-dependent muffin tin orbital $\chi_{RL}^0(\varepsilon, \mathbf{r}_R)$:

$$\chi_{RL}^0(\varepsilon, \mathbf{r}_R) = N_{R\ell}^0(\varepsilon)\phi_{R\ell}(\varepsilon, \mathbf{r}) + P_{R\ell}^0(\varepsilon)J_{RL}^0(\mathbf{r}_R) \quad r_R \leq s_R \quad (2.10)$$

$$= K_L^0(\mathbf{r}_R) \quad r_R \geq s_R \quad (2.11)$$

The tail $K_{RL}^0(\mathbf{r}_R)$ has the desirable property that closed forms exist for expanding it around a different site \mathbf{R}' in terms of the regular solutions $J_{R'L'}^0(\mathbf{r}_{R'})$,

$$K_{RL}^0(\mathbf{r}_R) = - \sum_{L'} J_{R'L'}^0(\mathbf{r}_{R'}) S_{R'L',RL}^0 \quad (2.12)$$

The expansion coefficients $S_{R'L',RL}^0$ form a so-called canonical structure constant matrix: they do not depend on the lattice constant, on the MT (or AS) potentials or on energy. Because of the augmentation with $J_{RL}^0(\mathbf{r}_R)$, the resulting MTO is no longer a solution of the Schrödinger equation (SE) inside its own sphere \mathbf{R} . When, however, a solution of the SE is sought in the form of a linear combination of MTOs centred on different sites,

$$\Psi(\varepsilon, \mathbf{r}) = \sum_{R,L} \chi_{RL}^0(\varepsilon, \mathbf{r}_R) C_{RL}^0 \quad (2.13)$$

then the partial wave solution is recovered if the augmenting term $J_{RL}^0(\mathbf{r}_R)$ on site \mathbf{R} is cancelled by the tails of MTOs centred on all other sites $\mathbf{R}' \neq \mathbf{R}$, expanded about \mathbf{R} . The condition for this to occur is the ‘‘tail-cancellation’’ condition:

$$\sum_{R',L'} [P_{R'L'}^0(\varepsilon)\delta_{RR'}\delta_{LL'} - S_{R'L',RL}^0] C_{R'L'}^0 = 0. \quad (2.14)$$

All of the information about the structural geometry of the system under investigation is contained in the structure constant matrix $S_{R'L',RL}^0$ while all of the information about the atomic species on site \mathbf{R} needed to calculate the electronic structure (eigenvalues and eigenvectors) is contained in the potential functions $P_{RL}^0(\varepsilon)$. These are determined by solving the radial Schrödinger equation for the corresponding spherically symmetrical atomic sphere potential for energy ε and angular momentum ℓ .

A disadvantage of these “conventional” MTOs is their infinite range. However, there is a remarkably simple generalization of the MTOs which allows their range to be modified by introducing a set of “screening” constants $\alpha_{R\ell}$ (not to be confused with the lead eigenmode index) while the “tail-cancellation” condition remains essentially unchanged:

$$\sum_{R',L'} [P_{RL}^\alpha(\varepsilon)\delta_{RR'}\delta_{LL'} - S_{RL,R'L'}^\alpha] C_{R'L'}^\alpha = 0. \quad (2.15)$$

$P^\alpha(\varepsilon)$ is a diagonal matrix related to $P^0(\varepsilon)$ by

$$P^\alpha(\varepsilon) = P^0(\varepsilon) + P^0(\varepsilon)\alpha P^0(\varepsilon) = P^0(\varepsilon) (1 - \alpha P^0(\varepsilon))^{-1}, \quad (2.16)$$

and

$$S^\alpha = S^0 + S^0\alpha S^\alpha = S^0 (1 - \alpha S^0)^{-1}, \quad (2.17)$$

For any set of $\alpha_{R\ell}$, the energy-dependent MTOs with the normalization

$$\sum_{R,L} \frac{\omega}{2} \dot{P}_{RL}^\alpha(\varepsilon) |C_{RL}^\alpha|^2 = 1, \quad (2.18)$$

form a complete set for the MT (AS) potential used in their construction. Here, \dot{P} denotes an energy derivative and (2.18) follows from the relation $N^\alpha(\varepsilon) = [(\omega/2)\dot{P}^\alpha(\varepsilon)]^{1/2}$. Sets of parameters $\alpha_{R\ell}$ have been found for which the “screened” structure constants $S_{RL,R'L'}^\alpha$ have very short range, decaying exponentially with the interatomic separation [40]. The set of parameters, $\beta_{R\ell}$, which yields the shortest range MTOs is called the “tight-binding” (TB) representation [39]. For close-packed structures, the range of $S_{RL,R'L'}^\beta$ is in practice limited to first- and second-nearest neighbours. This TB set, with $\alpha = \beta$, is what we will use from now, unless stated otherwise, since it will allow us to define principal layers with a minimal thickness.

For the determination of energy bands $\varepsilon(\mathbf{k})$, the tail-cancellation or KKR equations are inconvenient because the energy-dependence of the potential function makes it necessary to solve (2.14) or (2.15) by searching for the roots of a determinant, which is time consuming. Much more efficient methods have been developed based on energy-independent MTOs. However, to study transport we only need to know $P^\beta(\varepsilon)$ for a fixed energy, usually the Fermi energy. We assume that the Kohn-Sham equations have already been solved self-consistently (using for example a linearized method) so we have the potentials from which to calculate the potential functions. Although (2.15) can be brought into Hamiltonian form by linearizing the energy dependent potential function (see Appendix A.1), we will work directly with the more exact KKR equation.

2.2.2 Eigenmodes of the leads

We will assume that there exists two-dimensional translational symmetry in the plane perpendicular to the transport direction so that states can be characterized by a lateral wave vector \mathbf{k}_\parallel in the corresponding two-dimensional Brillouin zone. The

screened KKR equation [40] in the mixed representation of \mathbf{k}_{\parallel} and real space layer index I (see Fig. 2.1) is

$$-S_{I,I-1}^{\mathbf{k}_{\parallel}} \mathbf{C}_{I-1} + \left(P_{I,I}(\varepsilon) - S_{I,I}^{\mathbf{k}_{\parallel}} \right) \mathbf{C}_I - S_{I,I+1}^{\mathbf{k}_{\parallel}} \mathbf{C}_{I+1} = 0, \quad (2.19)$$

where $\mathbf{C}_I \equiv C_{Ii} \equiv C_{IR\ell m}$ is a $(l_{\max} + 1)^2 H \equiv M$ dimensional vector describing the amplitudes of the I -th layer with H sites and $(l_{\max} + 1)^2$ orbitals per site. $P_{I,I}$ and $S_{I,J}$ are $M \times M$ matrices. $P_{I,I}$ is a diagonal matrix of potential functions characterizing the AS potentials of layer I and

$$S_{I,J}^{\mathbf{k}_{\parallel}} = \sum_{\mathbf{T} \in \{\mathbf{T}_{I,J}\}} S^{\beta}(\mathbf{T}) e^{i\mathbf{k}_{\parallel} \cdot \mathbf{T}}, \quad (2.20)$$

where $\{\mathbf{T}_{I,J}\}$ denotes the set of vectors that connect one lattice site in the I -th layer with all lattice sites in the J -th layer.

By analogy with (2.2), equation (2.19) is the equation of motion we will use to calculate the amplitudes of right- and left-going waves which determine the scattering matrix. We will solve it for a fixed value of ε (usually ε_F), and some \mathbf{k}_{\parallel} to find $k_{\mu}(\varepsilon, \mathbf{k}_{\parallel})$ the component of the Bloch vector in the transport direction. To keep the notation simple, explicit reference to the \mathbf{k}_{\parallel} and ε dependence will be omitted from now on. The formalism to be described in the following can be applied to any electronic structure code based on the KKR equation (2.19), such as third-generation TB-LMTO [52–54].

Let us first consider the Bloch states in the ideal lead. To obtain linearly independent solutions, we set $\mathbf{C}_I = \lambda^I \mathbf{C}_0$, since in a periodic potential the wave function should satisfy Bloch's theorem. The potential function matrix is the same for all unit cells. The structure constant matrix depends only on the relative positions and, because that is how they are defined, there is only coupling between adjacent principal layers so the equation of motion becomes

$$\begin{pmatrix} S_{0,1}^{-1}(P - S_{0,0}) & -S_{0,1}^{-1}S_{1,0} \\ 1 & 0 \end{pmatrix} \begin{pmatrix} \mathbf{C}_I \\ \mathbf{C}_{I-1} \end{pmatrix} = \lambda \begin{pmatrix} \mathbf{C}_I \\ \mathbf{C}_{I-1} \end{pmatrix}, \quad (2.21)$$

The eigenvalue λ_{μ} can be written in the form $\lambda_{\mu} = \exp(i\mathbf{k}_{\mu} \cdot \mathbf{T}_0)$ with \mathbf{T}_0 connecting equivalent sites in adjacent principal layers. The wave vector \mathbf{k}_{μ} can be decomposed into \mathbf{k}_{\parallel} and a remainder which is in general not real, $\mathbf{k}_{\mu} = (\mathbf{k}_{\parallel}, \mathbf{k}_{\mu} - \mathbf{k}_{\parallel})$. Equation (2.21) has $2M$ eigenvalues and $2M$ eigenvectors, corresponding to M right-going and M left-going waves. By calculating the wavevectors and velocities (see Eq. (2.38) and Appendix A.1) of the lead eigenmodes, the propagating and evanescent states can be identified and sorted into right-going or left-going modes.

Letting $\mathbf{u}_1(-), \dots, \mathbf{u}_M(-)$ denote the left-going solutions \mathbf{C}_0 corresponding to eigenvalues $\lambda_1(-), \dots, \lambda_M(-)$ and $\mathbf{u}_1(+), \dots, \mathbf{u}_M(+)$ the right-going solutions corresponding to eigenvalues $\lambda_1(+), \dots, \lambda_M(+)$, the matrix $U_{i\mu}(\pm)$ is defined as

$$U(\pm) = (\mathbf{u}_1(\pm) \dots \mathbf{u}_M(\pm)) \quad (2.22)$$

and the matrix $\mathbf{\Lambda}(\pm)$ as the diagonal matrix with elements $\lambda_{\mu}(\pm)$. Following Ando, we next expand any left- or right-going wave, at $I = 0$ for example, as

$$\mathbf{C}_0(\pm) = U(\pm)\mathbf{C}(\pm). \quad (2.23)$$

Note that \mathbf{C}_0 is a vector whose elements are labelled i while the elements of the vector \mathbf{C} are labelled μ .

$$F(\pm) \equiv U(\pm)\mathbf{\Lambda}_{\pm}U^{-1}(\pm) \quad (2.24)$$

is the matrix of Bloch factors (including evanescent states) transformed onto the basis $|i\rangle$ and plays a central role in the following. Knowing it makes it possible to translate a state expressed in the basis $|i\rangle$ from layer J of the lead to layer I by

$$\mathbf{C}_I(\pm) = F^{I-J}(\pm)\mathbf{C}_J(\pm). \quad (2.25)$$

The F matrices can be used to find the Green functions of the lead (but it should be emphasized that these are not required in the Ando's approach). For example, the retarded surface Green function of the semi-infinite lead extending from $i = -\infty \dots 0$ is given simply by

$$g(\varepsilon) = F^{-1}(-)S_{01}^{-1} \quad (2.26)$$

The procedure described in this section should therefore be seen as an alternative to the recursive schemes for obtaining the surface Green functions commonly found in the literature (see *e.g.* Ref. [43]). The reader is referred to Refs. [55] and [56] for more detailed discussion.

2.2.3 Scattering problem

The scattering region \mathcal{S} , divided into N principal layers numbered 1 to N , is now inserted between the left and right leads. The resulting (scattering region + leads) problem is infinite dimensional in the real space MTO representation but, by making use of their translational symmetry, the leads can be incorporated as boundary conditions and the scattering problem can be reduced to a finite problem whose dimension is determined by the size of the scattering region (number of sites \times number of orbitals per site).

We set about decoupling the scattering region from the leads, first on the left-hand side, then on the right. The amplitude in the 0-th layer is first separated into right- and left- going components $\mathbf{C}_0 = \mathbf{C}_0(+) + \mathbf{C}_0(-)$. Because there is no scattering of Bloch states in the leads, the right- and left-going components can be translated to the left by one (principal layer) lattice spacing using the generalized Bloch factors (2.25) so the amplitude in layer -1 can be related to that in layer 0 as

$$\begin{aligned} \mathbf{C}_{-1} &= F_{\mathcal{L}}^{-1}(+)\mathbf{C}_0(+) + F_{\mathcal{L}}^{-1}(-)\mathbf{C}_0(-) \\ &= [F_{\mathcal{L}}^{-1}(+) - F_{\mathcal{L}}^{-1}(-)]\mathbf{C}_0(+) + F_{\mathcal{L}}^{-1}(-)\mathbf{C}_0. \end{aligned} \quad (2.27)$$

allowing us to express \mathbf{C}_{-1} in terms of \mathbf{C}_0 and $\mathbf{C}_0(+)$ and so eliminate it from the equation of motion for the 0-th layer

$$-S_{0,-1}\mathbf{C}_{-1} + (P_{0,0} - S_{0,0})\mathbf{C}_0 - S_{0,1}\mathbf{C}_1 = 0, \quad (2.28)$$

which becomes

$$\begin{aligned} &(P_{0,0} - \tilde{S}_{0,0})\mathbf{C}_0 - S_{0,1}\mathbf{C}_1 \\ &= S_{0,-1} [F_{\mathcal{L}}^{-1}(+) - F_{\mathcal{L}}^{-1}(-)]\mathbf{C}_0(+). \end{aligned} \quad (2.29)$$

Here \mathcal{L} denotes the left lead and $\tilde{S}_{0,0} = S_{0,0} + S_{0,-1}F_{\mathcal{L}}^{-1}(-)$. The quantity $S_{0,-1}F_{\mathcal{L}}^{-1}(-)$ is the ‘‘embedding potential’’ for the left lead and the net result is that the equations of motion have been truncated at layer 0.

On the right-hand side of the scattering region, we are interested in the situation where only right-going waves can exist in the $(N+1)$ -th layer, so

$$\mathbf{C}_{N+2} = F_{\mathcal{R}}(+)\mathbf{C}_{N+1}(+) \quad (2.30)$$

allowing \mathbf{C}_{N+2} to be eliminated from the EoM for \mathbf{C}_{N+1}

$$(P_{N+1,N+1} - \tilde{S}_{N+1,N+1})\mathbf{C}_{N+1} - S_{N+1,N}\mathbf{C}_N = 0, \quad (2.31)$$

where $\tilde{S}_{N+1,N+1} = S_{N+1,N+1} + S_{N+1,N+2}F_{\mathcal{R}}(+)$ and $-S_{N+1,N+2}F_{\mathcal{R}}(+)$ is the embedding potential for the right lead.

Making use of the lead boundary conditions, the tail cancellation condition for the scattering problem in real space is given by the set of inhomogeneous linear equations

$$\begin{pmatrix} (P - \tilde{S})_{0,0} & -S_{0,1} & 0 & \cdots & 0 & 0 \\ -S_{1,0} & (P - S)_{1,1} & -S_{1,2} & \cdots & 0 & 0 \\ 0 & -S_{2,1} & (P - S)_{2,2} & \cdots & \vdots & 0 \\ \vdots & \vdots & \cdots & \ddots & \vdots & 0 \\ 0 & 0 & \cdots & \cdots & (P - S)_{N,N} & -S_{N,N+1} \\ 0 & 0 & 0 & \cdots & -S_{N+1,N} & (P - \tilde{S})_{N+1,N+1} \end{pmatrix} \begin{pmatrix} \mathbf{C}_0 \\ \mathbf{C}_1 \\ \mathbf{C}_2 \\ \vdots \\ \mathbf{C}_N \\ \mathbf{C}_{N+1} \end{pmatrix} \\ \equiv (\mathbf{P} - \tilde{\mathbf{S}}) \begin{pmatrix} \mathbf{C}_0 \\ \mathbf{C}_1 \\ \mathbf{C}_2 \\ \vdots \\ \mathbf{C}_N \\ \mathbf{C}_{N+1} \end{pmatrix} = \begin{pmatrix} S_{0,-1} [F_{\mathcal{L}}^{-1}(+) - F_{\mathcal{L}}^{-1}(-)] \mathbf{C}_0(+) \\ 0 \\ 0 \\ \vdots \\ 0 \\ 0 \end{pmatrix} \quad (2.32)$$

which can be solved in terms of $\mathbf{g} = (\mathbf{P} - \tilde{\mathbf{S}})^{-1}$

$$\begin{pmatrix} \mathbf{C}_0 \\ \mathbf{C}_1 \\ \mathbf{C}_2 \\ \vdots \\ \mathbf{C}_N \\ \mathbf{C}_{N+1} \end{pmatrix} = \mathbf{g} \begin{pmatrix} S_{0,-1} [F_{\mathcal{L}}^{-1}(+) - F_{\mathcal{L}}^{-1}(-)] \mathbf{C}_0(+) \\ 0 \\ 0 \\ \vdots \\ 0 \\ 0 \end{pmatrix}$$

This treatment is very similar to the widely used surface Green function method [55]. The boundary conditions in (2.32) are explicitly defined by considering the Bloch wave coming from the left-hand side while for conventional retarded or advanced

Green functions the boundary conditions are specified by an infinitesimal imaginary part of the energy parameter ε .

We are now in a position where we can relate the outgoing wave amplitude in the right electrode to the incoming wave in the left electrode through the Green function by

$$\mathbf{C}_{N+1}(+) = \mathbf{C}_{N+1} = g_{N+1,0} S_{0,-1} [F_{\mathcal{L}}^{-1}(+) - F_{\mathcal{L}}^{-1}(-)] \mathbf{C}_0(+). \quad (2.33)$$

Using the transformation between the eigenstates and the localized basis functions $U_{i\alpha}(\pm)$, we obtain the transmission and reflection matrix elements [44]

$$t_{\mu\nu} = \left(\frac{v_\mu}{v_\nu} \right)^{1/2} \{ U_{\mathcal{R}}^{-1}(+) g_{N+1,0} S_{0,-1} [F_{\mathcal{L}}^{-1}(+) - F_{\mathcal{L}}^{-1}(-)] U_{\mathcal{L}}(+)\}_{\mu\nu} \quad (2.34)$$

$$r_{\mu\nu} = \left(\frac{v_\mu}{v_\nu} \right)^{1/2} \{ U_{\mathcal{L}}^{-1}(-) \langle g_{0,0} S_{0,-1} [F_{\mathcal{L}}^{-1}(+) - F_{\mathcal{L}}^{-1}(-)] - 1 \rangle U_{\mathcal{L}}(+)\}_{\mu\nu}, \quad (2.35)$$

where μ and ν label Bloch states and v_μ, v_ν are the components of the corresponding group velocities in the transport direction. Similarly, an incident wave from the right side is transmitted or reflected as

$$t'_{\mu\nu} = \left(\frac{v_\mu}{v_\nu} \right)^{1/2} \{ U_{\mathcal{L}}^{-1}(-) g_{0,N+1} S_{N+1,N+2} [F_{\mathcal{R}}(-) - F_{\mathcal{R}}(+)] U_{\mathcal{R}}(-)\}_{\mu\nu} \quad (2.36)$$

$$r'_{\mu\nu} = \left(\frac{v_\mu}{v_\nu} \right)^{1/2} \{ U_{\mathcal{R}}^{-1}(+) \langle g_{N+1,N+1} S_{N+1,N+2} [F_{\mathcal{R}}(-) - F_{\mathcal{R}}(+)] - 1 \rangle U_{\mathcal{R}}(-)\}_{\mu\nu}. \quad (2.37)$$

The group velocities in (2.34)-(2.37) are determined using the expression

$$v_\mu(\pm) = \frac{id}{\hbar} \left[\mathbf{u}_\mu^\dagger(\pm) S_{I,I+1}^{\mathbf{k}_\parallel} \mathbf{u}_\mu(\pm) \lambda_\mu - \text{h.c.} \right] \quad (2.38)$$

which is derived in Appendix A. Here, I and $I+1$ denote neighbouring principal layers in either left or right lead, $d = \mathbf{T}_0 \cdot \hat{n}$ is the distance between equivalent monolayers in adjacent principal layers and \hat{n} is a unit vector in the transport direction.

The conductance can now be calculated using the elements of the scattering matrix required in the Landauer-Büttiker formula (2.1), the transmission matrix (2.34). It can be shown [55] that this is fully equivalent to the popular Caroli's non-equilibrium Green functions formula [57]. It is, however, expressed in a more physically transparent fashion and avoids the use of complex energies in the Green's function approach (where they were introduced to stabilize the calculation of the surface Green function and to make self-consistent iteration more efficient by expressing the density matrix as a contour integral).

2.2.4 Disorder

Interfaces between materials with different lattice parameters [47] and disordered interfaces [9, 48] can be modelled very flexibly using lateral supercells. This approach allows us to study the effect of various types of disorder on transport properties, ranging from homogeneous interdiffusion (alloying) to islands, steps etc. The supercell description of disorder becomes formally exact in the limit of infinitely large supercells. In practice, satisfactory convergence is achieved for supercells of quite moderate size (see Sec. 2.3.3).

Leads

The factor limiting the “size” of scattering problem which can be handled in practice is the rank of the blocks of the block-tridiagonal equation of motion (2.19), which is proportional to the number of atoms in the lateral supercell. If performed straightforwardly in the manner outlined in Sec. 2.2.2, the solution of the lead equation (2.21) involves solving a non-Hermitian eigenvalue problem whose rank is twice as large. Unless use is made of the greater translational symmetry present in the leads, this can become the limiting step in the whole calculation. Doing so makes it possible to reduce the dimension of the lead state calculation to a size determined by the dimension of a primitive unit cell which is usually negligible.

We consider an $H_1 \times H_2$ lateral supercell defined by the real-space lattice vectors

$$\mathbf{A}_1 = H_1 \mathbf{a}_1 \quad \text{and} \quad \mathbf{A}_2 = H_2 \mathbf{a}_2 \quad (2.39)$$

where \mathbf{a}_1 and \mathbf{a}_2 are the lattice vectors describing the in-plane periodicity of a primitive unit cell (Fig. 2.2). The cells contained within the supercell are generated by the set of translations

$$\begin{aligned} \mathbf{T}_{\parallel \mathcal{T}} \in \mathbb{T} = \{ & \mathbf{T}_{\parallel} = h_1 \mathbf{a}_1 + h_2 \mathbf{a}_2 ; \\ & 0 \leq h_1 < H_1, 0 \leq h_2 < H_2 \} \end{aligned} \quad (2.40)$$

where $\mathcal{T} = 1, \dots, H_1 \times H_2$ is a convenient cell index. In reciprocal space the supercell Brillouin zone is defined by the reduced vectors

$$\mathbf{B}_1 = \mathbf{b}_1 / H_1 \quad \text{and} \quad \mathbf{B}_2 = \mathbf{b}_2 / H_2 \quad (2.41)$$

where \mathbf{b}_1 and \mathbf{b}_2 are the reciprocal lattice vectors corresponding to the real space primitive unit cell. As a result the Brillouin zone (BZ) is folded down, as shown schematically in Fig. 2.2 (bottom rhs), and the single $\mathbf{k}_{\parallel}^{\mathbb{S}}$ point (\mathbb{S} is used to label supercell quantities) in the supercell BZ corresponds to the set of $H_1 \times H_2$ \mathbf{k}_{\parallel} points in the original unfolded BZ

$$\begin{aligned} \mathbf{k}_{\parallel \mathcal{K}} \in \mathbb{K} = \{ & \mathbf{k}_{\parallel} = \mathbf{k}_{\parallel}^{\mathbb{S}} + h_1 \mathbf{B}_1 + h_2 \mathbf{B}_2 ; \\ & 0 \leq h_1 < H_1, 0 \leq h_2 < H_2 \} \end{aligned} \quad (2.42)$$

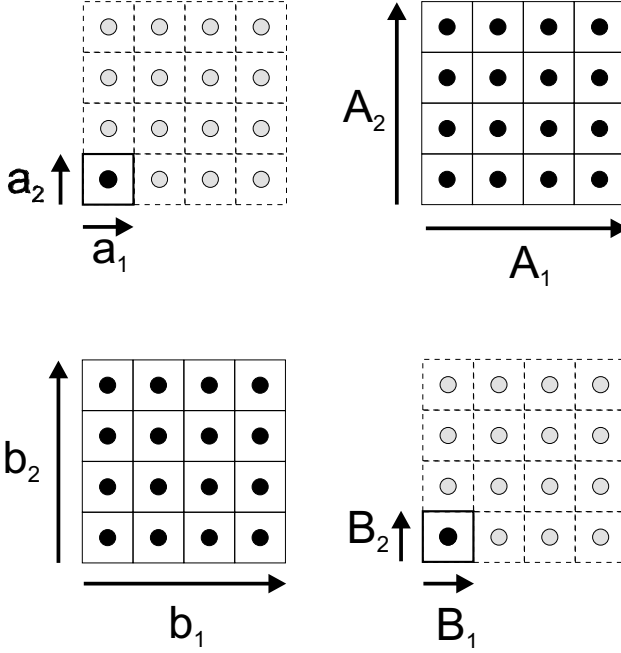


Figure 2.2: Illustration of lateral supercells and corresponding 2D interface Brillouin zones. Top panel: lattice vectors for a primitive unit cell containing a single atom (lhs) and a 4×4 supercell (rhs). Bottom panel: a single k -point in the BZ (rhs) corresponding to the 4×4 real-space supercell is equivalent to 4×4 k -points in the BZ (lhs) corresponding to the real-space primitive unit cell.

with $\mathcal{K} = 1, \dots, H_1 \times H_2$. Solutions associated with different $\mathbf{k}_{\parallel \mathcal{K}}$ in the primitive unit cell representation become different “bands” at the single $\mathbf{k}_{\parallel}^{\mathcal{S}}$ in the supercell representation.

The indices \mathcal{T} and \mathcal{K} provide a natural means of describing the supercell-related matrices $U^{\mathcal{S}}(\pm)$ and $F^{\mathcal{S}}(\pm)$ and their inverses in terms of $(H_1 \times H_2)^2$ sub-blocks with dimensions defined by the primitive unit cell. Thus $U_{\mathcal{T}\mathcal{K}}^{\mathcal{S}}(\pm)$ is the block containing the amplitudes of the modes associated with $\mathbf{k}_{\parallel \mathcal{K}}$ in the \mathcal{T} -th real-space cell.

Solving the single unit cell problem for the set of \mathbf{k}_{\parallel} -points belonging to \mathbb{K} (lhs of Fig. 2.2) and using the Bloch symmetry of the eigenmodes, we get trivially

$$U_{\mathcal{T}\mathcal{K}}^{\mathcal{S}}(\mathbf{k}_{\parallel}^{\mathcal{S}}) = e^{i\mathbf{k}_{\parallel \mathcal{K}} \cdot \mathbf{T}_{\mathcal{T}}} U(\mathbf{k}_{\parallel \mathcal{K}}) \quad (2.43)$$

where $U(\mathbf{k}_{\parallel\mathcal{K}})$ is the matrix (2.22) of modes for a primitive unit cell for $\mathbf{k}_{\parallel\mathcal{K}}$ and the \pm qualifier has been dropped for simplicity. Defining the matrix of phase factors

$$X(\mathbf{k}_{\parallel}^{\mathbb{S}}) = \begin{pmatrix} e^{i\mathbf{k}_{\parallel 1} \cdot \mathbf{T}_{\parallel 1}} & \dots & e^{i\mathbf{k}_{\parallel H} \cdot \mathbf{T}_{\parallel 1}} \\ \vdots & & \vdots \\ e^{i\mathbf{k}_{\parallel 1} \cdot \mathbf{T}_{\parallel H}} & \dots & e^{i\mathbf{k}_{\parallel H} \cdot \mathbf{T}_{\parallel H}} \end{pmatrix} \quad (2.44)$$

with $H \equiv H_1 \times H_2$, and its inverse $Y = X^{-1}$, we can straightforwardly determine

$$\left[U^{\mathbb{S}}(\mathbf{k}_{\parallel}^{\mathbb{S}}) \right]_{\mathcal{K}\mathcal{T}}^{-1} = U^{-1}(\mathbf{k}_{\parallel\mathcal{K}}) Y_{\mathcal{K}\mathcal{T}} \quad (2.45)$$

and

$$F_{\mathcal{T}_1 \mathcal{T}_2}^{\mathbb{S}}(\mathbf{k}_{\parallel}^{\mathbb{S}}) = \sum_{\mathcal{K}} X_{\mathcal{T}_1 \mathcal{K}} F(\mathbf{k}_{\parallel\mathcal{K}}) Y_{\mathcal{K} \mathcal{T}_2} \quad (2.46)$$

The procedure outlined above for determining the matrices describing the lead modes scales linearly with the size of the supercell *i.e.*, as $(H_1 \times H_2)$ rather than as $(H_1 \times H_2)^3$ which is the scaling typical for matrix operations. Another advantage is that it enables us to analyse the scattering. By keeping track of the relation between supercell “bands” and equivalent eigenmodes at different $\mathbf{k}_{\parallel\mathcal{K}}$ (Fig. 2.2) we can straightforwardly obtain from (2.34)-(2.37) $t_{\mu\nu}(\mathbf{k}_{\parallel\mathcal{K}_1}, \mathbf{k}_{\parallel\mathcal{K}_2})$ and other scattering coefficients. In other words the “interband” specular scattering in the supercell picture translates, in the presence of disorder in the scattering region, into the “diffuse” scattering between the \mathbf{k}_{\parallel} vectors belonging to the \mathbb{K} set.

2.3 Calculations

Even though the theoretical scheme outlined above contains no adjustable parameters, its practical implementation does involve numerous approximations, some physical, others numerical, which need to be evaluated. At present, any workable scheme must be based upon an independent particle approximation. The results of a transport calculation will be limited by the extent to which the single particle electronic structures used are consistent with the corresponding Fermi surfaces determined experimentally using methods such as de Haas-van Alphen measurements or the occupied and unoccupied electronic states close to the Fermi energy determined by, for example, photoelectron spectroscopy.

In this section we examine how various approximations affect our end results. We begin with the calculation of the scattering states in bulk Cu and bulk Co (2.3.1). These are then used to study specular scattering from an ideal ordered Cu|Co(111) interface (2.3.2) after which we describe how we model disordered interfaces (2.3.3) and how the results can be analysed.

2.3.1 Leads

For a crystalline conductor with Bloch translational symmetry, each state at the Fermi energy can move unhindered through the solid so that the transmission matrix is diagonal with $|t_{\mu\nu}|^2 = \delta_{\mu\nu}$. In this *ballistic* regime, (2.1) reduces to

$$G^\sigma(\hat{n}) = \frac{e^2}{h} \sum_{\mu k_\parallel} |t_{\mu\mu}^\sigma(\mathbf{k}_\parallel)|^2 = \frac{e^2}{h} N^\sigma(\hat{n}). \quad (2.47)$$

and calculation of the so-called *Sharvin* conductance becomes a matter of counting the number of modes (channels) propagating in the transport direction \hat{n} , denoted in (2.47) as $N^\sigma(\hat{n})$. To solve (2.21) in practice, the orbital angular momentum expansions in (2.12) and (2.13), which are in-principle infinite, must be truncated by introducing some cutoff in l , denoted l_{\max} . Usually, a value of $l_{\max} = 2$ or 3 is used, corresponding to *spd*- or *spdf*-bases.

The \mathbf{k}_\parallel summation is carried out by sampling, on a regular mesh, the 2D Brillouin zone (BZ) defined by the (lateral) translational periodicity perpendicular to \hat{n} . The results of carrying out this BZ summation are shown in Fig. 2.3 where $G^\sigma(\hat{n})$ is plotted as a function of $\Delta^2 k_\parallel / A_{BZ}$, the normalized area element per \mathbf{k}_\parallel -point for bulk *fcc* Cu and for the majority and minority spins of bulk *fcc* Co. When the 2D-BZ reciprocal lattice vectors are each divided into Q intervals, then $\Delta^2 k_\parallel / A_{BZ} = 1/Q^2$. It can be seen that the Sharvin conductance is converged to about 1% if $3600 = 60 \times 60$ points are used in the complete 2D-BZ and to about 0.2% for $102400 = 320 \times 320$ sampling points. The worst case is for the minority spin of Co which has a complex multi-sheeted Fermi surface. To see if there are any simple underlying trends in the convergence, we repeatedly bisect the intervals used in the BZ summation starting with $Q = 20$ and $Q = 22$, shown in the figure as squares and diamonds, respectively and least-squares fitted with the dashed and dash-dotted lines. The convergence is fairly uniform but not very systematic indicating that the summation is limited by fine structure in the integrand at the smallest length scale studied which can only be resolved by increasingly fine sampling. Thus there is nothing to be gained by developing more sophisticated interpolation schemes and when we introduce disorder in Section 2.3.3, this will be even more so. However, in the following we will see that the level of convergence we can achieve with discrete sampling is quite adequate and not a limiting step in the whole procedure.

The calculations shown in the figure were performed using an *spd*-basis, for an *fcc* lattice constant $a = 3.614 \text{ \AA}$ corresponding to the experimental volume of bulk (*fcc*) Cu and using the exchange-correlation potential calculated and parameterized by von Barth and Hedin [58]. For convenience, and to avoid repetition, we will refer to this in the following as a “standard” configuration. The converged values are given (underlined) in Table 2.1 together with values calculated using an *fcc* lattice constant $a = 3.549 \text{ \AA}$ corresponding to the volume of bulk *hcp* Co.² Because we shall be

2. The larger and smaller lattice constants correspond to Wigner-Seitz atomic sphere radii of 2.669 and 2.621 Bohr atomic units, respectively.

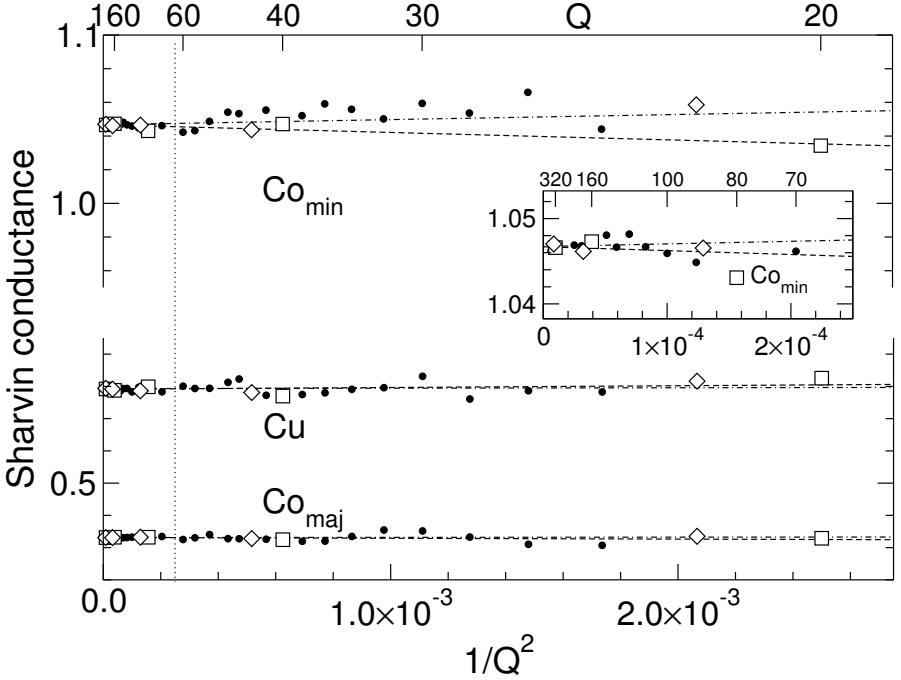


Figure 2.3: Sharvin conductance $G^\sigma(111)$ (in units of $10^{15} \Omega^{-1} \text{m}^{-2}$) for bulk fcc Cu and Co (majority and minority spin) plotted as a function of the normalized area element used in the Brillouin zone summation, $\Delta^2 \mathbf{k}_\parallel / A_{BZ} = 1/Q^2$. Q , the number of intervals along the reciprocal lattice vector is indicated at the top of the figure. The dashed line is the weighted (weighting Q^2) least-squares fit to the series $Q = 20, 40, 80, 160, 320$ shown as squares; the dash-dotted line is the weighted least-squares fit to the series $Q = 22, 44, 88, 176, 352$ shown as diamonds. The part of the curve for the Co minority spin case to the left of the vertical dotted line is shown on an expanded scale in the inset. An fcc lattice constant of $a = 3.614 \text{ \AA}$ and *spd* basis were used together with von Barth-Hedin's exchange-correlation potential.

studying Cu|Co interfaces where the volume per atom is not known very precisely from experiment, we will want to estimate the variation that can be expected when different but equally reasonable lattice constants are used. The increase of 3.4% (from 0.558 to $0.577 \times 10^{15} \Omega^{-1} \text{m}^{-2}$) observed for Cu can be attributed to the increased areal density of Cu atoms, $(3.614/3.549)^2$ corresponding to $\sim 3.7\%$. The Table also contains the corresponding results obtained with an *spdf*-basis. To the numerical accuracy shown, there is no difference between the *spd* and *spdf* case for Cu.

For Co majority spin states, there is a 4% decrease in the conductance on going from an *spd* to an *spdf* basis. For a lattice constant $a = 3.614 \text{ \AA}$, the magnetization is $1.684 \mu_B/\text{atom}$ for an *spd*- and $1.648 \mu_B/\text{atom}$ for an *spdf* basis corresponding, respectively, to $n_{\text{maj}} = 5.342$ and 5.324 electrons in the majority spin bands. Since

	$a(\text{\AA})$	basis	n_σ	$G^\sigma(111)$	
				present calc.	Schep ³
Copper	3.549	<i>spd</i>	5.5	0.577(0.577,0.577)	0.57
	3.549	<i>spdf</i>	5.5	0.577(0.577)	
	3.614	<i>spd</i>	5.5	<u>0.558</u> (0.559)	0.55
	3.614	<i>spdf</i>	5.5	0.558(0.558)	0.55
Cobalt majority	3.549	<i>spd</i>	5.323	0.469(0.459,0.467)	0.45
	3.549	<i>spdf</i>	5.304	0.449(0.440)	0.43
	3.614	<i>spd</i>	5.342	<u>0.466</u> (0.457)	0.45
	3.614	<i>spdf</i>	5.324	0.448(0.439)	
Cobalt minority	3.549	<i>spd</i>	3.677	1.082(1.081,1.082)	1.10
	3.549	<i>spdf</i>	3.696	1.120(1.125)	1.13
	3.614	<i>spd</i>	3.658	<u>1.046</u> (1.047)	1.06
	3.614	<i>spdf</i>	3.676	1.074(1.079)	

Table 2.1: The Sharvin conductances per spin (in units of $10^{15} \Omega^{-1}\text{m}^{-2}$) in the (111) direction for fcc Cu and Co using the experimental volumes of Cu and Co. The underlined numbers are the converged values discussed in relation to Fig. 2.3. Most of the results were obtained with von Barth-Hedin's exchange-correlation potential while the results in brackets are for Perdew-Zunger (PZ) and Vosko-Wilk-Nusair (VWN) parameterizations, respectively. Where a single number is given in brackets, it means that PZ and VWN potentials yield identical results to the accuracy given. The corresponding results of Schep et al. are given in the last column. The number of electrons with spin σ is given in the fourth column.

3. Ref [36].

all five (nominal) majority-spin d bands are full there are 0.342 and 0.324 electrons in the free-electron-like sp band. In a free electron picture the ratio of the projection of the spherical Fermi surfaces is $(0.324/0.342)^{2/3} = 0.96$, thus explaining the observed numerical result.

The Co majority-spin conductance scarcely changes with changing lattice constant, however. The origin of this behaviour lies in the volume dependence of the magnetic moment. When the lattice constant is decreased, the d bands broaden and the magnetic moment decreases from 1.684 to 1.646 μ_B /atom in the spd case with a corresponding decrease of the occupancy of the sp band from 0.342 to 0.323 majority-spin electrons. The corresponding 4% decrease in conductance is almost perfectly compensated by the increased areal density of atoms so there is no net change. For the minority-spin conductance, the same factors play a role but now the d bands are only partly filled. This results in complex Fermi surfaces for which simple estimates cannot

be made. In this case recourse must be made to full band structure calculations. We return to this in Sect. 2.3.2.

The calculations presented so far were carried out using the exchange-correlation potential calculated and parameterized by von Barth and Hedin [58]. This is only one of a number of potentials we could have used, none of which is clearly better than the others in describing the ground state properties of magnetic materials. To gauge the uncertainty arising from this arbitrary choice, a number of calculations were carried out using the potentials given by Perdew-Zunger [59] and Vosko-Wilk-Nusair [60] and the results are given in brackets in the Table. Using different exchange-correlation potentials leads to variation in the conductances of the order of 1 or 2 percent.

A different (but equivalent) approach was adopted by Schep *et al.* [1, 36] to the determination of the Sharvin conductances for the same systems using conventional first-principles LMTO-ASA bulk electronic band structures, i.e., using $\varepsilon_i(\mathbf{k})$ rather than $k_\mu(\varepsilon = \varepsilon_F, \mathbf{k}_\parallel)$ as used here. He expressed the Sharvin conductance as a projection of the Fermi surface onto a plane perpendicular to the transport direction and calculated the areas using a suitably modified 3D-BZ integration scheme. His results are also given in Table 2.1 and are as consistent with our present values as can be expected when using two entirely different computer codes.

In determining the conductance of the leads, the BZ summation does not present a problem. The uncertainties arising from small variations in the atomic volumes, from incompleteness of the basis and from the choice of LDA parameterization are of comparable size. The MTO-AS approximation can be systematically improved but only at substantial computational cost. Since there is currently no way to systematically improve upon the LDA we identify it and the lack of knowledge of the atomic structure as limiting factors in studying transport from first principles. Though the atomic structures could be determined theoretically by total energy minimization, the LDA again presents a barrier since it systematically underestimates lattice constants of transition metals in particular of the $3d$ series. Gradient corrections sometimes yield improvements but unfortunately not systematically so. We conclude that our knowledge of and ability to calculate from first principles Fermi surfaces for bulk magnetic materials such as Fe or Co does not at present justify using a more accurate but substantially more expensive computational scheme than the present one.

2.3.2 Ordered Interfaces

Cu and Co have slightly different atomic volumes. The equilibrium lattice constant of Cu is 3.614 \AA and of Co 3.549 \AA , assuming an *fcc* structure. Even in the absence of interface disorder, the lattice spacing will not be homogeneous and will depend on the lattice constant of the substrate on which the sample was grown, on the global and local concentrations of Cu and Co, and on other details of how the structure was prepared. In principle we could calculate all of this by energy minimization. However, we judge that the additional effort needed is not justified by current experimental knowledge. Instead, we content ourselves with estimating the uncertainty which results from plausible variations in the (interface) structure by considering two limiting cases and one intermediate case. In each case an *fcc* structure is assumed, with lattice

$a(\text{\AA})$	3.549		3.582	3.614
Basis	$spdf$	spd	spd	spd
$m_{\text{Cu}}(\text{bulk})$	0.000	0.000	0.000	0.000
$m_{\text{Cu}}(\text{int-4})$	0.001(1)	0.001	0.001	0.001
$m_{\text{Cu}}(\text{int-3})$	-0.001(0)	0.000	0.000	0.000
$m_{\text{Cu}}(\text{int-2})$	-0.005(5)	-0.005(4,5)	-0.005(4)	-0.005
$m_{\text{Cu}}(\text{int-1})$	0.002(4)	0.004(6,4)	0.003(4)	0.001(2)
$m_{\text{Co}}(\text{int+1})$	1.526(490)	1.578(45,73)	1.605(573)	1.636(01)
$m_{\text{Co}}(\text{int+2})$	1.621(597)	1.656(35,53)	1.673(53)	1.690(70)
$m_{\text{Co}}(\text{int+3})$	1.602(576)	1.645(21,41)	1.662(39)	1.680(59)
$m_{\text{Co}}(\text{int+4})$	1.610(587)	1.649(27,45)	1.665(45)	1.683(62)
$m_{\text{Co}}(\text{bulk})$	1.609(590)	1.646(22,42)	1.667(45)	1.684(62)
$G^{\text{maj}}(111)$	0.409(399)	0.431(21,29)	0.433(22)	<u>0.434</u> (24)
$G^{\text{min}}(111)$	0.378(379)	0.378(80,79)	0.371(73)	<u>0.364</u> (67)

Table 2.2: Variation of the layer-resolved magnetic moments (in Bohr magnetons) for Cu|Co(111) interfaces with basis set and lattice constant. The main results were obtained with von Barth-Hedin’s exchange-correlation potential while the results in brackets, where given, are for Perdew-Zunger and Vosko-Wilk-Nusair parameterizations, respectively. The underlined conductances are the converged values discussed in relation to Fig. 2.4. In the last two rows, the interface conductances are given in units of $10^{15} \Omega^{-1} \text{m}^{-2}$.

constants corresponding to (i) the atomic volume of Cu, (ii) the atomic volume of Co, (iii) an intermediate case with arithmetic mean of Cu and Co atomic volumes.

Our starting point is a self-consistent TB-LMTO SGF calculation [43] for the interface embedded between semi-infinite Cu and Co leads whose potentials and spin-densities were determined self-consistently in separate “bulk” calculations. The charge and spin-densities are allowed to vary in n_{Cu} layers of Cu and n_{Co} layers of Co bounding the interface. The results of these calculations for Cu|Co(111) interfaces and the three different lattice constants detailed above are given in Table 2.2 for $n_{\text{Cu}}=4$, $n_{\text{Co}}=4$. In the Cu layers, only tiny moments are induced. Only four layers away from the interface on the Co side, the magnetic moments are seen to be very close to the bulk values. At the interface, where the d -bandwidth is reduced as a result of the lower coordination number, the moments are *suppressed* rather than enhanced. This occurs because the majority-spin d bands are full and their number cannot increase. The width of the free-electron like sp band is less sensitive to the change in coordination and its exchange splitting also changes less. As a result, there is little change in the sp moment. When the d -bandwidth is reduced, there is conversion of minority- and majority-spin sp electrons, without loss of the sp moment, to the minority-spin d band with loss of d moment. This picture is supported by the full calculations.

Earlier we saw that an $\sim 2\%$ change in lattice constant changed the bulk magnetic moment of *fcc* Co by 2.3%. The effect of changing the basis, from spd to $spdf$, was

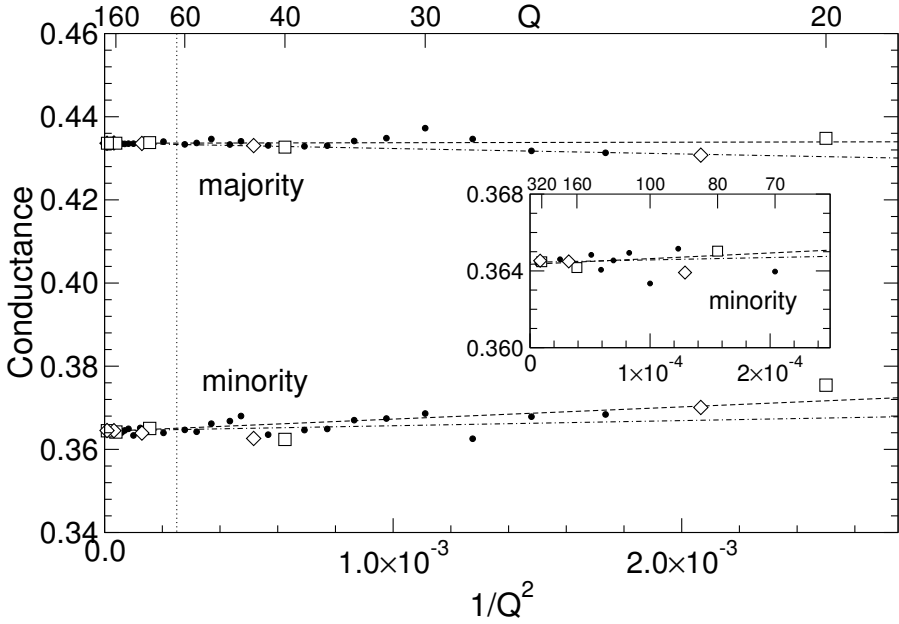


Figure 2.4: Interface conductance $G^\sigma(111)$ (in units of $10^{15} \Omega^{-1} \text{m}^{-2}$) for an fcc $\text{Cu|Co}(111)$ interface for majority and minority spins plotted as a function of the normalized area element used in the Brillouin zone summation, $\Delta^2 \mathbf{k}_\parallel / A_{\text{BZ}} = 1/Q^2$. Q , the number of intervals along the reciprocal lattice vector is indicated at the top of the figure. The dashed line is the weighted (weighting Q^2) least-squares fit to the series $Q = 20, 40, 80, 160, 320$ shown as squares; the dash-dotted line is the weighted least-squares fit to the series $Q = 22, 44, 88, 176, 352$ shown as diamonds. The part of the curve for the Co minority spin case to the left of the vertical dotted line is shown on an expanded scale in the inset. A “standard” configuration was used [61].

similar. From Table 2.2, the interface moments are seen to behave in a comparable fashion. The magnetic moment of the interface Co atoms decreases by 3.7%, from $1.636 \mu_B/\text{atom}$ for $a = 3.614 \text{ \AA}$ to $1.578 \mu_B/\text{atom}$ for $a = 3.549 \text{ \AA}$ for an *spd* basis and decreases from $1.578 \mu_B/\text{atom}$ to $1.526 \mu_B/\text{atom}$ for an *spdf* basis for $a = 3.549 \text{ \AA}$, a change of 3.4%. Thus the *sp* to d_{min} conversion is enhanced at the interface by the reduced *d*-bandwidth.

Once the interface potential has been obtained, the transmission matrix can be calculated and the BZ summation carried out. The convergence of this summation, shown in Fig. 2.4 for a lattice constant of $a = 3.614 \text{ \AA}$ and an *spd* basis, closely parallels that seen in Fig. 2.3 and therefore the \mathbf{k} -summation does not represent a

limitation in practice. Converged conductances

$$G^\sigma(\hat{n}) = \frac{e^2}{h} \sum_{\mu,\nu,\mathbf{k}_\parallel} T_{\mu\nu}^\sigma(\mathbf{k}_\parallel) = \frac{e^2}{h} \sum_{\mu,\nu,\mathbf{k}_\parallel} |t_{\mu\nu}^\sigma(\mathbf{k}_\parallel)|^2 \quad (2.48)$$

are given in the last two rows of Table 2.2. Though we will not concern ourselves in this publication with the application of the formalism we have been developing to a detailed interpretation of experimental observations, it should be noted that even a modest spin-dependence of “bare” interface conductances ($\sim 20\%$) can lead to spin-dependent interface resistances differing by a factor of $\sim 3 - 5$ once account is taken of the finiteness of the conductance of the perfect leads using a formula derived by Schep *et al.* [4]

$$R_{A/B}^\sigma = \frac{h}{e^2} \left[\frac{1}{\sum T_{\mu\nu}^\sigma} - \frac{1}{2} \left(\frac{1}{N_A^\sigma} + \frac{1}{N_B^\sigma} \right) \right] \quad (2.49)$$

where N_A^σ and N_B^σ , defined in (2.47), are the Sharvin conductances, in units of e^2/h , of the materials A and B forming the interface.

The majority-spin case can be readily understood in terms of the geometry of the Fermi surfaces of Cu and Co so we begin by discussing this simple case before examining the more complex minority-spin channel.

2.3.2.i) Clean Cu|Co (111) Interface: Majority Spins

In the absence of disorder, crystal momentum parallel to the interface is conserved. If, for a given value of \mathbf{k}_\parallel , there is a propagating state in Cu incident on the interface but none in Co, then an electron in such a state is completely reflected at the interface. Conversely, \mathbf{k}_\parallel 's for which there is a propagating state in Co but none in Cu also cannot contribute to the conductance. To determine the existence of such states, it is sufficient to inspect projections of the Fermi surfaces of *fcc* Cu and majority-spin Co onto a plane perpendicular to the transport direction \hat{n} , shown in Fig. 2.5 for $\hat{n} = (111)$. The first feature to note in the figure (left-hand and middle panels) is that per \mathbf{k}_\parallel there is only a single channel with positive group velocity so that the transmission matrix in (2.48) is a complex number whose modulus squared is a transmission probability with values between 0 and 1. It is plotted in the right-hand panel and can be interpreted simply. Regions which are depicted blue correspond to \mathbf{k}_\parallel 's for which there are propagating states in Cu but none in Co. These states have transmission probability 0 and are totally reflected. For values of \mathbf{k}_\parallel for which there are propagating states in both Cu and Co, the transmission probability is very close to one, depicted red. These states are essentially free electron-like states which have the same symmetry in both materials and see the interface effectively as a very low potential step. Close to the centre of the figure there is an annular region where there are propagating states in Co but none in Cu so they do not contribute to the conductance. Performing the sum in (2.48), we arrive at an interface conductance of $0.434 \times 10^{15} \Omega^{-1} \text{m}^{-2}$ to be compared to the Sharvin conductances given in Table 2.1 for Cu and Co; for $a = 3.614 \text{ \AA}$ and an *spd* basis these are, respectively, 0.558 and 0.466 in the same units. The interface conductance of 0.434 is seen to be essentially

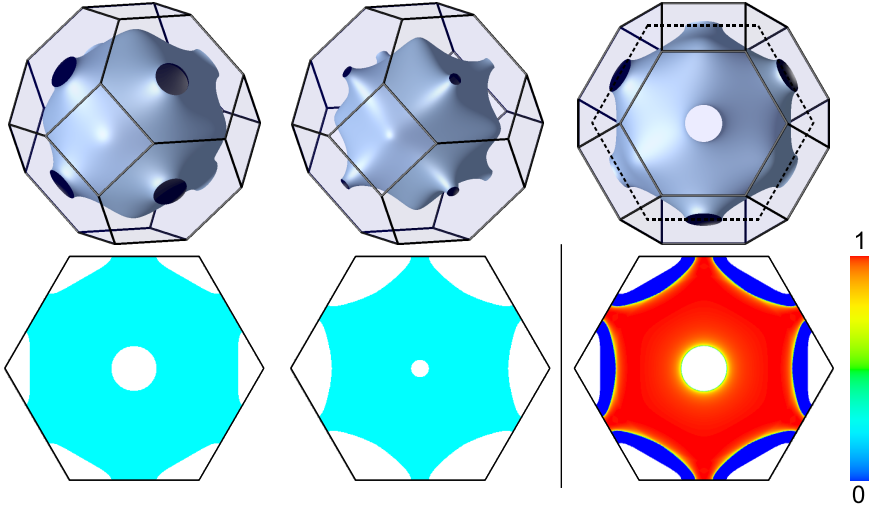


Figure 2.5: Top row, left-hand panel: Fermi surface (FS) of Cu; middle panel: majority-spin FS of Co; right-hand panel: Cu FS viewed along the (111) direction with a projection of the bulk fcc Brillouin zone (BZ) onto a plane perpendicular to this direction and of the two dimensional BZ. Bottom row, left-hand and middle panels: projections onto a plane perpendicular to the (111) direction of the Cu and majority-spin Co Fermi surfaces; right-hand panel: transmission probability for majority-spin states as a function of transverse crystal momentum, $T(\mathbf{k}_{\parallel})$ for an fcc Cu|Co(111) interface.

the Sharvin conductance of the majority states of Co reduced because the states closest to the Λ -axis (corresponding to the symmetry axis of the figures, the ΓL line in reciprocal space) do not contribute. The explanation of the 5% decrease found on going from an *spd* to an *spdf* basis, (0.431 to 0.409), parallels that given for the corresponding change in the Sharvin conductance of bulk Co (0.469 to 0.449 in Table 2.1).

2.3.2.ii) Clean Cu|Co (111) Interface: Minority Spins

The minority-spin case is considerably more complex because the Co minority-spin *d* bands are only partly filled, resulting in multiple sheets of Fermi surface. These sheets are shown in Fig. 2.6 together with their projections onto a plane perpendicular to the (111) transport direction. Compared to Fig. 2.5, one difference we immediately notice is that even single Fermi surface (FS) sheets are not single valued: for a given \mathbf{k}_{\parallel} there can be more than one mode with positive group velocity. The areas depicted green in the projections of the FS sheets from the fourth and fifth bands are examples where this occurs.

An electron incident on the interface from the Cu side, with transverse crystal momentum \mathbf{k}_{\parallel} , is transmitted into a linear combination of all propagating states with the same \mathbf{k}_{\parallel} in Co; the transmission matrix $t_{\mu\nu}^{\sigma}(\mathbf{k}_{\parallel})$ is in general not square but rectangular. The transmission probabilities $T_{\mu\nu}(\mathbf{k}_{\parallel})$ are shown in the bottom row of Fig. 2.6. Because there is only a single incident state for all \mathbf{k}_{\parallel} , the maximum transmission probability is one. Comparison of the total minority-spin transmission probability $T_{\mathcal{LR}}(\mathbf{k}_{\parallel})$ (Fig. 2.6, bottom right-hand panel) with the corresponding majority-spin quantity (bottom right-hand panel of Fig. 2.5) strikingly illustrates the spin-dependence of the interface scattering, much more so than the integrated quantities might have led us to expect; the interface conductances, 0.364 and $0.434 \times 10^{15} \Omega^{-1}\text{m}^{-2}$ from Table 2.2, differ by only $\sim 20\%$.

Three factors contribute to the large \mathbf{k}_{\parallel} -dependence of the transmission probability: first and foremost, the complexity of the Fermi surface of both materials but especially of the minority spin of Co; secondly and inextricably linked with the first because of the relationship $\hbar v_{\mathbf{k}} = \nabla_{\mathbf{k}}\varepsilon(\mathbf{k})$, the mismatch of the Fermi velocities of the states on either side of the interface. Thirdly, the orbital character of the states μ and ν which varies strongly over the Fermi surface and gives rise to large matrix element effects.

The great complexity of transition metal Fermi surfaces, clear from the figure and well-documented in standard textbooks, is not amenable to simple analytical treatment and has more often than not been neglected in theoretical transport studies. Nevertheless, as illustrated particularly well by the ballistic limit [1, 36], spin-dependent band structure effects have been shown to lead to magnetoresistance ratios comparable to what are observed experimentally in the current-perpendicular-to-plane (CPP) measuring configuration and cannot be simply ignored in any quantitative discussion. Most attempts to take into account contributions of the d states to electronic transport do so by mapping the five d bands onto a single tight-binding or free-electron band with a large effective mass.

Fermi surface topology alone cannot explain all aspects of the transmission coefficients seen in Fig. 2.6. For example, there are values of \mathbf{k}_{\parallel} , such as that labelled Y in the figure, for which propagating solutions exist on both sides of the interface yet the transmission probability is zero. This can be understood as follows. At $\mathbf{k}_{\parallel} = Y$, the propagating states in Cu have $\{s, p_y, p_z, d_{yz}, d_{3z^2-r^2}, d_{x^2-y^2}\}$ character (assuming the choice of in-plane axes as illustrated in the top righthand panel of Fig. 2.6) and are even with respect to reflection in the plane formed by the y -axis and the transport direction perpendicular to the (111) plane which we choose to be the z -axis. For this \mathbf{k}_{\parallel} the only propagating state in Co is in the fourth band. It has $\{p_x, d_{xy}, d_{xz}\}$ character which is odd with respect to reflection in the yz plane. Consequently, the corresponding hopping matrix elements in the Hamiltonian (and in the Green's function) vanish and the transmission is zero.

Along the k_y axis the symmetry of the states in Cu and those in the fourth band of Co remain the same and the transmission is seen to vanish for all values of k_y . However, at points further away from Λ , we encounter states in the third band of Co which have even character whose matrix elements do not vanish by symmetry and

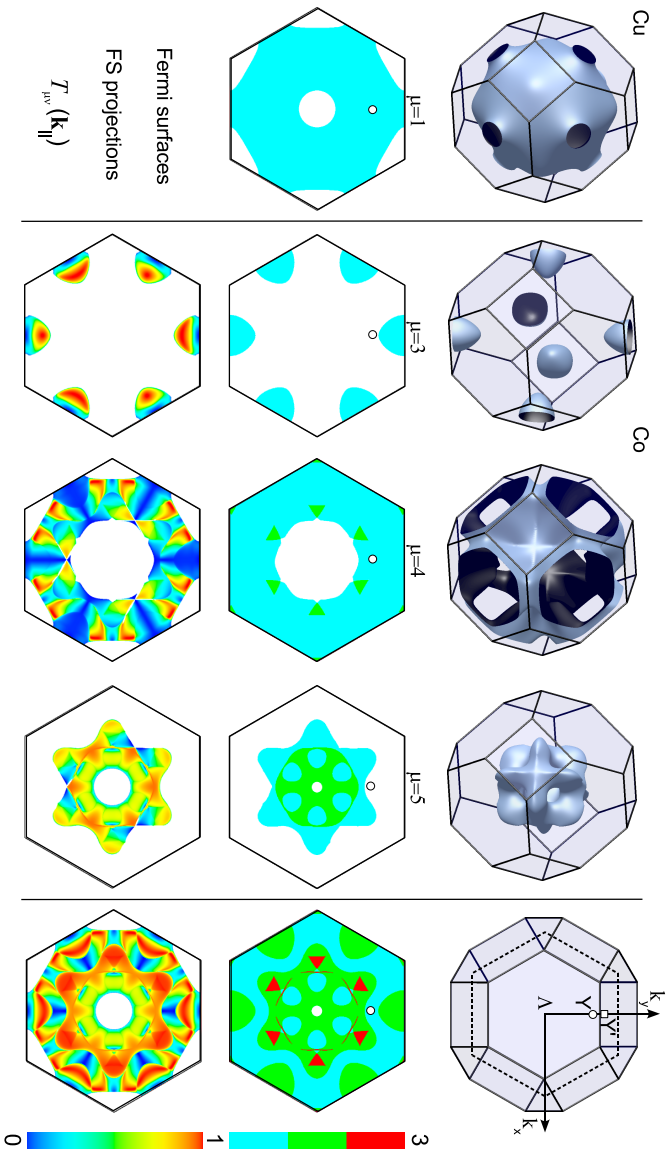


Figure 2.6: Top row, lefthand panel: Fermi surface (FS) of fcc Cu; middle panels: third, fourth and fifth FS sheets of minority-spin fcc Co; righthand panel: projection of the bulk fcc Brillouin zone (BZ) onto a plane perpendicular to the (111) direction and of the two dimensional BZ. Middle row: corresponding projections of individual FS sheets and (rhs) of Co total. The number of propagating states with positive velocity is colour-coded following the colour bar on the right. Bottom row: probability $T_{\mu\nu}^{\nu}(\mathbf{k}_{\parallel})$ for a minority-spin state on the single FS sheet of Cu ($\nu = 1$) to be transmitted through a Cu/Co(111) interface into FS sheet μ of fcc Co as a function of the transverse crystal momentum \mathbf{k}_{\parallel} . The point Y (indicated by a small open circle) is such that there are only propagating states in Cu and in the fourth FS sheet of Co. For the point Y' (indicated by a small open square) which is slightly further away from Λ , there is, in addition, a propagating state in the third FS sheet of Co.

we see substantial transmission probabilities. Similarly, for points closer to Λ , there are states in the fifth band of Co with even character whose matrix elements also do not vanish and again the transmission probability is substantial. Because it is obtained by superposition of transmission probabilities from Cu into the third, fourth and fifth sheets of the Co FS, the end result, though it may appear very complicated, can be straightforwardly analysed in this manner k-point by k-point.

Though the underlying lattice symmetry is only threefold, the Fermi surface projections shown in Fig. 2.6 have six-fold rotational symmetry about the line Λ because the bulk *fcc* structure has inversion symmetry (and time-reversal symmetry). The interface breaks the inversion symmetry so $T_{\mu\nu}(\mathbf{k}_{\parallel})$ has only threefold rotation symmetry for the individual FS sheets. However, in-plane inversion symmetry is recovered for the total transmission probability $T_{\mathcal{LR}}(-\mathbf{k}_{\parallel}) = T_{\mathcal{LR}}(\mathbf{k}_{\parallel})$ which has full sixfold symmetry. This follows from the time-reversal symmetry and is proven in Appendix A.2.

2.3.3 Interface Disorder

Instructive though the study of perfect interfaces may be in gaining an understanding of the role electronic structure mismatch may play in determining giant magnetoresistive effects, all measurements are made on devices which contain disorder, mostly in the diffusive regime. Because there is little information available from experiment about the nature of this disorder, it is very important to be able to model it in a flexible manner, introducing a minimum of free parameters. To model interfaces between materials with different lattice constants and disorder, we use the lateral supercells described in section 2.2.4. Since this approach is formally only valid if sufficiently large supercells are used, we begin by studying how the interface conductance depends on the lateral supercell size.

To perform fully self-consistent calculations for a number of large lateral supercells and for different configurations of disorder would be prohibitively expensive. Fortunately, the coherent potential approximation (CPA) is a very efficient way of calculating charge and spin densities for a substitutional disordered A_xB_{1-x} alloy with an expense comparable to that required for an ordered system with a minimal unit cell [62]. The output from such a calculation are atomic sphere potentials for the two sites, v_A and v_B . The layer CPA approximation generalizes this to allow the concentration to vary from one layer to the next [43].

Once v_A and v_B have been calculated for some concentration x , an $H = H_1 \times H_2$ lateral supercell is constructed in which the potentials are distributed at random, maintaining the concentration for which they were self-consistently calculated. The conductances calculated for $4 \leq \sqrt{H} \leq 20$ are shown in Fig. 2.7 for a Cu|Co(111) interface in which the Cu and the Co layers forming the interface are totally mixed to give two layers of 50%-50% interface alloy. For each value of H , the results for a number of different randomly generated disorder configurations are shown (15 for minority, 5 for minority spin). The sample to sample variation is largest for the

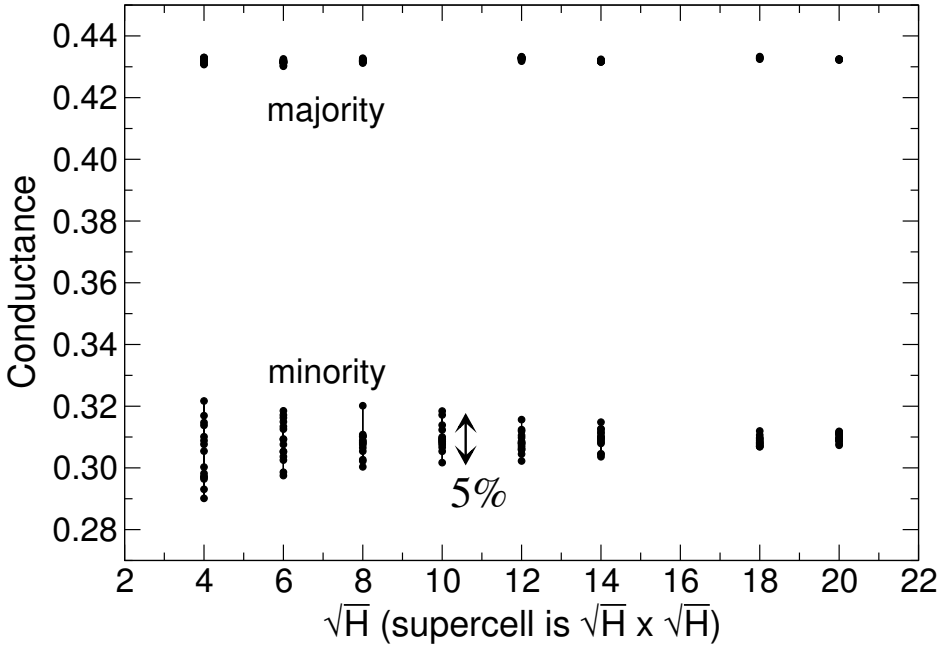


Figure 2.7: Interface conductance (in units of $10^{15} \Omega^{-1}\text{m}^{-2}$) for a disordered Cu|Co (111) interface modelled as 2ML of 50%-50% alloy in a $\sqrt{H} \times \sqrt{H}$ lateral supercell as a function of \sqrt{H} . The results are given for different randomly generated configurations of disorder (15 for minority spin, 5 for majority spin). Results are for a “standard” configuration [61].

minority spin case, ranging from $\pm 5\%$ for a modest 4×4 unit cell and decreasing to less than $\pm 1\%$ for a 20×20 unit cell. For $\sqrt{H} \sim 10$, the spread in minority spin conductances is $\sim 5\%$ which is comparable to the typical uncertainty we associated with the LDA error, the uncertainty in lattice constants or the error incurred by using the ASA.

Comparing now the conductances without and with disorder, we see that interface disorder has virtually no effect on the majority spin channel (0.434 versus $0.432 \times 10^{15} \Omega^{-1}\text{m}^{-2}$) which is a consequence of the great similarity of the Cu and Co majority spin potentials and electronic structures. However, in the minority-spin channel the effect (0.364 versus $0.31 \times 10^{15} \Omega^{-1}\text{m}^{-2}$) is much larger. As noted in the context of (2.49), a relatively small change in the interface transmission can lead to a large change in the interface resistance when account is taken of the finite conductance of the leads. We will return to the consequences for the spin-dependent interface resistance after completing the study of the interface transmission on which it is based.

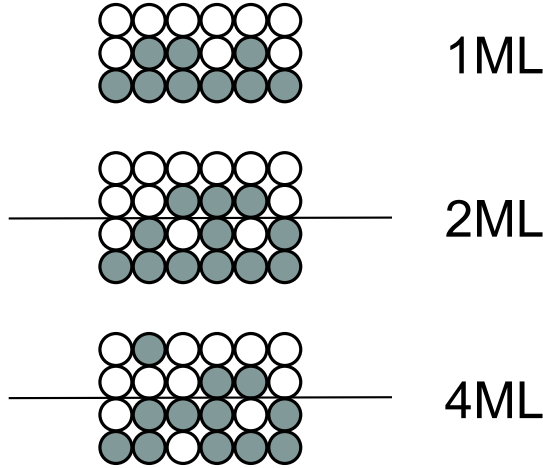


Figure 2.8: Illustration of 3 different models of interface disorder considered. Top (1ML): disorder is modelled using one monolayer (ML) of $[Cu_{1-x}Co_x]$ alloy between Cu and Co leads, denoted as $Cu[Cu_{1-x}Co_x]Co$. Middle (2ML): disorder modelled in two MLs as $Cu[Cu_{1-x}Co_x|Cu_xCo_{1-x}]Co$. Bottom (4ML): starting from the 2 ML disorder case, $1/3$ of the concentration x of impurity atoms is transferred to the next layer resulting in disorder in four MLs: $Cu[Cu_{1-\frac{x}{3}}Co_{\frac{x}{3}}|Cu_{1-\frac{2x}{3}}Co_{\frac{2x}{3}}|Cu_{\frac{2x}{3}}Co_{1-\frac{2x}{3}}|Cu_{\frac{x}{3}}Co_{1-\frac{x}{3}}]Co$.

Dependence of interface conductance on alloy concentration

The transmission probabilities can be classified as being *specular* or *diffuse* depending upon whether or not transverse momentum is conserved [13, 63]. In the presence of interface disorder, modelled here in lateral supercells, the conductance per unit area can be expressed as

$$\begin{aligned}
 G &= G_s + G_d \\
 &= \frac{e^2}{h} \sum_{\substack{\mu\nu \\ \mathbf{k}_{\parallel}}} T_{\mu\nu}(\mathbf{k}_{\parallel}, \mathbf{k}_{\parallel}) + \frac{e^2}{h} \sum_{\substack{\mu\nu \\ \mathbf{k}_{\parallel} \neq \mathbf{k}'_{\parallel}}} T_{\mu\nu}(\mathbf{k}_{\parallel}, \mathbf{k}'_{\parallel})
 \end{aligned} \quad (2.50)$$

where \mathbf{k}_{\parallel} and \mathbf{k}'_{\parallel} belong to the two dimensional Brillouin zone for (1×1) translational periodicity and $T_{\mu\nu}(\mathbf{k}_{\parallel}, \mathbf{k}'_{\parallel}) = t_{\mu\nu}(\mathbf{k}_{\parallel}, \mathbf{k}'_{\parallel})t_{\mu\nu}^{\dagger}(\mathbf{k}_{\parallel}, \mathbf{k}'_{\parallel})$. The transmission matrix elements between two Bloch states with the same \mathbf{k}_{\parallel} are defined to be specular, those between scattering states with different \mathbf{k}_{\parallel} as being diffuse. In the absence of interface disorder, there is by definition only a specular component.

The results in Fig. 2.7 were obtained for a structural model of the $Cu|Co(111)$ interface consisting of two monolayers (2ML) of 50%-50% alloy that was derived

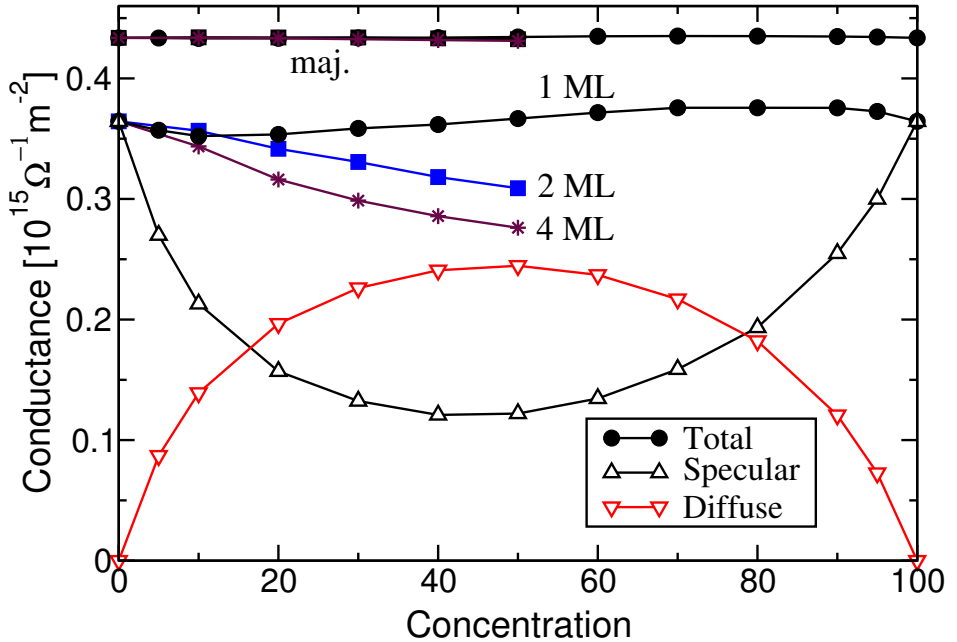


Figure 2.9: Interface conductance of a disordered Cu|Co (111) interface with disorder modelled in a 20×20 lateral supercell as a function of the concentration x (in percent) of Co in Cu. Results are shown for three different models with disorder in 1, 2 or 4 MLs which are described in Fig. 2.8 where x is also defined. Only a single disorder configuration was used and the size of the symbols corresponds to the spread in values found for this supercell size in Fig. 2.7. For 1ML, the total conductance is resolved into specular and diffuse components. Results are for a “standard” configuration [61].

from X-ray [64], NMR [65, 66], and magnetic EXAFS [67] studies. Though the most plausible model there is at present, it contains large uncertainties. This makes it important to explore the consequences of varying the parameters defining the model. To do so, we calculate the conductance using 20×20 lateral supercells as a function of alloy concentration for models in which the disorder is confined to one, two or four monolayers. The three models are defined in Fig. 2.8. From the results shown in Fig. 2.9, it can be seen that the interface transmission for majority-spin electrons depends only very weakly on alloy concentration and its spatial distribution: the results for the 1ML, 2ML and 4ML models cannot be distinguished on the scale of the figure. When the conductance is decomposed using (2.50), the diffuse component is found to be very small. Therefore, only the results for the minority-spin case need be examined in any detail.

We start by varying the alloy concentration over the full concentration range (0-100%) in steps of 10% for a disordered monolayer. The variation in the total transmission of $\sim 7\%$ seen in Fig. 2.9 (1ML), substantially exceeds the spread found for different configurations of disorder (which according to Fig. 2.7 is less than $\pm 1\%$ for a 20×20 lateral supercell) and is therefore statistically significant. Upon adding Co to a layer of Cu, the transmission decreases, reaches a minimum for $\sim 10\%$ Co, then increases monotonically up to $\sim 80\%$ Co where the transmission is *higher* than for a clean interface.⁴ 100% Co represents a clean interface again, so this limit must yield the same transmission as 0% Co.

The variation can be examined in terms of the specular and diffuse components defined in (2.50). From Fig. 2.9, it can be seen that, for the minority spin channel, the diffuse scattering by Co impurity atoms in Cu is stronger than that by Cu impurity atoms in Co. However, the specular scattering is also more strongly reduced by Co in Cu than by Cu in Co. The two effects largely cancel resulting in the undulatory total transmission as a function of the alloy concentration seen in the figure. The diffuse scattering has a maximum close to a 50%-50% alloy concentration where its contribution to the conductance is almost twice as large as from the specular scattering. While the conductance as such is scarcely affected, the strong diffuse scattering will play an important role in destroying the phase coherence of the electrons, ultimately justifying semiclassical descriptions of transport [68–70]. Qualitatively similar results for the specular and diffusive components of the transmission have been reported for the (100) orientation and 2ML model in Ref. [24].

If the disorder extends over more than a monolayer, then modelling the interface as several layers of homogeneous alloy is not obviously realistic. Instead, one might expect the layers closest to the interface to be most strongly mixed, the amount of mixing decreasing with the separation from the interface. A simple way to model this is to take two interface layers, one Cu and one Co, and to mix them in varying degrees. Denoting this Cu|Co interface as $\text{Cu}[\text{Cu}_{1-x}\text{Co}_x|\text{Cu}_x\text{Co}_{1-x}]$ Co we consider $0 \leq x \leq 0.5$ *i.e.*, the Cu concentration decreases monotonically from left to right. The calculated interface transmission is seen (Fig. 2.9, 2ML) to essentially interpolate linearly the results obtained previously for the clean ($x = 0$) and disordered ($x = 0.5$) cases.

A slightly more elaborate model can be constructed from the 2ML model by distributing the x impurity atoms so that $2x/3$ are in the interface layer while $x/3$ are to be found further from the original interface, in the following layer. This results in the concentration profile $\text{Cu}[\text{Cu}_{1-\frac{x}{3}}\text{Co}_{\frac{x}{3}}|\text{Cu}_{1-\frac{2x}{3}}\text{Co}_{\frac{2x}{3}}|\text{Cu}_{\frac{2x}{3}}\text{Co}_{1-\frac{2x}{3}}|\text{Cu}_{\frac{x}{3}}\text{Co}_{1-\frac{x}{3}}]$ Co. $x = 0$ corresponds to a completely ordered interface while the maximum value x can have so that the concentration decreases from left to right monotonically is 75%. This relatively small redistribution of intermixed atoms is seen to reduce the transmission by 15% for $x = 0.5$ (Fig. 2.9, 4ML). A detailed analysis of the different contributions to the interface scattering in the 2ML and 4ML cases will be given in

4. Interface disorder can *increase* interface transmission if electronic structure mismatch leads to a highly reflecting clean interface. For example, for the majority-spin electrons at an Fe/Cr (001) interface, this is the case. There, interface disorder in the form of two layers of 50%-50% alloy *reduced* the interface resistance by a factor three [9]. See also Chapter 3.

a separate publication.

2.3.4 Analysis of Interface Disorder Scattering

The scattering induced by two layers of 50%-50% alloy is illustrated in Fig. 2.10 and Fig. 2.11 for the majority and minority spins, respectively, of a Cu|Co(111) interface. Calculations were performed for the single $\mathbf{k}_{\parallel}^{\text{S}}$ point, Γ , and a 20×20 lateral supercell equivalent to using a 1×1 interface cell and k-space sampling with 20×20 points in the corresponding BZ. Disorder averaging was carried out using 5 (for majority spin) or 20 (for minority spin) disorder configurations generated randomly.

Figs. 2.10(a) and 2.10(b) show the majority-spin Fermi surface projections of *fcc* Cu and Co, respectively, obtained from “unfolding” the supercell calculation. The coarse 20×20 grid is seen to yield a good representation of the detailed Fermi surface projections shown in Fig. 2.5. $T(\mathbf{k}_{\parallel}, \mathbf{k}'_{\parallel})$ is shown in Fig. 2.10(c) for $\mathbf{k}_{\parallel} = Y$ on the k_y axis in Fig. 2.6. Specular scattering dominates with $T(\mathbf{k}_{\parallel} = Y, \mathbf{k}'_{\parallel} = Y) = 0.93$. The diffuse scattering is so weak that nothing can be seen on a scale of T from 0 to 1. To render it visible, a magnification by a factor 500 is needed, Fig. 2.10(d). The total diffuse scattering $T_d(Y) = \sum_{\mathbf{k}'_{\parallel} \neq Y} T(Y, \mathbf{k}'_{\parallel}) = 0.04$ can be seen from the figure to be made up of contributions of $T \sim 0.0004$ from roughly a quarter of the BZ (100 \mathbf{k}_{\parallel} points) centred on $\mathbf{k}_{\parallel} = Y$. The total transmission, $T_{total} = T_s + T_d = 0.93 + 0.04 = 0.97$, compared to a transmission of 0.99 in the absence of disorder. Similar results were obtained for other \mathbf{k}_{\parallel} points. In the majority case, there is thus a strong specular peak surrounded by a weak diffuse background.

The minority-spin Fermi surface projections of *fcc* Cu and Co are shown in Figs. 2.11(a) and 2.11(b), respectively. Compared to the corresponding panels in Fig. 2.6, the 20×20 point representation is seen to be sufficient to resolve the individual Fermi surface sheets of Co. To study the effect of interface disorder, we consider scattering out of two different \mathbf{k}_{\parallel} s in Cu (Figs. 2.11(c) and (d)). The first thing to note is the similarity of both transmission plots to the projected FS of Co, Fig. 2.11(b), suggesting very strong diffusive scattering proportional to the density of available final states.

The first case we consider is where $\mathbf{k}_{\parallel} = Y$ for which the transmission was zero as a result of the symmetry of the states along the k_y axis in the absence of disorder. $T(Y, \mathbf{k}'_{\parallel})$ is shown in Fig. 2.10(c). By contrast with the majority-spin case just examined, there is now scattering to all other k-points in the 2D BZ, $\sum_{\mathbf{k}'_{\parallel} \neq Y} T(Y, \mathbf{k}'_{\parallel}) = 0.58$ while $T(Y, Y)$ has only increased from 0.00 in the clean case, to 0.01 in the presence of disorder. The effect of disorder is to increase the total transmission, $T_{total}(Y) = \sum_{\mathbf{k}'_{\parallel}} T(Y, \mathbf{k}'_{\parallel})$ from 0.00 to $T_s(Y) + T_d(Y) = 0.01 + 0.58 = 0.59$; for states which were originally strongly reflected, disorder *increases* the transmission.

The second case we consider is that of a k-point slightly further away from the origin Λ along the k_y axis which had a high transmission, $T(Y') = 0.98$, in the

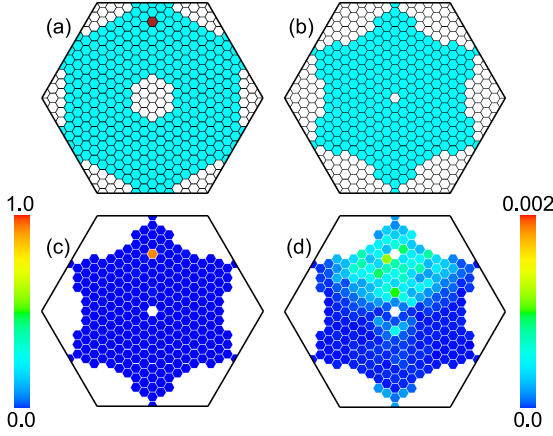


Figure 2.10: Fermi surface projections of majority-spin fcc Cu (a) and Co (b) derived from a single k -point using a 20×20 lateral supercell. The dark red point in the Cu Fermi surface projection corresponds to the point Y in the top righthand panel of Fig. 2.6. $T(Y, \mathbf{k}'_{\parallel})$ is shown in (c), and in (d) magnified by a factor 500 where the ballistic component $T(Y, \mathbf{k}'_{\parallel} = \mathbf{Y})$ is indicated by a white point because its value goes off the scale. The results were obtained by averaging over 5 different configurations of disorder.

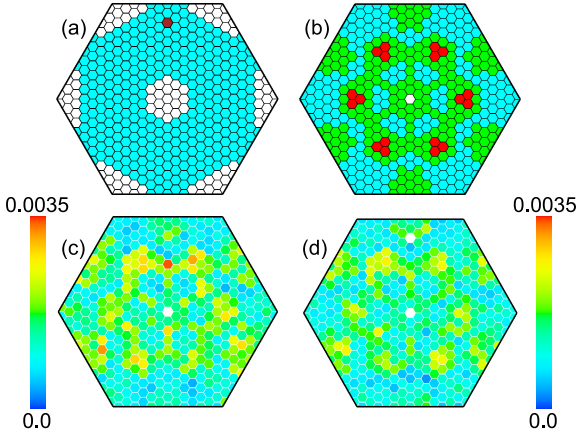


Figure 2.11: Fermi surface projections of minority-spin fcc Cu (a) and Co (b) derived from a single k -point using a 20×20 lateral supercell. The dark red point in the Cu Fermi surface projection corresponds to the point Y' in the top righthand panel of Fig. 2.6. (c) $T(Y, \mathbf{k}'_{\parallel})$ and (d) $T(Y', \mathbf{k}'_{\parallel})$ calculated using 20 different disorder configurations; the ballistic component $T(Y', \mathbf{k}'_{\parallel} = Y')$ is indicated by a white point because its value goes off scale. The results were obtained by averaging over 20 different configurations of disorder.

absence of disorder. For this k-point, $T(Y', \mathbf{k}'_{\parallel})$, shown in Fig. 2.10(d), looks very similar to Fig. 2.10(c). There is strong diffuse scattering with $\sum_{\mathbf{k}'_{\parallel} \neq Y'} T(Y', \mathbf{k}'_{\parallel}) = 0.54$ while $T(Y', Y')$ has been drastically decreased from 0.98 in the clean case, to 0.06 as a result of disorder. The total transmission, $T_{total}(Y') = T_s(Y') + T_d(Y') = 0.06 + 0.54 = 0.60$, is almost identical to what was found for the Y point. The effect of disorder has been to *decrease* the transmission for states which were originally weakly reflected. The strong k-dependence of the transmission found in the specular case is largely destroyed by a small amount of disorder in the minority-spin channel. The contribution from specular component (integrated over 2D BZ) is reduced to 15% of the total transmission.

2.3.5 Interface resistance

To the best of our knowledge, spin-dependent interface transmissions have not yet been measured directly. What is usually done [71, 72] is to measure total resistances for a whole series of magnetic multilayers in which the total number of interfaces and/or the thicknesses of the individual layers is varied. The measured results are interpreted in terms of volume resistivities and interface resistances. By applying an external magnetic field, the magnetizations of neighbouring layers which are oriented antiparallel (AP) can be forced to line up in parallel (P). By measuring the resistances in both cases, spin-dependent volume resistivities and interface resistances can be extracted using the two current series resistor model [68–70]. If we take expression (2.49) which relates the interface transmission to the interface resistance occurring in the 2CSR model as given [4, 33], we can study how typical uncertainties in interface transmission, arising from arbitrary assumptions about the interface disorder, lattice constant or basis set translate into uncertainty in predicted interface resistances. Using the transmission probabilities from Fig. 2.9 in (2.49) results in the curves shown in Fig. 2.12. For comparison, a range of literature values for the spin-dependent interface resistances derived from experiments on sputtered and MBE (molecular beam epitaxy) grown multilayers [73] is included in the figure.

For the minority-spin case, experimental values (in units of $\text{f}\Omega\text{m}^2$) range from 1.30–1.80 compared to calculated values of 1.29 for $\text{Cu}[\text{Cu}_{.3}\text{Co}_{.7}]\text{Co}$, through 1.37 for a disorder-free interface, to a value of 2.25 for the 4ML model with $x = 0.5$, $\text{Cu}[\text{Cu}_{.83}\text{Co}_{.17}|\text{Cu}_{.67}\text{Co}_{.33}|\text{Cu}_{.33}\text{Co}_{.67}|\text{Cu}_{.17}\text{Co}_{.83}]\text{Co}$. The influence of lattice constant and basis set on the clean interface resistance values is small (see Table 2.3). The present modelling of interface alloying shows that the interface resistance is more strongly dependent on the detailed spatial distribution of disorder than was previously found [9] where only the concentration range $x = 0.5 \pm 0.06$ of the 2ML interface alloy model extracted from experiment [64–67] was explored.

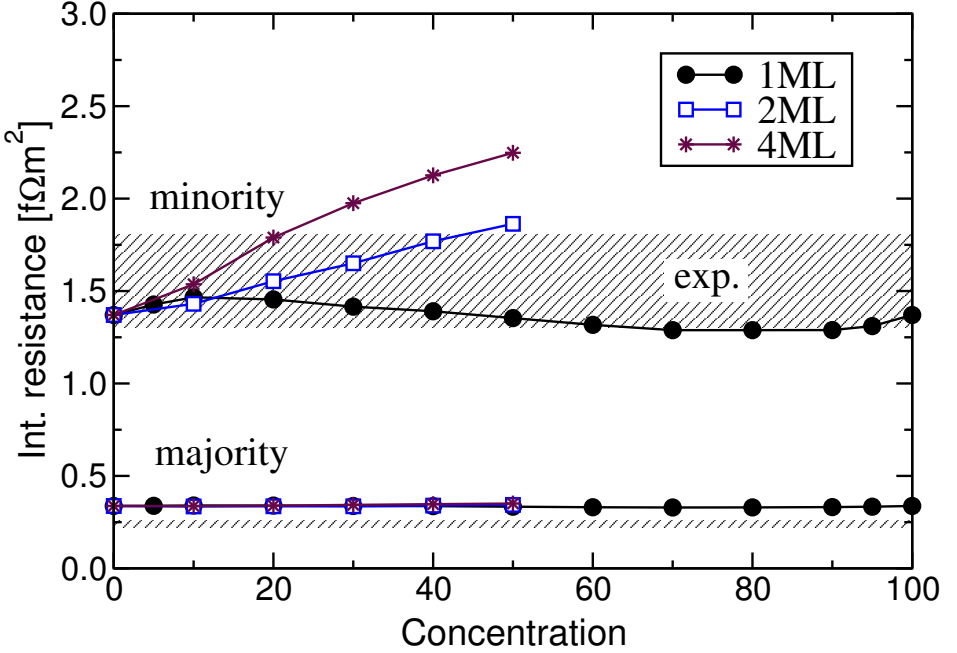


Figure 2.12: Interface resistance for disordered interfaces as a function of the alloy concentration used to model disordered interfaces calculated using (2.49) and the transmission probabilities shown in Fig. 2.9. The experimental values for sputtered and MBE grown multilayers cited in Table I of Ref. [73] span a range of values which is indicated by the shaded regions.

$a(\text{\AA})$	3.549	3.614
Basis	<i>spdf</i>	<i>spd</i>
$R^{\text{maj}}(111)$	0.46	0.39
$R^{\text{min}}(111)$	1.33	1.32

Table 2.3: Interface resistances, in units of $f\Omega\text{m}^2$, for ordered interfaces, calculated using expression (2.49) and the data from Tables 2.1 and 2.2. The values given here for a lattice constant of $a = 3.549\text{\AA}$ and *spd* basis differ slightly from those reported in Ref. [9] which were performed using energy-independent muffin-tin orbitals linearized about the centers of gravity of the occupied conduction states and not at the Fermi energy. The current implementation [48] uses energy-dependent, (non-linearized) MTO's, calculated exactly at the Fermi energy which improves the accuracy at no additional cost.

For the majority-spin case, the spread in values of the interface resistance extracted from experiment (for the same samples as for the minority-spin case) is quite small,

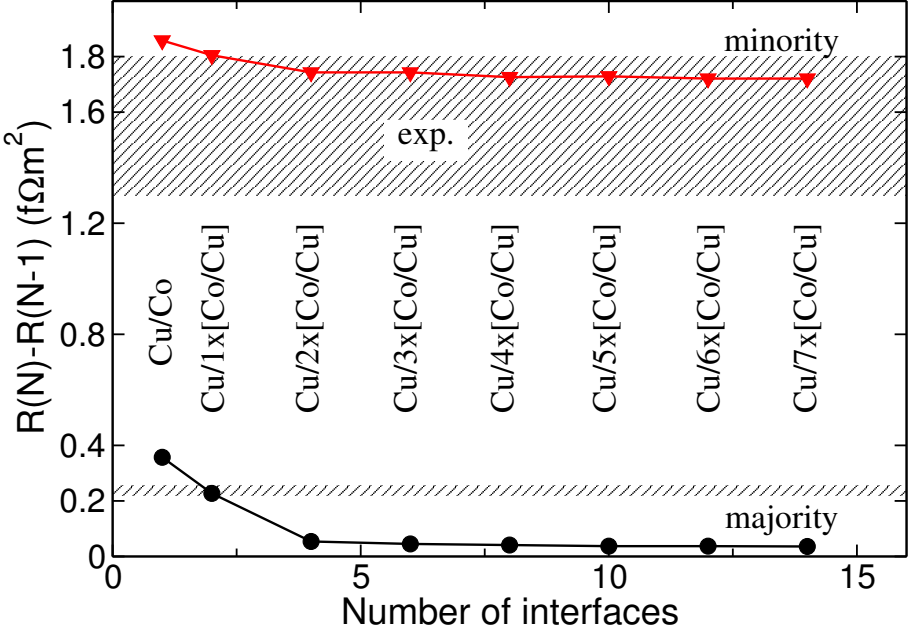


Figure 2.13: Differential interface resistance as the number of interfaces increase for a disordered Cu|Co(111) multilayer embedded between Cu leads. A 10×10 lateral supercell was used and the interface was modelled as two layers of 50%-50% alloy (2ML model). The results represent an average over 5 disorder configurations and were obtained for a “standard” configuration [61]. The range of experimental values [73] is indicated by the shaded regions.

0.22-0.25, and does not overlap with the values of 0.34 found for a lattice constant of $a = 3.614 \text{ \AA}$. Unlike the minority-spin case, changing the lattice constant or using an *spdf* basis leads to substantially *larger* values (Table 2.3). Because the majority-spin transmission does not depend on the details of the interface disorder, this cannot be the origin of the discrepancy. Motivated by the weak scattering in this case, we examine the validity [70, 73–76] of the 2CSR model by calculating the resistance of a magnetic multilayer containing a large number of disordered interfaces and plot the resistance added by each additional interface in Fig. 2.13. Compared to similar calculations in Ref. [9], the number of interfaces, size of lateral supercell (10×10) and disorder configurations averaged over are increased substantially. While the calculations are in very good agreement with Ohm’s law for the strongly scattering minority-spin case, it can be seen that this is not the case for the majority-spin electrons. For a small number of interfaces there is a clear breakdown of Ohm’s law and thus of the 2CSR model. The interface resistance eventually saturates at a value much lower than those extracted from experiment. While inclusion of bulk scattering will modify this picture somewhat, exploratory calculations [77] indicate that the type of

“bulk” impurities which may be reasonably expected to be found in sputtered or MBE grown multilayers affect the minority spin electrons much more than the majority spins. Agreement for the latter can only be achieved at the expense of ruining good agreement for the former.

2.4 Discussion

Details of a muffin tin orbital-based method suitable for calculating from first-principles scattering matrices involving layered magnetic materials have been given. In a wide range of applications [9, 45–50], it has been shown to be much more efficient and transparent than a previously used LAPW-based method [4, 6, 37]. Various other schemes have been developed for calculating the transmission of electrons through an interface (or a more extended scattering region) both from first principles [7, 8, 10–12, 14, 15, 17, 18, 34, 35, 37, 78], or using as input electronic structures which were calculated from first principles [19, 21, 22, 79–84]. Most are based upon a formulation for the conductance in terms of non-equilibrium Green’s functions [57] (NEGF) which reduces in the appropriate limit to the well known Fisher-Lee (FL) linear-response form [27] for the conductance of a finite disordered wire embedded between crystalline leads. Most implementations of the NEGF or FL schemes have two disadvantages. (i) The transmission is calculated for a complex energy which leads to difficulties in studying for example, tunneling magnetoresistance, where the finite imaginary part can give rise to an exponential decay which obscures the interesting physical decay of the transmission as a function of the barrier thickness. (ii) For a given value of transverse crystal momentum, the transmission is expressed as a trace over the basis set in terms of which the Green’s function and self-energy are expressed [55]. While this has the advantage that the total transmission can be calculated without explicitly determining the scattering states and can be computationally efficient, summation of the contributions from multiple scattering states can obscure real physical effects, for example, the role of the symmetries of individual scattering states seen in Fig. 2.6. Explicit determination of the scattering states not only makes a detailed analysis of the scattering possible. The full scattering matrix, expressed in terms of the scattering states, can be used to bridge [47] the gap between first-principles electronic structure calculations and phenomenological models of transport used to analyse complex situations where a full first-principles treatment is not practical.

We have instead made use of an alternative technique, suitable for Hamiltonians that can be represented in tight-binding form, that was formulated by Ando [44] and is based upon direct matching of the scattering-region wave function to the Bloch modes of the leads. The relationship between the wave function matching [44] and Green function [27, 57] approaches is not immediately obvious. It was suggested recently that WFM was incomplete [85] but the equivalence of the two approaches could be proven [55]. Schemes similar in spirit to our own, but based upon empirical tight-binding Hamiltonians have been presented by Sanvito *et al.* [22] and by Velev [23, 24]. In contrast to these schemes, our TB-MTO formalism is a parameter-free approach that has an advantage of self-consistent determination of potentials (on CPA level for

disordered systems) and spin densities for systems for which these are not known from experiment. Even though all tight-binding schemes should be fundamentally similar in performance, it would seem, judging from the size of systems to which it has been applied, that our implementation is nevertheless substantially more efficient than these empirical schemes. The scattering regions treated in Figs. 2.7, 2.9, 2.10 and 2.11 contained as many as 3200 atoms (20×20 lateral supercell \times 8 principal layers where the potential was allowed to deviate from its bulk values) or, in the case of Fig. 2.13, ~ 15000 atoms (10×10 lateral supercell \times 150 principal layers). Our WFM scheme should not be confused [24] with a recently developed transport formalism [8, 13] also based upon TB-LMTOs but which makes use of the Caroli NEFG expression for the conductance in terms of a trace and a complex energy. Khomyakov and Brocks [78] have developed a scheme analogous to ours but based upon pseudopotentials and a real space grid which make it more suitable for studying quantum wires or the type of open structures studied in molecular electronics, but is computationally much more expensive.

A third approach based upon “embedding” [86, 87] has been combined with full-potential linearized augmented plane wave method to yield what is probably the most accurate scheme to date [14, 15, 37] but like the real space grid WFM method [78], these methods are numerically very demanding.

2.5 Summary

Details of a wave-function matching method suitable for calculating the scattering matrices in magnetic metallic hybrid structures based upon first-principles tight-binding muffin tin orbitals have been given and illustrated with calculations for a variety of Cu|Co(111) interface-related problems. The minimal basis of localized orbitals is very efficient, allowing large lateral supercells to be handled. This allows us to model materials with large lattice mismatch or to study transport in the diffusive regime. Because the scattering states are calculated explicitly, the effect of various types of scattering can be analyzed in detail.

Acknowledgments

This work is part of the research program for the “Stichting voor Fundamenteel Onderzoek der Materie” (FOM) and the use of supercomputer facilities was sponsored by the “Stichting Nationale Computer Faciliteiten” (NCF), both financially supported by the “Nederlandse Organisatie voor Wetenschappelijk Onderzoek” (NWO). It was also supported by the European Commission’s Research Training Network *Computational Magneto-electronics* (contract No. HPRN-CT-2000-00143) as well as by the NEDO International Joint Research program *Nano-scale Magneto-electronics*. MZ wishes also to acknowledge support from KBN grant No. PBZ-KBN-044/P03-2001. We are grateful to: Ilya Turek for his TB-LMTO-SGF layer code which we used to generate self-consistent potentials and for numerous discussions about the method;

Anton Starikov for permission to use his version of the TB-MTO code based upon sparse matrix techniques with which we performed some of the calculations.

Bibliography

- [1] K. M. Schep, P. J. Kelly, and G. E. W. Bauer, *Phys. Rev. Lett.* **74**, 586 (1995).
- [2] P. Zahn, I. Mertig, M. Richter, and H. Eschrig, *Phys. Rev. Lett.* **75**, 2996 (1995).
- [3] P. Weinberger, P. M. Levy, J. Banhart, L. Szunyogh, and B. Újfalussy, *J. Phys.: Condens. Matter.* **8**, 7677 (1996).
- [4] K. M. Schep, J. B. A. N. van Hoof, P. J. Kelly, G. E. W. Bauer, and J. E. Inglesfield, *Phys. Rev. B* **56**, 10805 (1997).
- [5] P. Zahn, J. Binder, I. Mertig, R. Zeller, and P. H. Dederichs, *Phys. Rev. Lett.* **80**, 4309 (1998).
- [6] J. B. A. N. van Hoof, K. M. Schep, A. Brataas, G. E. W. Bauer, and P. J. Kelly, *Phys. Rev. B* **59**, 138 (1999).
- [7] J. M. MacLaren, X.-G. Zhang, W. H. Butler, and X. Wang, *Phys. Rev. B* **59**, 5470 (1999).
- [8] J. Kudrnovský *et al.*, *Phys. Rev. B* **62**, 15084 (2000).
- [9] K. Xia *et al.*, *Phys. Rev. B* **63**, 064407 (2001).
- [10] I. Riedel, P. Zahn, and I. Mertig, *Phys. Rev. B* **63**, 195403 (2001).
- [11] J. Taylor, H. Guo, and J. Wang, *Phys. Rev. B* **63**, 245407 (2001).
- [12] M. Brandbyge, J. L. Mozos, P. Ordejón, J. Taylor, and K. Stokbro, *Phys. Rev. B* **65**, 165401 (2002).
- [13] V. Drchal *et al.*, *Phys. Rev. B* **65**, 214414 (2002).
- [14] D. Wortmann, H. Ishida, and S. Blügel, *Phys. Rev. B* **65**, 165103 (2002).
- [15] D. Wortmann, H. Ishida, and S. Blügel, *Phys. Rev. B* **66**, 075113 (2002).
- [16] P. Weinberger, *Phys. Rep.* **377**, 281 (2003).
- [17] K. S. Thygesen, M. V. Bollinger, and K. W. Jacobsen, *Phys. Rev. B* **67**, 115404 (2003).
- [18] P. Mavropoulos, N. Papanikolaou, and P. Dederichs, *Phys. Rev. B* **69**, 125104 (2004).
- [19] J. Mathon, *Phys. Rev. B* **55**, 960 (1997).
- [20] J. Mathon, A. Umerski, and M. Villeret, *Phys. Rev. B* **55**, 14378 (1997).
- [21] E. Y. Tsybal and D. G. Pettifor, *J. Phys.: Condens. Matter.* **9**, L411 (1997).
- [22] S. Sanvito, C. J. Lambert, J. H. Jefferson, and A. M. Bratkovsky, *Phys. Rev. B* **59**, 11936 (1999).
- [23] J. Velev and Y. C. Chang, *Phys. Rev. B* **67**, 144425 (2003).
- [24] J. Velev and W. H. Butler, *Phys. Rev. B* **69**, 024404 (2004).
- [25] Y. Imry, *Introduction to Mesoscopic Physics*, 2 ed. (Oxford University Press, Oxford, 2002).
- [26] S. Datta, *Electronic Transport in Mesoscopic Systems* (Cambridge University Press, Cambridge, 1995).

- [27] D. S. Fisher and P. A. Lee, *Phys. Rev. B* **23**, 6851 (1981).
- [28] C. W. J. Beenakker, *Rev. Mod. Phys.* **69**, 731 (1997).
- [29] J. Kübler, *Theory of Itinerant Electron Magnetism* (Oxford University Press, Oxford, 2002).
- [30] P. Bruno, *J. Magn. & Magn. Mater.* **121**, 248 (1993).
- [31] M. D. Stiles, *J. Appl. Phys.* **79**, 5805 (1996).
- [32] M. D. Stiles, *Phys. Rev. B* **54**, 14679 (1996).
- [33] M. D. Stiles and D. R. Penn, *Phys. Rev. B* **61**, 3200 (2000).
- [34] M. D. Stiles and D. R. Hamann, *Phys. Rev. B* **38**, 2021 (1988).
- [35] M. D. Stiles and D. R. Hamann, *Phys. Rev. Lett.* **66**, 3179 (1991).
- [36] K. M. Schep, P. J. Kelly, and G. E. W. Bauer, *Phys. Rev. B* **57**, 8907 (1998).
- [37] J. B. A. N. van Hoof, *The Embedding Method*, PhD thesis, University of Nijmegen, Nijmegen, The Netherlands, 1997.
- [38] J. B. A. N. van Hoof, K. M. Schep, P. J. Kelly, and G. E. W. Bauer, *J. Magn. & Magn. Mater.* **177-181**, 188 (1998).
- [39] O. K. Andersen and O. Jepsen, *Phys. Rev. Lett.* **53**, 2571 (1984).
- [40] O. K. Andersen, O. Jepsen, and D. Glötzl, in, in *Highlights of Condensed Matter Theory*, edited by F. Bassani, F. Fumi, and M. P. Tosi, pp. 59–176, North-Holland, Amsterdam, 1985.
- [41] O. K. Andersen, Z. Pawłowska, and O. Jepsen, *Phys. Rev. B* **34**, 5253 (1986).
- [42] O. K. Andersen, O. Jepsen, and M. Šob, in, in *Electronic Band Structure and its Applications*, edited by M. Yussouff Vol. 283, pp. 1–57, Springer Lecture Notes, Berlin, 1987.
- [43] I. Turek, V. Drchal, J. Kudrnovský, M. Šob, and P. Weinberger, *Electronic Structure of Disordered Alloys, Surfaces and Interfaces* (Kluwer, Boston-London-Dordrecht, 1997).
- [44] T. Ando, *Phys. Rev. B* **44**, 8017 (1991).
- [45] K. Xia, P. J. Kelly, G. E. W. Bauer, A. Brataas, and I. Turek, *Phys. Rev. B* **65**, 220401 (2002).
- [46] M. Zwierzycki, Y. Tserkovnyak, P. J. Kelly, A. Brataas, and G. E. W. Bauer, *Phys. Rev. B* **71**, 064420 (2005).
- [47] K. Xia, P. J. Kelly, G. E. W. Bauer, and I. Turek, *Phys. Rev. Lett.* **89**, 166603 (2002).
- [48] M. Zwierzycki, K. Xia, P. J. Kelly, G. E. W. Bauer, and I. Turek, *Phys. Rev. B* **67**, 092401 (2003).
- [49] G. E. W. Bauer *et al.*, *Phys. Rev. Lett.* **92**, 126601 (2004).
- [50] G. E. W. Bauer *et al.*, *Phys. Rev. B* **72**, 155304 (2005).
- [51] We follow the notation used in reference [41].
- [52] O. K. Andersen and T. Saha-Dasgupta, *Phys. Rev. B* **62**, 16219 (2000).
- [53] R. W. Tank and C. Arcangeli, *phys. stat. sol. B* **217**, 89 (2000).
- [54] O. K. Andersen *et al.*, in, in *Electronic Structure and Physical Properties of Solids: The Uses of the LMTO Method*, edited by H. Dreyse, pp. 3–84, Springer Lecture Notes in Physics, New York, 2000.

- [55] P. A. Khomyakov, G. Brocks, V. Karpan, M. Zwierzycki, and P. J. Kelly, *Phys. Rev. B* **72**, 035450 (2005).
- [56] J. Velev and W. H. Butler, *J. Phys.: Condens. Matter.* **16**, R637 (2004).
- [57] C. Caroli, R. Combescot, P. Nozières, and D. Saint-James, *J. Phys. C: Sol. State Phys.* **4**, 916 (1971).
- [58] U. von Barth and L. Hedin, *J. Phys. C: Sol. State Phys.* **5**, 1629 (1972).
- [59] J. P. Perdew and A. Zunger, *Phys. Rev. B* **23**, 5048 (1981).
- [60] S. H. Vosko, L. Wilk, and M. Nusair, *Canadian Journal of Physics* **58**, 1200 (1980).
- [61] We adopt a “standard” configuration consisting of an *fcc* lattice with lattice constant of $a = 3.614\text{\AA}$, an *spd* basis, and von Barth-Hedin’s exchange-correlation potential.
- [62] P. Soven, *Phys. Rev.* **156**, 809 (1967).
- [63] P. Bruno, H. Itoh, J. Inoue, and S. Nonoyama, *J. Magn. & Magn. Mater.* **198-199**, 46 (1999).
- [64] L. L. Henry *et al.*, *Phys. Rev. B* **54**, 12336 (1996).
- [65] H. A. M. de Gronckel *et al.*, *Phys. Rev. B* **44**, 9100 (1991).
- [66] C. Mény, P. Panissod, and R. Loloee, *Phys. Rev. B* **45**, 12269 (1991).
- [67] C. Kapusta, P. Fischer, and G. Schütz, *J. Alloys Compd.* **286**, 37 (1999).
- [68] S. F. Zhang and P. M. Levy, *J. Appl. Phys.* **69**, 4786 (1991).
- [69] S. F. Lee *et al.*, *J. Magn. & Magn. Mater.* **118**, L1 (1993).
- [70] T. Valet and A. Fert, *Phys. Rev. B* **48**, 7099 (1993).
- [71] W. P. Pratt, Jr. *et al.*, *Phys. Rev. Lett.* **66**, 3060 (1991).
- [72] M. A. M. Gijs, S. K. J. Lenczowski, and J. B. Giesbers, *Phys. Rev. Lett.* **70**, 3343 (1993).
- [73] J. Bass and W. P. Pratt Jr., *J. Magn. & Magn. Mater.* **200**, 274 (1999).
- [74] M. A. M. Gijs and G. E. W. Bauer, *Adv. Phys.* **46**, 285 (1997).
- [75] E. Y. Tsybal, *Phys. Rev. B* **62**, 3608 (2000).
- [76] A. Shpiro and P. M. Levy, *Phys. Rev. B* **63**, 014419 (2000).
- [77] S. Gerritsen, An ab-initio calculation of the current-in-plane giant magnetoresistance of cu/co multilayers, Master’s thesis, University of Twente, Enschede, The Netherlands, 2002.
- [78] P. A. Khomyakov and G. Brocks, *Phys. Rev. B* **70**, 195402 (2004).
- [79] J. A. Støvneng and P. Lipavský, *Phys. Rev. B* **49**, 16494 (1994).
- [80] J. Cerdá, M. A. Van Hove, P. Sautet, and M. Salmeron, *Phys. Rev. B* **56**, 15885 (1997).
- [81] J. Mathon, *Phys. Rev. B* **56**, 11810 (1997).
- [82] W. H. Butler, X.-G. Zhang, T. C. Schulthess, and J. M. MacLaren, *Phys. Rev. B* **63**, 054416 (2001).
- [83] J. Mathon and A. Umerski, *Phys. Rev. B* **63**, 220403 (2001).
- [84] J. Mathon and A. Umerski, *Phys. Rev. B* **71**, 220402 (2005).

-
- [85] P. S. Krstić, X.-G. Zhang, and W. H. Butler, *Phys. Rev. B* **66**, 205319 (2002).
- [86] J. E. Inglesfield, *J. Phys. C: Sol. State Phys.* **14**, 3795 (1981).
- [87] S. Crampin, J. B. A. N. van Hoof, M. Nekovee, and J. E. Inglesfield, *J. Phys.: Condens. Matter.* **4**, 1475 (1992).

Chapter 3

nterface conductance and resistance of metallic multilayers

First-principles calculations of transmissions and interface resistances through metallic interfaces show a strong spin dependence (in case of Cr|Fe, Cu|Co, Cu|Ni, Co|Ni systems) and orientation dependence (for Cr|Fe). Since the interface scattering states are explicitly calculated, we have identified the channels and mechanisms (specular versus diffuse scattering) contributing to transport in the case of clean and disordered interfaces.

3.1 Introduction

The discovery of the giant magnetoresistance (GMR) [1, 2] effect and its successful application in the information storage technology shortly afterwards gave rise to the new field of research, the spin dependent transport. As exemplified by the case of GMR, the research in this field is usually motivated by two factors, that is interest in basic physical phenomena and the prospect of their application in the new breed of nanoscale devices [3–5].

The GMR (see Ref. [6–8] for review) occurs in magnetic tri- and multi-layers consisting alternately of magnetic and non-magnetic layers, *e.g.* Fe|Cr [1, 2, 9] and Co|Cu [10, 11]. In such systems a very large (200% and more) change in resistance is observed when the relative orientation of the magnetizations of the ferromagnetic layers is changed between antiparallel (AP) and parallel (P) configurations.

Early measurements of GMR were carried out with the current flowing parallel to the plane of the multilayers, that is in the so called current-in-plane (CIP) geometry. This configuration is easier experimentally and used in most current applications. However, it does not allow for an easy discrimination between the contribution from the spin-dependent scattering at the interfaces and in the bulk of the layers. This problem is solved in the current-perpendicular-to-the-plane (CPP) [10, 11] configuration making it, in spite of the experimental difficulties, more appealing for the fundamental study especially as it also yields higher GMR ratios. Results of numerous CPP

experiments interpreted in terms of the two current series resistor model (2CSR) [12–15] suggests strongly that, at least in this geometry and for sufficiently thin layers, the GMR is largely determined by the properties of the interfaces. Therefore, understanding the scattering at the interfaces goes long way towards understanding the GMR itself.

The spin-dependent scattering in magnetic multilayers was initially interpreted mainly in terms of defect (impurities, interface roughness etc.) scattering [16]. It has been however subsequently demonstrated by Schep *et al.* [17] that the discontinuity of electronic structures at the interfaces can, alone, give rise to substantial effect even in the absence of defect scattering. The magnetoelectronic devices commonly contain layers made of ferromagnetic transition metals, such as Co, Fe, or Ni, whose complicated electronic structure makes a simple free-electron description inappropriate. Therefore the theory aiming at understanding the microscopic origin of GMR should take the band structure effects into account preferably on *ab initio* level so as to incorporate the modifications of the local potentials at the interfaces (charge transfer etc.). In addition, as the manufacturing techniques are perfected and the characteristic lengths (layer thickness) of the devices decrease, the quantum effects can become noticeable. This calls for the full-quantum mechanical treatment.

Various approaches were proposed to study spin-dependent transport. The first theoretical works were based on the free-electron model and on the semiclassical Boltzmann equation [12–14, 16], or single-orbital tight-binding model [18]. These approaches ignore the realistic band structure of materials and make use of many phenomenological parameters. First-principles methods based on density functional theory (DFT) are the natural framework for material-specific transport properties calculations. Some studies take into account the complicated band structure of materials but the transport theory is simplified in several ways to make the calculations tractable [19]. Other *ab initio* approaches include Caroli formula based techniques, such as the tight-binding model with parameters fitted to first principles calculations [20–27], Green's function approach in combination with the Boltzmann equation [28, 29], or Kubo-Greenwood theory [30–32], one electron Green's functions with Caroli formula [33] and the transfer matrix concept [34] or, alternatively, transmission matrices [35, 36] combined with the Landauer-Büttiker approach [37].

The Caroli and Landauer-Büttiker formalisms were shown to be fully equivalent [38]. The latter approach however has an advantage of being more physically transparent as it expresses the system's conductance in terms of microscopic transmission coefficients. These can be also used in calculations for other transport-related phenomena such as current-induced magnetization reversal [39], Gilbert-damping enhancement via spin-pumping [40], spin injection from metallic ferromagnet into semiconductor [41–43] and Andreev reflection [44]. The interface resistances calculated using this approach without adjustable parameters has shown good agreement with experiment for most systems [11, 45–48]. Moreover, the same conceptual framework can be applied in case of *e.g.* nanowires or molecular junctions [49, 50]. Transmission and reflections matrices were also successfully used to discuss the oscillatory exchange coupling in magnetic multilayers [51–54].

The primary source of electrons scattering is the mismatch of the band structures

[17, 35] of respective materials. It can be however substantially modified by the presence of the disorder at the interface [36, 47], a factor frequently overlooked in *ab initio* transport calculations. Zahn *et al.* [29] have studied the influence of point defect scattering at the interfaces and how the position of the impurity influences the general trend of GMR in Co|Cu and Fe|Cr systems. The effect of interfacial disorder on transport properties in Co|Cu and Fe|Cr systems has also been investigated by using tight-binding model fitted to *ab initio* band structure methods and the disorder is introduced as a random variation of the on-site atomic energies of the atomic species [21, 22].

The purpose of the present work is to present the results of a systematic material-specific study of the electronic structure and the spin-dependent transport in nearly lattice matched materials (namely Cr|Fe, Cu|Co, Cu|Ni and Co|Ni) along [001], [011] and [111] directions. Our method takes into account, on *ab initio* level, the complexity of the 3d transition metals band structures and the effect of disorder, in the sense of substitutional alloying at the interface, on equal footing. The transport calculations are carried out within an efficient scheme based on a tight-binding muffin-tin-orbital (TB-MTO) implementation of the Landauer-Büttiker formalism and DFT [36]. Particular attention will be devoted to Cr|Fe system as it exhibits two interesting features: *i*) substantial anisotropy of transport properties for specular interfaces and *ii*) an *increase* of interface transmission in the presence of the disorder. The latter effect was previously reported by Xia *et al.* [47] (and rediscovered more recently in Ref. [25]) but at the time it was possible to offer only qualitative explanation.

The paper is organized as follows. In section Sec. 3.2 are given the computational details of the *ab initio* method used to obtain the electronic structure and transport properties. In Secs. 3.3 and 3.4 we present and discuss the results of the transport calculations in Cr|Fe, Cu|Co, Cu|Ni and Co|Ni systems along [001], [011] and [111] orientations. The energy dependence of the interface conductance and resistance are reported in Sec. 3.5. A short discussion of our results is given in Sec. 3.6.

3.2 Method

By means of first-principles calculations we studied the spin transport in a number of structures containing one or more interfaces between metallic layers. The transport problem is formulated, fully quantum mechanically, as a scattering problem [37]. Calculations of the transmission were carried out using the local spin-density approximation (LSDA) of the density functional theory (DFT) in a two-step procedure. First, the electronic structure and magnetic properties were obtained using the surface Green's function technique (SGF) [55] implemented within the framework of tight-binding linear muffin-tin orbitals (TB-LMTO) method in the atomic sphere approximation (ASA) [56]. The coherent potential approximation (CPA) method [55] was employed to model substitutional disorder at the interfaces. In the present study we consider nearly lattice matched materials forming an interface A|B (namely Cr|Fe, Cu|Co, Cu|Ni and Co|Ni) along (001), (011) and (111) orientations. The atomic sphere potentials of several monolayers (ML) on either side of the in-

interface were iterated to self-consistency while the potentials of more distant layers were fixed at their bulk values forming semi-infinite perfect leads. The disordered interfaces are modeled with one or more MLs of A_xB_{1-x} alloy. In the second step, the self-consistent potentials are used to calculate the transmission coefficients using a tight-binding (TB) muffin-tin orbital (MTO) implementation [36]. These are then used to determine the Landauer-Büttiker conductance:

$$G^\sigma(\hat{n}) = \frac{e^2}{h} \sum_{\mu,\nu,\mathbf{k}_\parallel} T_{\mu\nu}^\sigma(\mathbf{k}_\parallel) = \frac{e^2}{h} \sum_{\mu,\nu,\mathbf{k}_\parallel} |t_{\mu\nu}^\sigma(\mathbf{k}_\parallel)|^2 \quad (3.1)$$

with σ labeling spin and $t_{\mu\nu}^\sigma$ being the transmission coefficients between incoming states ν in material A and outgoing states μ in material B. In the transport calculations, substitutional disorder is modeled using large lateral supercells [36] where each site is randomly occupied by one of the atomic species with the appropriate concentration. Because a minimal basis set *spd* is used, we are able to treat large lateral supercells containing as many as 800 atoms. The integration in the two-dimensional Brillouin zone (2DBZ) is carried out with a \mathbf{k}_\parallel -mesh density corresponding to 10^5 points in the 2DBZ of a 1×1 interface unit cell.

Using Schep's *et al.* [45] formula

$$SR_{A/B}^\sigma = S \frac{h}{e^2} \left[\frac{1}{\sum |t_{\mu\nu}^\sigma|^2} - \frac{1}{2} \left(\frac{1}{N_A^\sigma} + \frac{1}{N_B^\sigma} \right) \right] \quad (3.2)$$

we can then calculate the interface resistance of an interface embedded in a diffusive system. S is the area of the interface and $N_{A(B)}$ are so called Sharvin conductances (to be discussed later) equal to the number of propagating modes at the Fermi energy for material $A(B)$.

In the following sections we will present and discuss the results of electronic structure and transport calculations through various metallic interfaces, namely Cr|Fe, Cu|Co, Cu|Ni and Co|Ni (001), (011) and (111) low index interfaces.

3.3 Cr|Fe

The first system that we consider is Cr|Fe along [001], [011] and [111] directions. In the first step we calculate the properties of bulk materials, *i.e.* the propagating states at Fermi energy and the magnetic profiles. Next we study scattering at clean and disorder interfaces. While discussing the results we identify and analyze various scattering mechanisms and compare specular versus diffuse scattering. This section will primarily focus on (001) interface. Results are also obtained for (011) and (111) orientations and the orientation dependence of the transmission is discussed.

3.3.1 Bulk materials

Both Fe and Cr have a *bcc* crystal structure and their lattice constants differ by less than one percent. In the following we assume common lattice constant for

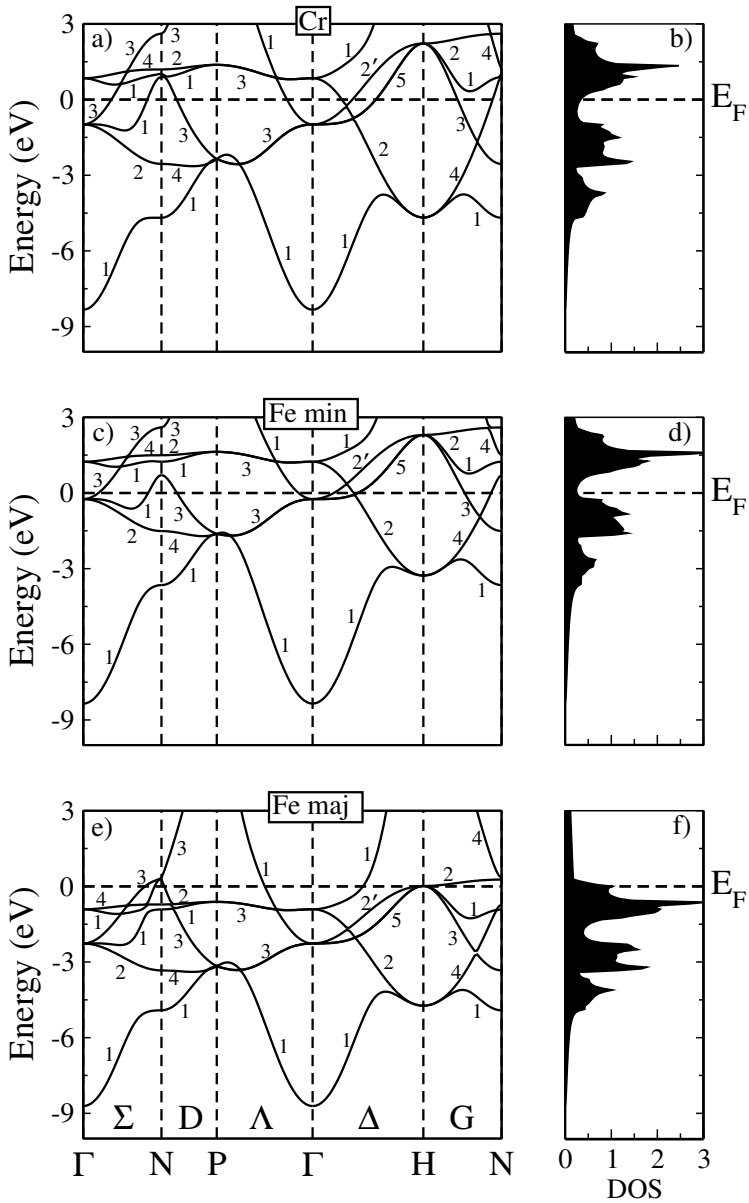


Figure 3.1: Electronic band structure (left panels) and density of states (right panels) of bcc Cr (a,b), Fe minority-spin (c,d) and majority-spin (e,f) electrons, respectively. The Fermi level (dashed horizontal line) lies within the d-bands for all the three band structures.

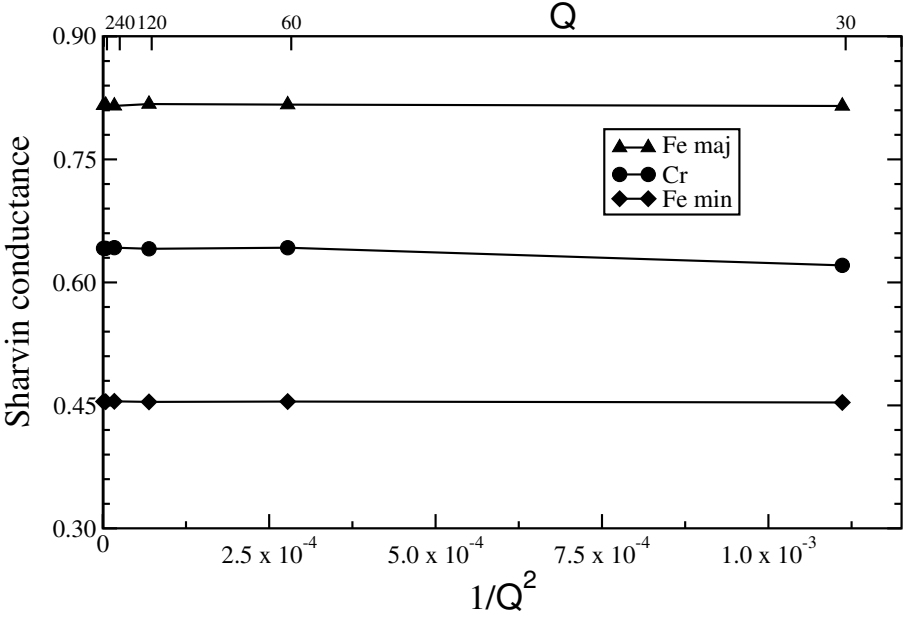


Figure 3.2: Sharvin conductance $G^\sigma(100)$ (in units of $10^{15} \Omega^{-1} \text{m}^{-2}$) for bulk bcc Cr and Fe (majority and minority spin) plotted as a function of the normalized area element used in the Brillouin zone summation, $\Delta^2 \mathbf{k}_\parallel / A_{BZ} = 1/Q^2$. Q , the number of intervals along the reciprocal lattice vector is indicated at the top of the figure, is taken as series of ($Q = 30, 60, 120, 240, 480$). A bcc lattice constant of $a = 2.871 \text{ \AA}$ and spd basis were used together with the exchange and correlation potential expressed as proposed by Ceperley and Alder [57] and parametrized by Perdew and Zunger [58].

both materials, $a = 2.871 \text{ \AA}$, equal to the experimental lattice constant of Fe. The exchange and correlation potential expressed as proposed by Ceperley and Alder [57] and parametrized by Perdew and Zunger [58] were used in calculations.

The bulk band structures and densities of states (DOS) of Cr and Fe are shown in Fig. 3.1. One immediately notices that the Cr and Fe minority bands are similarly shaped and positioned with respect to the Fermi energy (E_F). In both cases the Fermi level lies within the range of d -bands. In comparison the Fe majority bands are shifted down and their d -bands are almost completely filled. This difference between spin channels has direct consequences on transport properties discussed in the following sections.

The perfect leads can be characterized, in context of transport, by the so called Sharvin conductance which has a physical meaning of the Landauer-Büttiker

	$a(\text{\AA})$	basis	n_σ	(001)	(011)	(111)
Cr	2.87	<i>spd</i>	3.0	0.642	0.586	0.610
	2.87	<i>spdf</i>	3.0	0.686	0.632	0.662
Fe	2.87	<i>spd</i>	2.892	0.455	0.399	0.412
	min.	<i>spdf</i>	2.920	0.485	0.431	0.448
Fe	2.87	<i>spd</i>	5.108	0.815	0.781	0.817
	maj.	<i>spdf</i>	5.079	0.906	0.866	0.906

Table 3.1: The Sharvin conductances per spin (in units of $10^{15} \Omega^{-1} \text{m}^{-2}$) in the (001), (011) and (111) directions for bcc Cr and Fe using Fe bulk experimental lattice parameter. The data reported in this table was obtained with Perdew-Zunger parameterization for the exchange-correlation potential. The number of electrons with spin σ is given in the fourth column.

conductance for a ballistic system where $|t_{\mu\nu}|^2 = \delta_{\mu\nu}$:

$$G_{Sh}^\sigma(\hat{n}) = \frac{e^2}{h} \sum_{\mu k_{\parallel}} |t_{\mu\mu}^\sigma(\mathbf{k}_{\parallel})|^2 = \frac{e^2}{h} N^\sigma(\hat{n}). \quad (3.3)$$

where $N^\sigma(\hat{n})$ is the number of states propagating in the transport direction \hat{n} . Alternatively the Sharvin conductance can be interpreted as the surface area of the projection of the material's Fermi surface along the direction \hat{n} . In Fig. 3.2 $G_{Sh}^\sigma(\hat{n})$ is plotted as a function of $\Delta^2 k_{\parallel}/A_{BZ}$, the normalized area element per \mathbf{k}_{\parallel} -point (we use regular grid) for bulk bcc Cr and both spins of bcc Fe for (001) orientations. When the 2DBZ reciprocal lattice vectors are each divided into Q intervals, then $\Delta^2 k_{\parallel}/A_{BZ} = 1/Q^2$. The Sharvin conductance shown in this figure is converged to about 0.08% if $3600 = 60 \times 60$ points are used in the complete 2D-BZ and to about 0.04% for $230400 = 480 \times 480$ sampling points.

Table 3.1 summarizes the results of Sharvin conductance calculations at E_F for (001), (110) and (111) orientations. In each case we have performed calculations for two bases - *spd* and *spdf* - in order to estimate the uncertainties resulting from finite l cutoff in the angular momentum expansion of the wave function.

For both Cr and Fe minority electrons we observe a similar change in the conductances, there is between 6.9% to 8.5% increase on going from an *spd*- to *spdf*-basis. The difference is even larger in case of Fe majority electrons where we observe an increment of 11%. At the same time the magnetic moment of Fe atoms decrease by about 2.5% when we go from *spd* to *spdf* basis (see Table 3.2).

Schep *et al.*[35] have used a different (but equivalent) approach to calculate the Sharvin conductances for the same systems using conventional first-principles LMTO-ASA bulk electronic band structures. They used a slightly small lattice constant

$a = 2.861 \text{ \AA}$ for bulk *bcc* Cr and Fe. Their results with an *spd*-basis agree with ours up to within the error bar defined by the spread between our *spd* and *spdf* results.

3.3.2 Interfaces without defects

In this section we will study the effect of the band structure and the complicated topologies of the Fermi surfaces on transport through Cr|Fe interfaces paying particular attention to the symmetry and orbital character of states involved in scattering through the interface. Using the TB-LMTO SGF method and the ASA technique, we start by calculating self-consistent potentials and spin-densities of an interface embedded between two semi-infinite Cr and Fe leads. The potentials of Cr and Fe leads are determined in a separate bulk calculations. The charge and spin-densities are allowed to vary in n monolayers of Cr and Fe in the intermediate region between the leads. Since the interlayer distance d vary between different orientations, different values of n (larger n -s for smaller d -s) need to be taken in order to achieve satisfactory convergence. In particular we have $d/a = \sqrt{3}/6, 0.5$ and $\sqrt{2}/2$ for (111), (001) and (110) orientations respectively. Correspondingly we have assumed $n = 12, 10$ and 8 for these interfaces.

Table 3.2 gives the self-consistently determined magnetic profiles together with interface conductances and resistances calculated using Eqs. (3.1) and (3.2) for perfect and disordered (values in brackets) interfaces. Examining the magnetic profiles for three orientations we see that the magnetic moments of Fe atoms at the interface are generally reduced in comparison to their bulk values. The decrease is weakest for (110) orientation and roughly the same for (001) and (111) cases. This difference can be understood when we compare the changes to the local environment (*i.e.* the coordination zone) of Fe atoms introduced by the interface. In the case of an Fe atom in the monolayer right at the (110) interface, 2 of its 8 nearest neighbors (n.n.) and 2 of its 6 second nearest neighbors (s.n.n) are replaced by Cr atoms. The corresponding numbers for (001) and (111) orientations are 4 n.n + 1 s.n.n and 4 n.n + 3 s.n.n respectively. Accordingly we expect strongest and comparable modifications for the latter two orientations and somewhat weaker one for (110) as indeed happens. In addition we observe induced magnetic moments in Cr, with the moments in the first layer oriented in the direction opposite to the Fe moments, and decaying in quasi-periodic fashion with the increasing distance from the interface. The quasi-oscillations have period of roughly 2 MLs for (001) and (111) orientations and 3 MLs for (110). When comparing *spd* and *spdf* results we see that similarly to bulk the moments at the interface decrease by 8.5%, 5.6% and 14.9% for (001), (011) and (111) orientations, respectively. Opposite trend, *i.e.* the increase by 1.4%, 6.6% and 16.2%, is observed for the magnitudes of the Cr moments. The charge transfer from Fe to Cr at the (001) (0.095(0.101) electron/atom) and (111) (0.112(0.116) electron/atom) interfaces is about twice as big as that of (011) (0.053(0.058) electron/atom) for and *spd*-(*spdf*-)basis set.

Basis	(001)		(011)		(111)	
	<i>spd</i>	<i>spdf</i>	<i>spd</i>	<i>spdf</i>	<i>spd</i>	<i>spdf</i>
$m_{\text{Cr}}(\text{bulk})$	0.0	0.0				
$m_{\text{Cr}}(\text{int-12})$					0.031	0.026
$m_{\text{Cr}}(\text{int-11})$					-0.038	-0.030
$m_{\text{Cr}}(\text{int-10})$	0.041	0.034			0.041	0.031
$m_{\text{Cr}}(\text{int-9})$	-0.062	-0.052			-0.054	-0.038
$m_{\text{Cr}}(\text{int-8})$	0.083	0.068	-0.001	-0.000	0.046	0.033
$m_{\text{Cr}}(\text{int-7})$	-0.100	-0.079	0.002	0.002	-0.051	-0.031
$m_{\text{Cr}}(\text{int-6})$	0.116	0.094	-0.002	-0.002	0.075	0.052
$m_{\text{Cr}}(\text{int-5})$	-0.135	-0.109	0.003	0.004	-0.054	-0.030
$m_{\text{Cr}}(\text{int-4})$	0.153	0.127	-0.002	-0.002	0.073	0.058
$m_{\text{Cr}}(\text{int-3})$	-0.157	-0.124	-0.002	0.002	-0.143	-0.119
$m_{\text{Cr}}(\text{int-2})$	0.173	0.150	0.013	0.022	0.102	0.067
$m_{\text{Cr}}(\text{int-1})$	-0.285	-0.289	-0.128	-0.137	-0.218	-0.260
$m_{\text{Fe}}(\text{int+1})$	1.925	1.774	2.087	1.977	1.958	1.704
$m_{\text{Fe}}(\text{int+2})$	2.379	2.333	2.301	2.234	2.242	2.146
$m_{\text{Fe}}(\text{int+3})$	2.283	2.210	2.269	2.210	2.185	2.076
$m_{\text{Fe}}(\text{int+4})$	2.268	2.204	2.225	2.163	2.326	2.260
$m_{\text{Fe}}(\text{int+5})$	2.207	2.146	2.209	2.147	2.241	2.179
$m_{\text{Fe}}(\text{int+6})$	2.229	2.163	2.209	2.152	2.310	2.255
$m_{\text{Fe}}(\text{int+7})$	2.210	2.154	2.214	2.159	2.225	2.174
$m_{\text{Fe}}(\text{int+8})$	2.216	2.153	2.217	2.162	2.253	2.191
$m_{\text{Fe}}(\text{int+9})$	2.206	2.156			2.216	2.161
$m_{\text{Fe}}(\text{int+10})$	2.214	2.156			2.220	2.155
$m_{\text{Fe}}(\text{int+11})$					2.211	2.158
$m_{\text{Fe}}(\text{int+12})$					2.208	2.142
$m_{\text{Fe}}(\text{bulk})$	2.215	2.159				
G^{min}	0.352(0.355)	0.401	0.319(0.315)	0.364	0.337(0.335)	0.384
G^{maj}	0.112(0.255)	0.158	0.220(0.272)	0.271	0.273(0.306)	0.332
SR^{min}	0.961(0.930)	0.732	1.030(1.059)	0.793	0.931(0.948)	0.738
SR^{maj}	7.546(2.527)	5.032	3.053(2.180)	2.327	2.225(1.839)	1.704

Table 3.2: Variation of the layer-resolved magnetic moments (in Bohr magnetons) for Cr/Fe(001), (011) and (111) interfaces with basis set *spd* and *spdf*. The data reported in this table was obtained with Perdew-Zunger parameterization for the exchange-correlation potential. In the four last rows, the upper two rows are the interface conductances (G) given in units of $10^{15} \Omega^{-1} \text{m}^{-2}$ and the last two rows are the interface resistances (SR) [45, 47] in units of $10^{-15} \Omega \text{m}^2$ for ideal (and, in brackets, for disordered) interfaces. S is the area of the sample for which R is measured.

Figure 3.3 shows the conductances calculated using Eq. (3.1) for (001) interface and *spd*-basis set as the function of the area of normalized 2DBZ element, that is the number of \mathbf{k}_{\parallel} -points in the 2DBZ. The convergence of the results is similar to that of the Sharvin conductance shown in Fig. 3.2. The converged values of conductance and

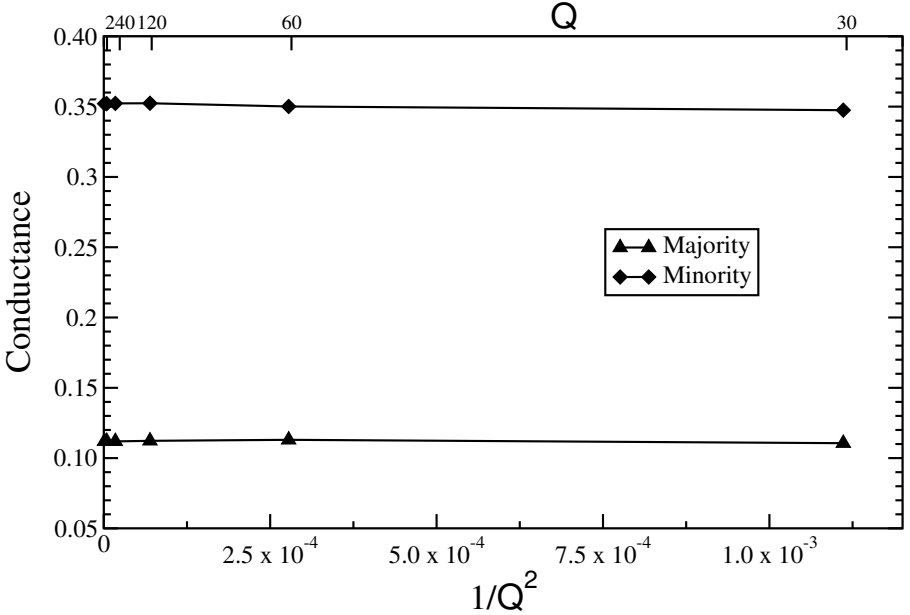


Figure 3.3: Interface conductance $G^\sigma(001)$ (in units of $10^{15} \Omega^{-1} \text{m}^{-2}$) for a bcc Cr|Fe(001) interface for majority and minority spin plotted as a function of the normalized area element used in the Brillouin zone summation, $\Delta^2 \mathbf{k}_\parallel / A_{BZ} = 1/Q^2$. Q , the number of intervals along the reciprocal lattice vector is indicated at the top of the figure, is taken as series of ($Q = 30, 60, 120, 240, 480$).

interface resistance are given in four bottom rows of Table 3.2 and will be discussed in detail in following section.

3.3.2.i) Cr|Fe(001) interface: Minority spins

In this and following sections we are going to present and analyze the transmission through the three low index interfaces starting with Cr|Fe(001) and minority channel. Before we proceed let us make a remark on the relation between 3D and 2D Brillouin zones (BZ). As the (perfect) interfaces possess only two-dimensional, in-plane translational symmetry it is of course natural to use \mathbf{k}_\parallel wave vectors within 2D BZ to label transmission coefficients, spectral functions etc. Note however that whereas the in-plane translations are the subset of the full 3D set of translations of Bravais lattice, the same inclusive relation does not in general hold for the vectors of 2D and 3D reciprocal lattice. This can be seen in Fig. 3.4 where in the top-right panel we show the Cr Fermi surface (FS) with its standard bulk BZ projected along [001] direction. The dashed rectangle indicates the area of 2D BZ. Once the “external” pieces of the projected bulk (3D) BZ are folded into the 2D BZ we arrive at the

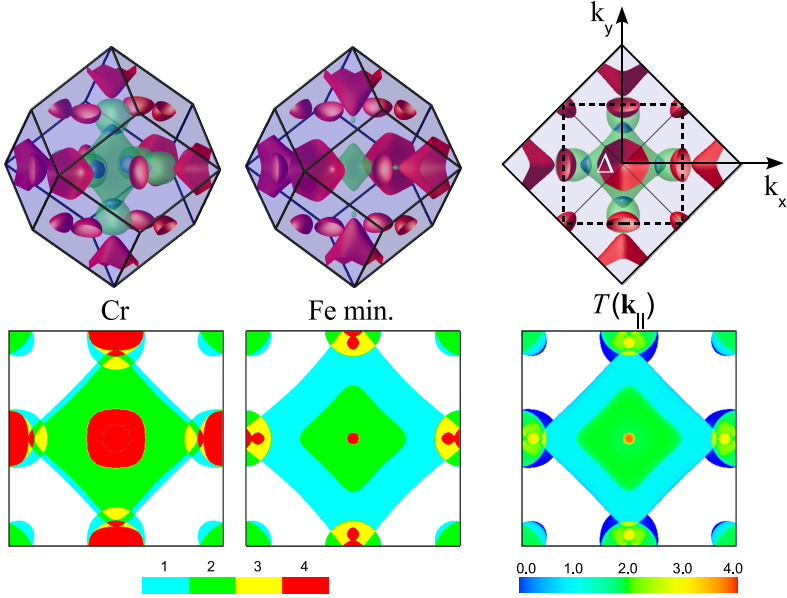


Figure 3.4: Top row, left-hand panel: Fermi surface (FS) of bcc Cr; middle panel: minority-spin FS of bcc Fe; right-hand panel: Cr FS viewed along the [001] direction with a projection of the bulk bcc Brillouin zone (BZ) (solid lines) onto a plane perpendicular to this direction. The dashed square represents the 2D BZ. Bottom row, left-hand and middle panels: projections onto a plane perpendicular to the [001] direction of the Cr and minority-spin Fe Fermi surfaces with the number of the right-going states shown using the color scale; right-hand panel: \mathbf{k}_{\parallel} -resolved transmission probability for majority-spin states, $T(\mathbf{k}_{\parallel})$ for a bcc Cr|Fe(001) interface.

bottom-left panel which shows the number of states in Cr using color scale. Similar procedure for Fe yields the bottom-middle panel. The relation between 3D and 2D BZ for other orientations will be shown in subsequent sections.

Because of conservation of transverse momentum (\mathbf{k}_{\perp} , momentum parallel to the interface), the transmission through a specular interface is non-zero only between states with the same values of \mathbf{k}_{\perp} . If, for a given value of \mathbf{k}_{\perp} , there is a propagating state in Cr incident on the interface but none in Fe, then an electron in such state is completely reflected at the interface. Conversely, the \mathbf{k}_{\perp} point for which there is a propagating state in Fe but none in Cr also cannot contribute to the conductance. The first factor determining the transparency of the perfect interface is therefore simply the amount of the overlap between the projected FSs of both materials. The bottom-right panel of Fig. 3.4 shows the transmission probability from Cr into Fe. The areas where the Cr states are perfectly reflected are marked as deep blue and the white space means the absence of states in Cr.

When there are n propagating states in the left and m in the right lead, the upper theoretical limit of the transmission is given simply by the smaller of the two numbers, $\min(m, n)$. The similarity in the *bcc* bulk Cr and Fe minority band structures (see Fig. 3.1) is also reflected in their Fermi surfaces (FS) as can be seen in Fig. 3.4. We expect therefore that in the region of the overlap the transmission should approach the theoretical limit. The plots in the bottom row of Fig. 3.4 demonstrate that it is indeed so. Taking for example the center of 2D BZ ($\bar{\Gamma}$ point) we see that there are four states at either side of the interface. What is more the states in Fe and Cr are very similar belonging to Δ_2 ($d_{x^2-y^2}$ orbitals), Δ_2' (d_{xy}) and doubly degenerated Δ_5 (p_x , p_y , d_{xz} and d_{yz}) irreducible representations (note that we assume differently oriented coordination system for each interface with z axis normal to the interface plane). The transmission between the states of the same symmetry is high and together they yield $T(\mathbf{k}_{\parallel} = \bar{\Gamma}) = 3.8$. In the area surrounding the center of 2D BZ the transmission approaches two and further away one which is seen to be equal to the number of states available in Fe. Close to the edges of the 2D BZ we see the areas where there are again up to four states at either side. Also here the total transmission is high and approaches 3. The average transmission from Cr into Fe is equal to 0.55(0.58) for *spd*(*f*) basis [0.77(0.83) from Fe into Cr] and is seen to be limited mainly by the overlap between the projections of the equivalent sheets of the Fermi surfaces – compare *e.g.* the sizes of the central “rotated squares” in the bottom-left and middle panels of Fig. 3.4.

Performing the sum in Eq. (3.1) we obtain an interface conductance of $0.352(0.401) \times 10^{15} \Omega^{-1} \text{m}^{-2}$ for an *spd*(*f*)-basis set which is essentially the Sharvin conductance of Fe minority states reduced because of the overlap factor. Taking the expression [45, 47] given in Eq. (3.2) we calculated the interface resistance from the Sharvin and interface conductances discussed above. Shown in the last two rows of Tab. 3.2 the computed value is $0.961 f\Omega \text{m}^2$ in case of *spd*-basis set. If we include *f*-electrons, this value is reduced to $0.732 f\Omega \text{m}^2$.

3.3.2.ii) Cr|Fe(001) interface: Majority spins

Compared with relatively simple minority channel the majority case is much more complicated as the electronic structures of Cr and Fe no longer resemble each other. This was already apparent in Fig. 3.1 (top vs. bottom panel) and is further illustrated in Fig. 3.5. The Fe majority *d*-bands are mostly filled whereas they were only partially filled in case of the minority-spin. This gives rise to a large difference in the band structure at the Fermi energy for both materials. There are four bands in Fe (Fig. 3.1e) crossing the Fermi energy along $\Gamma - H$ direction hence there are four Fermi surface sheets, shown in Fig. 3.5 (top row) together with their projections onto a plane perpendicular to the [001] transport direction. Note that the 3rd and 4th bands of Fe are degenerate at $\bar{\Gamma}$ and occupy small area in reciprocal space so we represent them in the same figure. The projected FSs are shown in (Fig. 3.5c,d,e) and respective transmissions in (Fig. 3.5f,g,h,i,j,k).

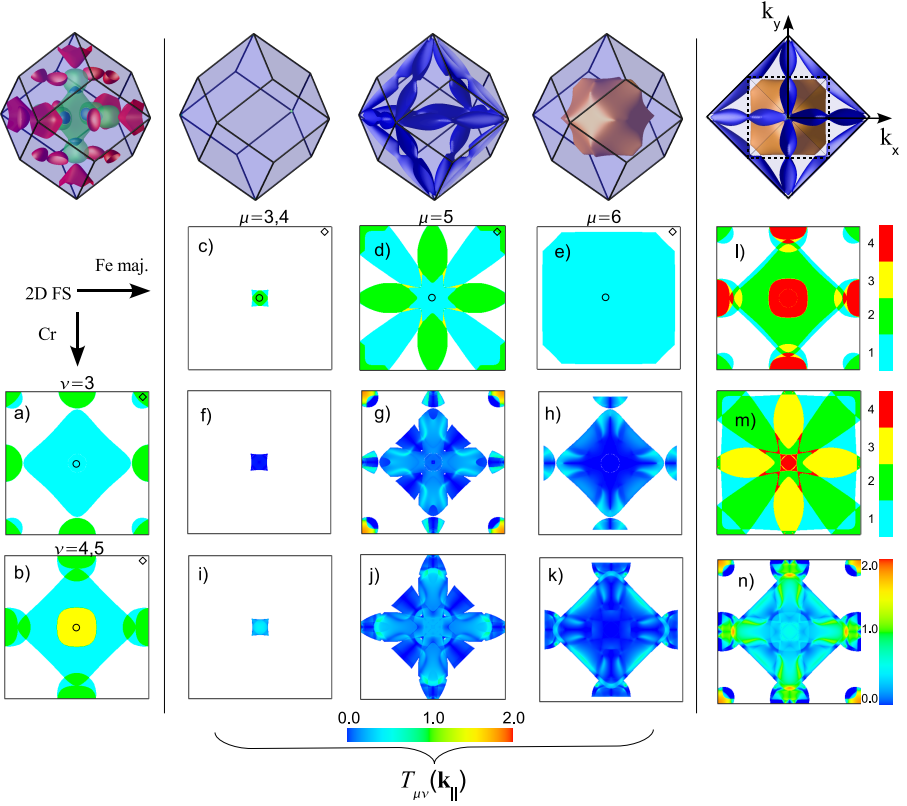


Figure 3.5: Top row, left-hand panel: Fermi surface (FS) of bcc Cr; middle panel: third-fourth, fifth and sixth FS sheets of majority-spin of bcc Fe; right-hand panel: Fe FS viewed along the [001] direction with a projection of the bulk bcc Brillouin zone (BZ) (solid lines) onto a plane perpendicular to this direction. The dashed square represents the 2D BZ. Second row: corresponding projections of individual FS sheets (c,d,e) and total FS of Fe (m). (l) is the 2D projection of the total FS of Cr. The number of propagating states with positive velocity is color-coded following the color bar on the right. Third and fourth row: projection of the third (a) and fourth and fifth (b) FS sheets of bcc Cr. (f, g, and h) and (i, j and k) \mathbf{k}_{\parallel} -resolved transmission probability $T_{\mu\nu}(\mathbf{k}_{\parallel})$ between various sheets of Cr's and Fe's FS. Bottom row: right-hand panel: \mathbf{k}_{\parallel} -resolved total transmission probability for majority-spin states, $T(\mathbf{k}_{\parallel})$ for a bcc Cr|Fe(001) interface. The color coding for the FS sheets (a,b,c,d,e) is the same as that of (l,m).

Not surprisingly the average transmission is much lower in this case – 0.17(0.23) from Cr into Fe for *spd(f)*-basis and 0.14(0.17) from Fe into Cr, that is respectively 2 and 5 times less than in minority channel. Accordingly the transmission probabilities between various sheets of FS shown in panels f-k) are mostly very small. The interface

conductance is equal to $0.112 \times 10^{15} \Omega^{-1} \text{m}^{-2}$ for an *spd*-basis set, only about 14% of the Sharvin conductance for Fe majority spin electrons. Including the *f*-electrons in our calculations will increase this ratio to 17% and the interface conductance to $0.158 \times 10^{15} \Omega^{-1} \text{m}^{-2}$ (see Table 3.2). Note that while the interface conductance (Table 3.2) is reduced when going from minority to majority case, the opposite is true for Fe Sharvin conductances (Table 3.1). The low transparency of interface in majority channel can not therefore be explained simply by the availability of states in Fe.

In order to understand why the transmission is so low, it is useful to start again with the states at the central $\bar{\Gamma}$ point, indicated by circle (\circ) in Fig. 3.5a-e). As before we have 4 states at each side of the interface. We have previously identified the symmetries of states in Cr as Δ_2 , Δ_2' and two Δ_5 . In Fe we have Δ_2' , twice Δ_5 and highly symmetric Δ_1 (*s*, *p_z* and $d_{3z^2-r^2}$) state. Out of these Cr's Δ_2 and Fe's Δ_1 states have no matching counterparts on the other side of the interface and do not contribute to conductance. The remaining states are pairwise symmetry-compatible and have finite transmission probabilities. Their total contribution amount however to only about 0.6 (with 3 being the upper theoretical limit). This poor matching can be explained by the velocity mismatch mechanism. Guided by the results of the free electron model, where $T = 4v_L v_R / (v_L + v_R)^2$ with $v_{L(R)}$ being the group velocity components normal to the interface, we expect transmission to be strongly reduced whenever the velocities of states at either side of the interface approach zero. This is in fact what happens. Looking at the $\Gamma - H$ direction in Fig. 3.1e we see that the Δ_2' and Δ_5 states in Fe intersect the Fermi energy right at the band edge and consequently have vanishingly small velocity along this direction.

Similar situation occurs *e.g.* when we move vertically away from the center towards the edge of the 2D BZ that is we consider states with \mathbf{k} vectors parallel to the (100) plane (*yz* in the system of coordinates defined in Fig. 3.4). The states in Fe and Cr can be then classified as being even or odd under the reflection with respect to this plane. Choosing for example the \mathbf{k}_{\parallel} point halfway between center and the edge of the 2D BZ we have two odd states in the 3rd and 4th band of Cr (consisting of *p_x*, *d_{xy}* and *d_{xz}* orbitals) versus two odd states in the 5th band and one even state in the 6th band of Fe. The odd states in Fe consist of the same orbitals as their Cr counterpart and the even one has *s*, *p_y*, *p_z*, *d_{yz}*, $d_{3z^2-r^2}$ and $d_{x^2-y^2}$ character. Because of strict odd-even orthogonality the 6th Fe band does not contribute to transport. The transmission probabilities between the remaining pairs of odd states are non-zero but small. For our point of choice they amount to only 0.45 of total transmission out of theoretically possible 2. The transmission is, again, reduced because of the velocity mismatch. The same holds of course for equivalent symmetry lines.

The only regions with sizeable transmission are the small pockets in the corners of the 2D BZ. At both sides of the interface we have there two states of D_3 and D_4 symmetry which are (pairwise) symmetry-compatible. What is more the states in Fe intersect the Fermi level at much steeper level than *e.g.* states at $\bar{\Gamma}$. This can be seen for D_3 states in the Fig.3.1e for $N - P$ direction. The D_4 states appear in the corner of 2D BZ because of downfolding and are therefore not visible in the standard band structure plot. The two scattering channels are nearly saturated with $T = 1.85$. The

surface area of regions in question is however too small to have a meaningful impact on the total, integrated conductance.

An interesting evolution occurs in the orbital character of the states as we move along the diagonal of the 2D BZ away from the center. Focussing *e.g.* on the direction towards the top-right corner we encounter states with the \mathbf{k} vectors parallel to $(\bar{1}10)$ which can be classified again as even or odd under the reflection with respect to the this plane. Once we moved sufficiently far from the $\bar{\Gamma}$ point there are two even states in Cr and one odd (5th FS) and one even (6th FS) state in Fe. The transmission between even states [Fig. 3.5h) and k)] is small and it can not be explained by velocity mismatch anymore – the states in the 6th FS of Fe cross the Fermi level at steep angles and possess Fermi velocities quite comparable to their Cr counterparts. The numerical results can be explained when we analyze not only the formal symmetry but also the details of orbital composition. The states in 6th band of Fe are derived from the highly symmetric Δ_1 states in the center and consequently are initially dominated by s , p_z and $d_{3z^2-r^2}$ orbitals. The even states in Cr on the other hand originate from much less symmetric Δ_5 (one of the two) and $\Delta_{2'}$ states are mostly composed of $p_{x(y)}$, d_{xy} , d_{xz} and d_{yz} orbitals. Comparing the two sets of orbitals one notices that while being even with respect to the $(\bar{1}10)$ plane, the states in Cr exhibit much more modulation in the plane of interface $[(001)]$ than the Fe states. This is of course why these states are strictly orthogonal in the center of 2D BZ. Once we move further away from the center the orbital composition of states in question changes so that they become more similar. The states in Fe become less symmetric and the Cr ones develop the “outreaching” s , p_z and $d_{3z^2-r^2}$ orbitals. The resulting increase in transmission can be seen, under close inspection, in the h), k) and n) panels of Fig. 3.5 (look at the edges of the “rotated square” in the center). The increase is too small to change the overall poor transmission for (001) orientation but will become more important for (110) and (111) interfaces.

In conclusion the low conductance (transmission) of Cr|Fe(001) interface stems from two factors: *i)* velocity mismatch between symmetry-compatible states in Cr and in 3rd,4th and 5th FS of Fe, *ii)* near orthogonality of states in the 6th FS of Fe to the strongly d -hybridized states in Cr.

The poor transmission results in the interface resistance about seven times larger than that corresponding value for minority channel. It is $7.546 f\Omega\text{m}^2$ in the case of an *spd*-basis set. This value is decreased to $5.032 f\Omega\text{m}^2$ for an *spdf*-basis calculation.

3.3.2.iii) Cr|Fe(011) and (111) interfaces

In this section we are going to discuss the properties of the Cr|Fe interface for the (110) and (111) orientation.

Starting with (110) case we have Figs. 3.6 and 3.7 showing the Fermi surfaces viewed along [110] direction (top row), their downfolded projections and transmission probabilities in the suitable 2D BZ for both spin channels. The minority case presents

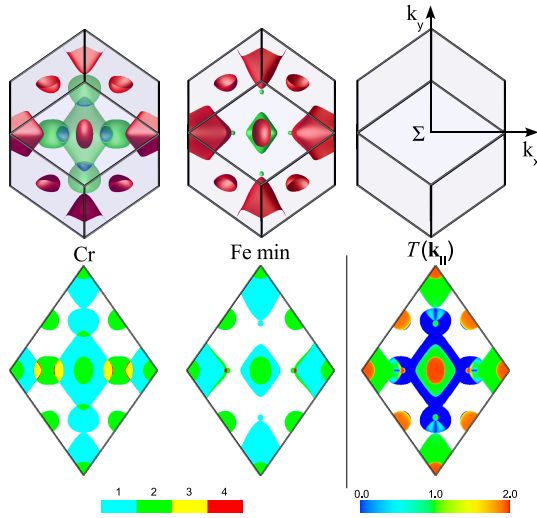


Figure 3.6: Top row, left- and right-hand: Fermi surface (FS) of bcc Cr and minority-spin Fe viewed along [011] direction. Bottom row, left-hand and middle-panels: projections onto (011) plane of Cr and minority-spin Fe Fermi surfaces. Right-hand panel: k_{\parallel} -resolved transmission probability for Cr|Fe (011) interface for minority-spin case.

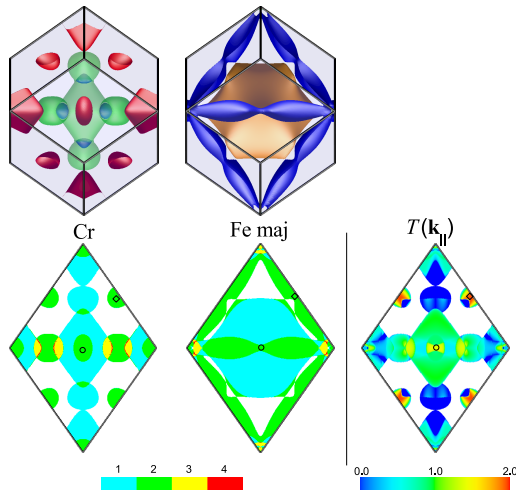


Figure 3.7: Top row, left- and right-hand: Fermi surface (FS) of bcc Cr and majority-spin Fe viewed along [011] direction. Bottom row, left-hand and middle-panels: projections onto (011) plane of Cr and majority-spin Fe Fermi surfaces. Right-hand panel: k_{\parallel} -resolved transmission probability for Cr|Fe (011) interface for majority-spin case.

no surprises. The interface conductance and resistance, given in Table 3.2 remain in the same range as the values for (001) interface. The slight decrease of the conductance reflects the variation in the Sharvin conductances of both materials. Comparing the projected Fermi surfaces and transmission probabilities, shown in the bottom row of Fig. 3.6 we see that the available channels in Fe tend to be well saturated. Therefore, similarly as in (001) case the conductance is determined mostly by the topologies of respective Fermi surfaces, *i.e.* the amount of their overlap in projection along [110]. The average transmission from Cr into Fe is equal to 0.54(0.58) for $spd(f)$ basis and 0.80(0.75) in the opposite direction, that is quite similar as in (001) case.

The majority case is more interesting. Looking at the numbers in Table 3.2 we see that the interface conductance is now twice as large as it was in the case of (001) interface. This variation bears no resemblance whatsoever to the behavior of either Sharvin conductance. The corresponding interface resistance is roughly halved. Let us, as we did for (001) case, start by analyzing the symmetries of the states in the center of the 2D BZ indicated on Fig. 3.7 by the circle (\circ). This point corresponds to the $\Gamma - N$ direction in Fig. 3.1 and the two states present at either side of the interface belong to the Σ_1 (3rd “red” FS in Cr; 5th “blue” FS in Fe; s , p_z , $d_{3z^2-r^2}$ and $d_{x^2-y^2}$ orbitals) and Σ_3 (4th “green” FS in Cr; 6th “brown” FS in Fe; p_y , d_{yz}) irreducible representations. The transmission between Σ_1 state is nearly perfect, but the velocity mismatch reduces the transmission for the other pair to lower, but still meaningful 0.5. Once we move away from the center (especially along y axis) the velocities in the 6th Fe bands increase to the level comparable with their Cr counterparts and the transmission becomes nearly perfect. Comparing the projected FSs and transmission probabilities we see that the states in the 6th FS of Fe are transmitted into very efficiently almost everywhere in the region of overlap between this FS and the central “green” fragment (4th band) of Cr’s FS. This activation of previously idle 6th FS of Fe is largely responsible for the observed increase of the conductance. The other regions of high transmission - the “hot” pockets in the middle of the 2D BZ’s faces - correspond to the same fragments of the FS seen previously in the corners of 2D BZ for (001) case. The averaged transmission probabilities for majority (110) interface are 0.38(0.43) from Cr to Fe [$spd(f)$ basis] and 0.28(0.32) from Fe into Cr, about two times larger than for (001).

The interface conductances and resistances for (111) orientation given in Table 3.2 are close to those for (110) interface with minority values close also to the (001) ones. The majority conductance is again about twice as large that of the (001) interface. The Fermi surfaces viewed along [111] and corresponding transmission probabilities are given in Figs. 3.8 and 3.9. The 2B BZ, shown in the top-right panel of Fig. 3.8 is three times smaller than that of the projection of the 3D BZ. The resulting massive downfolding (with up to 6 states stacked at one \mathbf{k}_{\parallel} point) makes the interpretation of the plots from the bottom row more difficult in this case. Nonetheless we see that the once again transmission for the well-matched minority states follows the number of available states in Fe (the number of states in Cr being generally larger in this case) with resulting saturation of most available channels. The average transmissions are: 0.55(0.58) from Cr into Fe and 0.82(0.86) from Fe into Cr.

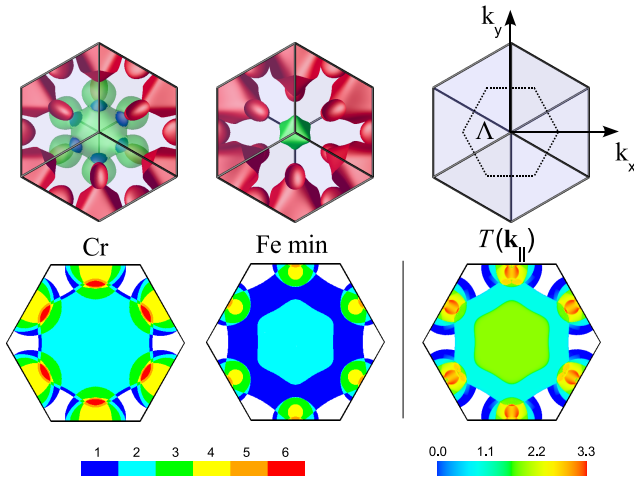


Figure 3.8: Top row, left-hand and middle-panel: Fermi surface (FS) of bcc Cr and minority-spin Fe viewed along [111] direction. Right-hand: bulk BZ projected along [111] (solid lines) and 2D Brillouin zone for (111) orientation (dotted lines). Bottom row, left-hand and middle-panels: projections onto (111) plane of Cr and minority-spin Fe Fermi surfaces. Right-hand panel: \mathbf{k}_{\parallel} -resolved transmission probability for Cr|Fe (111) interface for minority-spin case.

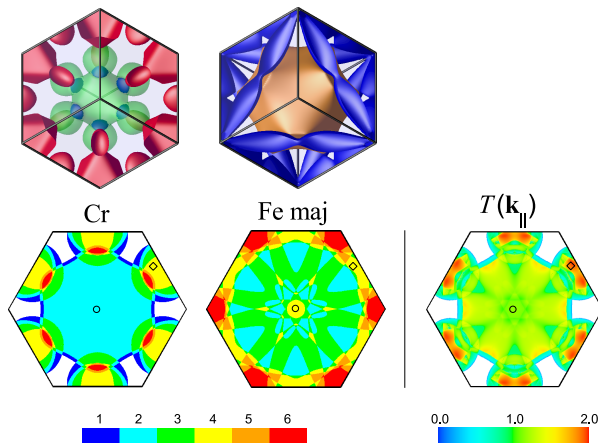


Figure 3.9: Top row, left-hand and middle-panel: Fermi surface (FS) of bcc Cr and majority-spin Fe viewed along [111] direction. Bottom row, left-hand and middle-panels: projections onto (111) plane of Cr and majority-spin Fe Fermi surfaces. Right-hand panel: \mathbf{k}_{\parallel} -resolved transmission probability for Cr|Fe (111) interface for majority-spin case.

The transmission probability for majority spins (Fig. 3.9) while not spectacularly high remains respectable (above 1) throughout most of the 2D BZ. In the center (marked as \circ) most of the total $T = 1.27$ transmission goes into the Λ_1 state belonging to the 6th band of FS. At the very edge of the 2D BZ (\diamond) we have in Cr one even and three odd (with respect to the $(\bar{1}10)$ plane, now coinciding with the yz plane) states. In Fe on the other hand we have three even and one odd states. As the even and odd states are orthogonal we have maximum possible transmission of 2 coming from one odd and one even “channels”. The actual transmission is seen to be close to this limit. The main effect responsible for the increase of conductance (compared to (001) interface) in majority channel is again the fact that states in the 6th band of Fe are now available for scattering into and contribute to the conductance. The average transmission probabilities are: 0.45(0.50) from Cr into Fe and 0.33(0.37) the other way around.

3.3.2.iv) The origin of anisotropy of interface conductance

In the preceding sections we have discussed and compared the transport properties of the three low index interfaces – (001), (110) and (111). We have seen that the interface conductance for the well matched minority spin channel exhibits only limited amount the orientation dependence. What is more the ordering of the calculated values, $G_{(011)}^\downarrow < G_{(111)}^\downarrow < G_{(001)}^\downarrow$, follows the ordering of the smaller of the two Sharvin conductances *i.e.* the one for minority Fe. In general the transparency of the Cr|Fe interfaces in minority channel is determined straightforwardly by the topology of the Fermi surfaces, that is their overlap in the projection along a given direction.

For the poorly matched majority channel the interface conductances not only do not follow the ordering of the Sharvin conductances but exhibit changes which are orders of magnitude larger than the changes of the latter quantity. In particular comparing the numbers in Table 3.2 we see factor two and more difference between the results for (001) and for (110) and (111) interfaces. As we have discussed in the earlier sections this increase can be attributed in the large part to the activation of the large, central 6th Fermi surface of Fe. For the latter two interfaces it can contribute substantially to the total transmission as seen most clearly in Fig. 3.7. The states from which the transmission originates belong to the 4th and (depending on the orientation) 3rd bands of Cr. We have already pointed out one reason for which such change can occur while discussing, in Sec. 3.3.2.ii), the changing character of states along the diagonal of (001) 2D BZ. We have seen that when going away from the Δ ($\Gamma - H$) direction the gradual lowering of the symmetry of the Δ_1 -derived states in Fe and the simultaneous evolution of the Cr states resulted in increasing the transmission. The effect is however moderate whereas *e.g.* for (110) orientation we see that the transmission is close to one from the very onset of the overlap between Cr’s 4th and Fe’s 6th bands. We conclude therefore that simply changing the orientation of the interface along which the states are to be matched is enough to substantially alter the transmission between the same groups of states. This conclusion is of course hardly surprising for transition metals with states of non-trivial symmetry. Nonetheless, it is perhaps useful to present the cartoon picture of how such change can appear

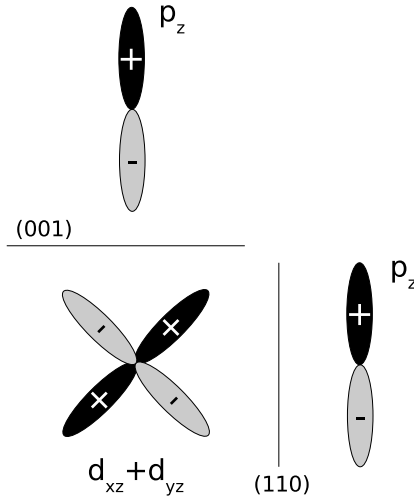


Figure 3.10: Schematic illustration of the origin of the scattering anisotropy for (001) and (110) interfaces. The plane of the drawing is assumed to be $(\bar{1}10)$

concentrating on (001) and (110) as the extreme cases.

As we have seen the states in the 6th FS of Fe are derived from the Δ_1 state and consequently are going to be dominated by the s , p_z and $d_{3z^2-r^2}$ orbitals at least for \mathbf{k}_{\parallel} points close to the center of the (001) 2D BZ. The Δ_5 and Δ_2' derived states in Cr on the other hand are going to have substantial $p_{x(y)}$, d_{xy} , d_{xz} and d_{yz} contributions. For the sake of present discussion we are assuming the system of coordinates defined in Fig. 3.4 with x, y and z axes along $[100]$, $[010]$ and $[001]$ directions respectively. Concentrating, as we did in Sec. 3.3.2.ii), on the states with \mathbf{k} vectors parallel to the $(\bar{1}10)$ plane we get the Cr and Fe states even with respect to that plane, which in the case of Cr means equal contribution from orbitals oriented along the x and y axes - $p_{x(y)}$ and $d_{x(y)z}$. Let us assume further that that we consider states which do not deviate too much from the $\Gamma - H$ ($[001]$) direction. In Figure 3.10 we compare the matching of the d_{xz} and d_{yz} in Cr with the p_z orbital in Fe through the two interfaces. In the case of (001) orientation the basic symmetry dictates orthogonality. The same holds also for s and $d_{3z^2-r^2}$ orbitals with their full axial symmetry along $[001]$ direction. However, when p_z orbital faces the Cr states across (110) interface, we see that it possesses the same basic modulation along $[001]$ direction as the even combination of d_{xz} and d_{yz} orbitals. The same argument could be also given for other orbitals. Therefore, changing the orientation of the interface from (001) to (110) removes the orthogonality of states in question. Our simplistic cartoon neglects the geometry of the bcc lattice, however even if it is taken into account the result remains the same.

This basic effect coupled with the changes in the orbital composition, discussed in Sec. 3.3.2.ii), account for the “activation” of the 6th FS of majority Fe states and the increase of the conductance.

3.3.3 Disordered interfaces

All experimental systems are bound to exhibit certain amount of disorder. It is therefore necessary to extend our study to the case of non-specular interfaces. Various kinds of disorder are in principle possible at the interfaces between two metals with very limited amount of information about the detailed structure of the interface is available from experiment to guide theorist. However, there is an experimental evidence indicating that there is a significant intermixing of Cr and Fe atoms at the interface [59, 60]. For our lattice matched Cr|Fe system we choose to study substitutional disorder by placing one or more monolayers of random $\text{Cr}_x\text{Fe}_{1-x}$ alloy at the interface where x is allowed to vary between layers. The alloy is modelled using large (typically 16×16) lateral supercells repeated periodically in plane. Having established, in the previous sections, the amount of variation between *spd* and *spdf* results we restrict ourselves now to the smaller *spd* basis set. The uncertainty of the results, when averaged over 20 configurations of disorder, is about 0.05% for the minority spin channel and 3.80% for majority spin case which is comparable to the errors associated with LDA and ASA approximation.

In the bottom rows of Table 3.2 we list the results of the calculations with the two monolayers of 50%-50% ($x = 0.5$) alloy introduced at the interface. For the three low index orientations considered, the interface disorder has practically no effect on the well-matched minority spin channel. The change in the interface conductances and resistances is insignificant. For example, for (001) orientation the values for sharp and disorder interfaces are 0.352 versus $0.355 \times 10^{15} \Omega^{-1}\text{m}^{-2}$ and 0.961 versus $0.930 f \Omega\text{m}^2$, respectively, for the interface conductances and resistances with an *spd*-basis set. The situation is fairly similar for (110) and (111) interfaces. This is not surprising – the minority electrons crossing the interface experience only very modest potential step. Consequently mixing of the atoms, and associated atomic spheres potentials, at the interface is going to have only very minor effect on the motion of the carriers. In poorly matched majority channel on the other hand we see more substantial effects. In all three cases the disorder *increases* the interface conductance. The effect is modest for (110) and (111) orientation but surprisingly large for (001) case where we see factor two difference in conductance between clean and disordered case. The associated change of interface resistance is even larger and reaches factor of three. This effect was previously reported by Xia *et.al* in Ref. [47] but at the time the authors were able to offer only qualitative discussion of its origin. We see also that the disorder substantially reduce the differences between different orientations.

In order to better understand the effect of disorder on transmissions and interface resistances, we have separated the ballistic or specular (\mathbf{k}_{\parallel} -conserving) from the diffuse (\mathbf{k}_{\parallel} -nonconserving) transmission through the disordered interfaces according

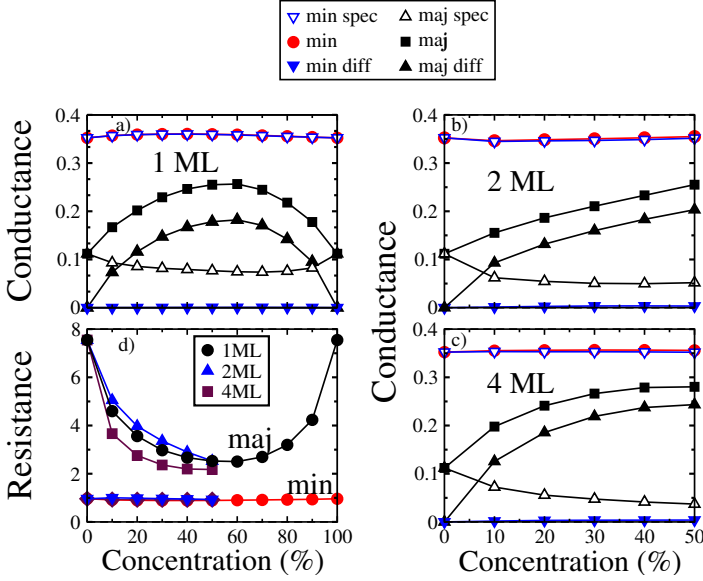


Figure 3.11: Interface conductance (a,b,c) (in units of $10^{15} \Omega^{-1} \text{m}^{-2}$) and resistance (d) (in units of $\text{f} \Omega \text{m}^2$) of disordered Cr|Fe (001) interface with disorder modeled in a 16×16 lateral supercell as a function of the concentration x (in percent) of Cr in Fe. Results are shown for three different models, described in the text, with disorder in 1, 2 or 4 MLs. Only a single disorder configuration was used. The total conductance (\blacksquare for majority and \bullet for minority electrons) is resolved into specular (\triangle for majority and ∇ for minority electrons) and diffuse (\blacktriangle for majority and \blacktriangledown for minority electrons) components.

to [25, 61, 62].

$$G = G_s + G_d = \frac{e^2}{h} \sum_{\mu\nu} T_{\mu\nu}(\mathbf{k}_{\parallel}, \mathbf{k}_{\parallel}) + \frac{e^2}{h} \sum_{\substack{\mu\nu \\ \mathbf{k}_{\parallel} \neq \mathbf{k}'_{\parallel}}} T_{\mu\nu}(\mathbf{k}_{\parallel}, \mathbf{k}'_{\parallel}) \quad (3.4)$$

where \mathbf{k}_{\parallel} and \mathbf{k}'_{\parallel} belong to the two dimensional Brillouin zone for (1×1) translational periodicity and $T_{\mu\nu}(\mathbf{k}_{\parallel}, \mathbf{k}'_{\parallel}) = t_{\mu\nu}(\mathbf{k}_{\parallel}, \mathbf{k}'_{\parallel}) t_{\mu\nu}^{\dagger}(\mathbf{k}_{\parallel}, \mathbf{k}'_{\parallel})$. In the absence of interface disorder, there is by definition only specular component.

We are going to consider three different models of interface disorder. These are: *i*) 1 ML of $\text{Cr}_{1-x}\text{Fe}_x$, *ii*) disorder modelled by 2 MLs: $\text{Cr}_{1-x}\text{Fe}_x | \text{Cr}_x\text{Fe}_{1-x}$ and *iii*) disorder spread across 4 MLs: $\text{Cr}_{1-\frac{x}{3}}\text{Fe}_{\frac{x}{3}} | \text{Cr}_{1-\frac{2x}{3}}\text{Fe}_{\frac{2x}{3}} | \text{Cr}_{\frac{2x}{3}}\text{Fe}_{1-\frac{2x}{3}} | \text{Cr}_{\frac{x}{3}}\text{Fe}_{1-\frac{x}{3}}$ (see Fig. 2.8). The results reported in Table 3.2 correspond to the 2 ML model with $x = 0.5$.

The results of calculations for the most interesting (001) case are shown in Fig. 3.11. For the minority channel we see that the transmission remains almost perfectly specular for all three models of the disorder and for all values of x . In the case corresponding to the results of Table 3.2 (2 ML, $x = 0.5$) the specular component of the interface conductance is $0.352 \cdot 10^{15} \Omega^{-1} \text{m}^{-2}$ while the diffuse component is only about $0.003 \cdot 10^{15} \Omega^{-1} \text{m}^{-2}$.

In the majority channel we observe the reduction of the specular component. It remains, however in the same range of values as for the sharp interface even for $x = 0.5$. The increase in the total conductance/transmission comes from the diffusive part, which overcomes the specular one already for concentration in the range of 10%. This is true even for relatively weakly disordered 1 ML case. Once the concentration reaches 50% the total conductances are roughly comparable, with the 4 ML case being the largest. This is seen as well for the interface resistances [panel d)] where the three models converge around the same value in the middle of the plot. Not surprisingly the ratio of diffusive to specular components is also largest for the 4 ML model. Interestingly in this case we see the signs of saturation of the total conductance and resistance which suggests that only limited number of channels can be opened by the disorder before the effect is cancelled by the increased backscattering.

We conclude that the observed increase of the conductance through Cr|Fe interface is mediated by the large diffusive component of the transmission in the presence of interface disorder. This is consistent with the fact that the low conductance of the specular (001) interface was related in large part to the incompatible symmetries of the states in Cr and majority states in Fe. Diffusive scattering allows electrons to circumvent this obstacle. For (110) and (111) interfaces where the transparency was higher to start with, the effect of disorder is more modest.

3.4 Interfaces with fcc materials: Cu|Co, Cu|Ni and Co|Ni

This section focuses on the transport properties of interfaces between lattice-matched materials with *fcc* crystalline structure, namely Cu|Co, Cu|Ni and Co|Ni. The results of calculations will be presented for (001), (011) and (111) interfaces. Note that an extended study of the Cu|Co (111) interface is reported in a Chapter 2.

3.4.1 Technical aspects

The calculation of the electronic structure for each system is carried out using the common lattice constant equal to that of the substrate. We have neglected any tetragonal distortions that may arise from small differences between the two lattice parameters. For Cu|Co and Cu|Ni, where Co has an *fcc* lattice, we used the experimental lattice constant (3.614 \AA) of bulk *fcc* Cu for both materials. For Co|Ni we take $a = 3.549 \text{ \AA}$ which corresponds to the experimental volume of bulk *hcp* Co. The

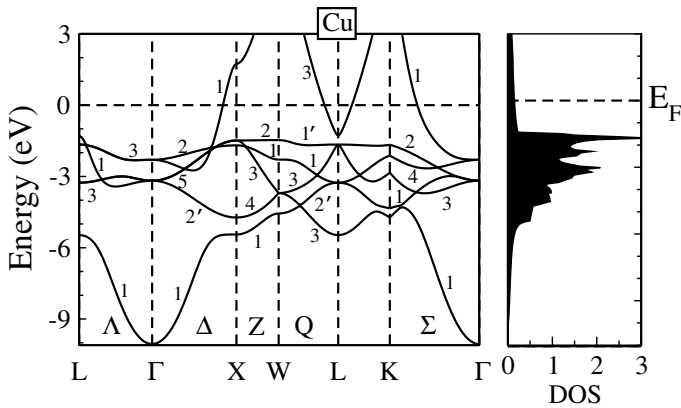


Figure 3.12: Electronic band structure (left panel) and density of states (right panel) of fcc Cu. The band structure is characterized by a fully occupied d band. The Fermi level (dashed horizontal line) lies within the sp -band.

self-consistent potentials and spin-densities were obtained using an spd basis and the von Barth and Hedin functional for the exchange-correlation potential.[63] We model disorder at interface using two monolayers containing a 50%-50% substitutional alloy where the potentials were determined using CPA. The potentials of Cu, Co and Ni leads are determined in a separate bulk self-consistent calculations. Lateral supercell of 10×10 was used in the transport calculations for the disordered systems. A detailed study of various parameters that may influence the convergence of the results were presented and discussed for the Cu|Co (111) system earlier in Chapter 2.

Below we briefly discuss the main features of the bulk electronic structure crucial for determining the propagating states in the leads. The bulk band structure and the density of states of the Cu, Co and Ni *fcc* leads are shown in Figs. 3.12 and 3.13. The band structure of non-magnetic Cu is characterized by a fully occupied d band and the presence of a dispersive sp -band, similar to a free-electron band, crossing the Fermi level. In contrast to what was seen for *bcc* Cr and Fe in Fig. 3.1, this time the majority-spin bands of magnetic elements, Co and Ni, are similar to the bands of non-magnetic metal (Cu) with sp band being at the Fermi energy. Consequently for these systems the majority electrons form a low resistance channel. These bands are also distinguishable by a very low density of states at the Fermi energy (Figs. 3.12 right panel and Figs. 3.13b,f). The latter, though, lies within the d -bands of minority-spin electrons. For these electrons there is a strong $sp-d$ hybridization which mixes the sp and d states. The bands in the minority spin case are characterized by a high density of states as shown in figures 3.13d,h and are expected to match poorly with the states in Cu.

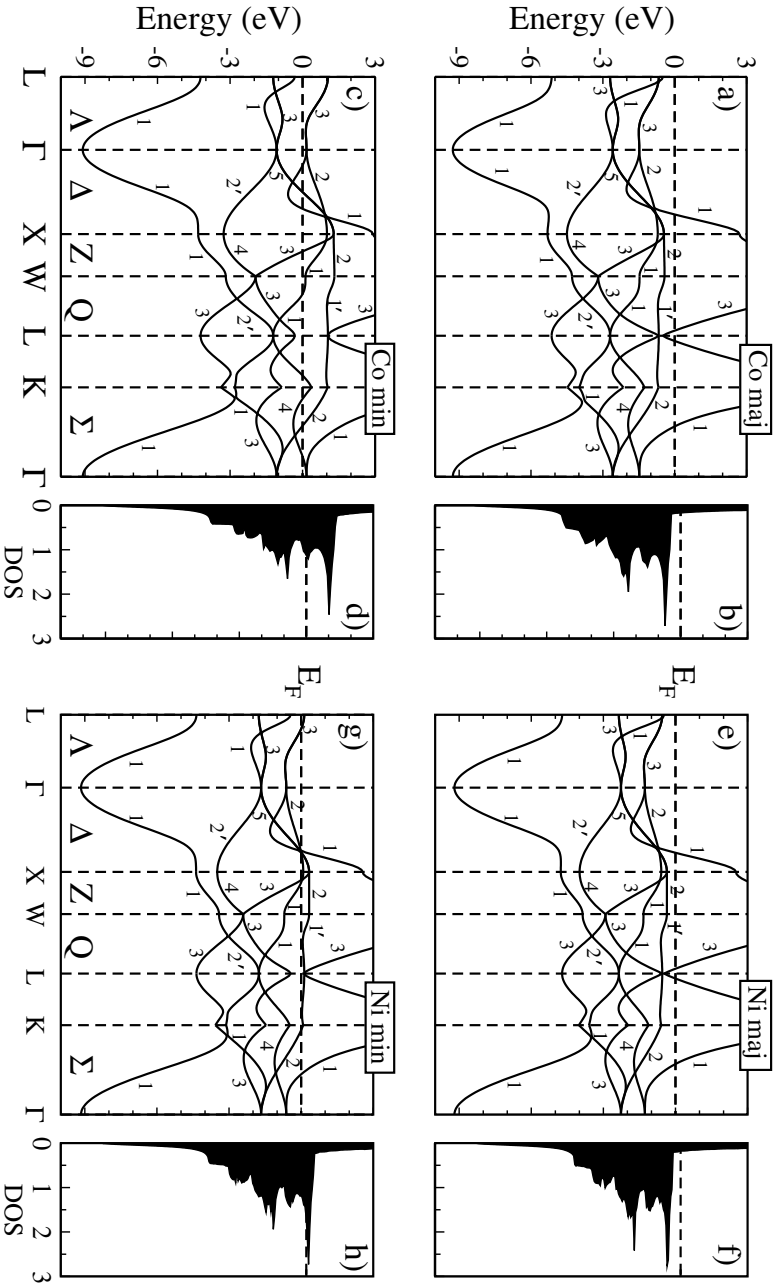


Figure 3.13: Electronic band structure and density of states of fcc Co (a,b,c,d) and Ni (e,f,g,h) for both majority- (top row) and minority-spin (bottom row) electrons, respectively. The Fermi level (dashed horizontal line) lies within the d-bands of minority-spin electrons. For these electrons there is a strong sp-d hybridization which mixes the sp and d states. Note that the majority-spin bands of Co and Ni are very similar and only a highly conducting sp band crosses the Fermi energy.

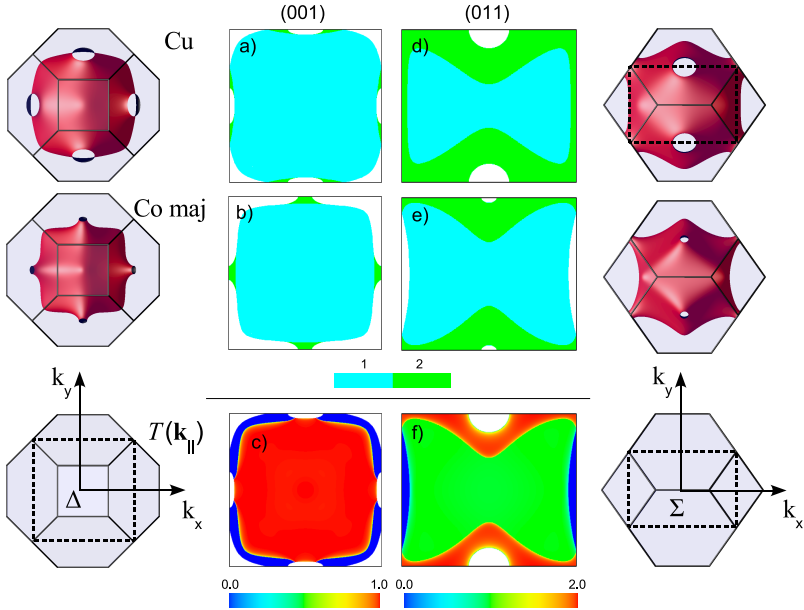


Figure 3.14: Top and bottom rows : FSs of fcc Cu and majority spin Co viewed along the [001] and [011] directions with a projection of the bulk bcc Brillouin zone (BZ) (solid lines) onto a plane perpendicular to these directions; 2D BZ (dashed lines) for both orientations is shown against the projection of the bulk BZ. Middle Panels: FS projections onto a plane perpendicular to the [001] (a,b) and [011] (d,e) directions of the Cu and Co majority-spin folded into the 2D BZ. The number of propagating states is shown using the color scale; \mathbf{k}_{\parallel} -resolved transmission probability for majority-spin states, $T(\mathbf{k}_{\parallel})$ for an fcc Cu|Co (001) and (011) oriented interfaces, respectively.

3.4.2 Magnetotransport results

In this section we present the results of the calculations of the transmission probabilities, interface conductances and resistances for (001), (011) and (111) oriented interfaces for both majority- and minority-spin channels. The effect of disorder on these quantities will be addressed and we will discuss the ballistic versus diffuse scattering.

3.4.2.i) Majority-spin channel

Figures 3.14–3.16 show the bulk FSs of Cu and Co and Ni majority electrons viewed along the appropriate direction, their projections folded into the 2D BZs and

\mathbf{k}_{\parallel} -resolved transmission probabilities ($T(\mathbf{k}_{\parallel})$) through the interfaces for (001), (110) and (111) orientations. We skip (111) interface for Cu|Co system as it was extensively

$A B$		G_A	G_B	$G_{A B}$	2AR
Cu Co	(001)	0.554	0.486	0.456(0.454)	0.26(0.27)
majority	(011)	0.588	0.502	0.456(0.456)	0.35(0.35)
$a_{fcc} = 3.614 \text{ \AA}$	(111)	0.559	0.466	0.434(0.432)	0.34(0.35)
Cu Co	(001)	0.554	1.107	0.318(0.318)	1.79(1.79)
minority	(011)	0.588	1.035	0.310(0.347)	1.89(1.55)
$a_{fcc} = 3.614 \text{ \AA}$	(111)	0.559	1.047	0.364(0.314)	1.38(1.81)
Cu Ni	(001)	0.554	0.474	0.442(0.435)	0.31(0.34)
majority	(011)	0.588	0.491	0.434(0.430)	0.44(0.46)
$a_{fcc} = 3.614 \text{ \AA}$	(111)	0.559	0.453	0.403(0.399)	0.48(0.51)
Cu Ni	(001)	0.554	1.330	0.426(0.418)	1.07(1.11)
minority	(011)	0.588	1.290	0.399(0.409)	1.27(1.21)
$a_{fcc} = 3.614 \text{ \AA}$	(111)	0.559	1.258	0.429(0.389)	1.04(1.28)
Co Ni	(001)	0.493	0.491	0.487(0.487)	0.02(0.02)
majority	(011)	0.508	0.505	0.503(0.503)	0.01(0.01)
$a_{fcc} = 3.549 \text{ \AA}$	(111)	0.469	0.465	0.463(0.462)	0.02(0.02)
Co Ni	(001)	1.153	1.387	0.561(0.567)	0.99(0.97)
minority	(011)	1.069	1.343	0.598(0.616)	0.83(0.78)
$a_{fcc} = 3.549 \text{ \AA}$	(111)	1.082	1.315	0.634(0.585)	0.74(0.87)

Table 3.3: The Sharvin conductances, interface conductance (in units of $10^{15} \Omega^{-1} \text{m}^{-2}$) and the interface resistance [10] AR (in units of $\text{f} \Omega \text{m}^2$) for ideal and for disordered (in brackets) interfaces .

discussed in Chapter 2. The calculation of the interface conductance was carried out by performing the summation in Eq. (3.1) over the 2D BZ represented by the dashed figures shown in the corner panels of Figs. 3.14 and 3.15. The results of these calculations are summarized in Table 3.3.

In the absence of disorder, the transverse momentum (\mathbf{k}_{\parallel}) is conserved and the upper limit of transmission is given by the number of states available at the sides of the interface. These numbers are denoted using color coding on the projected FS plots (Figs. 3.14– 3.16). In all three metals the majority-spin electrons are characterized by a simple Fermi surfaces which can be described as (distorted) spheres with necks extending towards the boundaries of the bulk BZ. Even though this FSs are single-sheeted, *i.e.* there is only one band at the Fermi energy, when the FS is folded into 2D BZ we can have up to two states per \mathbf{k}_{\parallel} point. This happens most notably for (110) orientation and to a lesser extent for (001). For these interfaces the transmission can be as high as 2. From Figs. 3.14, 3.15 and 3.16 we see that the transmission is very high all throughout the 2D BZs and is limited only by the overlap between projected FSs and the number of states available on both sides of the interface. This

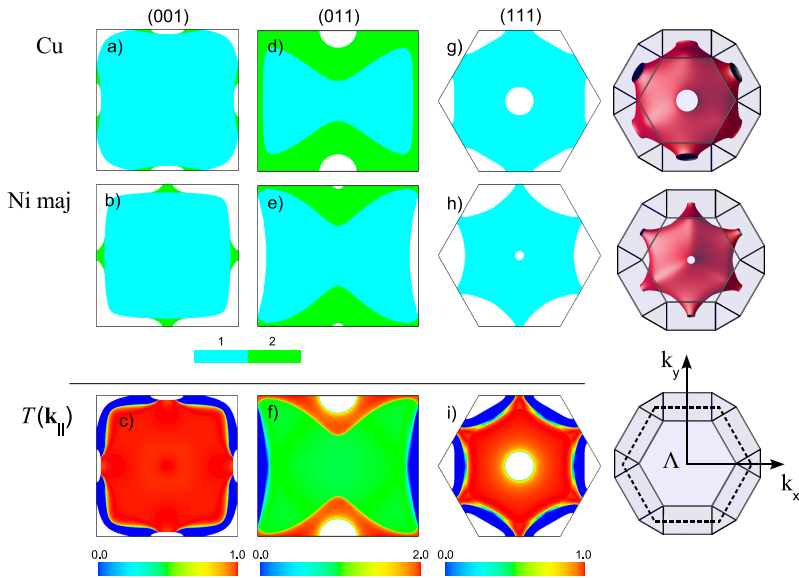


Figure 3.15: Fermi surfaces, their projections in 2D BZs and k_{\parallel} -resolved transmission probability for Cu|Ni (001), (011) and (111) interfaces for majority spin electrons.

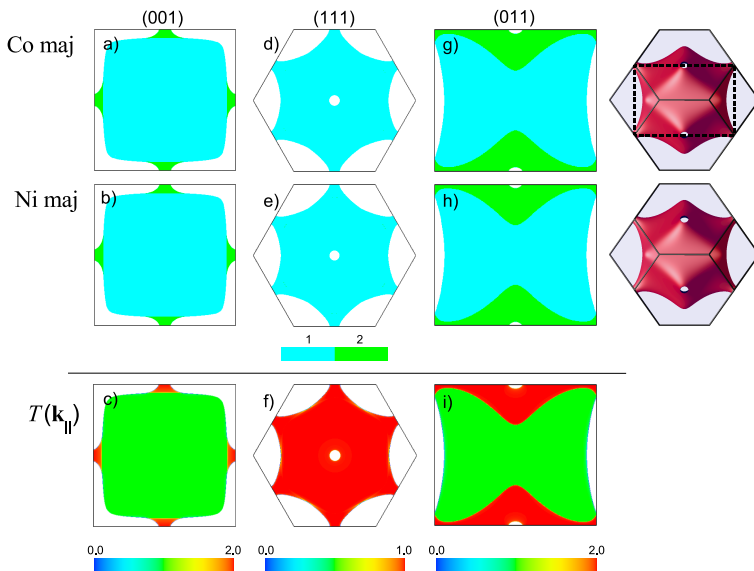


Figure 3.16: Fermi surfaces, their projections in 2D BZs and k_{\parallel} -resolved transmission probability for Co|Ni (001), (011) and (111) interfaces for majority spin electrons.

is of course understandable in view of the similarities between the respective band structures.

In the case of Cu|Co, the uniformly good transmission yields, using Eq. (3.1), the interface conductance of $0.456 \times 10^{15} \Omega^{-1}\text{m}^{-2}$ for (001) and (110) orientations and $0.434 \times 10^{15} \Omega^{-1}\text{m}^{-2}$ for (111). Similar values (see Table 3.3) and their ordering were obtained for majority Cu|Ni and Co|Ni systems. The average transmission from Cu into Co for (001), (110) and (111) orientations are respectively 0.82, 0.78 and 0.78 and from Co into Cu: 0.93, 0.90 and 0.93. The values for Cu|Ni are very similar and for Co|Ni they approach unity. Comparing the values in first three columns of Table 3.3 we see that the interface conductance for majority channel follows closely the smaller of the two Sharvin conductances. The interface resistances (last column of Table 3.3) are low (compared *e.g.* to Cr|Fe system) or, in case of Co|Ni negligible, and like conductances depend very little on the orientation.

The presence of disorder at the interfaces has essentially no effect on the transmission for the majority-spin case. The change in the interface conductances and resistances is insignificant. If one decomposes the scattering into ballistic and diffuse components one clearly sees that the specular scattering remains strongly dominant. Indeed, using eq. (3.4) and considering the example of (001) oriented interface, the specular part of the interface conductance is $0.442 \times 10^{15} \Omega^{-1}\text{m}^{-2}$ while that of the diffuse part is $0.012 \times 10^{15} \Omega^{-1}\text{m}^{-2}$ for Cu|Co interface, 0.409 and $0.026 \times 10^{15} \Omega^{-1}\text{m}^{-2}$ for Cu|Ni (001) interface. Similar values were obtained for other orientations.

In case of Co|Ni the scattering is purely ballistic along the three low index orientations. The (small) change in the interface resistance is noticeable only for Cu|Ni system, where we see about 10%, 5% and 6% enhancement compared to the values determined, respectively, for (001), (011) and (111) sharp interfaces. This is of course hardly surprising in view of the close similarity of the band structures discussed above which suggests that electrons passing through the interface experience only minor change of the effective potential. Consequently, mixing the atomic species at the interface (interdiffusion) will not substantially change the potential landscape and will not change the scattering behaviour of the electrons.

3.4.2.ii) Minority-spin channel

The minority-spin bands of Co and Ni are characterized by a strong hybridization mixing the *sp* and *d* orbitals at the Fermi energy. As seen from Figs. 3.12 and 3.13c,g, there is a large band mismatch between Cu and minority states in Co, and consequently the transmission of the minority-spin channel is expected to be poor. This is mostly true also for Cu|Ni interface although the situation here is less clear because of the relatively weak exchange splitting of the Ni's band structures. The case of Co|Ni system is exceptional since the band structures exhibit exchange-splitting in both metals. The minority- and majority-spin bands of these materials can be qualitatively seen as rigidly shifted in energy with respect to each other (Fig. 3.13).

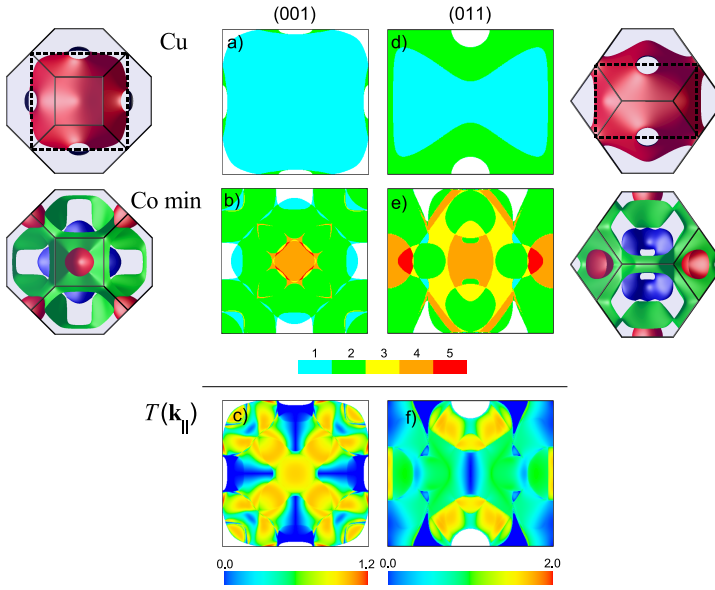


Figure 3.17: k_{\parallel} -resolved transmission probability for CuCo (001) and (011) interfaces for minority spin electrons.

Figures 3.17–3.19 show the minority-spins Fermi surfaces and transmission probabilities for Cu|Co, Cu|Ni and Co|Ni interfaces. The calculated conductances and resistances are summarized in Table 3.3.

The large values of minority-spins densities of states are reflected also in the values of Sharvin conductances. The calculated values are twice as large in the case of Cu|Co system and almost three times as large for Cu|Ni and Co|Ni systems (see Tab. 3.3) as their majority-spins counterparts.

Concentrating first on the Cu|Co interface we see that the conductances (Table 3.3) are noticeably smaller than the majority-spin ones. From Eq. (3.1) we get 0.318 , 0.310 and $0.364 \times 10^{15} \Omega^{-1} \text{m}^{-2}$, for (001), (011) and (111) oriented interfaces, respectively. Note that this decrease of conductances happens in spite of the larger number of states (in comparison to majority channel) available in Co. The conductance values correspond to average transmission from Cu into Co of 0.57 , 0.53 and 0.65 . When the transmission is assumed to be from Co into Cu it is much less – 0.29 , 0.30 and 0.35 – because of the larger number of propagating states (Sharvin conductance) in Co. Examining the k_{\parallel} resolved transmission probabilities in Fig. 3.17 reveals more qualitative difference than would be apparent from relatively modest changes in the

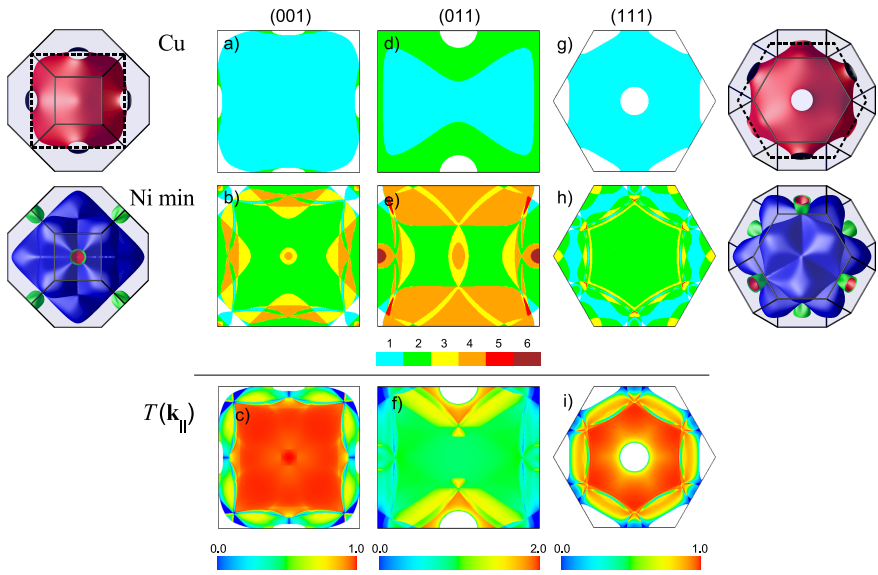


Figure 3.18: $k_{||}$ -resolved transmission probability for CuNi (001), (011) and (111) interfaces for minority spin electrons.

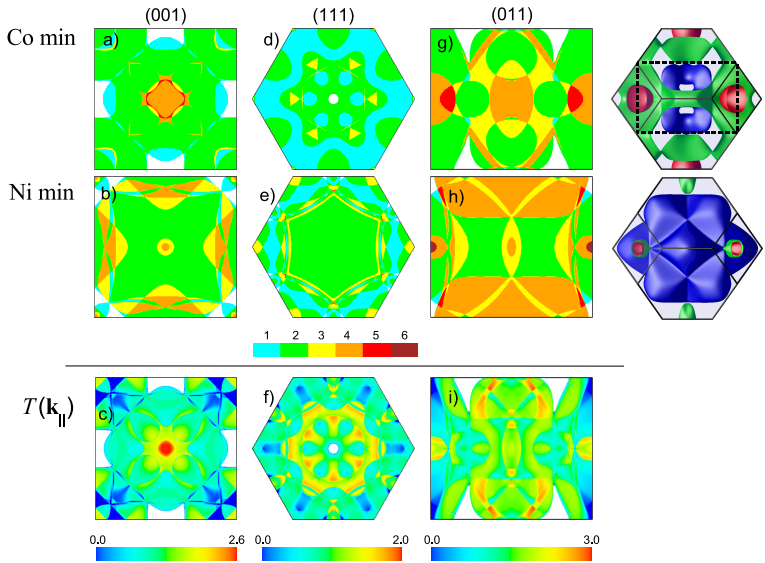


Figure 3.19: $k_{||}$ -resolved transmission probability for CoNi (001), (011) and (111) interfaces for minority spin electrons.

total, integrated conductance values. The large differences between the bulk and projected Fermi surfaces result in complicated patterns of transmission. On one hand we see the regions of high transmission approaching the upper theoretical limit, given usually by the number of states in Cu as it tends to be smaller the number of Co states. On the other hand we also see the areas of 2D BZ where the transmission is much lower, or just zero. The reduction comes, as we discussed in detail for the Cr|Fe interface, from either velocity or symmetry mismatch of the states facing each other across the interface. These areas contribute the overall reduction of the conductances shown in Table 3.3.

The situation is altered even more with the introduction of the disorder, modeled as two monolayers of 50%–50% alloy at the interface. The integrated conductances (shown in brackets in Table 3.3) exhibit only modest changes with the (001) values unchanged, (011) ones increased and (111) ones decreased in comparison with the sharp, specular interfaces. Truly qualitative changes become apparent only when we separate the conductance into the specular and diffusive parts as defined by Eq. (3.4). With the introduction of disorder at the Cu|Co(001) interface the specular conductance of the minority-spin channel drops from 0.318 to $0.058 \times 10^{15} \Omega^{-1}\text{m}^{-2}$. The decrease in the specular component is exactly compensated by the diffuse contribution of $0.260 \times 10^{15} \Omega^{-1}\text{m}^{-2}$. The interplay between specular and diffusive parts generates the changes in total transmission seen for (011) and (111) interfaces. The most important result however is that even in the presence of relatively weak disorder considered here the scattering in minority channel at the Cu|Co interfaces becomes predominantly diffusive which results in the loss of coherence.

Comparing now the interface resistances, calculated using Eq. (3.2), for majority and minority spins we see the differences which by far exceed those seen for conductances. For these quantities, suitable for parameterization of interfaces embedded in the diffusive system, the spin-dependency comes from the Sharvin conductances, that is the numbers of channels (states) available in a given material. As we have commented earlier Sharvin conductances for magnetic materials are indeed strongly spin-dependent – see the G_B column in Table 3.3.

Inspecting now the minority-spins transmission plots for Cu|Ni (Fig. 3.18) we see that while they exhibit relatively reach structure, reflecting the complexity of multiple-sheet minority-spins FS of Ni, (Fig. 3.15), the transmission values tend to be high. In fact comparing the numbers given in Table 3.3 we observe that while the conductance in majority channel is higher than the minority one for (001) and (011) orientations the situation is reversed for (111) orientation. In general the majority and minority values are rather close in spite of substantial differences seen in the densities of states [Figs. 3.12 and 3.13f),g)] and Sharvin conductances. We can understand this situation by noticing that while the relatively weak exchange splitting in Ni is sufficient to place the minority d -band at the Fermi energy, it is not quite strong enough to entirely displace the bands of similar character in Cu and Ni. This can be seen *e.g.* along the $\Gamma - K$ direction, equivalent to the center of the 2D BZ for (011) interface, where the same Σ_1 states in both Cu and Ni are present at the Fermi energy. In comparison these states in Co are shifted away from the Fermi level which results in the zero transmission region visible in the center of Fig. 3.17f).

Similarly as for Cu|Co, the disorder can either diminish [(001) and (111)] or increase, (011), the interface conductance with changes being rather modest in magnitude. Decomposing the conductance for disordered (111) interface, equal to $0.389 \cdot 10^{15} \Omega^{-1} \text{m}^{-2}$, into the specular and diffusive components we obtain 0.229 for the former and $0.160 \cdot 10^{15} \Omega^{-1} \text{m}^{-2}$ for the latter. In this case the specular conductance drops by almost 50% in comparison to the sharp interface but, unlike for Cu|Co system, it is not dominated by the diffusive contribution. The decomposition for (001) interface yields comparable numbers, that is 0.260 and $0.158 \cdot 10^{15} \Omega^{-1} \text{m}^{-2}$ respectively.

As in the Cu|Co case, the interface resistances show greater degree of spin-dependence than one would suspect comparing only interface conductances. As previously it is related to the spin-dependence of Sharvin conductances.

The minority-spin interface conductance in case of Co|Ni interfaces are larger than those for the other two *fcc* systems, Cu|Co and Cu|Ni. However, when compared to the number of states (Sharvin conductances) available at both sides of the interface they yield average transmission probabilities which are not overly high. Taking for example (001) interface we get, for specular system, average transmission of 0.49 from Co into Ni and 0.40 the other way around. This relatively low transmission can be surprising as, at the first sight, the bulk band structures of Co and Ni [Figs. 3.13c,g)] resemble each other. However, as we discussed earlier, even the relatively small difference in their position is in some cases enough to change the character of states present at the Fermi energy [compare *e.g.* $\Gamma - K$ direction in Figs. 3.13d) and h)]. The differences become more apparent when we compare the Fermi surfaces and their projections shown in Fig. 3.19. The figures in the left and middle column demonstrate that the relatively small shift between the two band structures is enough to produce the Fermi surfaces of notably different character and topology. This results in transmission probabilities which, as a rule, fall short of their upper theoretical limit (the smaller of two numbers of states at a given point). As the consequence in spite of the large Landauer-Büttiker conductance the interface resistance in the minority channel, given by Eq. (3.2), is much higher than the majority one and assumes values comparable to those for the other two interfaces.

Also for Co|Ni the effect of disorder in minority channel depends on the orientation. For (001) and (011) interfaces we observe a small enhancement of the integrated values of the transmission. As previously the net effect is the result of partial compensation of disorder-induced decrease of specular component by the diffusive contribution. For the (001) interface, the specular component of the conductance decreases by 48% from 0.561 to 0.290 in units of $10^{15} \Omega^{-1} \text{m}^{-2}$ while the diffuse part is as large as $0.277 \cdot 10^{15} \Omega^{-1} \text{m}^{-2}$.

For (111) interfaces the 8% reduction in net conductance results from the decrease in specular channel from 0.634 to $0.277 \cdot 10^{15} \Omega^{-1} \text{m}^{-2}$ which is only partially made up for by the appearance of the diffusive part equal to $0.308 \cdot 10^{15} \Omega^{-1} \text{m}^{-2}$.

3.4.2.iii) Conclusions

In the preceding sections we have presented and discussed results of first principle calculations of interface scattering for three lattice-matched *fcc* systems: Cu|Co,

Cu|Ni and Co|Ni.

The general picture which emerges from comparison of the three cases is that in the majority channel, with only single *sp* band at the Fermi energy, the transmission is uniformly high and the conductance is determined simply by the overlap of the projections of respective Fermi surfaces along the transport direction. The disorder has usually negligible effect on this channel and the transmission, for the substitutional disorder we considered, remains specular.

The minority spin electrons with strongly *d*-hybridized bands at the Fermi energy in magnetic elements form high resistance channel as the results of the mismatch of the electronic structures at the interface. The disorder has only modest effect on the total conductance which, depending on the system and the orientation, can either increase or decrease. The main effect is the change of the *character* of the conductance. For Cu|Co system the transmission in the presence of interdiffusion is almost completely dominated by the diffusive scattering. For the other two systems the specular and diffusive components are roughly comparable. These findings are of importance *e.g.* when discussing the validity of the serial resistor model[12–14] commonly used in the interpretation of CPP-GMR experiments.

It might be worthwhile bringing the reader’s attention to the fact that the relation between the two transport coefficients – interface conductance and resistance – given in Table 3.3 is far from trivial. This is especially clearly seen for the case of Co|Ni interface. For this system we see, when going from majority to minority spins, an increase of *both* interface conductance and resistance. This apparent contradiction results from the fact that the two quantities describe the transport properties of the interface in different physical regimes. The Landauer-Büttiker interface conductance [Eq. (3.1)] corresponds to the measurements in the point-contact geometry. The Schep’s *et al.*[45] formula [Eq. (3.2)] for interface resistance is meant for use in diffusive systems where the ohmic regime is realized. The renormalization of the “bare” Landauer-Büttiker term defined by Eq. (3.2) can be seen as subtraction of the spurious contact resistances inherently present in Eq. (3.1). In spite of its simplicity Eq. (3.2) was shown in the past to be successful in addressing the experiments usually carried out in the diffusive regime.

3.5 Energy dependence

We have so far discussed the transport properties of intermetallic interfaces in the linear response regime. Accordingly we have calculated the interface conductances and resistances at the Fermi energy, E_F . There exist however experiments, most notably those involving spin valve transistor[64, 65], where electrons cross the interface at different energies [66]. Motivated by this we will now discuss the energy dependence of transport through Fe|Cr|Fe (001) and Co|Cu|Co (111) structures with the thickness of the non-magnetic spacer equal to 10 ML. To this end the transmission probabilities in Eqs. (3.1) and (3.2) were calculated for the range of energies below and above the Fermi energy within the rigid band approximation. Common lattice constants of $a = 2.871 \text{ \AA}$ for Fe-based and $a = 3.614 \text{ \AA}$ for Co-based spin valves and

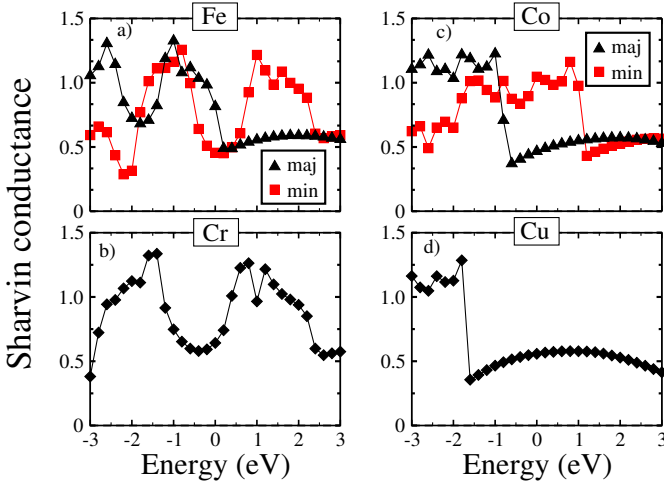


Figure 3.20: Sharvin conductance (in units of $10^{15} \Omega^{-1} \text{m}^{-2}$) as a function of energy for bulk bcc Fe and Cr (001) (left panel) and fcc Co and Cu (111) (right panel). The Fermi energy (E_F) is set to zero.

spd-basis set were used. We considered both parallel (P) and antiparallel (AP) magnetic configurations of the magnetic moments of ferromagnetic leads. The disorder was modeled using 2 MLs of 50%-50% alloy at the interface.

Figure 3.20 shows the Sharvin conductances, calculated using Eq. (3.3), for the bulk *bcc* Fe, Cr along [001] and *fcc* Co, Cu along [111] direction as a function of energy. Comparing these with the densities of states (DOS) shown in Fig. 3.1, 3.12 and 3.13 we notice that there exists a rough correspondence between the two quantities. For the energies which, for the given metal and the spin channel, lie within the range of the *d*-bands the Sharvin conductances tend to be large and vary strongly with the energy. The minima of the curves for Fe and Cr correspond to the equivalent features seen in DOS. For the energies above the *d*-bands range the curves become smoother and the values generally smaller. This happens at about 0.5 eV above E_F , set here to zero, for Fe majority and 2.5 eV for Fe minority and Cr. The corresponding values for fcc metals are about -1.2, -0.4 and 1.2 eV for Cu, Co majority and minority respectively. We note however that there is no simple proportionality between DOS and Sharvin conductance.

The interface conductances and resistances are shown in Fig. 3.21 as functions of energy for sharp and dirty interfaces in Fe|Cr|Fe (001) and Co|Cu|Co (111) spin valves. Starting with Fe|Cr|Fe we observe that for energies above -1.5 eV the minority channel dominates the conductance in the parallel configuration. This follows

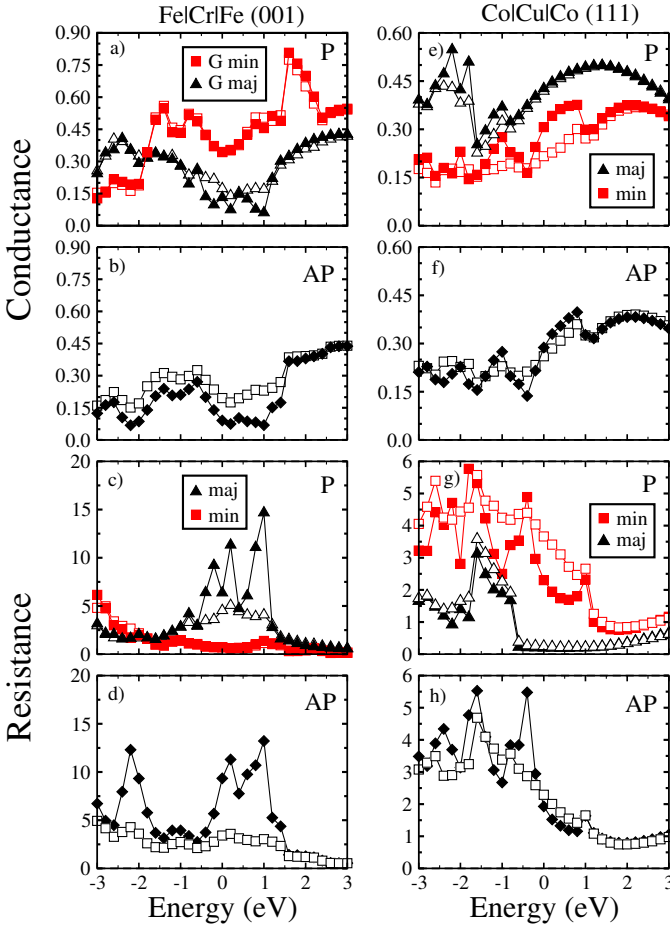


Figure 3.21: Interface conductance (in units of $10^{15} \Omega^{-1} \text{m}^{-2}$) and resistance (in units of $10^{-15} \Omega \text{m}^2$) as a function of energy for parallel (P) and antiparallel (AP) coupling between the magnetizations of the ferromagnets in bcc Fe|Cr|Fe (001) (left panel) and fcc Co|Cu|Co (111) (right panel) oriented interfaces. The data of calculations with sharp (dirty) interfaces is represented by solid (open) symbols. The Fermi energy, here the reference energy, is set to zero.

from the similarities of the respective electronic structures discussed in the preceding sections. The good transmission through both interfaces results in the curve which retains some resemblance to the Sharvin conductances shown in Fig. 3.20, with maxima in the positions determined by the superimposition of the Sharvin conductance curves for Fe minority and Cr. The conductance of the poorly matched majority channel is typically much smaller and, for energies within the range of Fe

majority d -bands, does not resemble either of the Sharvin conductances. The curve for AP configuration is seen to follow roughly the smaller of the two conductances for P configuration, that is G_{maj} for energies below -1.5 eV and G_{min} above that value. The disorder has negligible effect on majority channel in P configuration and tend to increase the conductance in P minority and (more strongly) in AP case. For the two latter cases the disorder reduces the energy dependence making the curves smoother. This is seen more clearly in the interface resistances [Fig. 3.21c) and d)].

The magnetoresistance is defined as

$$MR = \frac{G_{maj} + G_{min} - 2G_{AP}}{2G_{AP}} \quad (3.5)$$

where G_{maj} and G_{min} are the interface conductances in the P configuration and G_{AP} is the interface conductance of either spin in the AP configuration. The magnitude of MR , at E_F , is found to be 163% for sharp interfaces and decreases substantially to 32% with defect scattering. In the P configuration, the specular component of the interface conductance for majority channel decreases by as much as 85%, dropping from 0.132 to $0.02 \times 10^{15} \Omega^{-1} \text{m}^{-2}$ while the diffuse component is $0.153 \times 10^{15} \Omega^{-1} \text{m}^{-2}$. The interface conductance of the minority-spin channel remains almost unchanged, the specular conductance decreases by less than 2%, from 0.344 to $0.338 \times 10^{15} \Omega^{-1} \text{m}^{-2}$. Disorder has much larger effect in the AP than the P configuration. The specular component of the interface conductance decreases by as much as 95%, it drops from 0.091 to 0.004 in units of $10^{15} \Omega^{-1} \text{m}^{-2}$ while the diffuse component is $0.157 \times 10^{15} \Omega^{-1} \text{m}^{-2}$ for either spins.

In the case of Co|Cu|Co (111) spin valve [Fig. 3.21e)–h)] the transmission in P configuration is dominated by the majority-spin channel in the entire energy interval considered. The difference between the two spin-channels depends strongly on the energy changing from very modest *e.g.* for energies around 0.5 and -1 eV to very substantial (factor 2 and more) below -2 eV. Above the range of the d -bands (above -0.5 eV for majority and 1 eV for minority spins) both curves become smoother reflecting the free-electron like of the respective bands. For energies above 1 eV when the d -bands are left behind for both spin-channels the conductances start to converge slowly. However, the polarization remains non-zero up until the 3 eV that is in the whole energy range considered here. Similarly as in the case of Fe|Cr|Fe the AP conductance resembles the low-conductance channel in P configuration, *i.e.* for Co|Cu|Co the minority spin conductance. The disorder tends to lower the conductance in the P configuration and has more pronounced effect on the minority channel. In the AP case it can either decrease or increase the conductance and is seen to average out the quasi-oscillations of the curve. The MR , at the Fermi energy, is predicted to be low, about 28% for sharp interfaces. This value decreases to about 22% for disordered interfaces. In the P configuration, defect scattering has a very small effect on the total transmission for the majority-spin electrons. The specular component of the interface conductance in this channel decreases by only about 7%, it drops from 0.427 to 0.398 in units of $10^{15} \Omega^{-1} \text{m}^{-2}$ while the diffuse component, very small,

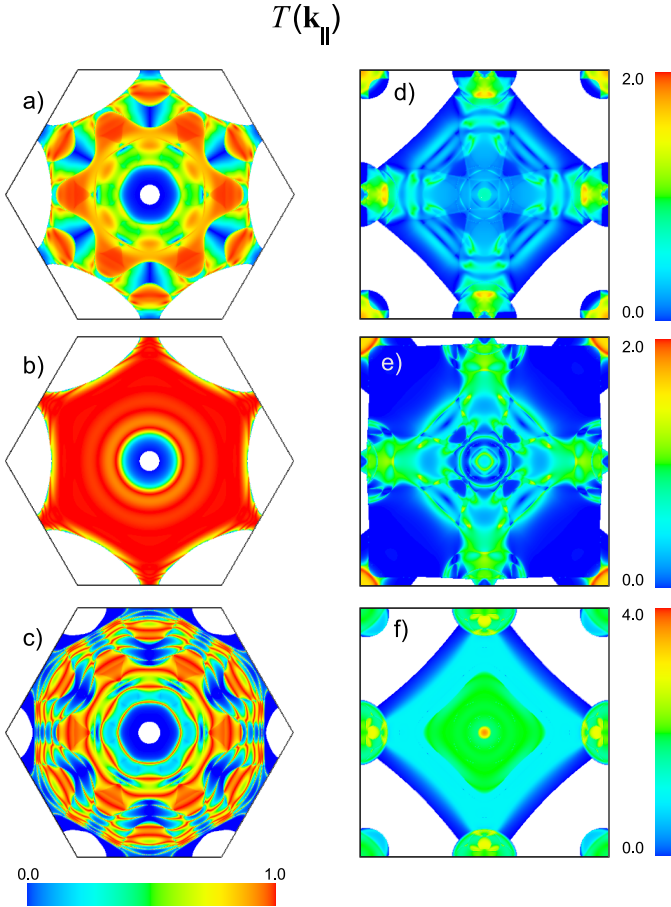


Figure 3.22: k_{\parallel} -resolved transmission probability for CoCuCo (111) (left panel) and FeCrFe (001) (right panel) trilayers at the Fermi energy. (a,d) both spins in antiparallel configuration; (b,e) Majority spin and (c,f) minority in the parallel configuration.

is $0.021 \times 10^{15} \Omega^{-1}\text{m}^{-2}$. In the case of the minority-spin channel, the scattering is dominated by the diffuse component, which is $0.205 \times 10^{15} \Omega^{-1}\text{m}^{-2}$. The specular component decreases by as much as 96%, it drops from 0.307 to 0.012 in units of $10^{15} \Omega^{-1}\text{m}^{-2}$. For the AP configuration, the effect of disorder is much stronger, the ballistic component decreases by as high as 85%, it drops from 0.288 to 0.042 in units of $10^{15} \Omega^{-1}\text{m}^{-2}$ while the diffuse part is about $0.220 \times 10^{15} \Omega^{-1}\text{m}^{-2}$.

The transmission probabilities as a function of the transverse momentum \mathbf{k}_{\parallel} are shown in Fig. 3.22 for either spins in the AP configuration [panel a) and d)] majority and minority spins in the P configuration [panels b), c), e) and f)]. Comparing these

plots with the single interface transmissions shown for Cr|Fe in Figs. 3.4 and 3.5 and for Cu|Co in Figs. 5 and 6 of Ref. [36] we see that the spin valve transmissions for P configuration retains basic resemblance to their single interface counterparts. The AP transmissions can be seen as intermediate case between majority and minority spins transmissions. The multiple reflections in the non-magnetic spacer give rise to the interference patterns visible especially clearly for Co|Cu|Co in P configuration.

3.6 Discussion and Summary

In this section we compare our results to the existing data in the literature. Different first-principles techniques based on the Landauer-Büttiker's and/or Schep's formulae [45] were used to calculate the spin-dependent specular interface resistance using transmission probabilities. The results of these calculations through various metallic interfaces along different orientations are given in Ref. [36, 45–48, 53, 54, 67]. While there is a general agreement on the magnitude of the obtained values but there remain small discrepancies which are ascribed to the difference in the computation techniques used. Comparison of the present work and the earlier mentioned results is found to be in a good agreement with experiments [11, 68] for specular interfaces Cu|Co and Fe|Cr systems. This agreement is improved by including disorder at the interface, present work and Ref. [36, 47].

The effect of disorder on conductance through interfaces Cu|Co and Fe|Cr along [001] orientation has been studied by different authors [20–22, 25, 33, 69, 70]. As reported previously by Xia *et al.* [47], and seen recently by Velev *et al.* [25], substitutional disorder at the interfaces reduces the interface conductance in case of Cu|Co system but enhances it in case of the majority spin channel of Fe|Cr and minority spin channel for Cu|Co, Cu|Ni and Co|Ni systems along [011] orientation. For the latter case the change is rather modest. By far Cu|Ni and Co|Ni systems are the less studied systems compared to the other two systems presented in this work. Only few theoretical [26, 46, 54, 71] and experimental transport studies [72, 73] have been carried out for these two systems, Cu|Ni and Co|Ni.

An interesting effect is that observed in the transport of hot-electrons in the spin valve transistor structures made of Cu/Co system. An effect of more than 390% CPP magnetocurrent was measured by Monsma *et al.* [65, 74] in the spin valve transistor. In this device the carriers were injected at an energy of 0.7 eV, fixed by the height of a Schottky barrier. At an energy of about 0.8 eV above E_F we obtain a magnetocurrent (CPP-GMR at a fixed energy) of 253% which decreases to about 45% with disorder at the interfaces.

In summary, we have studied the spin-polarized transport properties in a series of lattice matched materials, namely Cr|Fe, Cu|Co, Cu|Ni and Co|Ni systems along [001], [011] and [111] orientations. We have observed a strong spin dependence for all the systems studied and an orientation dependence of the interface conductance in Cr|Fe system. The interface conductance for sharp interfaces is 2 and 3 times, respectively for (011) and (111) interfaces, larger than that of Cr|Fe (001). This anisotropy in the conductance is completely destroyed by defect scattering at the interface. De-

pending on the system and the crystallographical orientation, substitutional disorder at the interfaces can increase or decrease the interface conductance and reversely the interface resistance. Concentrating on the more particular Cr|Fe (001) interface we have carried out a detailed study of the effect of defect scattering on the transport properties. Ballistic versus the diffusive components of the interface transmission were separated. We found that the increase of the conductance is mediated by a large diffusive component of the interface transmission in the presence of disorder. This is a consequence on the fact that the Cr|Fe (001) interface is characterized by a large mismatch in the majority band structure of Fe and that of Cr. The interface resistance is reduced by disorder by a factor 3. The effect of disorder on (011) and (111) interfaces is much smaller. In the last part we have presented the energy dependence of the transmission in the Fe|Cr|Fe (001) and Co|Cu|Co (111) trilayers. The results are analyzed in terms of the bulk density of states and the band structures. The effect of disorder was considered too.

Bibliography

- [1] M. N. Baibich *et al.*, Phys. Rev. Lett. **61**, 2472 (1988).
- [2] G. Binash, P. Grünberg, F. Saurenbach, and W. Zinn, Phys. Rev. B **39**, 4828 (1989).
- [3] G. A. Prinz, J. Magn. & Magn. Mater. **200**, 57 (1999).
- [4] S. A. Wolf *et al.*, Science **294**, 1488 (2001).
- [5] S. S. Parkin *et al.*, Proceedings of The IEEE **91**, 661 (2003).
- [6] M. A. M. Gijs and G. E. W. Bauer, Adv. Phys. **46**, 285 (1997).
- [7] J. P. Ansermet, J. Phys.: Condens. Matter. **10**, 6027 (1998).
- [8] E. Y. Tsymbal and D. G. Pettifor, Solid State Physics **56**, 113 (2001).
- [9] M. A. M. Gijs, S. K. J. Lenczowski, and J. B. Giesbers, Phys. Rev. Lett. **70**, 3343 (1993).
- [10] W. P. Pratt, Jr. *et al.*, Phys. Rev. Lett. **66**, 3060 (1991).
- [11] J. Bass and W. P. Pratt Jr., J. Magn. & Magn. Mater. **200**, 274 (1999).
- [12] S. F. Zhang and P. M. Levy, J. Appl. Phys. **69**, 4786 (1991).
- [13] S. F. Lee *et al.*, J. Magn. & Magn. Mater. **118**, L1 (1993).
- [14] T. Valet and A. Fert, Phys. Rev. B **48**, 7099 (1993).
- [15] S. S. P. Parkin, Phys. Rev. Lett. **71**, 1641 (1993).
- [16] R. E. Camley and J. Barnaś, Phys. Rev. Lett. **63**, 664 (1989).
- [17] K. M. Schep, P. J. Kelly, and G. E. W. Bauer, Phys. Rev. Lett. **74**, 586 (1995).
- [18] Y. Asano, A. Oguri, and S. Maekawa, Phys. Rev. B **48**, 6192 (1993).
- [19] R. K. Nesbet, J. Phys.: Condens. Matter. **6**, L449 (1994).
- [20] E. Y. Tsymbal and D. G. Pettifor, J. Phys.: Condens. Matter. **8**, L569 (1996).
- [21] E. Y. Tsymbal and D. G. Pettifor, Phys. Rev. B **54**, 15314 (1996).
- [22] R. J. Baxter, D. G. Pettifor, and E. Y. Tsymbal, Phys. Rev. B **71**, 024415 (2005).

- [23] M. Villeret, J. Mathon, R. B. Muniz, and J. D. E. Castro, Phys. Rev. B **57**, 3474 (1998).
- [24] I. Turek, J. Kudrnovský, V. Drchal, L. Szunyogh, and P. Weinberger, Phys. Rev. B **65**, 125101 (2002).
- [25] J. Velev and W. H. Butler, Phys. Rev. B **69**, 024404 (2004).
- [26] S. Sanvito, C. J. Lambert, J. H. Jefferson, and A. M. Bratkovsky, Phys. Rev. B **59**, 11936 (1999).
- [27] K. P. McKenna, L. A. Michez, G. J. Morgan, and B. J. Hickey, Phys. Rev. B **72**, 054418 (2005).
- [28] I. Mertig, Rep. Prog. Phys. **62**, 237 (1999).
- [29] P. Zahn, J. Binder, and I. Mertig, Phys. Rev. B **72**, 174425 (2005).
- [30] W. H. Butler, X. G. Zhang, D. M. C. Nicholson, and J. M. MacLaren, Phys. Rev. B **52**, 13399 (1995).
- [31] P. Weinberger, Phys. Rep. **377**, 281 (2003).
- [32] P. Mavropoulos, N. Papanikolaou, and P. Dederichs, Phys. Rev. B **69**, 125104 (2004).
- [33] J. Kudrnovský *et al.*, Phys. Rev. B **62**, 15084 (2000).
- [34] D. Wortmann, H. Ishida, and S. Blügel, Phys. Rev. B **66**, 075113 (2002).
- [35] K. M. Schep, P. J. Kelly, and G. E. W. Bauer, Phys. Rev. B **57**, 8907 (1998).
- [36] K. Xia, M. Zwierzycki, M. Talanana, P. J. Kelly, and G. E. W. Bauer, Phys. Rev. B **73**, 064420 (2006).
- [37] S. Datta, *Electronic Transport in Mesoscopic Systems* (Cambridge University Press, Cambridge, 1995).
- [38] P. A. Khomyakov, G. Brocks, V. Karpan, M. Zwierzycki, and P. J. Kelly, Phys. Rev. B **72**, 035450 (2005).
- [39] K. Xia, P. J. Kelly, G. E. W. Bauer, A. Brataas, and I. Turek, Phys. Rev. B **65**, 220401 (2002).
- [40] M. Zwierzycki, Y. Tserkovnyak, P. J. Kelly, A. Brataas, and G. E. W. Bauer, Phys. Rev. B **71**, 064420 (2005).
- [41] M. Zwierzycki, K. Xia, P. J. Kelly, G. E. W. Bauer, and I. Turek, Phys. Rev. B **67**, 092401 (2003).
- [42] G. E. W. Bauer *et al.*, Phys. Rev. B **72**, 155304 (2005).
- [43] G. E. W. Bauer *et al.*, Phys. Rev. Lett. **92**, 126601 (2004).
- [44] K. Xia, P. J. Kelly, G. E. W. Bauer, and I. Turek, Phys. Rev. Lett. **89**, 166603 (2002).
- [45] K. M. Schep, J. B. A. N. van Hoof, P. J. Kelly, G. E. W. Bauer, and J. E. Inglesfield, Phys. Rev. B **56**, 10805 (1997).
- [46] M. D. Stiles and D. R. Penn, Phys. Rev. B **61**, 3200 (2000).
- [47] K. Xia *et al.*, Phys. Rev. B **63**, 064407 (2001).
- [48] C. Galinon *et al.*, Appl. Phys. Lett. **86**, 182502 (2005).
- [49] P. A. Khomyakov and G. Brocks, Phys. Rev. B **70**, 195402 (2004).
- [50] P. A. Khomyakov and G. Brocks, Phys. Rev. B **74**, 1 (2006), cond-mat/0604485.

- [51] P. Bruno, J. Magn. & Magn. Mater. **121**, 248 (1993).
- [52] M. D. Stiles, Phys. Rev. B **48**, 7238 (1993).
- [53] M. D. Stiles, Phys. Rev. B **54**, 14679 (1996).
- [54] M. D. Stiles, J. Appl. Phys. **79**, 5805 (1996).
- [55] I. Turek, V. Drchal, J. Kudrnovský, M. Šob, and P. Weinberger, *Electronic Structure of Disordered Alloys, Surfaces and Interfaces* (Kluwer, Boston-London-Dordrecht, 1997).
- [56] O. K. Andersen, O. Jepsen, and D. Glötzl, in, in *Highlights of Condensed Matter Theory*, edited by F. Bassani, F. Fumi, and M. P. Tosi, pp. 59–176, North-Holland, Amsterdam, 1985.
- [57] D. M. Ceperley and B. J. Alder, Phys. Rev. Lett. **45**, 566 (1980).
- [58] J. P. Perdew and A. Zunger, Phys. Rev. B **23**, 5048 (1981).
- [59] A. Davies, J. A. Stroscio, D. T. Pierce, and R. J. Celotta, Phys. Rev. Lett. **76**, 4175 (1996).
- [60] D. Venus and B. Heinrich, Phys. Rev. B **53**, R1733 (1996).
- [61] P. Bruno, H. Itoh, J. Inoue, and S. Nonoyama, J. Magn. & Magn. Mater. **198-199**, 46 (1999).
- [62] V. Drchal *et al.*, Phys. Rev. B **65**, 214414 (2002).
- [63] U. von Barth and L. Hedin, J. Phys. C: Sol. State Phys. **5**, 1629 (1972).
- [64] T. Banerjee, E. Haq, M. H. Siekman, J. C. Lodder, and R. Jansen, Phys. Rev. Lett. **94**, 027204 (2005).
- [65] R. Jansen, J. Phys. D: Appl. Phys. **36**, R289 (2003).
- [66] W. H. Rippard and R. A. Buhrman, Phys. Rev. Lett. **84**, 971 (2000).
- [67] G. E. W. Bauer, K. M. Schep, K. Xia, and P. J. Kelly, J. Phys. D: Appl. Phys. **35**, 2410 (2002).
- [68] A. Zambano, K. Eid, R. Loloee, W. P. Pratt, Jr., and J. Bass, J. Magn. & Magn. Mater. **253**, 51 (2002).
- [69] E. Y. Tsymbal, Phys. Rev. B **62**, 3608 (2000).
- [70] K. Carva, I. Turek, J. Kudrnovský, and O. Bengone, Phys. Rev. B **73**, 144421 (2006).
- [71] M. Weissmann, A. M. Llois, R. Ramirez, and M. Kiwi, Phys. Rev. B **54**, 15335 (1996).
- [72] J. M. Gallego, D. Lederman, S. Kim, and I. K. Schuller, Phys. Rev. Lett. **74**, 4515 (1995).
- [73] D. Lederman, J. M. Gallego, S. Kim, and I. K. Schuller, J. Magn. & Magn. Mater. **183**, 261 (1998).
- [74] D. J. Monsma, J. C. Lodder, T. J. A. Popma, and B. Dieny, Phys. Rev. Lett. **74**, 5260 (1995).

Chapter 4

rientation-dependent transparency of metallic interfaces

As devices are reduced in size, interfaces start to dominate electrical transport making it essential to be able to describe reliably how they transmit and reflect electrons. For a number of nearly perfectly lattice-matched materials, we calculate from first-principles the dependence of the interface transparency on the crystal orientation. Quite remarkably, the largest anisotropy is predicted for interfaces between the prototype free-electron materials silver and aluminium for which a massive factor of two difference between (111) and (001) interfaces is found.

4.1 Introduction

A recurring theme in condensed matter physics in the last twenty years has been the discovery of new physical effects and properties in systems with reduced dimensions; the prospect of exploiting these effects and properties in logical processing, sensing and storage devices is an important driving force behind nano-science and -technology. In semiconductors, the electronic structures of the electrons responsible for conduction can be described using simple models. The same is not true of the ferromagnetic transition metals which form the basis for magnetoelectronics. It is the non-trivial spin-dependence of the transmission and reflection of electrons at magnetic interfaces which provides the key to understanding phenomena such as oscillatory exchange coupling, giant- and tunneling- magnetoresistance, spin transfer torque, spin-pumping and spin injection [1]. For well-studied material combinations such as Co|Cu and Fe|Cr, modest spin-dependence of the interface transmission [2–4] of the order of 10-20% is sufficient to account for experimental observations [5].

However, the confrontation of theory and experiment just referred to is at best indirect and model-dependent. Even though the theory of transport in small struc-

tures is formulated in terms of transmission and reflection matrices [6], measuring interface transparencies directly has proven quite difficult [7]. To identify interfaces suitable for experimental study, we have undertaken a systematic materials-specific study of the orientation dependence of the interface transmission between pairs of isostructural metals whose lattice constants match within a percent or so in the hope that it will prove possible to grow such interfaces epitaxially.

One of the metal pairs we studied was Al|Ag. Both metals have the fcc crystal structure and their lattice constants are matched within 1%. Aluminium is a textbook [8] example of a system well described by the (nearly) free electron model. Silver, also usually assumed to be a free electron-like material, is a noble metal with high conductivity which is frequently used for electrical contacting. We found that in spite of the simplicity of both metals' electronic structures the transmission through Al|Ag interfaces can differ quite significantly from the predictions of the free electron model. In particular, between (111) and (001) orientations we find a factor 2 difference in interface transmission for clean Al|Ag interfaces. For free electrons the anisotropy should vanish. Our result is insensitive to interface disorder. We identify a new factor responsible for this difference which is not related to the standard velocity- [9, 10] or symmetry-mismatch [11, 12] mechanisms.

A free electron description of interface scattering, in which the effect of the crystal potential on transport is completely neglected, underlies the BTK theory [13] used to interpret [9, 10] Andreev reflection (AR) experiments. Point contact AR experiments are increasingly used to identify the pairing symmetry of superconductors and, in the field of magnetoelectronics, to determine the polarization of magnetic materials [14, 15]. Our finding that the electronic structure can have such a large effect on the interface transmission, implies that experiments should be analysed using more sophisticated models.

4.2 Method

Our study was based upon first-principles calculations of the interface electronic structure performed within the framework of density functional theory (DFT) and the local spin density approximation (LSDA). Bulk and interface potentials were determined self-consistently using the tight binding linearized muffin tin orbital (TB-LMTO) [16] surface Green's function method [17]. We assumed common lattice constants for both metals of a given structure e.g. $a_{Al} = a_{Ag} = 4.05 \text{ \AA}$. The potentials obtained in this way were used as input to a TB-MTO wavefunction-matching [4, 12] calculation of the transmission and reflection coefficients between Bloch states on either side of the interface. The efficiency of this approach is such that interface disorder can be modelled using large lateral supercells. For disordered systems, the potentials were calculated using the layer CPA (coherent potential approximation). The results of the calculations for a number of lattice-matched materials are summarized in Table 4.1.

4.3 Orientation dependence of the transmission

The Sharvin conductances, G_A and G_B , reported in the third and fourth columns of Table 4.1 are proportional to the number of states at the Fermi level propagating in the transport direction. They are properties of the bulk materials which are determined by the area of the Fermi surface projections and are a measure of the current-carrying capacity of the conductor in the ballistic regime. The largest intrinsic orientation dependence, seen to be about 13 %, is found for W; for Al and Ag, respectively, it is less than 8% and 5%.

$A B$		G_A	G_B	$G_{A B}$	$2SR$
Al Ag	(111)	0.69	0.45	0.41 (0.36)	0.64 (0.92)
$a_{fcc} = 4.05 \text{ \AA}$	(110)	0.68	0.47	0.30 (0.32)	1.60 (1.39)
	(001)	0.73	0.45	0.22 (0.24)	2.82 (2.37)
Al Au	(111)	0.69	0.44	0.41 (0.35)	0.60 (0.99)
$a_{fcc} = 4.05 \text{ \AA}$	(001)	0.73	0.46	0.24 (0.26)	2.37 (2.14)
Pd Pt	(111)	0.62	0.71	0.55 (0.54)	0.30 (0.33)
$a_{fcc} = 3.89 \text{ \AA}$	(001)	0.58	0.70	0.52 (0.51)	0.37 (0.39)
W Mo	(001)	0.45	0.59	0.42 (0.42)	0.42 (0.42)
$a_{bcc} = 3.16 \text{ \AA}$	(110)	0.40	0.54	0.37 (0.38)	0.52 (0.47)
Cu Co	(111)*	0.56	0.47	0.43 (0.43)	0.34 (0.35)
majority	(001)	0.55	0.49	0.46 (0.45)	0.26 (0.27)
$a_{fcc} = 3.61 \text{ \AA}$	(110)	0.59	0.50	0.46 (0.46)	0.35 (0.35)
Cu Co	(111)*	0.56	1.05	0.36 (0.31)	1.38 (1.82)
minority	(001)	0.55	1.11	0.32 (0.32)	1.79 (1.79)
$a_{fcc} = 3.61 \text{ \AA}$	(110)	0.59	1.04	0.31 (0.35)	1.89 (1.55)
Cr Fe	(111)	0.61	0.82	0.27 (0.31)	2.22 (1.84)
majority	(001)	0.64	0.82	0.11 (0.25)	7.46 (2.55)
$a_{bcc} = 2.87 \text{ \AA}$	(110)*	0.59	0.78	0.22 (0.27)	3.04 (2.18)
Cr Fe	(111)	0.61	0.41	0.34 (0.34)	0.93 (0.95)
minority	(001)	0.64	0.46	0.35 (0.35)	0.98 (0.95)
$a_{bcc} = 2.87 \text{ \AA}$	(110)*	0.59	0.40	0.32 (0.32)	1.03 (1.06)

Table 4.1: Sharvin conductances and interface transmissions in units of $10^{15} \Omega^{-1} m^{-2}$, interface resistances SR [2, 4] for ideal (and, in brackets, for disordered) interfaces in units of $10^{-15} \Omega m^2$. S is the area of the sample for which R is measured. Interface disorder was modelled in 10×10 lateral supercells with two layers of 50-50 alloy. The largest uncertainty between different configurations of disorder is about 2.3%. The values given are for a single spin. For the pairs of materials and orientations indicated by a (*), comparison of the interface resistances shown in the last two columns with experimental values extracted from measurement on multilayers by the MSU group [5, 7] yields reasonable quantitative agreement [2, 4, 12].

The interface transmission in column five of Table 4.1 is expressed as a conductance, $G_{A/B} = e^2/h \sum_{\mu\nu} T_{\mu\nu}$, where $T_{\mu\nu}$ is the probability for the incoming state ν in material A to be transmitted through the interface into the outgoing state μ in material B. For most pairs of materials¹ the orientation dependence of $G_{A/B}$ is modest ($\sim 15\%$ for Mo|W) and the interface conductance itself tends to be slightly smaller than the lower of the two Sharvin conductances. For these systems the behaviour of the transmission appears to be determined by the projection of the Fermi surfaces. However, this is not so for Al|Ag and Al|Au interfaces. Here we observe a large anisotropy in the transport properties. The factor 2 difference in transmission between (111) and (001) orientations² results in a factor 4 difference between interface resistances estimated using the method of [2, 4].

The transmission probability for the (111) and (001) orientations is plotted in Figs. 4.1c and 4.1f as a function of the wave-vector component parallel to the interface, \mathbf{k}_{\parallel} , within the 2D interface Brillouin zones (BZ). A qualitative difference between the two orientations can be observed. In the (111) case, the transmission is almost uniformly high wherever there are states on both sides of the interface. The (001) orientation exhibits more variation with high transmission in the central and outer regions of the 2D BZ but much lower in a ring-shaped region in between. The presence of this ‘‘cold ring’’ is the reason why the total transmission is lower for the (001) orientation. Explaining the transparency anisotropy of Al|Ag interfaces requires finding an explanation for the low transmission values in this region of the 2D BZ.

Two mechanisms are usually taken into account when analysing the scattering at perfect interfaces. The first, velocity mismatch, is the modulation of the transmission by a factor reminiscent of the free electron formula for the transmission through a potential step: $T = 4v_L v_R / (v_L + v_R)^2$ where $v_{L/R}$ are the components of the Fermi velocities in the transport direction on the left and right sides of the interface. This modulation is indeed present in our calculated transmissions but its effect tends to be noticeable only when one of the velocities is almost vanishingly small. Naive application of the free electron formula yields uniformly good transmission³ independent of the orientation. Symmetry mismatch, the second mechanism, can suppress the

1. Fe|Cr is an exception. For the majority spin channel, a large orientation dependence of the interface transmission is predicted. Unlike in the case of Al|Ag, this result is very sensitive to interface disorder. In addition, a single spin channel cannot be studied directly making it difficult to obtain an unambiguous experimental result.

2. We performed an extensive series of total energy calculations using LDA and GGA approximations to relax the various Al|Ag interfaces. Only a small dependence of the interface energy on the orientation was found. The transport calculations were repeated using the resulting relaxed geometries. The effect on the interface transmission is less than 3%, which is negligible on the scale of the predicted factor of 2 orientation dependence.

3. Moreover the free electron formula would lead to the violation of the unitarity of the scattering matrix (*i.e.* the conservation of particles) whenever there is more than one state on either side of the interface.

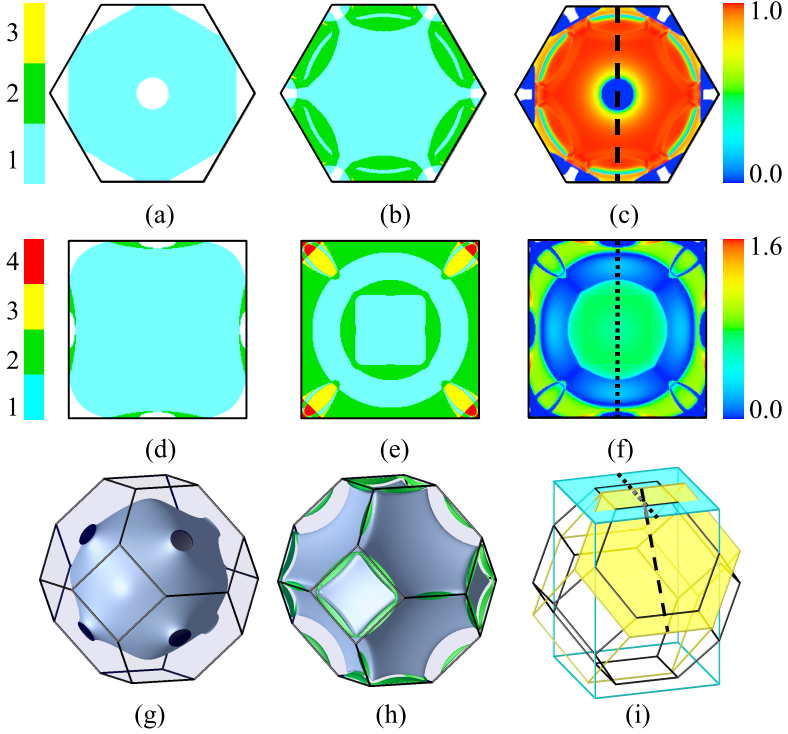


Figure 4.1: Top row: Fermi surface projections for (a) Ag, (b) Al and (c) transmission probabilities in 2DBZ for (111) orientation. Middle row: Same for (001) orientation. The colour bars on the left indicate the number of scattering states in the leads for a given two dimensional wavevector \mathbf{k}_{\parallel} . The transmission probabilities indicated by the colour bars on the right can exceed 1 for \mathbf{k}_{\parallel} s for which there is more than one scattering state in both Ag and Al. Bottom row: Fermi surfaces of (g) Ag and (h) Al, (i) the interface adapted BZ for (001) and (111) orientations. The vertical dashed line in (c) and on the yellow plane in panel (i) indicate the cross-section used in the left-hand panel of Fig. 4.2 while the vertical dotted line in (f) and on the blue plane in panel (i) indicate the cross-section used in the right-hand panel.

transmission between states of incompatible symmetries (e.g. even vs. odd etc.). Examination of the eigenvectors demonstrates that this is not the case for the Al|Ag system. For example, states on both sides of the interface, with \mathbf{k}_{\parallel} along the vertical dotted line in Fig. 4.1f, are even under reflection in the plane defined by this line and the (001) transport direction. Their orbital composition ($s, p_y, p_z, d_{yz}, d_{3z^2-r^2}, d_{x^2-y^2}$ where the y axis is parallel to the dotted line and z is the transport direction) is essentially the same for both materials. The same holds for states along other symmetry lines/planes and general \mathbf{k}_{\parallel} points (in the sense of orbital composition). The

origin of the “cold ring” must be sought elsewhere.

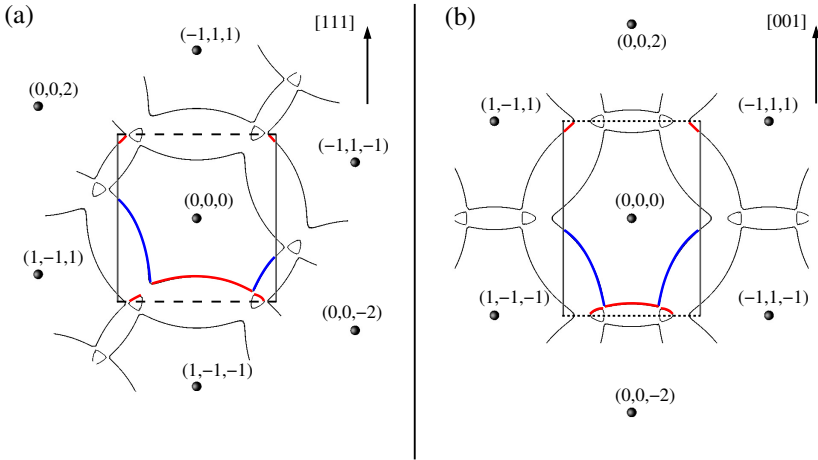


Figure 4.2: Intersection of a (110) plane with the Al Fermi surface and with the interface adapted BZs indicated in Fig. 4.1i (where the meaning of the dashed and dotted lines is explained). The labelled dots indicate the positions of the RL sites with coordinates given in units of $2\pi/a$. The red (blue) lines indicate regions of high (low) transmission.

In spite of the failure of the free electron transmission formula, this simple model serves as a useful starting point for analysing the Fermi surface (FS) topologies. In the simplest possible approach, we model the FS of Ag (shown in Fig. 4.1g) as a sphere which fits into the first BZ. A larger sphere, accommodating three electrons, is needed for trivalent Al. In an extended zone scheme, conservation of momentum parallel to the interface dictates that the transmission through a specular interface is non-zero only between states with the same values of \mathbf{k}_{\parallel} ; these are the \mathbf{k}_{\parallel} -vectors belonging to the region where projections of the Fermi spheres on a plane perpendicular to the transport direction overlap. For systems with lattice periodicity, we must use a downfolded FS, with fragments of the original FS sphere back-translated into the 1st Brillouin zone, a procedure which can be realized geometrically by placing spheres accommodating three electrons on reciprocal lattice (RL) sites and then only considering the fragments in the first BZ. Examination of the FS of Al calculated from first-principles (Fig. 4.1h) and its cross-section (Fig. 4.2) reveals that, in spite of its apparent complexity, it remains essentially (piecewise) spherical. For some values of \mathbf{k}_{\parallel} (see Figs. 4.1b and 4.1e), Al can now have more than one propagating state. Nevertheless, in the free electron limit, the downfolded states are strictly orthogonal to the states in Ag and the total transmission is unchanged. For a reduced zone scheme, we formulate the following rule: *The transmission between states in two (nearly) free*

electron materials which have the same k_{\parallel} , but originate from reciprocal lattice sites whose parallel components do not coincide, vanishes in the free electron limit and is expected to be strongly suppressed for nearly free electron like materials.

Obviously, the truly free electron system can not exhibit anisotropy. However, in the presence of the periodic potential the original, piecewise-spherical Fermi surface and consequently the transmission is going to be modified. Firstly, since the wave functions are no longer pure plane waves, the strict orthogonality of the downfolded states is relaxed and the transmission can assume finite although typically small values (hence *suppressed* instead of *zero* in the above rule). Secondly, the shape of the Fermi surface changes with the modifications being strongest in the vicinity of RL planes where, for Al, we observe the opening of gaps between previously connected fragments. The anisotropy is mostly related to this second effect.

In Fig. 4.2, we show the intersection of the Al FS with a (110) plane. The two plots are rotated so that the vertical axis in Fig. 4.2a is the [111] direction while in Fig. 4.2b it is [001]. In both cases the positions of the nearest RL sites (on which spheres are centred) are shown together with the cross-section through the relevant interface-adapted Brillouin zone, which is different for each orientation; see Fig. 4.1i. We can now readily identify spheres from which various fragments of the Fermi surface originate and mark those fragments with positive (upward) velocities, according to the rule given above, as having high (red) or low (blue) transmissions. In the (001) case, the “high” fragments originate from (0,0,0) and (0,0,-2) centred spheres. Comparing Figs. 4.1f and 4.2b, we note that the position of the gaps opened between these spheres by Bragg reflection on the (001) and (00 $\bar{1}$) planes coincides, in projection along the [001] direction, with the position of the “cold ring” in Fig. 4.1f. The other states present in this region originate from (1,-1,-1) (and equivalent) centred spheres, are therefore nearly orthogonal to states in Ag centered on (0,0,0) and so have low transmission. In the (111) case however, the large fragments of FS belonging to the same (1,-1,-1) sphere have high transmissions (Fig. 4.2a) and dominate transport. In addition, the effect of gap-opening is reduced in this orientation because of the rotation. Combination of these two factors results in the almost uniformly high transmission seen in Fig. 4.1c.

We can now finally identify the origin of the transmission anisotropy for Al|Ag interface. It stems from two factors: (i) the near orthogonality of the downfolded Al states to those belonging to the simple Ag sphere and (ii) the gaps opened in the continuous free electron Fermi surface by the periodic potential. The latter factor is of course related to the symmetry of the underlying crystal lattice and directly responsible for the introduction of the orientation dependence. For Al|Au interfaces, the interface transmissions and resistances are very similar to the Al|Ag case.

4.4 Summary

The orientation dependence of the interface transmission of six metal pairs with the same structure and lattice parameter was calculated. For *fcc* Ag|Al a factor two difference between the (111) and (001) orientations was found and explained within

the free electron model. The predicted anisotropic interface resistance and Andreev reflection (not shown) are not very sensitive to interface disorder and should be observable experimentally.

Acknowledgments: This work is part of the research program of the “Stichting voor Fundamenteel Onderzoek der Materie” (FOM) and the use of supercomputer facilities was sponsored by the “Stichting Nationale Computer Faciliteiten” (NCF), both financially supported by the “Nederlandse Organisatie voor Wetenschappelijk Onderzoek” (NWO). It is also supported by “NanoNed”, a nanotechnology programme of the Dutch Ministry of Economic Affairs. MZ wishes also to acknowledge support from KBN grant No. PBZ-KBN-044/P03-2001. We are grateful to Anton Starikov for permission to use his sparse matrix version of the TB-MTO code.

Bibliography

- [1] see the collection of articles, in *Ultrathin Magnetic Structures I-IV*, edited by J. A. C. Bland and B. Heinrich, Springer-Verlag, Berlin, 1994-2005.
- [2] K. M. Schep, J. B. A. N. van Hoof, P. J. Kelly, G. E. W. Bauer, and J. E. Inglesfield, *Phys. Rev. B* **56**, 10805 (1997).
- [3] M. D. Stiles and D. R. Penn, *Phys. Rev. B* **61**, 3200 (2000).
- [4] K. Xia *et al.*, *Phys. Rev. B* **63**, 064407 (2001).
- [5] J. Bass and W. P. Pratt Jr., *J. Magn. & Magn. Mater.* **200**, 274 (1999).
- [6] C. W. J. Beenakker, *Rev. Mod. Phys.* **69**, 731 (1997).
- [7] C. Galinon *et al.*, *Appl. Phys. Lett.* **86**, 182502 (2005).
- [8] N. W. Ashcroft and N. D. Mermin, *Solid State Physics* (Holt-Saunders International Editions, Philadelphia, 1976).
- [9] I. I. Mazin, *Phys. Rev. Lett.* **83**, 1427 (1999).
- [10] I. I. Mazin, A. A. Golubov, and B. Nadgorny, *J. Appl. Phys.* **89**, 7576 (2001).
- [11] M. Zwierzycki, K. Xia, P. J. Kelly, G. E. W. Bauer, and I. Turek, *Phys. Rev. B* **67**, 092401 (2003).
- [12] K. Xia, M. Zwierzycki, M. Talanana, P. J. Kelly, and G. E. W. Bauer, *Phys. Rev. B* **73**, 064420 (2006).
- [13] G. E. Blonder, M. Tinkham, and T. M. Klapwijk, *Phys. Rev. B* **25**, 4515 (1982).
- [14] R. J. Soulen Jr. *et al.*, *Science* **282**, 85 (1998).
- [15] S. K. Upadhyay, A. Palanisami, R. N. Louie, and R. A. Buhrman, *Phys. Rev. Lett.* **81**, 3247 (1998).
- [16] O. K. Andersen, O. Jepsen, and D. Glötzel, in *Highlights of Condensed Matter Theory*, edited by F. Bassani, F. Fumi, and M. P. Tosi, pp. 59–176, North-Holland, Amsterdam, 1985.
- [17] I. Turek, V. Drchal, J. Kudrnovský, M. Šob, and P. Weinberger, *Electronic Structure of Disordered Alloys, Surfaces and Interfaces* (Kluwer, Boston-London-Dordrecht, 1997).

Chapter 5

arameter-free study of the electronic, magnetic and transport properties of a model spin-valve transistor structure

In the operation of spin-valve transistors (SVT), use is made of the spin-dependent attenuation of hot electrons in a magnetic material - a volume effect. The downside of this attenuation is an unacceptably small collector current. Little attention has been paid in this context to spin-dependent interface scattering which, in the linear response regime, is the origin of the giant magnetoresistance effect. To gain some insight into the importance of this interface term, we have studied spin-dependent transmission through a model GaAs|Fe|Cr|Fe|GaAs (001) SVT structure as a function of energy for clean and disordered metallic interfaces using first-principles electronic structure calculations. In the absence of disorder and inelastic scattering, we find large magnetocurrents arising from materials-related symmetry incompatibilities when the transverse momentum is small as it is in GaAs, but small transfer ratios. Interface disorder at the metallic interfaces is found to reduce the magnetocurrent but increase the transfer ratio considerably.

5.1 Introduction

Where conventional electronics is based upon charge transport in semiconductors, magnetoelectronics is concerned with harnessing the extra degree of freedom provided by the electron spin to make sensors and memory elements based upon the giant magnetoresistance (GMR) and tunnel magnetoresistance (TMR) effects. The prospect of combining the advantages of conventional charge-based, semiconductor electronics with spin-based, transition metal magnetoelectronics has posed the question of how best to inject spins into semiconductors [1, 2]. A practical all-semiconductor device

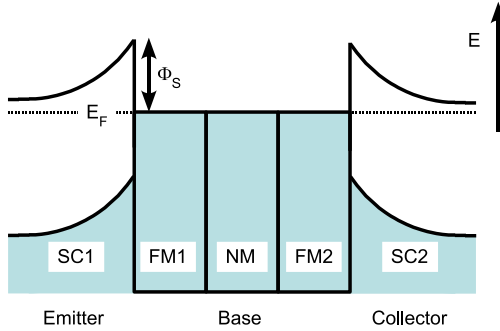


Figure 5.1: Schematic layout of a spin valve transistor. *n*-type semiconductor emitter (SC1: left) and collector (SC2: right) sandwich the metallic spin valve base (FM1|NM|FM2: middle). A Schottky barrier (SB) of height Φ_S is formed at each SC|FM interface of this three terminal device. The injection and collection of hot electrons is done across the two SBs.

would require a room temperature (RT) magnetic semiconductor but the Curie temperatures of magnetic semiconductors are at present too low [3]. GMR and TMR devices work at RT because they are based upon transition metal itinerant ferromagnets with Curie temperatures far larger than this, leading to the study of hybrid transition-metal|semiconductor devices. Whereas spin-dependent transport [4] in metallic devices is mostly studied in the linear response regime, in hybrid devices such as the spin-valve transistor (SVT) [5–7], the electrons responsible for transport are *hot electrons*, substantially above the Fermi energy. The number of experiments on hot electron transport is relatively small and correspondingly few theoretical studies have been carried out [8–11].

A three-terminal device with semiconducting (SC) emitter and collector and a layered metallic magnetic base [12], the SVT is essentially a metal-base transistor [13] with a spin valve forming the metal base; see Fig. 5.1. When a forward bias is applied between the base and the emitter, a current I_e is injected over the Schottky barrier (SB) and enters the base at energies many kT above the Fermi energy. As these hot electrons enter the base and travel through it, they undergo various “volume” and “interface”, elastic and inelastic scattering processes which change their energies as well as their momenta. They then reach the collector side of the SVT where they encounter a second SB. Electrons are only able to enter the collector and contribute to the collector current I_c if (i) they have retained sufficient energy to overcome the second SB at the collector side and (ii) they propagate in states with transverse crystal momentum \mathbf{k}_{\parallel} which matches that of states in the semiconductor collector, \mathbf{k}'_{\parallel} . All other electrons that, as a result of scattering in the base layers, have either lost too much energy or arrive with the wrong momentum will thermalize and contribute

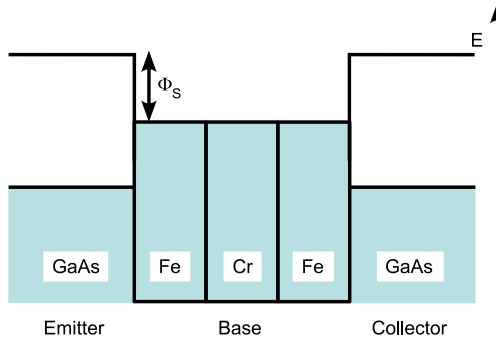


Figure 5.2: Scheme of the lattice matched GaAs|Fe|Cr|Fe|GaAs SVT studied in the present work in the flat band regime.

to the base current.

In transition-metal ferromagnets, spin-dependent scattering gives rise to a spin-dependent “volume” attenuation which is the main physical principle underlying the operation of the SVT [14]. Spin-up and spin-down electrons are scattered differently as they traverse the base and their scattering depends on the relative orientation of the magnetizations in the ferromagnetic layers which can be parallel or antiparallel (achieved experimentally by application of an external magnetic field). Because the scattering in the base is strongly spin-dependent, SVTs exhibit very large magnetocurrents (MC). Defined as the ratio of the collector currents in the parallel (P) and antiparallel (AP) magnetic configurations of the base, $MC = I_c^P / I_c^{AP} - 1$ can be as high as 400% at room temperature [15, 16]. At the same time the volume attenuation is responsible for one of the main drawbacks of the SVT: an unacceptably small “transfer ratio” α . Defined as the ratio of the collector to the emitter current, $\alpha = I_c / I_e$ is only of the order of 10^{-6} which seriously limits the applicability of the device [12].

There have been quite a number of experimental [17–23] and theoretical [24–30] studies of the elastic and inelastic scattering undergone by hot electrons in transition metals: the origin of the volume attenuation. Relatively little attention has been paid to interface effects [8] - which is somewhat surprising since spin-dependent interface scattering at the Fermi energy is what is mainly responsible for GMR and TMR. This spin-dependent interface scattering ultimately derives from the spin-dependent mismatch of transition metal electronic structures [31–35] which single-band, free-electron or tight-binding models do not describe satisfactorily. In the theoretical studies by Yamauchi and Mizushima [10] and Vlutters *et al.* [8] the electronic structures were described using such single-band models. To model results measured for a Si|Pt|Ni₈₀Fe₂₀|Au|Co|Au|Si SVT, a spin-dependent interface scattering was introduced in terms of a single parameter in Ref. [14]. In the present work we explore

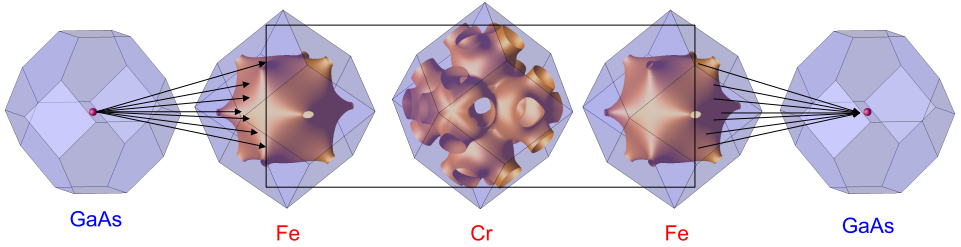


Figure 5.3: Schematic representation of the momentum bottle neck in the SVT. The surfaces of constant energies (SCE) are calculated for the materials GaAs, Fe and Cr at an energy $E = E_F + 0.790$ eV, just above the bottom of the conduction band minimum of GaAs in the flat band limit. For simplicity, only one SCE sheet is shown for the majority channel in a parallel configuration. The arrows indicate the additional channels which are opened for transport through the metallic base in the presence of disorder when transverse momentum is not conserved.

the energy- and spin-dependence of the transmission of electrons through a model GaAs|Fe|Cr|Fe|GaAs SVT structure in the flat-band limit [13]; see Fig. 5.2. We focus our attention on the influence of realistic band structures on the elastic scattering of electrons and, in particular, examine the effect of interface disorder on the so-called “momentum bottleneck” illustrated in Fig. 5.3.

For n -type GaAs, the states available to mobile charge carriers are the free-electron like conduction band states. For energies just above the bottom of its conduction band, the surfaces of constant energy (SCE) in momentum space are small spheres (Fig. 5.3, left-hand side) centred on the origin of the Brillouin zone Γ , with small values of the crystal momentum \mathbf{k} . In the metallic base, there are a number of s , d states present at the same energy, with crystal momenta throughout the Brillouin zone (BZ); the SCEs are much larger (Fig. 5.3, middle three panels) and very much more complex, which is typical of transition metal partially-filled d -bands. If the semiconductor emitter and metallic base are lattice matched and there is no disorder, then the resulting translational periodicity parallel to the interface requires that the transverse component of the crystal momentum \mathbf{k}_{\parallel} be conserved. This means that a much more limited set of states - those with matching transverse momentum - is available to the electrons coming from the emitter. The same condition holds at each interface in the base until the electron comes to the collector where it must again have the correct - small - transverse momentum to enter the collector (Fig. 5.3, right-hand side). In an ideal crystalline SVT in the absence of disorder, electrons injected from the emitter pass through the device into the collector without being scattered; their transverse momentum is conserved at each interface, $\mathbf{k}_{\parallel} = \mathbf{k}'_{\parallel}$.

In the presence of disorder, or when the SVT is made of materials with incommensurate lattice parameters, translational symmetry parallel to the interface is broken

and the transverse momentum need no longer be conserved. This opens up more channels for conduction in the metallic base. Nevertheless, only states with small transverse momenta can enter the collector because for energies just above the bottom of the SC conduction band, only such states exist: this is the momentum bottleneck. It is not a priori clear whether breaking of translational symmetry is more or less favourable for the operation of SVTs and difficult to derive insights from oversimplified models of the metallic band structures.

The object of this paper is to construct a “semirealistic” model SVT and use it to investigate the type of band structure effects which might be found with transition metals. We have chosen the GaAs|Fe|Cr|Fe|GaAs system for our study because the lattice constants of cubic Fe, Cr and GaAs are the same to better than 2%: epitaxial Fe|Cr multilayers are prepared routinely, Fe can be grown epitaxially on GaAs, so such a SVT structure could in principle be made. It is also essential to have lattice matching to perform detailed electronic structure calculations using existing methods [35].

The calculation of the transmission through the SVT device is done in a two-step procedure. In the first step (Sec. 5.2), the electronic structure and magnetic properties (potentials and spin densities) are determined self-consistently for the electronic ground state using a tight-binding [36–38] linearized muffin-tin orbital [39] (TB–LMTO) surface Green’s function (SGF) method [40]. Substitutional disorder is handled using the coherent potential approximation (CPA) [41], also self-consistently. In the second step (Sec. 5.3), the potentials are used as inputs to calculate energy dependent transmission matrices using a TB–MTO wave-function matching scheme (WFM) and modelling substitutional disorder at the interfaces by means of large lateral supercells [34, 35]. The results are discussed and some conclusions drawn in Sec. 5.4. Some technical aspects of calculating the band structure of zinc-blende GaAs using the LMTO-ASA method are given in Appendix B.1.

5.2 Ground State Calculations

After a brief description of the SVT structure, a number of technical details of the method used for the self-consistent electronic structure calculations are given in Sec. 5.2.1. The calculated electronic and magnetic properties of the SVT are described and discussed in Sec. 5.2.2.

For the reasons outlined in the Introduction, the SVT structure we have chosen to investigate is an ideal, lattice-matched AsGa|Fe|Cr|Fe|GaAs (001) heterostructure with Ga terminated interfaces [42–44]; see Fig. 5.2. The lattice constant of GaAs, $a_{\text{GaAs}} = 5.654 \text{ \AA}$, is almost twice that of bcc Fe, $a_{\text{Fe}} = 2.871 \text{ \AA}$. We assume that bcc Fe grows epitaxially on top of zinc-blende (zb) GaAs adopting its lattice parameter and we neglect the small lattice mismatch of 1.6 %. The separation between the Fe and GaAs planes forming the interface is determined by conserving the volume of the individual atoms. For the metallic base, unless stated otherwise, the following thicknesses in monolayers (ML) of Fe and Cr was used: GaAs|Fe(10 ML)|Cr(10 ML)|Fe(11 ML)|GaAs (001); one 11 ML thick layer was used to facilitate having a

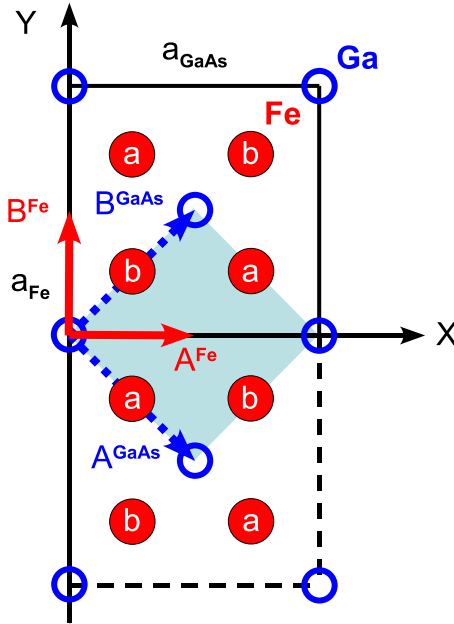


Figure 5.4: Illustration of the relationship between the GaAs fcc and Fe bcc lattices with lattice constants a_{GaAs} and a_{Fe} respectively. $(A^{\text{Fe}}, B^{\text{Fe}})$ and $(A^{\text{GaAs}}, B^{\text{GaAs}})$ describe the 2D translation symmetry of ideal Fe and GaAs (001) surfaces, respectively. The Ga atoms in the top layer of GaAs are shown as small blue circles, the first layer of Fe atoms as larger filled red circles. The interface unit cell shown shaded contains one Ga atom and two inequivalent Fe atoms.

Ga termination on each side of the device.

5.2.1 Method

The starting point for the transmission calculations is a potential profile for the SVT which is calculated self-consistently within the framework of the local spin density approximation (LSDA) of density functional theory (DFT) valid for describing ground state properties such as charge and spin distributions. Throughout this study the exchange and correlation potentials we use are those calculated by Ceperley and Alder (CA) [45] and parametrized by Perdew and Zunger (PZ) [46].

To solve the Kohn-Sham (KS) equations of DFT, the wave functions are expanded in a minimal basis set (*spd*) of TB-LMTOs: tight-binding [36–38] linearized muffin-tin orbitals [39]. Since the atomic spheres approximation (ASA) [39] used for the potential works very well for close-packed solids, we adopt the usual procedure [47]

of introducing additional “empty spheres” at the tetrahedral interstitial positions in the zb structure, *i.e.* atomic spheres without nuclear charge, effectively converting the open diamond structure into a close-packed one where every sphere has eightfold coordination. Besides Ga and As atoms at $(0, 0, 0)$ and $(\frac{1}{4}, \frac{1}{4}, \frac{1}{4})$, the unit cell of GaAs then contains two types of empty spheres, E_1 and E_2 at $(\frac{1}{2}, \frac{1}{2}, \frac{1}{2})$ and $(\frac{3}{4}, \frac{3}{4}, \frac{3}{4})$ positions, respectively, all in units of $a_{\text{GaAs}} = 5.654 \text{ \AA}$. In our calculations we use the lattice constant of bulk GaAs corresponding to a Wigner-Seitz atomic sphere radius for Fe of 2.6304 a.u. For simplicity, equal sphere sizes are used for Ga, As, E_1 and E_2 ; more details are given in Appendix B.1.

The SVT structure sketched in Fig. 5.2 does not have translational periodicity in the transport direction. To calculate its electronic structure and magnetic properties (potentials and spin densities) self-consistently, the (scalar-relativistic) surface Green’s function technique (SGF) [40] was used. The in-principle infinite Hamiltonian describing the open system can be reduced to finite size if the Hamiltonian can be expressed in real space in block tridiagonal form. In that case the semiinfinite leads can be transformed away to appear as energy-dependent embedding potentials or self-energies sited on the boundary layers. The size of the blocks which are called “principal layers” (PL) is determined by the range of the physical interaction and by the range of the basis functions used to express the Hamiltonian in matrix form. By using TB-LMTOs the size of the principal layers is minimized. Their range is such that for a (001) orientation interface, the PL is two MLs thick. In the semiconductor, one of these layers contains Ga atoms (and an empty sphere) while the other layer contains As atoms (and an empty sphere). The translational periodicity parallel to the interface is such that the 2D interface unit cell contains four atoms: Ga, E_1 , As and E_2 ; see Fig. 5.4. On the metal side, each ML contains two inequivalent Fe (or Cr) atoms (which we label a and b). In the following, we used an angular momentum cutoff of $\ell_{\text{max}} = 2$ (*spd* basis) combined with the ASA. Disorder was modelled using a version of the coherent potential approximation [41] (CPA) suitable for layered structures [40].

5.2.2 Electronic Structure

We begin with a brief description of those aspects of the electronic structure which will be needed to understand the energy dependent transmission in Sec. 5.3.

Bulk band structures of GaAs, Fe and Cr

DFT is designed to describe ground state properties such as charge and spin densities and does so remarkably well. The Kohn-Sham eigenvalues are also known to give a good description of the experimental single particle eigenvalue spectrum in most respects. One well-documented deficiency is the failure to reproduce the single particle gap of even weakly correlated semiconductors and insulators that is systematically and seriously underestimated by the LDA [48]. The experimental band gap of zb GaAs is 1.52 eV [13] while that obtained using the LDA, and the TB-LMTO-ASA method as implemented in Ref. [40] is only 0.59 eV. We corrected the band gap of

GaAs using a self-consistent “scissor-operator”-type correction term as follows. For bulk GaAs, an attractive constant term was added to the potential inside the As atomic sphere and the KS equations iterated to self-consistency. This procedure was carried out for different values of the constant until a value was found which reproduced the experimental band gap. The resulting band structure is plotted in Fig. 5.5c in the k_z direction for the point $\mathbf{k}_{\parallel} = 0$, i.e., the Γ –X direction for bulk GaAs or the point $\bar{\Gamma}$ in the two-dimensional BZ (2DBZ). In the (001) direction, the lowest conduction band of GaAs with Δ_1^{zb} symmetry transforms according to the fully symmetric irreducible representation of the symmetry group of the zb structure in this direction, C_{2v} .

The in-plane periodicity and thus the common two-dimensional unit cell and Brillouin zone are determined by the semiconductor since one zb GaAs lattice constant is set to match two of bcc Fe (Fig. 5.4). For ferromagnetic bcc Fe, the bulk band structure in the k_z direction for $\mathbf{k}_{\parallel} = 0$ is shown in Fig. 5.5(a) for the majority spin and in Fig. 5.5(b) for the minority spin channel. For non-magnetic bcc Cr, the corresponding bands are shown in Fig. 5.5(d). The relationship between the GaAs zb and Fe or Cr bcc lattice constants is such that at $\mathbf{k}_{\parallel} = 0$ we find not only Fe and Cr bands from the bulk Γ –H direction (full lines) but, in addition, bands downfolded from the bulk N–P–N direction (dashed lines). In this way the number of Fe and Cr bands at $\bar{\Gamma}$ is doubled. Though the GaAs|Fe (001) interface has the C_{2v} reduced point group symmetry (which is also the symmetry of the complete SVT), to avoid confusion with the literature the Fe and Cr bands in Fig. 5.5 are labelled according to the space group symmetry of the bulk lattice: $\Delta_{1,2,2',5}$ irreducible representations along the Γ –H direction and $D_{1,2,3,4}$ irreducible representation along the N–P–N (D) direction. The GaAs bands in Fig. 5.5c are aligned (see below) with the joint Fe|Cr|Fe Fermi energy so that the Fe|GaAs SB height is in agreement with experiment.

Interfaces

In principle we could simply perform a self-consistent calculation for the full GaAs|Fe|Cr|Fe|GaAs SVT to determine its potential and spin profile. In practice, it turns out to be more efficient for such a large system to make use of the near perfect screening of 10 MLs of metal to factor self-consistency for the full SVT into that of GaAs|Fe and Fe|Cr|Fe subsystems which are first solved separately. For sufficiently thick Fe, the spin-densities in Fe far from the interfaces will be identical and equal to the bulk spin-density. The separate atomic sphere spin and charge densities can then be patched together to construct a starting spin-density for the full system which converges rapidly. Using 10-11 ML thick metallic layers, this procedure will be useful if the spin and charge density in the fifth and sixth layers of Fe do not differ much in the subsystem calculations.

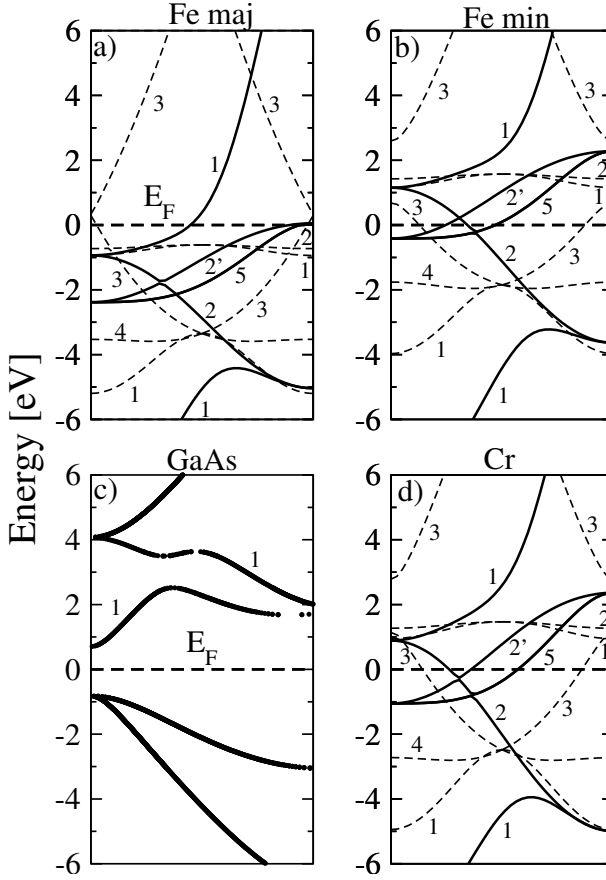


Figure 5.5: Energy band structures along (001) at $\bar{\Gamma}$ point of (a) Fe majority spin states, (b) minority spin states, (c) GaAs and (d) Cr. The Fermi energy is shown by a horizontal dashed line. The numbers denote the symmetries of the bands along the Δ direction ($\Gamma - H$) (solid lines) and the D direction ($N - P - N$) (dashed lines) [49] (a,b,d) for a bcc crystal structure. In (c) the bands are plotted along the Δ direction ($\Gamma - X$) for the zb structure.

We begin by determining self-consistently the potential profile of the Fe|GaAs interface using a Ga-terminated AsGa|Fe (001) interface [42]. The region where it differs from the bulk values is determined empirically by systematically increasing the number of layers of “interface” Fe and GaAs whose spin and charge densities are iterated to self-consistency sandwiched between “bulk” Fe and GaAs. These are allowed to vary in n_{Ga} and n_{As} layers of $(\text{Ga} + E_1)$ and $(\text{As} + E_2)$, and n_{Fe} layers of Fe bounding the interface. In practice, values of $n_{\text{Ga}} + n_{\text{As}} = 6, 8, 10, 16, 20, 30$ MLs of GaAs in contact with Fe and $n_{\text{Fe}} = 8$ MLs of Fe in contact with GaAs were tested. The magnetic profile of Fe|GaAs is given in Table 5.1. Five MLs from the interface

Fe GaAs		Fe Cr				
Layer	clean	Layer	P		AP	
			clean	dirty	clean	dirty
$m_{\text{Fe}}(\text{bulk})$	2.155	$m_{\text{Fe}}(\text{bulk})$	2.155	2.155	2.155	2.155
$m_{\text{Fe}}(\text{int-6b})$	2.148					
$m_{\text{Fe}}(\text{int-6a})$	2.136	$m_{\text{Fe}}(\text{int-10})$	2.155	2.153	2.154	2.153
$m_{\text{Fe}}(\text{int-5b})$	2.146	$m_{\text{Fe}}(\text{int-9})$	2.148	2.151	2.148	2.151
$m_{\text{Fe}}(\text{int-5a})$	2.185	$m_{\text{Fe}}(\text{int-8})$	2.152	2.150	2.152	2.148
$m_{\text{Fe}}(\text{int-4b})$	2.136	$m_{\text{Fe}}(\text{int-7})$	2.149	2.158	2.146	2.160
$m_{\text{Fe}}(\text{int-4a})$	2.115	$m_{\text{Fe}}(\text{int-6})$	2.165	2.149	2.170	2.147
$m_{\text{Fe}}(\text{int-3b})$	2.193	$m_{\text{Fe}}(\text{int-5})$	2.143	2.175	2.139	2.177
$m_{\text{Fe}}(\text{int-3a})$	2.182	$m_{\text{Fe}}(\text{int-4})$	2.196	2.187	2.196	2.189
$m_{\text{Fe}}(\text{int-2b})$	2.232	$m_{\text{Fe}}(\text{int-3})$	2.206	2.281	2.206	2.280
$m_{\text{Fe}}(\text{int-2a})$	2.203	$m_{\text{Fe}}(\text{int-2})$	2.315	2.034	2.319	2.038
$m_{\text{Fe}}(\text{int-1b})$	1.657	$m_{\text{Fe}}(\text{int-1})$	1.819	2.139	1.849	2.134
$m_{\text{Fe}}(\text{int-1a})$	1.976	$m_{\text{Cr}}(\text{int-1})$		-0.337		-0.361
$m_{\text{Ga}}(\text{int+1})$	-0.016	$m_{\text{Fe}}(\text{int+1})$		1.752		1.773
$m_{\text{As}}(\text{int+2})$	0.042	$m_{\text{Cr}}(\text{int+1})$	-0.139	0.009	-0.189	0.042
$m_{\text{Ga}}(\text{int+3})$	0.006	$m_{\text{Cr}}(\text{int+2})$	0.059	0.044	0.130	-0.002
$m_{\text{As}}(\text{int+4})$	0.004	$m_{\text{Cr}}(\text{int+3})$	-0.056	-0.006	-0.138	0.048
$m_{\text{Ga}}(\text{int+5})$	0.001	$m_{\text{Cr}}(\text{int+4})$	0.032	0.004	0.150	-0.062
$m_{\text{As}}(\text{int+6})$	0.001	$m_{\text{Cr}}(\text{int+5})$	-0.023	0.000	-0.149	0.069
$m_{\text{Ga}}(\text{int+7})$	0.000	$m_{\text{Cr}}(\text{bulk})$	0.000	0.000	0.000	0.000
$m_{\text{As}}(\text{int+8})$	0.000					
$m_{\text{Ga}}(\text{bulk})$	0.000					
$m_{\text{As}}(\text{bulk})$	0.000					

Table 5.1: Layer resolved magnetic moments (in Bohr magnetons) for an Fe|GaAs interface and an Fe|Cr|Fe (001) trilayer. The 2DBZ integration was carried out with $48 \times 48 = 2304$ and $60 \times 60 = 3600$ k_{\parallel} -mesh points in the full 2DBZ corresponding to the 1×1 interface unit cells for Fe|GaAs and Fe|Cr|Fe (001), respectively. The magnetic moments contained in the empty spheres are not reported in this table, their values at the interface are less than $0.009 \mu_B$ and decrease to zero well before the last GaAs layer considered. Each layer in the Fe half-space in Fe|GaAs (001) slab contains 2 inequivalent atoms (a,b). Only the moments of half the slab of Fe|Cr|Fe (001) are shown here. The other half can be obtained from the symmetry (antisymmetry) of the P (AP) configuration. The “dirty” interfaces Fe|Cr are modelled by two MLs of 50%-50% alloy.

the average magnetic moment per Fe is $(2.146 + 2.185)/2 = 2.166 \mu_B$ and 6 MLs away it is $(2.148 + 2.136)/2 = 2.142 \mu_B$ compared to a calculated bulk value of $2.155 \mu_B$; the average moment over layers 5 and 6 is equal to the bulk value but there is still an oscillation of amplitude $0.01 \mu_B$. At the interfaces with GaAs, Fe displays a reduced average magnetic moment of $(1.657 + 1.976)/2 = 1.817 \mu_B/\text{atom}$. On the GaAs side,

only very small moments of $-0.016\mu_B$ and $0.042\mu_B$ are induced on the closest Ga and As atoms, respectively and the spin-density decays to a negligible values 6 MLs from the interface. The potential 16 MLs from the interface yields a band structure indistinguishable from the bulk band structure (Fig. 5.5c). In the rest of our study 16 MLs of GaAs in the (001) direction will be treated as “interface” layers in which the potential is allowed to deviate from that of bulk GaAs and is calculated self consistently.

In order to reproduce the experimentally known SB height, $\Phi_S = 0.7$ eV [50, 51], a procedure analogous to that used to obtain the experimental band gap for bulk GaAs was used: a constant term was added to the potentials inside the Ga, As, E_1 and E_2 atomic spheres and the potential profile iterated to self-consistency. The SB height for this potential profile was then determined and the whole procedure repeated with a different constant term until a value was found which yielded the desired value of $\Phi_S = 0.7$ eV.

The next step is to calculate the electronic and magnetic properties of a Fe(10ML)|Cr(10ML)|Fe(11ML) (001) trilayer sandwiched by bulk Fe for P and AP configurations of the bulk Fe layers. The magnetization profiles are symmetric (P) or antisymmetric (AP) with respect to inversion about the inversion centre in the middle of the Cr layer so only the independent half of the layer-resolved magnetic moments are given in Table 5.1. The magnetic moment of bulk Fe with our choice of lattice constant, exchange-correlation potential etc. is $2.155\mu_B$. This value is only attained ~ 10 MLs away from the Fe|Cr interface but the average moments from layers 5 and 6 are $(2.143 + 2.165)/2 = 2.154\mu_B$ and $(2.139 + 2.170)/2 = 2.155\mu_B$ for the P and AP configurations, respectively i.e. this far from the interface the Fe moment is oscillating by only $\pm 0.01\mu_B$. At the Fe|Cr interface the Fe moment is reduced to 1.819 (P) and 1.849 (AP). A moment is induced in Cr antiparallel to the Fe moment. Bulk bcc Cr in the LSDA orders antiferromagnetically (AF) but the size of the moment depends very sensitively on the details of the calculation: the volume chosen, exchange-correlation potential etc. We see this AF ordering in the change of sign of the Cr moment from layer to layer. For the P configuration and 10 MLs of Cr, this oscillation is incompatible with the magnetism of the bounding Fe layers and the Cr magnetic moment decays quite fast. For the AP configuration no such frustration occurs and the Cr moment does not decay but its value is still quite small, of order $0.15\mu_B$.

The results reported above were for ideal ordered interfaces. We model disorder (restricted to the Fe|Cr interface) by considering two “dirty” MLs of alloy where the concentration of each species is 50%. The magnetic moments at the interfaces are slightly modified for both Fe and Cr (“dirty” column in Table 5.1). For the alloy ML in direct contact with Fe, the Fe and Cr atoms have magnetic moments of 2.139 (2.134) μ_B /atom and -0.337 (-0.361) μ_B /atom, respectively for P (AP) configurations. For the alloy ML in direct contact with Cr the corresponding moments are 1.752 (1.773) μ_B /atom for Fe and 0.009 (0.042) μ_B /atom for Cr in P(AP) configuration, respectively. The alloy Fe moments are aligned with the moments in the Fe layer while the Cr moments are antialigned. The resulting “frustration” leads to a quenching of the moments in the Cr in both cases.

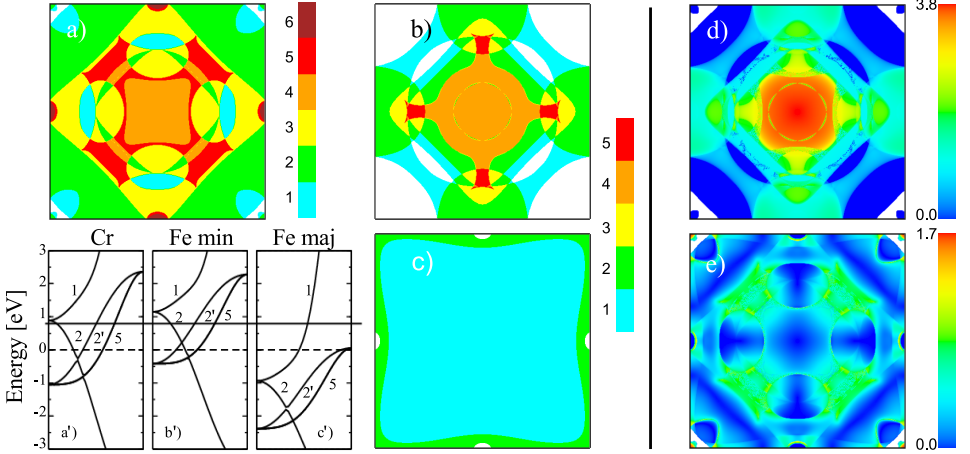


Figure 5.6: Projections of surfaces of constant energy $E = E_F + 0.790$ eV onto a plane perpendicular to the transport direction for Cr (a), Fe minority (b) and Fe majority (c). Transmission probabilities $T^\sigma(E = E_F + 0.790, \mathbf{k}_\parallel)$ through the Cr|Fe (001) interface are shown in figures (d) and (e) for minority and majority electrons, respectively. These calculations were carried out for a 1×1 interface unit cell. The corresponding “simplified” bulk band structures of Cr (a’), Fe minority (b’) and Fe majority (c’), respectively, plotted along the Δ direction ($\Gamma - H$) are shown in the bottom left-hand panel where the dashed horizontal line denotes the Fermi energy and the full horizontal line the energy $E = E_F + 0.790$ eV.

Finally, the AS potentials, charge and spin densities calculated above are used as inputs to a calculation for the full GaAs|Fe(10 ML)|Cr(10 ML)|Fe(11 ML)|GaAs structure which converges rapidly and yields a magnetization profile which does not differ appreciably from that just described. The second step of our two step procedure is to use these potentials as inputs to calculate energy dependent transmission matrices. The results of these calculations are presented in the next section.

5.3 Transmission Calculations

The transport of hot electrons in the SVT is formulated quantum mechanically as a scattering problem. We calculate the normalized transmission probability through the device at a fixed energy E

$$\tilde{T}^\sigma(E) = \frac{1}{T_{Sh}^\sigma(E)} \sum_{\mu, \nu, \mathbf{k}_\parallel} |t_{\mu\nu}^\sigma(E, \mathbf{k}_\parallel)|^2 \quad (5.1)$$

where σ is the spin index, $\sigma = \uparrow, \downarrow$ (or *maj*, *min*). $t(E, \mathbf{k}_\parallel)$ is a matrix of transmission coefficients calculated at energy E using a wave-function matching[52, 53] scheme[34,

35] based on the TB-MTO method and ν and μ denote incoming and transmitted Bloch waves, respectively. Close to the bottom of the conduction band, the surfaces of constant energy are very small on a scale of π/a and only a very small number of states in the semiconductor emitter and collector contribute to the transmission. To factor out this effect as we increase the energy, the total transmission is renormalized with the number of conduction channels available in the semiconductor at energy E . This is just the Sharvin transmission $T_{Sh}^\sigma(E)$ of the semi-infinite leads with $T_{Sh}^\uparrow(E) = T_{Sh}^\downarrow(E)$.

Before discussing the transport in the SVT it is useful to examine the most important features of the ideal Cr|Fe (001) interface transmission when there is only one metal atom per ML, without the downfolding of the bands seen in Figs. 5.5(a,b,d). Two-dimensional projections of the surfaces of constant energy are shown for a non-magnetic Cr lead in Fig. 5.6(a), and for the minority and majority spins of a ferromagnetic Fe lead at $E - E_F = 0.790$ eV in Figs. 5.6(b) and (c), respectively. This energy is just above the bottom of the GaAs conduction band in the flat band limit; it is indicated by the full horizontal line in the bottom left-hand panel of Fig. 5.6 where the bands for the 1×1 interface unit cell are shown. The dispersion of the Fe majority-spin band at this energy is very free-electron-like, Fig. 5.6(c'), leading to a simple SCE, shown in Fig. 5.3, with a single conduction channel for all \mathbf{k}_\parallel except at the zone boundaries where there are two. Fig. 5.6(b') shows that this energy intersects a number of Fe minority-spin *sd* bands, leading to a very complicated SCE; from Fig. 5.6(b) as many as 5 propagating states are seen to occur for a given \mathbf{k}_\parallel . The same is true of Cr whose SCE is shown explicitly in Fig. 5.3; its projection in Fig. 5.6(a) exhibits as many as 6 propagating states. For an ideal Cr|Fe interface the transverse momentum is conserved and the transmission probability $T^\sigma(E, \mathbf{k}_\parallel)$ at this energy is shown in Figs. 5.6(d) and (e) for minority and majority spins respectively. For some \mathbf{k}_\parallel with N_{Cr} propagating states on one side and N_{Fe} on the other, the maximum transmission is $\min(N_{Cr}, N_{Fe})$. The maximum transmission in Figs. 5.6(d) is found by inspection to be about 3.8 over a large region around $\bar{\Gamma}$, the centre of the 2DBZ and very close to the maximum possible with 4 propagating states on either side of the interface. Summation over all \mathbf{k}_\parallel in the 2DBZ results in an integrated value of 1.2. In the majority spin case, the states on either side of the interface have very different orbital character and the transmission is overall quite low. In particular, it essentially vanishes in the region about $\bar{\Gamma}$. Only in the very corners of the 2DBZ where there are 2 Cr propagating states does the maximum transmission reach a value of ~ 1.7 . The integrated value is only 0.3, a factor of four lower than that for the minority spin channel.

The very different behaviour close to $\bar{\Gamma}$ for the majority and minority spin channels will be of particular importance for understanding the transmission through the complete SVT because the propagating states in GaAs are to be found in this region of momentum space. For energies just above the bottom of the conduction band, the surfaces of constant energy in GaAs are essentially spheres centred on Γ whose projections are circles with area proportional to $2m_c^*(E - E_c)/\hbar^2$. Here E_c is the bottom of the conduction band with Δ_1^{zb} symmetry and m_c^* its effective mass.

The summation over \mathbf{k}_\parallel in Eq.(5.1) requires some care. For energies very close

to the bottom of the conduction band at $E - E_F = 0.7$, we need a dense mesh of sampling points about $\bar{\Gamma}$. As we go higher in energy a bigger region of momentum space must be sampled, but a less dense mesh is required. In the calculations to be discussed below, we used an energy step of 0.045 eV and sampling densities ranging from the equivalent of 2048×2048 in the full 2DBZ of a (1×1) interface unit cell for low energies decreasing to 512×512 for higher energies. This is sufficient to yield integrated transmission probabilities which are converged to better than 2%

The TB-MTO basis allows us to model disorder[34, 35, 54] without compromising the description of the transition metal band structure. To model interface disorder at the Fe|Cr interfaces, 4×4 lateral supercells containing 16 Ga (or As) atoms and 16 empty spheres in each layer of GaAs and 32 atoms in each layer of Fe or Cr in the metal base were used. This corresponds to a scattering region containing approximately 1500 atoms.

5.3.1 Defect-free Interfaces

We begin our study of the transmission through the complete SVT structure by considering ideal, defect-free interfaces for which \mathbf{k}_{\parallel} is conserved. $T^{\sigma}(E)$ is shown in Fig. 5.7 for P and AP aligned Fe layers. For the parallel configuration, the transmission exhibits a large spin asymmetry, especially at lower energies where the minority channel is dominant; in the range $E - E_F = 0.7 - 1.0$ eV, T^{min} is about 2 to 4 orders of magnitude larger than T^{maj} . This is curious because it is exactly the opposite of what is observed in spin-injection studies through Fe|GaAs [43, 44] or Fe|InAs [54] interfaces where the majority channel is dominant. In the energy range up to 1 eV, we find a transmission polarization, defined as $(T^{maj} - T^{min})/(T^{maj} + T^{min})$, which is negative and as high as -99 %; see Table 5.2. With increasing energy, this value starts decreasing slowly and changes sign at about 1.15 eV. We will see below that the increase in T^{maj} is due to the occurrence, at about 0.92 eV above E_F , of Cr bands with the same Δ_1 symmetry as the majority spin Fe electrons. The trends seen in Fig. 5.7(a), the large spin asymmetry, its sign and decrease with increasing energy can all be qualitatively understood in terms of the symmetry of the bulk band structures of GaAs, Fe and Cr shown in Fig. 5.5.

For the energy $E = E_F + 0.790$ eV, slightly above the bottom of the GaAs conduction band, the transmission probabilities for majority and minority spin channels in the P configuration are plotted as a function of \mathbf{k}_{\parallel} in Fig. 5.8. For the majority spin channel, the transmission is seen to be a smooth function of \mathbf{k}_{\parallel} but is very small with a maximum value less than 10^{-5} . This value is about 5 orders of magnitude smaller than the maximum value found for the minority spin transmission which by contrast, has a singular, spiky behaviour as a function of \mathbf{k}_{\parallel} . A very fine mesh of sampling points is required to converge the 2DBZ summation to determine the total transmission (Fig. 5.9).

For energies close to the bottom of the GaAs conduction band, transmission is restricted to a very small number of channels close to $\bar{\Gamma}$. Precisely at $\bar{\Gamma}$, the eigenstates

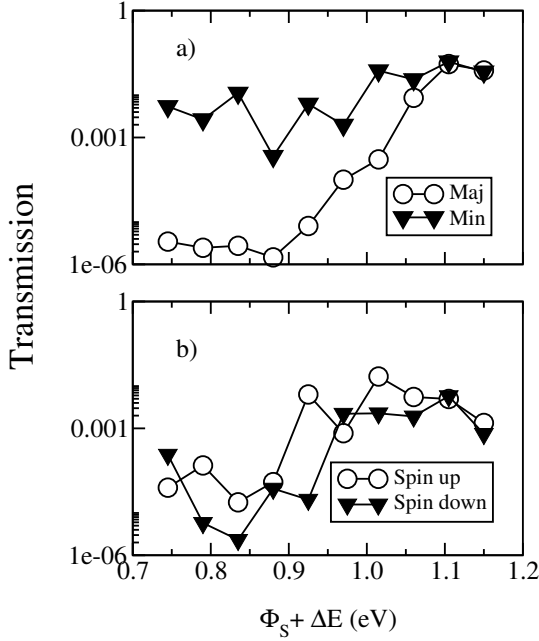


Figure 5.7: *Transmissions of (a) P and (b) AP configuration in the SVT as a function of the energy above $E_F + \Phi_S$ for majority (\circ) and minority (\blacktriangledown) spins. Φ_S , equal to 0.7 eV [50, 51], is the height of the Schottky barrier. The values reported here are normalized to the so-called Sharvin transmissions of GaAs.*

of the SVT transform according to the irreducible representations of the point group of $\bar{\Gamma}$, which is C_{2v} and can be formed from states with the corresponding symmetries in the individual materials whereby it should be noted that the symmetry labels at $\bar{\Gamma}$ for Fe and Cr refer to the C_{4v} point group but in GaAs to the C_{2v} point group. The states at $\bar{\Gamma}$ in GaAs transform according to the Δ_1^b irreducible representation of the C_{2v} point group. At the interface with Fe, they can match [43, 44, 54] to states in Fe which transform according to the Δ_1 and Δ_2' irreducible representations of the C_{4v} point group. Therefore we begin with an analysis of what happens at the $\bar{\Gamma}$ point.

For the Fe majority spin channel, there are states with Δ_1 and D_3 symmetry at $\bar{\Gamma}$ (Fig. 5.5) but only the former couple to the Δ_1^b states. $T_{\text{GaAs,Fe}}^{maj}$ (the spin-dependent transmission probability from GaAs in to Fe) decreases slowly from a large value of ~ 0.5 at $\bar{\Gamma}$. In Cr, there are no states with Δ_1 symmetry at this energy and the transmission from the left Fe slab to the right Fe slab through Cr might be expected to vanish at $\bar{\Gamma}$. However, this reasoning only considers coupling to propagating states in Cr which is only strictly correct for infinitely thick Cr. For a finite layer of Cr, evanescent states with the appropriate symmetry make a

Energy (eV)	α^*	MT (%)	Pol(%)
0.745	5.45×10^{-3}	1800	-99
0.790	2.65×10^{-3}	1800	-99
0.835	11.30×10^{-3}	56000	-99
0.880	0.35×10^{-3}	300	-99
0.925	6.20×10^{-3}	2	-99
0.970	2.10×10^{-3}	30	-90
1.015	38.35×10^{-2}	100	-98

Table 5.2: Energy dependence of the “transfer factor”, $\alpha^*(E) = T_P^{maj}(E) + T_P^{min}(E) \equiv T_P(E)$, the “magnetotransmission” $MT(E) = T_P(E)/T_{AP}(E) - 1$ and the polarization (for the P configuration) in the energy range 0.745 – 1.015 eV for clean interfaces.

tiny but non-zero contribution to the transmission so that at $\bar{\Gamma}$, $T_{\text{Fe,Fe}}^{maj} \sim 10^{-7}$. The evaluation of the product ($T_{\text{GaAs,GaAs}}^\sigma \approx T_{\text{GaAs,Fe}}^\sigma T_{\text{Fe,Fe}}^\sigma T_{\text{Fe,GaAs}}^\sigma$) yields $T_{\text{GaAs,GaAs}}^{maj} \sim 0.25 \times 10^{-7}$ (the spin-dependent transmission probability from Fe through Cr into Fe). This underestimates quite considerably the “exact” value found in Fig. 5.8 of 10^{-6} .

What we have neglected is the possibility of multiple reflections at the partially reflecting, transverse-momentum conserving interfaces. We can make a simple estimate of the maximum size of the enhancement possible if we assume that all the phase factors conspire to give constructive interference [44]. If we do this, we find that

$$t_{\text{GaAs,GaAs}} \approx \frac{t_{\text{GaAs,Fe}} t_{\text{Fe,Fe}} t_{\text{Fe,GaAs}}}{(1 - |r_{\text{GaAs,Fe}}| |r_{\text{Fe,Fe}}|)(1 - |r_{\text{Fe,Fe}}| |r_{\text{Fe,GaAs}}|)} \quad (5.2)$$

(up to a phase factor). Evaluating this expression with the same transmission probabilities used above leads to $T_{\text{GaAs,GaAs}}^{maj} \sim 3 \times 10^{-6}$, confirming that multiple reflections can indeed not be neglected.

In the minority spin channel case, states in the energy region of interest with d_{xy} orbital character which transform according to the Δ_2' irreducible representation on Fe atoms, can couple to the Δ_1^{zb} states. The x and y directions are indicated in Fig. 5.4. Because these orbitals are in-plane, their coupling to the GaAs states is expected to be much weaker compared with that of the Fe Δ_1 majority spin states and indeed, at $\bar{\Gamma}$ and at $E = E_F + 0.790$ eV, $T_{\text{GaAs,Fe}}^{min} \sim 10^{-2}$. The Fe Δ_2 states with $d_{x^2-y^2}$ character, Δ_5 states with p_x , p_y , d_{xz} or d_{yz} character, and the downfolded $D_{1,2,3}$ states can also not couple to Δ_1^{zb} so their contribution to the transmission through the single GaAs|Fe interface is zero. At the Fe|Cr interface, these Δ_2' minority states are perfectly transmitted, $T_{\text{Fe,Fe}}^{min} \sim 1$. This is not surprising since the minority spin band structure of Fe matches that of Cr very well. Evaluating

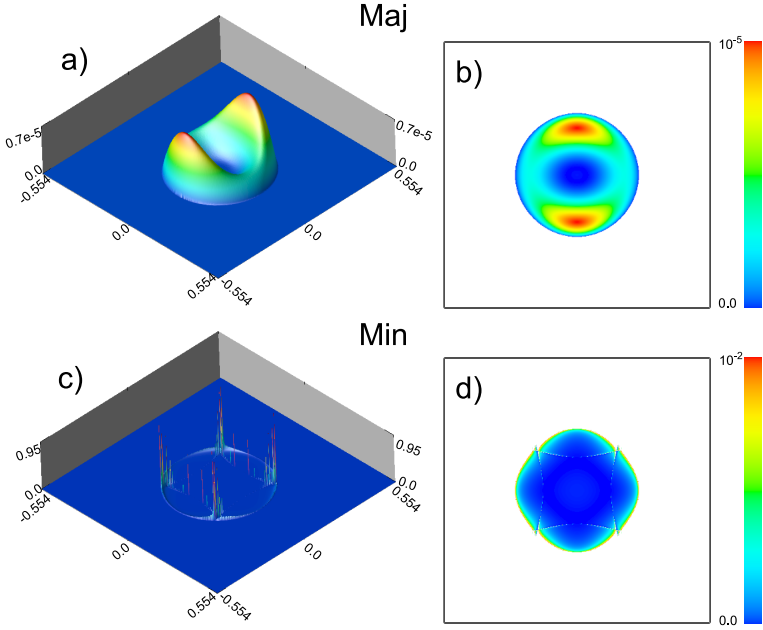


Figure 5.8: Transmission probabilities through the SVT as a function of \mathbf{k}_{\parallel} for Ga-termination and sharp metallic Fe|Cr interfaces. The upper plot is for majority (a,b) and the lower is for minority (c,d) spin channels. Figures (b,d) are the two-dimensional projections of the top view of figures (a,c). These figures are plotted at an energy of 0.790 eV above E_F , corresponding to the second energy point in Fig. 5.7, and only the central 1.5% of the 2DBZ area is shown here (the values on the horizontal axes are given in the units of $2\sqrt{2}\pi/a_{\text{GaAs}}$). Different vertical scales are used for majority and minority spins.

the product ($T_{\text{GaAs,GaAs}}^{\sigma} \approx T_{\text{GaAs,Fe}}^{\sigma} T_{\text{Fe,Fe}}^{\sigma} T_{\text{Fe,GaAs}}^{\sigma}$) again, the total transmission for this channel is 10^{-4} which is 2 orders of magnitude higher than that of the majority spin and in agreement with the results of the full calculation. Because the reflection at the Fe|Cr interface, $r_{\text{Fe,Fe}}$ is virtually zero, the correction for multiple reflection using Eq. (5.2) also vanishes.

The symmetry arguments just used are only valid at the $\bar{\Gamma}$ point so the analysis we have just carried out only helps to understand (i) the spin dependence of the transmission at energies sufficiently low that $\bar{\Gamma}$ is representative and (ii) the curious dominance of the minority spin transmission observed at the beginning of this section: the previously observed dominance of the majority spin transmission through Fe|GaAs [43, 44] or Fe|InAs [54] interfaces is reversed by the opaqueness of the Fe|Cr interface when transport is restricted to a small area around $\bar{\Gamma}$. At energies as low as $E = E_F + 0.790$, just 0.09 eV above the bottom of the conduction band, large

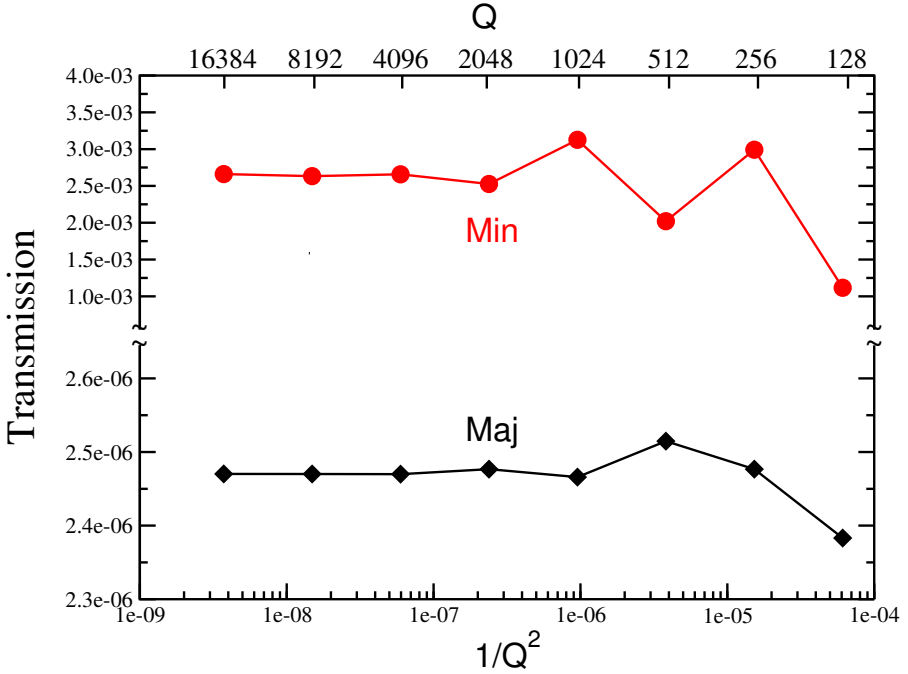


Figure 5.9: Summation of the transmission probabilities shown in Fig. 5.8 over \mathbf{k}_{\parallel} to obtain $T^{\sigma}(E = E_F + 0.790)$ normalized according to Eq. (5.1) for a SVT in the P configuration. For majority and minority spins, T is plotted as a function of the normalized area element used in the 2D Brillouin zone summation, $\Delta^2\mathbf{k}_{\parallel}/ABZ = 1/Q^2$. Q , the number of intervals along the reciprocal lattice vector is indicated at the top of the figure.

deviations from the behaviour at $\bar{\Gamma}$ are seen in Fig. 5.8.

At higher energies, the most important effect comes when a band with Δ_1 symmetry is encountered at 0.92 eV in Cr. This leads directly to a striking increase in $T_{\text{Fe,Fe}}^{\text{maj}}(E)$ at this energy since there is a state with this symmetry over the full energy range of interest in the Fe majority spin bands. In the Fe minority spin band structure, the Δ_1 band starts at about 1.1 eV but at this energy a large part of the 2DBZ is involved, so the transmission is already quite high and symmetry filtering no longer plays an important role.

For AP orientation of the Fe layers we find transmissions which lie between the minority and majority values calculated for the P configuration, see Fig. 5.7. This is quite reasonable. What we did not expect is a large asymmetry between the spin-up and spin-down transmissions. Nevertheless, in Fig. 5.7(b) we see very substantial differences between the two spin channels, as large as two orders of magnitude at 0.925 eV. The origin of these differences can be traced to the fact that one Fe layer is 10MLs, the other 11 MLs thick, and to the importance of multiple reflections which

leads to a large sensitivity of the transmission on layer thickness. This sensitivity threatens to make our whole undertaking of dubious value. We will see in the next section, however, that it disappears as soon as a modest amount of interface disorder is introduced and we will dispense with any more detailed analysis of the specular AP case.

For specular interfaces, the energy dependent “magnetotransmission”, $T_P(E)/T_{AP}(E) - 1$, which will ultimately enter into the calculation of the magnetocurrent [12] exhibits values of the order of 10^3 for small energies; see Table 5.2. The “transfer factor” $\alpha^*(E)$, defined as the sum of the majority and minority spin transmission for a parallel configuration, which will enter into the calculation of the transfer ratio is of the order of 10^{-3} .

5.3.2 Disordered interfaces

The results obtained in the previous section for specular interfaces in the ballistic regime were dominated by matrix element effects resulting from the symmetry of Bloch states on either side of the interfaces, and from constructive and destructive interference resulting from conservation of transverse momentum. In real devices it is extremely difficult to observe such coherent effects, especially in systems involving transition metal|semiconductor interfaces which are apparently quite disordered. Even the best interfaces between two transition metals are considered to contain substantial amounts of disorder [55–58]. In this section, we will address the influence of relatively weak disorder at the Fe|Cr interfaces on the energy and spin dependent transmission. In the presence of disorder, the transmission can be expressed as the sum of two contributions, (i) a ballistic part, where the transmission is between two Bloch states with the same \mathbf{k}_{\parallel} , and (ii) a diffusive part, where the transmission is between two Bloch states with different \mathbf{k}_{\parallel} . We want to investigate to what extent the high asymmetry in the transmission observed in the case of specular interfaces (Fig. 5.7) will survive interface disorder and how the magnetotransmission and transfer factor will be affected. As in our previous work [34, 35, 59–61], and motivated by experimental studies [55–58], disorder at the Fe|Cr interface will be modeled using two monolayers of 50-50 alloy where the sites are randomly occupied by Fe or Cr atoms.

In Fig. 5.10, the spin-dependent transmission through the SVT with disordered Fe|Cr interfaces are shown as a function of the energy ΔE above SB for both P and AP configurations. For the P magnetic configuration (Fig. 5.10a), the minority spin transmission increases modestly while there is a huge increase in the majority spin transmission, by as much as five orders of magnitude at low energies. This can be simply understood in terms of the large disorder-induced increase of transmission through an Fe|Cr (001) interface in the majority spin channel [34]. The effect is compounded in the SVT by the restriction of the transverse momentum to a small area

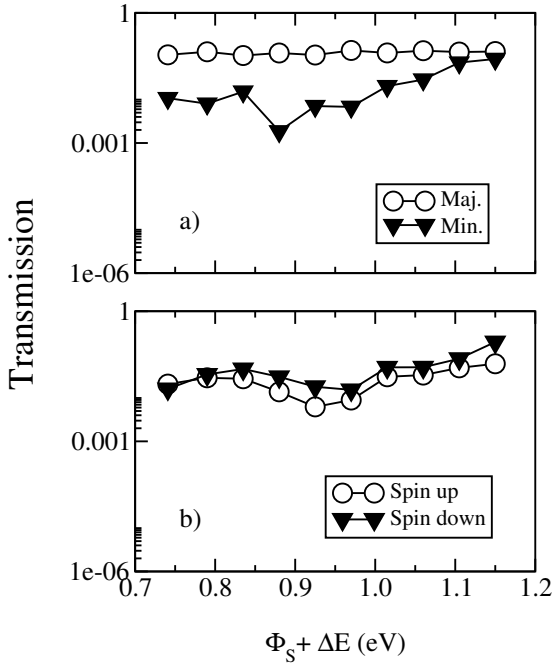


Figure 5.10: Renormalized transmissions of a) *P* and b) *AP* configuration in the SVT as a function of the energy above $E_F + \Phi_S$ for majority (\circ) and minority (\blacktriangledown) spins in case of disordered metallic *Fe|Cr* interfaces.

Energy (eV)	α^*	MT (%)	Pol (%)
0.703	0.20×10^{-1}	170	100
0.745	0.80×10^{-1}	180	30
0.790	1.35×10^{-1}	110	90
0.835	1.20×10^{-1}	60	75
0.880	1.20×10^{-1}	170	95
0.925	1.15×10^{-1}	370	85
0.970	1.45×10^{-1}	490	90
1.015	1.40×10^{-1}	70	70

Table 5.3: Energy dependence of the “transfer factor”, $\alpha^*(E) = T_P^{maj}(E) + T_P^{min}(E) \equiv T_P(E)$, the “magnetotransmission” $MT(E) = T_P(E)/T_{AP}(E) - 1$ and the polarization (for the *P* configuration) in the energy range 0.745 – 1.015 eV for disordered *Fe|Cr* interfaces. The transfer factor is calculated as the sum of majority and minority normalized transmissions in the *P* configuration.

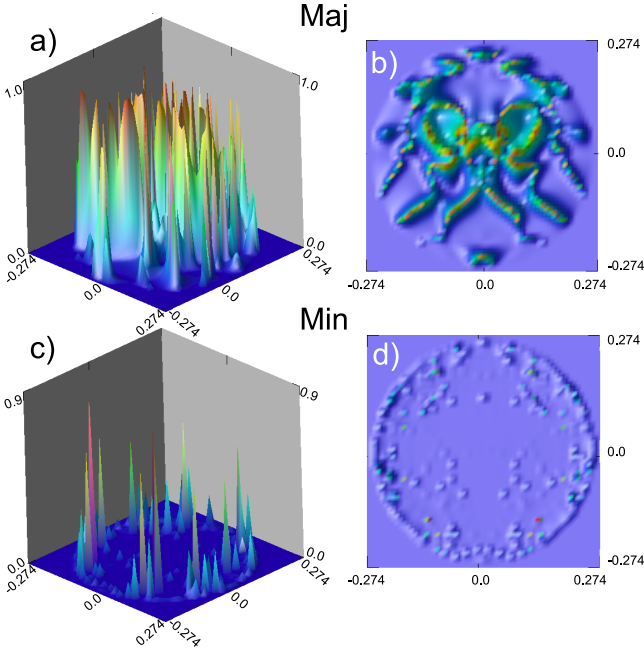


Figure 5.11: Transmission probabilities through the SVT as a function of \mathbf{k}_{\parallel} for Ga-termination and disordered metallic Fe|Cr interfaces. The upper plot is for majority (a,b) and the lower is for minority (c,d) spin channels. (b,d) are the top-view figures of their 3D counterparts (a,c). These figures are plotted at an energy of 0.790 eV above E_F , corresponding to the second energy point in Fig. 5.10, and only the central 12% of the 2DBZ area is shown here (the values on the horizontal axes are given in the units of $2\sqrt{2}\pi/4a_{GaAs}$).

around $\bar{\Gamma}$ when the electrons are emitted from GaAs with this (crystal) momentum. It is graphically illustrated by comparing the transmission probabilities plotted in Fig. 5.11 as a function of \mathbf{k}_{\parallel} with the specular case at the same energy in Fig. 5.8. The increase in the majority spin channel transmission is immediately apparent.

Compared to the specular case, the spin asymmetry is reversed. The polarization is smaller in absolute size, but still sizeable; see Table 5.3. An obvious consequence of the increased majority spin transmission is a very strong enhancement of the total transmission in the P configuration and consequently of the transfer factor also given in Table 5.3.

The spin asymmetry we found for the specular AP configuration is almost completely suppressed by disorder; Fig. 5.10(b). As in the specular case, the spin up and

spin down transmissions are now intermediate between the majority and minority spin cases for the P configuration for the same reason. In the absence of constructive and destructive interference, we expect to be able to factorize the transmission through an SVT such as this into terms describing the transmission through individual interfaces. A consequence of this factorization is that the transmission in the AP configuration (for one spin direction) is essentially the geometric mean of the majority and minority spin transmissions for the P configuration. The reduction of the difference between majority and minority spin transmissions in the P configuration then inevitably leads to a reduced magnetotransmission.

5.4 Discussion and Conclusion

SVTs are usually operated in a regime in which their behaviour is largely determined by inelastic scattering in the base of the device formed by relatively thick magnetic and non-magnetic metallic layers, a volume effect [12]. Ignoring inelastic scattering completely, we have studied the transmission of electrons well above the Fermi energy in a model GaAs|Fe|Cr|Fe|GaAs (001) SVT structure, taking into account the full electronic band structure of both materials (metals and semiconductors). When the interfaces are specular, details of the electronic structure play a very important role and lead to large spin-dependent transmissions and dependence on the relative orientations of the magnetic layers, P or AP. These effects are so sensitive to disorder, however, that it is doubtful if they can be observed experimentally. It is much more interesting to be able to consider the more realistic case of disordered interfaces where we find that disorder counterintuitively leads to large enhancement of the transmission through a SVT in the P configuration. If we were to assume a thermionic emission-type distribution of the current $I_e^\sigma(E)$ injected from the emitter [8], and calculate the collector current as $I_c^P = \sum_\sigma \int I_e^\sigma(E) T_P^\sigma(E) dE$, this would give rise to a large transfer ratio because $T_P(E)$ is large and does not have a strong energy dependence when interface disorder is present. We could calculate the magnetocurrent in a very similar fashion and would find values of the order of 100% because the magnetotransmission $MT(E)$ also does not exhibit a very strong energy dependence; see Table 5.3.

These findings suggest an interesting alternative scenario for SVT operation. Instead of using thick magnetic layers and making use of the volume inelastic scattering effect, we propose using thin magnetic layers to reduce the inelastic scattering as much as possible which will increase the transfer ratio, and to rely on the interface scattering to provide the spin-dependence needed to make a magnetic sensor.

Since disorder at the Fe|Cr interfaces is so important, we should then ask what will happen if disorder is included at the GaAs|Fe interface. The spin dependence of the transmission through a clean GaAs|Fe interface is much larger than the spin dependence of the transmission through a disordered Fe|Cr interface. For the same disorder as used here, a transmission ratio of T_P^{min}/T_P^{maj} of about 3 is found in the relevant energy region 0.7-1.0 eV above the Fermi energy for an Fe|Cr|Fe sandwich [62]. We immediately note that this asymmetry is opposite to that found for the

GaAs|Fe interface so that using clean GaAs|Fe and disordered Fe|Cr interfaces may not be optimal. The magnetotransmission (P vs AP) for the Fe|Cr|Fe sandwich is small. Nevertheless, the result of having a small spin dependent interface transmission embedded in a spin independent diffusive medium can still give rise to large net spin dependent scattering [32, 34, 35] making a detailed study of this system necessary. Unfortunately, while we have some indications of the roughness and disorder at metallic interfaces, we have very little useful information about the nature of metal-semiconductor interfaces especially when more than a single interface is prepared which leads to substantially more disorder at one of the interfaces because of growth mechanisms.

Bibliography

- [1] G. Schmidt, D. Ferrand, L. W. Molenkamp, A. T. Filip, and B. J. van Wees, *Phys. Rev. B* **62**, 4790 (2000).
- [2] G. Schmidt, *J. Phys. D: Appl. Phys.* **38**, R107 (2005).
- [3] T. Dietl, H. Ohno, F. Matsukura, J. Cibert, and D. Ferrand, *Science* **287**, 1019 (2000).
- [4] see the collection of articles, in *Ultrathin Magnetic Structures I-IV*, edited by J. A. C. Bland and B. Heinrich, Springer-Verlag, Berlin, 1994-2005.
- [5] D. J. Monsma, J. C. Lodder, T. J. A. Popma, and B. Dieny, *Phys. Rev. Lett.* **74**, 5260 (1995).
- [6] K. Mizushima, T. Kinno, T. Yamauchi, and K. Tanaka, *IEEE Trans. Mag.* **33**, 3500 (1997).
- [7] D. J. Monsma, R. Vlutters, and J. C. Lodder, *Science* **281**, 407 (1998).
- [8] R. Vlutters *et al.*, *Phys. Rev. B* **65**, 024416 (2001).
- [9] J. Hong and R. Q. Wu, *J. Appl. Phys.* **95**, 4240 (2004).
- [10] T. Yamauchi and K. Mizushima, *Phys. Rev. B* **61**, 8242 (2000).
- [11] M. Hehn, F. Montaigne, and A. Schuhl, *Phys. Rev. B* **66**, 144411 (2002).
- [12] R. Jansen, *J. Phys. D: Appl. Phys.* **36**, R289 (2003).
- [13] S. M. Sze, *Physics of Semiconductor Devices*, second ed. (John Wiley & Sons, New York, United States of America, 1981).
- [14] R. Vlutters, O. M. J. van 't Erve, S. D. Kim, R. Jansen, and J. C. Lodder, *Phys. Rev. Lett.* **88**, 027202 (2002).
- [15] P. S. A. Kumar *et al.*, *J. Magn. & Magn. Mater.* **214**, L1 (2000).
- [16] R. Jansen, S. D. Kim, R. Vlutters, O. M. J. van 't Erve, and J. C. Lodder, *Phys. Rev. Lett.* **87**, 166601 (2001).
- [17] D. P. Pappas *et al.*, *Phys. Rev. Lett.* **66**, 504 (1991).
- [18] G. Schönhense and H. C. Siegmann, *Annalen der Physik* **2**, 465 (1993).
- [19] J. C. Gröbli, D. Oberli, and F. Meier, *Phys. Rev. B* **52**, 13095 (1995).
- [20] A. Filipe *et al.*, *Phys. Rev. Lett.* **80**, 2425 (1998).

- [21] D. Oberli, R. Burgermeister, S. Riesen, W. Weber, and H. C. Siegmann, Phys. Rev. Lett. **81**, 4228 (1998).
- [22] M. Aeschlimann *et al.*, Phys. Rev. Lett. **79**, 5158 (1997).
- [23] R. Knorren, K. H. Bennemann, R. Burgermeister, and M. Aeschlimann, Phys. Rev. B **61**, 9427 (2000).
- [24] H. J. Drouhin, Phys. Rev. B **56**, 14886 (1997).
- [25] J. Hong and D. L. Mills, Phys. Rev. B **59**, 13840 (1999).
- [26] E. Zarate, P. Apell, and P. M. Echenique, Phys. Rev. B **60**, 2326 (1999).
- [27] W. H. Rippard and R. A. Buhrman, Phys. Rev. Lett. **84**, 971 (2000).
- [28] R. Knorren, G. Bouzerar, and K. H. Bennemann, J. Phys.: Condens. Matter. **14**, R739 (2002).
- [29] T. Banerjee, E. Haq, M. H. Siekman, J. C. Lodder, and R. Jansen, Phys. Rev. Lett. **94**, 027204 (2005).
- [30] V. P. Zhukov, E. V. Chulkov, and P. M. Echenique, Phys. Rev. B **73**, 125105 (2006).
- [31] K. M. Schep, P. J. Kelly, and G. E. W. Bauer, Phys. Rev. Lett. **74**, 586 (1995).
- [32] K. M. Schep, J. B. A. N. van Hoof, P. J. Kelly, G. E. W. Bauer, and J. E. Inglesfield, Phys. Rev. B **56**, 10805 (1997).
- [33] K. M. Schep, P. J. Kelly, and G. E. W. Bauer, Phys. Rev. B **57**, 8907 (1998).
- [34] K. Xia *et al.*, Phys. Rev. B **63**, 064407 (2001).
- [35] K. Xia, M. Zwierzycki, M. Talanana, P. J. Kelly, and G. E. W. Bauer, Phys. Rev. B **73**, 064420 (2006).
- [36] O. K. Andersen and O. Jepsen, Phys. Rev. Lett. **53**, 2571 (1984).
- [37] O. K. Andersen, O. Jepsen, and D. Glötzel, in, in *Highlights of Condensed Matter Theory*, edited by F. Bassani, F. Fumi, and M. P. Tosi, pp. 59–176, North-Holland, Amsterdam, 1985.
- [38] O. K. Andersen, Z. Pawłowska, and O. Jepsen, Phys. Rev. B **34**, 5253 (1986).
- [39] O. K. Andersen, Phys. Rev. B **12**, 3060 (1975).
- [40] I. Turek, V. Drchal, J. Kudrnovský, M. Šob, and P. Weinberger, *Electronic Structure of Disordered Alloys, Surfaces and Interfaces* (Kluwer, Boston-London-Dordrecht, 1997).
- [41] P. Soven, Phys. Rev. **156**, 809 (1967).
- [42] S. C. Erwin, S. H. Lee, and M. Scheffler, Phys. Rev. B **65**, 205422 (2002).
- [43] O. Wunnicke, P. Mavropoulos, R. Zeller, P. H. Dederichs, and D. Grundler, Phys. Rev. B **65**, 241306 (2002).
- [44] P. Mavropoulos, O. Wunnicke, and P. Dederichs, Phys. Rev. B **66**, 024416 (2004).
- [45] D. M. Ceperley and B. J. Alder, Phys. Rev. Lett. **45**, 566 (1980).
- [46] J. P. Perdew and A. Zunger, Phys. Rev. B **23**, 5048 (1981).
- [47] D. Glötzel, B. Segall, and O. K. Andersen, Sol. State Comm. **36**, 403 (1980).
- [48] R. M. Martin, *Electronic Structure: Basic Theory And Practical Methods* (Cambridge University Press, Cambridge, United Kingdom, 2004), pp. 42–44.

- [49] J. Callaway and C. S. Wang, *Phys. Rev. B* **16**, 2095 (1977).
- [50] S. Kreuzer *et al.*, *Appl. Phys. Lett.* **80**, 4582 (2002).
- [51] S. Kreuzer *et al.*, *Physica E* **16**, 137 (2003).
- [52] T. Ando, *Phys. Rev. B* **44**, 8017 (1991).
- [53] P. A. Khomyakov, G. Brocks, V. Karpan, M. Zwierzycki, and P. J. Kelly, *Phys. Rev. B* **72**, 035450 (2005).
- [54] M. Zwierzycki, K. Xia, P. J. Kelly, G. E. W. Bauer, and I. Turek, *Phys. Rev. B* **67**, 092401 (2003).
- [55] H. A. M. de Gronckel *et al.*, *Phys. Rev. B* **44**, 9100 (1991).
- [56] C. Mény, P. Panissod, and R. Loloee, *Phys. Rev. B* **45**, 12269 (1991).
- [57] L. L. Henry *et al.*, *Phys. Rev. B* **54**, 12336 (1996).
- [58] C. Kapusta, P. Fischer, and G. Schütz, *J. Alloys Compd.* **286**, 37 (1999).
- [59] K. Xia, P. J. Kelly, G. E. W. Bauer, A. Brataas, and I. Turek, *Phys. Rev. B* **65**, 220401 (2002).
- [60] K. Xia, P. J. Kelly, G. E. W. Bauer, and I. Turek, *Phys. Rev. Lett.* **89**, 166603 (2002).
- [61] M. Zwierzycki, Y. Tserkovnyak, P. J. Kelly, A. Brataas, and G. E. W. Bauer, *Phys. Rev. B* **71**, 064420 (2005).
- [62] M. Talanana, M. Zwierzycki, P. J. Kelly, and G. E. W. Bauer, to be submitted.

Appendix A

ppendix to Chapter 2

A.1 Velocities

Let us start by deriving the expression for the group velocity of an eigenstate of a general tight-binding Hamiltonian, which for a translationally invariant system can be written in the Bloch representation as:

$$\mathcal{H}_{RL,R'L'}(\mathbf{k}) = \sum_{\mathbf{T}} e^{i\mathbf{k}\cdot\mathbf{T}} \mathcal{H}_{RL,(R'+T)L'} \quad (\text{A.1})$$

where RL ($L = lm$) labels the sites and orbitals within the unit cell and \mathbf{T} runs over lattice vectors. The energy eigenvalues $\varepsilon_{\mu}(\mathbf{k})$ are the expectation values

$$\varepsilon_{\mu}(\mathbf{k}) = \mathbf{a}_{\mu}^{\dagger}(\mathbf{k}) \mathcal{H}(\mathbf{k}) \mathbf{a}_{\mu}(\mathbf{k}) \quad (\text{A.2})$$

where the eigenvectors $\mathbf{a}_{\mu}(\mathbf{k})$ are indexed by RL and we assume the normalization $\mathbf{a}_{\mu}^{\dagger} \cdot \mathbf{a}_{\mu} = 1$. It is now straightforward to calculate the group velocity of the propagating mode

$$\mathbf{v}_{\mu} = \frac{1}{\hbar} \frac{\partial \varepsilon_{\mu}(\mathbf{k})}{\partial \mathbf{k}} = \frac{i}{\hbar} \sum_{\mathbf{T}} \mathbf{T} e^{i\mathbf{k}\cdot\mathbf{T}} \times \sum_{RL,R'L'} a_{RL}^* \mathcal{H}_{RL,(R'+T)L'} a_{R'L'} \quad (\text{A.3})$$

In the mixed representation $|I, \mathbf{k}_{\parallel}\rangle$ defined in section 2.2.2 (A.3) gives for the velocity in the stacking direction

$$v_{\mu} = \frac{id}{\hbar} [\mathbf{a}_{\mu}^{\dagger} \mathcal{H}_{I,I+1}(\mathbf{k}_{\parallel}) \lambda_{\mu} \mathbf{a}_{\mu} - \text{h.c.}] \quad (\text{A.4})$$

where d is the distance between equivalent monolayers in adjacent principal layers (PL), the hopping is assumed (as in section 2.2.2) to extend only between neighbouring PLs and $\lambda_{\mu} = \exp(i\mathbf{k} \cdot \mathbf{T}^0)$ with \mathbf{T}^0 connecting equivalent sites in the neighbouring PLs.

(A.3) and (A.4) are nothing other than the expectation values of a standard tight-binding velocity operator [1, 2], which can be written in second quantization form as:

$$\begin{aligned} \hat{v} &= \frac{i}{\hbar} \sum_{T,T'} (\mathbf{T}' - \mathbf{T}) \\ &\times \sum_{RL,R'L'} \mathcal{H}_{(R+T)L,(R'+T')L'} \hat{c}_{(R+T)L}^\dagger \hat{c}_{(R'+T')L'} \end{aligned} \quad (\text{A.5})$$

The velocity defined in this way describes the motion of an electron between neighbouring unit cells, *i.e.*, the motion related to the overall current carried by the state. Using the relation between the generalized Bloch matrices (2.24) and the surface Green function one can, equivalently, express (A.3) using the latter quantities. More details can be found in Ref. [3].

In the screened representation, the KKR tail-cancellation equation of Sec. 2.2 has the algebraic structure of a tight binding Hamiltonian, but is nonlinear in energy. In order to find equivalents of (A.3) and (A.4) for our MTO formalism, we must relate it to the linearized MTO (LMTO) Hamiltonian. Introducing the Hermitian matrix [4, 5]

$$\begin{aligned} h^\alpha(\varepsilon) &= -[\dot{P}^\alpha(\varepsilon)]^{-1/2} (P^\alpha(\varepsilon) - S^\alpha) [\dot{P}^\alpha(\varepsilon)]^{-1/2} \\ &= -P^\alpha(\varepsilon) [\dot{P}^\alpha(\varepsilon)]^{-1} + [\dot{P}^\alpha(\varepsilon)]^{-1/2} S^\alpha [\dot{P}^\alpha(\varepsilon)]^{-1/2}, \end{aligned} \quad (\text{A.6})$$

fixing the energy at $\varepsilon = \varepsilon_F$ and defining the potential parameters [5, 6]

$$\sqrt{d^\alpha} = [\dot{P}^\alpha(\varepsilon_F)]^{-1/2} \quad (\text{A.7a})$$

and

$$c^\alpha = -P^\alpha(\varepsilon_F) / \dot{P}^\alpha(\varepsilon_F) + \varepsilon_F, \quad (\text{A.7b})$$

we arrive at

$$h^\alpha \equiv h^\alpha(\varepsilon_F) = c^\alpha + \sqrt{d^\alpha} S^\alpha \sqrt{d^\alpha} - \varepsilon_F. \quad (\text{A.8})$$

Equation (A.8) has the form of a two-center tight binding Hamiltonian whose energy is given relative to ε_F . It provides the lowest order approximation [4, 5] to the full LMTO Hamiltonian and yields eigenvalues correct to first order in $(\varepsilon - \varepsilon_F)$. Consequently the error introduced by using (A.8) in (A.3) is also of the first order and vanishes for states at the Fermi energy. For such states the eigenvectors of (A.8) are equal to those of (2.15) up to the (position and orbital dependent) scaling factor:

$$\mathbf{c}_\mu(\mathbf{k}) = (\dot{P}^\alpha(\varepsilon_F))^{-1/2} \mathbf{a}_\mu(\mathbf{k}) \quad (\text{A.9})$$

Using (A.6) and (A.9) in (A.4) we arrive at equation (2.38).

A.2 Symmetry relations

If we look closely at the transmission probabilities in Fig. 2.6, we see that the sheet resolved transmissions exhibit the geometrical symmetry of the underlying lattice

(*i.e.* the three-fold rotational axis). The total transmission probability on the other hand possesses an extra inversion symmetry, $T(\mathbf{k}_{\parallel}) = T(-\mathbf{k}_{\parallel})$, which results in plots with a six-fold rotational axis. This higher symmetry is the manifestation of the fundamental time-reversal symmetry obeyed in the absence of spin-orbit coupling and a magnetic field. In the case of the bulk system time-reversal symmetry grants that for every eigenstate $\psi_{\alpha}(\mathbf{k})$ there exists the counterpart with the same energy and opposite wave vector (*i.e.* $\varepsilon_{\alpha}(\mathbf{k}) = \varepsilon_{\alpha}(-\mathbf{k})$) and the wave functions are related by the complex conjugate. The situation is more complicated in the case of the scattering state. Consider a state incoming from the left lead and scattered in the middle region. The wave function consists then of the incoming and reflected states in the left lead

$$\Psi_{\mathcal{L}}^r(\mathbf{k}_{\parallel}) = \psi_{\mu}^+(\mathbf{k}_{\parallel}) + \sum_{\mu'} r_{\mu'\mu}(\mathbf{k}_{\parallel}) \psi_{\mu'}^-(\mathbf{k}_{\parallel}) \quad (\text{A.10})$$

and of the transmitted states in the right lead

$$\Psi_{\mathcal{R}}^r(\mathbf{k}_{\parallel}) = \sum_{\nu} t_{\nu\mu}(\mathbf{k}_{\parallel}) \psi_{\nu}^+(\mathbf{k}_{\parallel}). \quad (\text{A.11})$$

The time reversal operation transforms the above “retarded” state into the “advanced” one in which a number of incoming states (from the left and the right) combine to produce a single outgoing state on the left, *i.e.*

$$\Psi_{\mathcal{L}}^a(-\mathbf{k}_{\parallel}) = \sum_{\mu'} r_{\mu'\mu}^*(\mathbf{k}_{\parallel}) \psi_{\mu'}^+(-\mathbf{k}_{\parallel}) + \psi_{\mu}^-(-\mathbf{k}_{\parallel}) \quad (\text{A.12})$$

and

$$\Psi_{\mathcal{R}}^a(-\mathbf{k}_{\parallel}) = \sum_{\nu} t_{\nu\mu}^*(\mathbf{k}_{\parallel}) \psi_{\nu}^-(-\mathbf{k}_{\parallel}). \quad (\text{A.13})$$

Equations (A.12) and (A.13) impose a set of conditions on the values of scattering coefficients for the states with $-\mathbf{k}_{\parallel}$. Combined with the analogous conditions derived for the states with the incoming state in the right lead, they are compactly expressed as

$$I = S(-\mathbf{k}_{\parallel}) S^*(\mathbf{k}_{\parallel}) \Rightarrow S(-\mathbf{k}_{\parallel}) = S^T(\mathbf{k}_{\parallel}). \quad (\text{A.14})$$

The scattering matrix S is defined as

$$S = \begin{pmatrix} r & t' \\ t & r' \end{pmatrix} \quad (\text{A.15})$$

where $r^{(\prime)}$ and $t^{(\prime)}$ are matrices in the space of the lead modes and the primed coefficients describe scattering of the states incoming from the right. More specifically we have:

$$t_{\nu\mu}(-\mathbf{k}_{\parallel}) = t'_{\mu\nu}(\mathbf{k}_{\parallel}) \quad \text{and} \quad r_{\mu'\mu}(-\mathbf{k}_{\parallel}) = r_{\mu\mu'}(\mathbf{k}_{\parallel}) \quad (\text{A.16})$$

Equation (A.16) gives

$$T_{\mathcal{L}\mathcal{R}}(-\mathbf{k}_{\parallel}) = \sum_{\nu\mu} |t_{\nu\mu}(-\mathbf{k}_{\parallel})|^2 = \sum_{\mu\nu} |t'_{\mu\nu}(\mathbf{k}_{\parallel})|^2 = T_{\mathcal{R}\mathcal{L}}(\mathbf{k}_{\parallel}) \quad (\text{A.17})$$

In addition, for any two-terminal device, the Hermiticity of the scattering matrix guarantees that $T_{\mathcal{R}\mathcal{L}}(\mathbf{k}_{\parallel}) = T_{\mathcal{L}\mathcal{R}}(\mathbf{k}_{\parallel})$ (see Ref. [7]) which finally proves the in-plane inversion symmetry mentioned at the beginning. The last step can not however be taken for the partial (FS resolved) transmission probabilities. These quantities thus possess only the geometrical symmetry of the system.

Bibliography

- [1] J. Kudrnovský *et al.*, Phys. Rev. B **62**, 15084 (2000).
- [2] G. D. Mahan, *Many-Particle Physics*, 2nd ed. ed. (Plenum Press, New York and London, 1990).
- [3] P. A. Khomyakov, G. Brocks, V. Karpan, M. Zwierzycki, and P. J. Kelly, Phys. Rev. B **72**, 035450 (2005).
- [4] O. K. Andersen, O. Jepsen, and D. Glötzel, in, in *Highlights of Condensed Matter Theory*, edited by F. Bassani, F. Fumi, and M. P. Tosi, pp. 59–176, North-Holland, Amsterdam, 1985.
- [5] O. K. Andersen, Z. Pawłowska, and O. Jepsen, Phys. Rev. B **34**, 5253 (1986).
- [6] O. K. Andersen, O. Jepsen, and M. Šob, in, in *Electronic Band Structure and its Applications*, edited by M. Yussouff Vol. 283, pp. 1–57, Springer Lecture Notes, Berlin, 1987.
- [7] S. Datta, *Electronic Transport in Mesoscopic Systems* (Cambridge University Press, Cambridge, 1995).

Appendix B

Appendix to Chapter 5

B.1 GaAs bulk band structure

To better understand how the details of the calculation method and the various approximations used can affect the numerical results, we evaluated the influence of various parameters on the latter. We have looked at how does an *spd* versus *spdf* localized basis sets and ASA versus so-called combined correction term (supposed to be more accurate [1]) to the one-electron LMTO Hamiltonian and overlap matrices affect the energy band gap (E_g) of GaAs as a function of the size of the Wigner Seitz radii (WSR) of the atomic (Ga and As) and empty (E_1 and E_2) spheres. Fig. B.1 summarizes the results of our calculations. These results are obtained by using the TB-LMTO method as implemented in the Stuttgart code (see Ref. [2–4]).

Shown in Fig. B.1(a) the band gap of GaAs when the ratio (r_A/r_B) of WSR of the empty to the atomic spheres increases. We observe a proportionality between E_g and the WSR of Ga and As atoms, when WSR (Ga, As) decreases E_g decreases as well. There is a transition from an insulator to metallic behaviour. The Ga and As atomic spheres are equal and vary from 3.000 to 2.110 a.u while the empty spheres, also with equal sizes, vary from 2.110 to 3.000 a.u. [6]. If one includes the combined correction term the band gap decreases substantially when the size of the atomic spheres decreases (the region where the atomic spheres are larger than the empty spheres, $r_A/r_B < 1$). In the limit where the kinetic energy of the electrons in the interstitial region is neglected, the band gap of GaAs can reach values as high as 2.00 eV. Furthermore, including the f-electrons decreases even more E_g , but less as does the combined correction term.

In Fig. B.1b the band gap of GaAs is calculated when the WSR of Ga and As are equal to that of the surrounding empty spheres E_2 and E_1 , respectively. Most of the features observed in Fig. B.1a are retained in this case too. It shows mainly that E_g

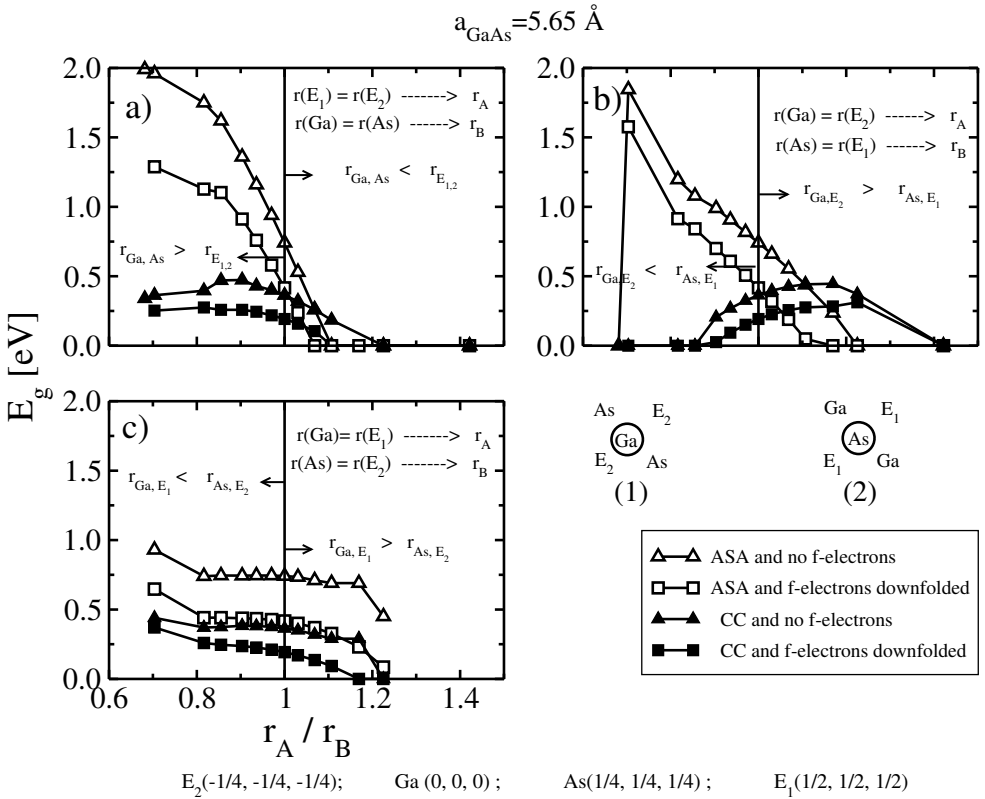


Figure B.1: Energy band gap, E_g , of zinc-blende GaAs as a function of the size of WSR of the atomic (Ga and As) and empty (E_1 and E_2) spheres. Filled (empty) triangles denote results with (without) combined correction term to the one-electron LMTO Hamiltonian and overlap matrices. Triangles (squares) denote results where the *spd* (*spd*) localized basis set is used, *f*-electrons are downfolded [5]. (1) and (2) configurations show the chemical surrounding of the atomic species Ga and As. The last line gives the positions of the atomic and empty spheres in a zinc-blende unit cell.

decreases rapidly when the ratio $r_{(A=\text{Ga}, E_2)}/r_{(B=\text{As}, E_1)}$ decreases, so does also the effect of including *f*-electrons (downfolded) and the combined correction term.

In the limits when $\text{WSR}(\text{Ga}, E_2)$ equals 2.110 a.u. and $\text{WSR}(\text{As}, E_1)$ equals 3.000 a.u. the total valence charge is 1.354, 0.252, 4.935 and 1.458 electrons, respectively for Ga, E_2 , As and E_1 . We observe a large charge transfer ($3.000 - 1.354 = 1.646$ electrons) from Ga into the interstitial empty spheres due to the shrink in in the size of the Ga atomic sphere whereas most of that of As atomic sphere is retained, only a fraction of a hundred is lost. There is a large (30%) overlapping between As and E_1 spheres and a small one between the rest of the spheres. When one increases the volume of

the Ga atomic sphere (that of As decreased), the valence charge on Ga increases up to 2.378 electrons for a WSR of 2.6304 a.u. (4.248 electrons in As with the same size of the atomic sphere) and E_g decreases. If one includes the combined correction term to the Hamiltonian and overlap matrices, GaAs remains as a semiconductor in only a small interval ($r_A/r_B \in [0.90, 1.42]$) of WSR, [2.490,3.000] a.u. for Ga and [2.757, 2.110] a.u. for As.

Fig. B.1c illustrates the case when the WSR of two spheres, sitting on two sites symmetrically equivalent, are taken equal, that is $r_{Ga} = r_{E_1}$ and $r_{As} = r_{E_2}$. Compared to Figs. B.1a,b, E_g is very little sensible to the variation of the atomic and empty spheres WSR sizes, we observe a “plateau” in the band gap curve on a wide range of WSR centered around the value $r_A/r_B = 1$, equivalent to all equal spheres with a WSR of 2.6304 a.u. The valence charge is 2.378, 4.248, 0.754 and 0.620 electrons, respectively for Ga, E_1 , As and E_2 . The atomic overlapping between the spheres is everywhere 14%. The energy band gap of 0.74 eV is reduced to 0.36 eV when one includes the combined correction term. Furthermore, these two values are even more reduced to 0.24 and 0.16 eV, respectively, if one uses an *spdf* basis set.

Bibliography

- [1] G. B. Bachelet and N. E. Christensen, Phys. Rev. B **31**, 879 (1985).
- [2] O. K. Andersen, Phys. Rev. B **12**, 3060 (1975).
- [3] O. K. Andersen and O. Jepsen, Phys. Rev. Lett. **53**, 2571 (1984).
- [4] O. K. Andersen, O. Jepsen, and D. Glötzel, in, in *Highlights of Condensed Matter Theory*, edited by F. Bassani, F. Fumi, and M. P. Tosi, pp. 59–176, North-Holland, Amsterdam, 1985.
- [5] W. R. L. Lambrecht and O. K. Andersen, Phys. Rev. B **34**, 2439 (1986).
- [6] N. E. Christensen, Phys. Rev. B **30**, 5753 (1984).



Summary

Magnetoelectronics is a rapidly growing field where basic research is moving very fast towards smaller structures of nanoscale dimensions and novel materials. Much of the interest in magnetoelectronics is motivated by its potential applications in science and technology. The developments in this field of research are mostly connected to the giant magnetoresistance (GMR) and tunnel magnetoresistance (TMR) phenomena. These transport phenomena are based on the up and down spin of electrons, therefore the electronic transport is spin-dependent. Spin-dependent transport will occur naturally in any material for which there is an imbalance in the spin populations at the Fermi energy. Spintronics, or spin electronics, is another fast emerging field. It relies on the active control and manipulation of the spin degree of freedom of electrons, as well as their electrical charge, in semiconductor based devices. By incorporating spin-dependent properties and magnetism in semiconductor based structures, new applications can be achieved which can go beyond magnetoresistive effects in metallic systems.

The aim of the present thesis is to study theoretically the spin-dependent transport properties in nanoscale hybrid and inhomogeneous structures. Typical structures contain one or several interfaces formed by magnetic, nonmagnetic and/or semiconductor materials. Since, at the atomic scale, there are discontinuities in the electronic structure at the interfaces therefore a quantum mechanical treatment is the most appropriate framework for a rigorous description of electronic transport. The electronic structure and magnetic properties have been obtained using the surface Green's function technique (SGF) implemented within the framework of tight-binding linear muffin-tin orbital (TB-LMTO) method in the atomic sphere approximation (ASA). The coherent potential approximation (CPA) method has been employed to model substitutional disorder at the interfaces. This first-principles approach allows us to take into account the complex nature of the transition metal electronic structures and to be able to describe interfaces realistically. To study coherent electronic spin transport in mesoscopic systems, we have developed a general, efficient and flexible method, suitable for Hamiltonians that can be represented in a tight-binding form and based on direct matching of the scattering region wave function to Bloch modes of the leads. This method is based on the Landauer-Büttiker formulation of transport theory using a first-principles TB-MTO implementation. Combined with the local spin density approximation (LSDA) of the density functional theory (DFT)

and supercell technique, our approach has been applied to calculate the scattering matrices, entering the conductance and/or resistance calculations, for a variety of hybrid systems of current interest.

In Chapter 1 we give a general introduction to the fields of magnetoelectronics and spintronics. Some background of the calculation details, namely the density functional theory and the conductance calculation within the Landauer–Büttiker approach, is briefly presented. A short description of the spin-valve transistor is provided.

In Chapter 2 we present the details of an efficient wave-function matching formalism suitable for the calculation of the transmission and reflection matrices from first principles in layered materials. Within the framework of spin density functional theory and using TB–MTO representation, scattering matrices are determined by matching the wave-functions at the boundaries between leads which support well-defined scattering states and the scattering region. The calculation scales linearly with the number of principal layers N in the scattering region and as the cube of the number of atoms H in the lateral supercell. For metallic systems for which the required Brillouin zone sampling decreases as H increases, the final scaling goes as H^2N . Because a minimal basis-set of localized orbitals is used, namely *spd(f)*, we are able to treat large lateral supercells. In practice, the efficiency of the basis set allows scattering regions for which $H^2N \sim 10^6$ to be handled. This allows us to study transport properties in the diffusive regime and modeling materials with large lattice mismatch. The method is illustrated for Cu|Co multilayers and single interfaces using large lateral supercells (up to 20×20) to model interface disorder. Because the scattering states are explicitly found, “channel decomposition” of the interface scattering for clean and disordered interfaces can be performed.

In Chapter 3 we carry out a systematic material-specific study of the electronic and the spin-dependent transport properties in nearly lattice matched materials, namely Cr|Fe, Cu|Co, Cu|Ni and Co|Ni along [001], [011] and [111] directions. The calculated *3d* transition metals band structures and their Fermi surfaces have been used for the interpretation of the results of the transport calculations, *e.g.* to explain the anisotropy in transport properties for specular interfaces observed in the Cr|Fe system. The effect of defect scattering has been considered too. It reduces the transmission probability and thus increases the interface resistance for some systems (like in Cu|Co, Cu|Ni and Co|Ni systems). On the other hand the opposite happens for Cr|Fe system, that is, defect scattering enhances substantially the interface transmission. For the Cr|Fe (001) interface, with higher spin asymmetry, the interface resistance for the majority spin-channel decreases by a factor 3. This surprising large effect of defect scattering on this particular orientation of Cr|Fe system will be considered in more details by separating the ballistic versus the diffusive components of the interface transmission.

Chapter 4 is devoted to studying the orientation-dependent transparency of metallic interfaces. As devices are reduced in size, interfaces start to dominate electrical transport making it essential to be able to describe reliably how they transmit and reflect electrons. In this chapter, for a number of nearly perfectly lattice-matched materials, we calculate the dependence of the interface transparency on the crystal orientation. Quite remarkably, a large anisotropy is predicted for interfaces between

the prototype free-electron materials Ag and Al, a factor of 2 difference between the (111) and (001) orientations has been found. To interpret this behavior use is made of the calculated Fermi surfaces and their projections along these two directions. Similar results for Al|Au interfaces have been obtained.

Motivated by the transport measurements (electrical and magnetic response) in the spin-valve transistor we have decided to carry out a study of a model structure to understand the spin-dependent transport properties in this device (Chapter 5). In the operation of spin-valve transistors (SVT), use is made of the spin-dependent attenuation of hot electrons in a magnetic material - a volume effect. The downside of this attenuation is an unacceptably small collector current. Little attention has been paid in this context to spin-dependent interface scattering which, in the linear response regime, is the origin of the GMR effect. To gain some insight into the importance of this interface term, we have studied the spin-dependent transmission through a model GaAs|Fe|Cr|Fe|GaAs (001) SVT structure as a function of energy for clean and disordered metallic interfaces using the transport method developed in Chapter 2. In the absence of disorder and inelastic scattering, we find large magnetocurrents arising from materials-related symmetry incompatibilities when the transverse momentum is small as it is in GaAs, but small transfer ratios. Interface disorder at the metallic interfaces is found to reduce the magnetocurrent but increases the transfer ratio considerably.



Résumé

La magnétoélectronique est un sujet qui jouit d'une croissance rapide ou la recherche fondamentale avance à grands pas vers des structures de plus en plus petites, de dimensions de l'ordre du nanomètre et vers des matériaux nouveaux. L'intérêt porté à la magnétoélectronique provient de la curiosité scientifique qu'elle suscite aussi bien de ses applications technologiques potentielles. Les développements dans ce domaine concernent, notamment, les phénomènes de la magnétorésistance géante (GMR) ainsi que de la magnétorésistance tunnel (TMR). Pour ces phénomènes le transport dépend de la polarisation en spin des électrons. Le transport dépendant en spin a lieu naturellement dans tout système qui présente une différence de population des deux orientations de spin au niveau de Fermi. La "spintronique", ou "électronique de spin", est un autre domaine émergent. Elle concerne la manipulation du spin des électrons (ou trous) qui servent de "porteurs" d'information à côté de leurs charges électriques, dans des composants à base de semi-conducteurs. En incluant le transport dépendant du spin et le magnétisme dans les composants à base de semi-conducteurs, de nouvelles applications, qui vont au-delà des effets magnétorésistifs dans les systèmes métalliques, peuvent être réalisées.

Le but de cette thèse est l'étude théorique du transport dépendant de spin dans des structures hybrides. Ces structures contiennent une ou plusieurs interfaces formées en juxtaposant des matériaux magnétiques, non-magnétiques et/ou semi-conducteurs. La description quantique est nécessaire du fait de la discontinuité de la structure électronique à l'échelle atomique au niveau de ces interfaces. La structure électronique et les propriétés magnétiques des interfaces sont obtenues à l'aide de la méthode des fonctions de Green de surface (SGF) implémentées dans le cadre de la méthode linéarisée des orbitales muffin-tins en liaisons fortes (TB-LMTO) et dans l'approximation des sphères atomiques (ASA). L'approximation du potentiel cohérent (CPA) est utilisée pour tenir compte du désordre substitutionnel aux interfaces. Cette méthode, dite de premiers principes ou *ab initio*, nous permet de tenir compte de la nature complexe de la structure électronique des métaux de transition et des semi-conducteurs ainsi que de décrire les interfaces d'une manière réaliste. Pour étudier le transport électronique cohérent de spin dans les systèmes mesoscopique nous avons développé une méthode générale, efficace et flexible, appropriée aux Hamiltoniens qui peuvent être écrits sous forme liaisons-fortes. Elle est basée sur le raccordement de la fonction d'onde de la région où la diffusion a lieu aux modes de Bloch des électrodes. Cette

méthode est basée sur la formulation de Landauer–Büttiker de la théorie du transport formulée dans le cadre de la méthode TB–MTO. Combinée avec l’approximation de densité locale (LDA) de la théorie de la fonctionnelle de densité (DFT) et de la technique de la supercellule, notre méthode est appliquée aux calculs des matrices de diffusion qui entrent dans le calcul des conductances et/ou résistances pour divers systèmes hybrides qui présentent un intérêt d’actualité.

Dans le chapitre 1 nous présentons une introduction générale relative à la magnétoélectronique et à la spintronique. Un bref aperçu des détails concernant la théorie de la fonctionnelle de densité et le calcul des conductances par l’approche de Landauer–Büttiker, est aussi donné. Une brève description du transistor à base de “valve de spin” est fournie.

Dans le chapitre 2 nous présentons les détails d’un formalisme pertinent, basé sur le raccordement des fonctions d’onde, approprié au calcul des matrices de transmission et de réflexion à partir des méthodes de premiers principes appliquées aux systèmes en (multi)couches. En utilisant la méthode TB–MTO, dans le cadre de la DFT, les matrices de diffusion sont déterminées en raccordant les fonctions d’ondes aux frontières des électrodes, qui ont des états de diffusion bien définis, avec la région active de diffusion. Les calculs sont linéairement proportionnels au nombre de “couches principales” N dans la région active de diffusion et d’une manière cubique par rapport au nombre d’atomes H dans la supercellule latérale. Pour les systèmes métalliques dont la zone de Brillouin échantillonnée diminue en augmentant H , les calculs augmentent finalement avec H^2N . Nous pouvons traiter des supercellule de grandes dimensions latérales car nous utilisons une base minimale de fonctions d’onde, à savoir $spd(f)$. En pratique, cette base nous permet de traiter des régions active de diffusion pour lesquelles $H^2N \sim 10^6$. Cela nous permet d’étudier les propriétés de transport dans le régime diffusif ainsi que modéliser les matériaux présentant une différence conséquente entre leurs paramètres de réseaux respectifs. La méthode est appliquée à des multicouches de Cu|Co ainsi qu’à des interfaces, en utilisant de grandes supercellules latérales (de taille jusqu’à 20×20) pour modéliser le désordre aux interfaces. Dans la mesure où les états de diffusion sont obtenus explicitement, la “décomposition en états” (channel decomposition) de diffusion aux interfaces pures ainsi que désordonnées peut être faite.

Dans le chapitre 3 nous présentons une étude systématique du transport électronique dépendant de spin dans des matériaux dont les paramètres de maille sont très proches, à savoir Cr|Fe, Cu|Co, Cu|Ni et Co|Ni suivant les directions [001], [011] ainsi que [111]. La structure de bandes des métaux de transitions $3d$ et leurs surfaces de Fermi sont utilisées pour expliquer les résultats des calculs de transport, et en particulier, l’anisotropie des propriétés de transport observée aux interfaces pures du système Cr|Fe. Les effets de la diffusion due aux défauts sont aussi étudiés. Ceux-ci réduisent la probabilité de transmission et donc augmentent la résistance de quelques uns de ces systèmes (comme Cu|Co, Cu|Ni et Co|Ni). En revanche, c’est le contraire qui se produit dans le cas du système Cr|Fe où la diffusion par les défauts augmente d’une manière considérable la transmission à travers l’interface. Dans le cas de l’interface Cr|Fe (001), qui présente une plus haute asymétrie en spin, la résistance à l’interface, pour les spins majoritaires, diminue d’un facteur de 3. Cet effet, grand et

surprenant, de la diffusion par des défauts est étudié avec plus de détails en séparant les composantes balistiques et “diffusantes” de la transmission à l’interface.

La transparence, des interfaces métalliques, dépendante de l’orientation cristalline est présentée dans le chapitre 4. La réduction de la taille des composants électroniques fait que les interfaces dominent le transport et cela demande une description fiable de la manière avec laquelle ces interfaces transmettent ou réfléchissent les électrons. Dans ce chapitre, nous calculons la dépendance de la transparence de l’interface en fonction de l’orientation cristalline d’un nombre de matériaux ayant des mailles proches (ou égales). Une grande anisotropie est trouvée aux interfaces des deux matériaux Ag et Al, prototypes de systèmes à électrons libres: une différence d’un facteur de 2 entre les orientations (111) et (001) est un fait exceptionnel. Nous avons interprété ce résultat à partir des surfaces de Fermi calculées pour les deux matériaux ainsi que de leurs projections sur ces deux directions. Des résultats similaires sont aussi trouvés pour les interfaces Al|Au.

Motivés par des mesures de transport (mesure de réponses électrique et magnétique) dans les transistors à “valve de spin”, nous avons mené une étude sur une structure modèle pour comprendre les propriétés de transport dépendant du spin de ce composant électronique (Chapter 5). Dans les “valve de spin” on exploite l’atténuation dépendante du spin des électrons “chauds” dans le matériau magnétique. Ceci est un effet de volume. L’inconvénient de cette atténuation est qu’elle a pour conséquence un courant collecteur très faible. Dans ce contexte, peu d’intérêt a été porté à la diffusion dépendante en spin qui, en régime de réponse linéaire, est à l’origine de l’effet GMR. Pour comprendre le rôle de l’interface, nous avons étudié la transmission dépendante en spin d’un système modèle, GaAs|Fe|Cr|Fe|GaAs (001), en fonction de l’énergie pour des interfaces pures et désordonnées à l’aide de la méthode développée dans le chapitre 2. En l’absence de désordre ainsi que de diffusion inélastique, nous trouvons de grands “magnétocourants” dus aux incompatibilités entre les symétries des matériaux quand “l’impulsion” transversale est “petite” comme dans le cas de GaAs, mais avec des taux de transfert faibles. Nous avons trouvé que le désordre aux interfaces réduit le “magnétocourant” mais augmente le taux de transfert d’une manière considérable.

amenvatting

Magnetoelektronica is een snelgroeiend vakgebied waar basisonderzoek zich richt op nieuwe materialen en steeds kleiner wordende structuren met een nanoschaal afmetingen. Een groot deel van de interesse in magnetoelektronica wordt gestimuleerd door de potentiële toepassingsmogelijkheden in zowel wetenschap als technologie. De ontwikkelingen in dit onderzoeksgebied zijn hoofdzakelijk verbonden met de fenomenen van giant magnetoresistance (GMR) en tunnel magnetoresistance (TMR). Deze transport aanpak is gebaseerd op het feit dat elektronen ofwel een up ofwel een down spin hebben, zodat het transport spinafhankelijk is. Spinafhankelijk transport gebeurt spontaan in elk materiaal waar de twee spinpopulaties niet in evenwicht zijn rond de Fermi-energie. Spintronica, of spinelektronica, is een ander snel opkomend gebied dat steunt op de actieve controle en manipulatie van de spinvrijheidsgraden in plaats van de elektrische lading van elektronen in halfgeleidertoepassingen. Door het invoeren van magnetisme en spinafhankelijke eigenschappen in halfgeleidertoepassingen kunnen nieuwe toepassingen worden ontwikkeld die de magnetoresistive effecten van metallische systemen te boven gaan.

Het doel van deze thesis is de theoretische studie van spinafhankelijke transporteigenschappen in hybride en inhomogene structuren met nanometer afmetingen. Dergelijke structuren bevatten één of meerdere interfaces tussen magnetische, niet-magnetische en/of halfgeleider materialen. Gezien er, op atomaire schaal, discontinuïteiten in de ladingsstructuur optreden aan deze interfaces is een kwantummechanische aanpak nodig om een rigoureuze beschrijving van het elektronisch transport te kunnen geven. De elektronische structuur en de magnetische eigenschappen werden verkregen door gebruik te maken van de oppervlakte Greense functie techniek (SGF) geïmplementeerd binnen het raamwerk van de tight-binding linear muffin-tin orbital (TB-LMTO) methode in de atomaire sfeer benadering (ASA). De coherente potentiaal benaderingsmethode (CPA) werd gebruikt om substitutionele wanorde aan de interfaces te modelleren. Deze first-principles aanpak staat ons toe de complexe natuur van de elektronische structuur van transitie-metalen in acht te nemen en zo de interfaces realistisch te beschrijven. Om coherente elektronische spintransport in mesoscopische systemen te bestuderen hebben we een algemene, efficiënte en flexibele methode ontwikkeld, aangewezen voor Hamiltonianen die in een tight-binding vorm kunnen gerepresenteerd worden en gebaseerd op het rechtstreeks afstemmen van de golf functie in het verstrooiingsgebied op de Blochmodes van de leads. Deze methode

is gebaseerd op de Landauer–Büttiker formulering van transporttheorie gebruik makende van een first-principles TB–MTO implementatie. Onze aanpak, in combinatie met de lokale spin dichtheidsbenadering (LSDA) van de dichtheidsfunctionaaltheorie (DFT) en de supercel techniek, is gebruikt geweest om de verstrooiingsmatrices, welke in de geleidings- en/of weerstandsberoeeningen te voorschijn komen, van een set verschillende types hybride systemen te berekenen.

In hoofdstuk 1 geven we een algemene inleiding tot magnetoelektronica en spintronica. We geven een korte bespreking van enkele achterliggende methoden van de berekeningen, meer bepaald dichtheidsfunctionaaltheorie en de berekening van geleiding in het Landauer–Büttiker formalisme. We eindigen met een korte beschrijving van de spin-valve transistor.

In hoofdstuk 2 geven we de bijzonderheden van een efficiënt formalisme voor het afstemmen van de golffuncties, ideaal voor het berekenen van transmissie- en reflectiematrices, vanuit first-principles, van gelaagde materialen. Binnen het raamwerk van spindichtheidsfunctionaaltheorie en gebruik makende van de TB–MTO voorstelling worden de verstrooiingsmatrices vastgelegd door het verbinden van de golffuncties op de grenzen tussen de leads, welke goed gedefinieerde verstrooiingstoestanden bevatten, en het vertrooiingsgebied. De berekening schaaft lineair met het aantal principale lagen N in het verstrooiingsgebied en als een derde macht met het aantal atomen H per zijdelingse supercel. Voor metallische systemen, waarvoor het benodigde sample van de Brillouinzone verkleint als H vergroot, is de uiteindelijke schaling evenredig met H^2N . Omdat er wordt gebruik gemaakt van een minimale basisset van gelokaliseerde orbitalen, namelijk *spd* (f), is het mogelijk grote laterale supercellen te behandelen. De efficiëntie van de basisset staat ons toe in praktisch verstrooiingsgebieden te behandelen waarvoor $H^2N \sim 10^6$. Dit geeft ons de mogelijkheid om transporteigenschappen in het diffuse regime te bestuderen en het modelleren van gelaagde materialen met sterk verschillende roosterconstanten. De methode is toegelicht, voor zowel gelaagde Cu|Co systemen als een enkelvoudige interface, gebruik makende van grote laterale supercellen (tot 20×20), om wanorde in de interface te modelleren. Omdat de verstrooiingstoestanden expliciet gevonden worden is het mogelijk een “channel decompositie” van de interface verstrooiingstoestanden voor zowel zuivere als wanordelijke interfaces uit te voeren.

In hoofdstuk 3 voeren we een systematische materiaalspecifieke studie uit van de elektronische en spinafhankelijke transporteigenschappen voor gelaagde materialen waarvan de roosterconstanten van de componenten bijna hetzelfde zijn, meer bepaald Cr|Fe, Cu|Co, Cu|Ni en Co|Ni langs de [001], [011] en [111] richtingen. De berekende bandstructuren en hun Fermi-oppervlakken voor deze $3d$ transitie-metalen zijn dan gebruikt bij het interpreteren van de resultaten van de transportberekeningen. *Bvb.* bij het verklaren van de anisotropie in de transporteigenschappen van scherpe interfaces zoals geobserveerd in het Cr|Fe systeem. Het effect van verstrooiing aan defecten werd ook in beschouwing genomen. Enerzijds verkleint het de transmissiewaarschijnlijkheid en zodoende vergroot het de interfaceweerstand voor bepaalde systemen (bvb. Cu|Co, Cu|Ni en Co|Ni). Anderzijds gebeurt net het tegengestelde voor het Cr|Fe systeem, waar verstrooiing aan defecten de interfacetransmissie fors versterkt. In het geval van de Cr|Fe (001) interface, met zijn hogere spinasymmetrie, verkleint de interfaceweers-

tand voor het spinmajoriteitskanaal met een factor drie. Dit verrassend groot effect van de verstrooiing aan defecten in deze specifieke richting van het Cr|Fe systeem zullen we in meer detail beschouwen door de interfacetransmissie op te splitsen in een ballistische en een diffuse component.

Hoofdstuk 4 is gewijd aan de studie van oriëntatieafhankelijke transparantie van metallische interfaces. Bij steeds kleiner wordende systemen zijn het de interfaces die het transport beginnen domineren zodat het betrouwbaar kunnen beschrijven van hoe ze elektronen reflecteren en doorlaten essentieel wordt. Voor een aantal systemen waarbij de roosterconstanten van de samenstellende componenten quasi identiek zijn hebben we de afhankelijkheid van de interfacetransparantie ten aanzien van de kristaloriëntatie berekend. Tamelijk opvallend is dat een grote anisotropie wordt voorspeld voor interfaces tussen de prototype vrije elektron materialen Ag en Al. In deze gevallen vinden we een factor twee verschil tussen de (111) en de (001) richting. Om dit gedrag te verklaren werd gebruik gemaakt van de berekende Fermi-oppervlakken en hun projecties langs de deze twee richtingen. Soortgelijke resultaten werden bekomen voor de Al|Au interfaces.

Op basis van de transportmetingen (elektrische en magnetische respons) op de spin-valve transistor hebben we besloten een studie te doen van een modelstructuur om zo de spinafhankelijke transporteigenschappen van dit systeem te begrijpen (Hoofdstuk 5). De werking van de spin-valve transistor (SVT) maakt gebruik van spinafhankelijke attenuatie van hete elektronen in een magnetisch materiaal - een volume effect. Het nadeel van deze attenuatie is een onaanvaardbaar kleine collectorstroom. In deze context is nog maar weinig aandacht besteed aan spinafhankelijke interfaceverstrooiing welke, in het lineaire respons regime, de oorzaak is van het GMR effect. Om inzicht in het belang van deze interfaceterm te verwerven hebben we de spinafhankelijke transmissie, door een GaAs|Fe|Cr|Fe|GaAs (001) model-SVT structuur, als functie van de energie, voor zowel scherpe als wanordelijke metallische interfaces, bestudeerd, gebruik makende van de in hoofdstuk 2 ontwikkelde transportmethode. Bij het ontbreken van wanorde en inelastische verstrooiing vinden we dat er grote magnetische stromen ontstaan, ten gevolge van materiaal eigen symmetrie-incompatibiliteiten wanneer de transversale impuls klein is, zoals in GaAs, terwijl de transferratio klein is. Wanorde aan de metallische interfaces blijkt de magnetische stroom te verkleinen terwijl het de transferratio fors vergroot.



acknowledgments

Tamezwarut, ad bduḡ s wid iyi-d qarben s waṭtas, aṭtas. Ur bedduḡ ara mebla ma zwareḡ s Dalila awk d Masin. Awniniḡ tanmirt tameqwrahant i kunwi id-dibedden ar ḡuri ayen kkan xemsa iseggwasen agi i nesεedda dagi di “La Hollande”. Am ass am yid, xas ma yella ar ḡuri tikwal xelḡen-iyi, kunwi tsebrem-assen. Tikwal diḡent llan d ussan waren imi hwaḡḡen aṭtas lxwedma, uxemmem d laεqel. Ulac id-iṭtasen s shala! I keč a Masin, ur teṭṭuḡ ara, imi yal abrid teqqaređ-as: “ A mammas, babas iruḡ ḡer lbiru ad iḡer.” Ṭmenniḡ-ak ammi aṭ-ṭawiđ ula d keččini abrid ifazzen, nnig win ibwi babak. Tura akka kfan wussan agi deggwacu ṭheggiḡ *adlis*-iw n doktora ihi ad sεuḡ aṭtas lweqt akken a nelεeb arnu a neffeḡ i tlata yidneḡ. Anuḡ ad-neḡar imekwan awk icebḡen dḡa dagi i “La Hollande” neḡ ar tmura nniḡen. Ikunwi diḡent ay imawlan-iw, iḡulan-iw awk laεmum-iw tanmirt! Ur kwen-ṭṭuḡ ara ula d kunwi a xwali iyi-d iqarben. Ula d kem a xati Fetta teddiđ-d, ur kem-ṭṭuḡ ara. Acukan ur-d uffriḡ ara lehdur ara ami-d yinin ayen bḡiḡ am-d iniḡ. S tefses kan, tanmirt tameqwrahant a xati!

The years spent in Twente doing my PhD now come to the end!

First of all I would like to take this opportunity to express my sincere gratitude to the people who helped me or who contributed, in one way or another, to carry out this PhD thesis to the end. The atmosphere of *de werkbeprekingen*, the meetings and conferences have been particularly very interesting for the success of our research. Special thanks go to Prof. Dr. Paul J. Kelly and Dr. Maciej Zwierzycki for guiding me through these years of my PhD research. I learned that writing and running big computer codes do not produce publishable results by themselves. ;-) Many thanks Dr. Geert Brocks for always being there answering my questions. Thanks a lot for your availability for all of you.

Coming from Algeria to The Netherlands to do a PhD is a very exciting and challenging experience for me. At the end of these five years I learned so many things, discovered numerous as well as different cultures, met very kind people who made my (or our) stay here in Holland very enjoyable. Some of you have been a source of endless support. I would like to thank all of you, one by one, and say that I am grateful to you:

My promotor and daily supervisor Prof. Paul Kelly, thanks for the time you spent in supporting me and my work during these years I lived in Enschede. I learned many

things from this very useful experience, like how to cope with pressure, sorting out priorities, choosing the right objectives, ... I guess not only me but all the CMSers enjoyed all the social events that your wife Andrea and You have organized and welcomed all the people of CMS group. Many thanks for the two of you for all those dinners and drinks, your hospitality, the pleasant and the warm atmosphere that surrounded them. Thanks Paul for your comments, suggestions and contributions to the manuscripts I have written.

Dr. Maciej Zwierzycki, thanks for the time we spent together and the good company either here in Enschede or during conferences. Thanks also for all those nice pictures you have made in various occasions. Many thanks for all those fruitful discussions we have had, your advices while I was programming the transport code and also for helping me to understand various theoretical problems. Please find here my recognition to your help, the quality and the effort you put in correcting my manuscripts.

Dr. Geert Brocks, thanks for assisting me in a couple of situations to deal with dutch paper work. Well, sometimes the language they use is not accessible even for dutch native speakers :-). Thanks for being there to listen to my talk rehearsals, whenever Paul or Maciej are away, your comments and suggestions were more than useful. I have had a great pleasure during all the discussions we had together, whether they are scientific, cultural, political or sports related. You always came up with something you have read or saw in the news. Geert, I never understood why I never got to switch and talk to you in dutch as I do with the next three guys. I am sorry!

Els Braker, Gerrit van Hummel and Theo Valkering (and your partners), your presence and availability at CMS were vital to all these years my family and I spent in Twente. Thanks for your help and being there to answer all my questions. Bedankt voor alle uw adviezen en het aantal discussies die hebben wij gehad. You guys, indirectly, helped me to keep practicing my dutch and improve it on the daily basis. Thanks a lot!

Along these years, I shared the office with Victor Popa. Together with Paul Rusu, both from Romania, our itinerary crossed in more than once. We had great time together. Many thanks guys for all the conversations we had, this includes the hot ones while discussing DFT and electronic structure calculations and programming, politics and sports. It was also with great pleasure that I have shared with you all those moments in down town or simply those many times going out together for fun, I really enjoyed them! Thanks for all those invitations to your places and the nice chats we have had. Many thanks for your friendship guys. Victor and Andrea Merticaru, your wife, thank you so much for all this many years we knew each other and particularly the first year when I came here to Enschede.

Petr Khomyakov, Volodymyr Karpan, Anton Starikov and Illya Marushchenko, your presence in the group was such a wonderful life experience for me, you added color to the group. The interesting scientific discussions I have had with you guys will always remain in my memories. Thanks guys for sharing all these moments together. Of course I won't forget the basketball, football and sailing we played and enjoyed together. Petr, thanks for sharing these many years at CMS group where we stayed for more than 4 years. Volodymyr, we have had so many discussions about spin

transport, thanks. Anton, I cannot forget your help about the transport code and taking care, days and nights, of the cluster for our calculations to run unhindered. I was delighted by all those chats on Linux and the Open Source world. With you guys, very often we shared our thoughts about politics in our countries.

New comers at the group, Suleyman Er, Gianluca Giovanetti, Danny Vanpoucke, Qinfang Zhang and Zhicheng Zhong, thank you for making the life so enjoyable. Gianluca, thanks for your friendship and welcoming me at your place in Leiden. I enjoyed a lot your Italian cooking. Danny, thanks a lot for your help and being available whenever I was looking for you, particularly all the translations into dutch including the “samenvatting” of this thesis. You too PengXiang Xu, we got to know first by e-mail during our collaboration and then during your visit to our group in Twente, thanks for your kindness.

Former members of the group, Prof. Dr. Jeroen van den Brink and Dr. Ke Xia, I am grateful to your help and all the scientific as well as general discussions we have had. Many thanks Jeroen for your kindness and availability. Former master students, Sijmen Gerritsen, Bart Husken and Geert Willem Spakman, I appreciated a lot your openness and your help. Thanks for the conversations we have had during your stay in Enschede and at FOM meetings.

I would like to thank all the members of the SMI group, led by Prof. Cock Lodder and Dr. Ronnie Jansen for inviting me to their local seminars and discover the experimental world. My gratitude goes also to MESA+ Institute for Technology for supporting my PhD project.

Je profite de cette occasion qui m'est offerte pour aussi adresser mes plus vifs remerciements à mes anciens promoteurs Prof. Mouloud Benakki et Dr. Claude Demangeat. Je tiens également à remercier les membres de ces deux groupes, notamment au LPCQ, Drs Said Bouarab, Hamid Bouzar, Ali Hadj-Larbi, Mourad Zemirli, Hamid Ziane, et à l'IPCMS, Mebarek Alouani, Hugues Dreyssé, Ahsan Khan, Salvador Meza-Aguilar et Bernard M'Passi Mabiala. Merci pour des discussions scientifiques et conseils précieux. Je veux en suis très reconnaissant. Je ne peux terminer cette longue liste sans en rajouter une, je pense notamment à tous mes amis qui sont éparpillé par ci par là: Abderhmane, Ali, Amar Kh., Arezki Ch., Boussad, Chabha, Djamel, Djindjin, Fadhila, Hacene, Hakim(2), Kamel(2), Karim(4), Leila, Mahdi, Menad, Meziane, Mohand(2), Moh Mehiri, Moussa, Rachid, Said, Samir, Seddik, Seghir, Yacine, Yuyu, ... je vous suis très reconnaissant pour votre amitié et pour toutes ces années qu'on avait passé ensemble du primaire à l'université. Dommage que cette distance n'ait pas arrangé les choses.

Finally, Dalila I want to thank you deep in my heart for giving me the most valuable and biggest support I could get, which of course I really needed during the course of this PhD. Simply thanks for standing by me. To you Masin, you were my lantern. Thanks you two guys for making home so warm! I owe everything to my parents who have educated me, were always there whenever I needed them and have given to me unrelenting support.

Enschede, June 2006
Mohand Talanana



ist of publications

- [1] On the transparency of metallic interfaces,
P. X. Xu, K. Xia, M. Zwierzycki, M. Talanana, P. J. Kelly,
Phys. Rev. Lett. **96**, 176602 (2006).
- [2] First-principles scattering matrices for spin-transport,
K. Xia, M. Zwierzycki, M. Talanana, P. J. Kelly and G. E. W. Bauer,
Phys. Rev. **B 73**, 064420 (2006); (cond-mat/0508373).
- [3] Pd/Ag and Pd/Au interface specific resistances and interfacial spin flipping,
C. Galinon, K. Tewolde, R. Loloee, W.-C. Chiang, S. Olson, H. Kurt, W. P. Pratt,
Jr., J. Bass, P. X. Xu, Ke Xia and M. Talanana,
Appl. Phys. Lett. **86**, 182502 (2005).
- [4] Ab initio study of the magnetic configurations on the (001) surfaces of binary
FePd and FeRh ordered alloys,
C. Dahmoune, S. Lounis, M. Talanana, M. Benakki, S. Bouarab and C. Demangeat,
J. Magn. Magn. Mat. **240** , 368 (2002).
- [5] Magnetic reconstructions at the surface of the B2 FeV alloy,
M. Talanana, M. Benakki, F. Amalou, S. Bouarab and C. Demangeat,
Eur. Phys. J. **B 22**, 497 (2001).
- [6] Origin of dead magnetic Fe overlayers on V(110),
J. Izquierdo, R. Robles, A. Vega, M. Talanana, and C. Demangeat,
Phys. Rev. **B 64**, 060404 (2001).
- [7] Parameter-free study of the electronic, magnetic and transport properties of a
model spin-valve transistor structure,
M. Talanana, M. Zwierzycki, P. J. Kelly and G. E. W. Bauer,
Phys. Rev. **B** (to be submitted).
- [8] Interface conductance and resistance of metallic multilayers,
M. Talanana, M Zwierzycki, P. J. Kelly, and G. E. W. Bauer,
Phys. Rev. **B** (to be submitted).

urriculum vitae

Name: Mohand Talanana

Date of birth: March 17th, 1973

Place of birth: Iadjemat, Tizi-Ouzou, Algeria

Marital status: Married

EDUCATION

- Oct. 2000:** **Master of Science (M.Sc.)** in Computational Solid State Physics: *Surface magnetism of binary ordered alloys and thin films on metallic substrates*
Supervisors: Pr. Dr. M. Benakki and Dr. C. Demangeat.
USTHB Algiers and Tizi-Ouzou Universities (Algeria) and IPCMS–Louis Pasteur University, Strasbourg (France).
- Jun. 1997:** **Bachelor of Science(B.Sc.)** in Solid State Physics, Tizi-Ouzou University (Algeria).
- Jun. 1991:** **Baccalaureate** (High School Diploma), Mathematics, Secondary School Azazga-Tizi-Ouzou (Algeria).

PROPOSITIONS

belonging to the PhD thesis

“Spin transport from first-principles: metallic multilayers and a model spin-valve transistor”

by

Mohand Talanana

1. Electrons have spin as well as charge, and this may make all the difference in future electronics. (G. A. Prinz; *Physics Today* **48**, 58(1995))
2. Spin, the “internal degree of freedom” of the electron, was suggested theoretically in early 1925 by Ralph Kronig. When Wolfgang Pauli heard about the idea, he criticized it severely. Largely due to Pauli’s criticism, Kronig decided not to publish his idea.
3. The complexity of the transition metals ($3d$, $4d$, ...) band structure requires a *first-principles* approach using density functional theory (DFT).
4. The *ab initio* TB–MTO wave-function matching scheme is a very efficient, flexible and physically transparent implementation of the Landauer–Büttiker formalism suitable for studying mesoscopic transport in inhomogeneous layered transition metal magnetic materials within DFT–LSDA.
5. The transmission probability through specular interfaces depends on the number of propagating states with positive group velocity, the mismatch of the group velocities (complex band structures) of the states on either side of the interface and matrix elements effects resulting from the symmetry of Bloch states.
6. A large orientation dependence of the interface transmission is predicted for Al|Ag, Al|Au and Fe|Cr majority spin channel. For the latter system, this anisotropy is very sensitive to interface disorder.
7. The orientation dependence of the interface transmission in Al|Ag can be explained within the limit of free electron model.
8. Unfortunately, there is a very limited amount of information about the detailed structure and nature of imperfections at metal–metal and/or metal–semiconductor interfaces available from experiment to guide theorists.
9. Disorder, counterintuitively, enhances substantially the transmission through the model GaAs|Fe|Cr|Fe|GaAs (001) spin-valve transistor structure.
10. Spintronics and magnetoelectronics, exciting and fascinating new nanoelectronics adventures.

Enschede, June 2006



Summary

The aim of this thesis, “*Spin transport from first-principles: metallic multilayers and a model spin-valve transistor*”, is to study theoretically the spin-dependent transport properties in nanoscale hybrid and inhomogeneous structures. Typical structures contain one or several interfaces formed by magnetic, nonmagnetic and/or semiconductor materials. Since, at the atomic scale, there are discontinuities in the electronic structure at the interfaces therefore a quantum mechanical treatment is the most appropriate framework for a rigorous description of electronic transport. The electronic structure and magnetic properties have been obtained using the surface Green’s function technique (SGF) implemented within the framework of tight-binding linear muffin-tin orbital (TB–LMTO) method in the atomic sphere approximation (ASA). The coherent potential approximation (CPA) method has been employed to model substitutional disorder at the interfaces. This first-principles approach allows us to take into account the complex nature of the transition metal electronic structures and to be able to describe interfaces realistically. To study coherent electronic spin transport in mesoscopic systems, we have developed a general, efficient and flexible method, suitable for Hamiltonians that can be represented in a tight-binding form and based on direct matching of the scattering region wave function to Bloch modes of the leads. This method is based on the Landauer–Büttiker formulation of transport theory using a first-principles TB–MTO implementation. Combined with the local spin density approximation (LSDA) of the density functional theory (DFT) and supercell technique, our approach has been applied to calculate the scattering matrices, entering the conductance and/or resistance calculations, for a variety of hybrid systems (ferromagnetic, nonmagnetic and/or semiconductor materials) of current interest.